CHEMICAL AND HYDROMECHANICAL CUE STRUCTURE IN THE CONTEXT OF TURBULENT ODOR PLUME TRACKING

A Thesis

Presented to

The Academic Faculty

By

Brian D. Dickman

In Partial Fulfillment

Of the Requirements for the Degree

Doctor of Philosophy in Civil Engineering

School of Civil and Environmental Engineering

Georgia Institute of Technology

December 2008

CHEMICAL AND HYDROMECHANICAL CUE STRUCTURE

IN THE CONTEXT OF TURBULENT ODOR PLUME TRACKING

Approved by:

Dr. Donald R. Webster, Advisor
School of Civil and Environmental Engineering
Georgia Institute of Technology

Dr. Marc J. Weissburg
School of Biology
Georgia Institute of Technology

Dr. Minami Yoda
School of Mechanical Engineering
Georgia Institute of Technology

Dr. Philip J. W. Roberts
School of Civil and Environmental Engineering
Georgia Institute of Technology

Dr. Terry W. Sturm
School of Civil and Environmental Engineering
Georgia Institute of Technology

Date Approved: 14 November 2008

Acknowledgements

I want to acknowledge and thank my advisor, Dr. Donald Webster, for direction, guidance and the opportunity to work on this project. His attention to the work in this study and availability made this thesis possible. Much gratitude also goes to Dr. Marc Weissburg, for insightful comments and interest in the subject. I was fortunate to find a project funded by the National Science Foundation awarded to Don and Marc.

This thesis would not have been possible without the extensive help of Jennifer Page in the School of Biology. There were many days things did not look so bright, but we have finally reached the end. No more blindfolds! In addition, Kimberlee Stephenson, from the School of Biology, assisted with crab trials and crab blindfolding.

I wish to express thanks and appreciation to my committee members, Dr. Philip J. W. Roberts, Dr. Terry W. Sturm and Dr. Minami Yoda, for their time and helpful comments on this study.

James Bullock in Civil and Environmental Engineering created the template for two animations of successful crab tracks. Andy Udell in the Mason Lab assisted greatly with equipment setup and installation of a 480-V outlet for the monster laser. The entire computer support staff for the School of Civil and Environmental Engineering deserves many accolades, reviving dead computers and hard drives throughout the last five years.

Lastly, I would like to mention my fellow graduate students in Environmental Fluid Mechanics for their friendship and humor throughout my time at Georgia Tech.

Table of Contents

Acknowledgements iii

List of Tables vii

List of Figures viii

List of Symbols xxix

Summary xxxiiii

Chapter 1 Introduction 1

Chapter 2 Literature Review 5

2.1 Fundamentals of turbulence 5
2.1.1 General scaling laws 7

2.2 Boundary layers 10

2.3 Passive scalar plumes 16
2.3.1 Time-averaged concentration and basic scaling arguments 19
2.3.2 Fluctuating concentration – instantaneous plume information 22

2.4 Olfactory navigation 26
2.4.1 Orientation Strategies 27
2.4.2 Animal tracking studies 30

2.5 Contributions of current research 37

Chapter 3 Experimental Description 41

3.1 Flow facility 41

3.2 Flow and plume parameters 43
3.2.1 Flow conditions 43
3.2.2 Plume parameters 44

3.3 Measurement system 46
3.3.1 Laser-induced fluorescence 46
3.3.1.1 3DLIF Resolution 49
3.3.2 3DLIF system setup 51
3.3.3 LIF Calibration 53
3.3.4 Lens vignette, pixel sensitivity and laser light attenuation 54
3.3.4.1 Magnification and optical distortion 60

3.3.4.2 Coordinate determination 64
3.3.4.3 Pixel-by-pixel calibration procedure 67
3.3.4.4 Quantifying the black level 67
3.3.5 Data Processing 70

3.4 Behavioral trials 72
3.4.1 Blindfolding of the crab specimens 72
3.4.2 Kinematic data and physical limitations 73

Chapter 4 Physical Characteristics of the Plumes 76

4.1 Continuous plume 77

4.2 Meandering plume 95

4.3 Pulsed plume 116

4.4 Conclusions 131

Chapter 5 Odorant Plume Tracking by Blue Crabs 134

5.1 Vector analysis of crab tracks 135

5.2 Kinematic analysis of successful blue crab searches 139
5.2.1 Displacement vector correlations 141
5.2.2 Displacement vector alignments and distributions 145
5.2.2.1 Continuous plume 145
5.2.2.2 Meandering plume 151
5.2.2.3 Pulsed plume 158
5.2.3 Stochastic nature of blue crab navigation 164

5.3 Extraction of concentration data for successful blue crab searches 168
5.3.1 Antennules zones 168
5.3.1.1 Continuous Plume Tracks 170
5.3.1.2 Meandering Plume Tracks 174
5.3.1.3 Pulsed Plume Tracks 177
5.3.2 Outer chemosensors 181
5.3.2.1 Validity of the Measurement Technique 185
5.3.3 Sampling Procedure Results 189
5.3.3.1 Continuous plume 193
5.3.3.2 Meandering plume 196
5.3.3.3 Pulsed Plume 198

Chapter 6 Summary and Discussion 202

6.1 Summary 202
6.1.1 Odorant concentrations at the antennules and mouth parts 202
6.1.2 Transverse movements and outer chemosensory organs 203

6.1.3 Hypotheses concerning blue crab tracking behavior 204
6.1.4 Statistics of crab tracking kinematics 205
6.1.5 Plume characteristics 206
6.1.5.1 Continuous plume 206
6.1.5.2 Meandering plume 207
6.1.5.3 Pulsed plume 208

6.2 Conclusions 208

6.3 Unique contributions and applications 209

6.4 Future directions 211

Appendix A Time traces of antennules sampling zone – Continuous plume 217

Appendix B Time traces for outer chemosensors – Continuous plume 225

Appendix C Time traces of antennules sampling zone – Meandering plume 236

Appendix D Time traces for outer chemosensors – Meandering plume 243

Appendix E Time traces of antennules sampling zone – Pulsed plume 253

Appendix F Time traces for outer chemosensors – Pulsed plume 259

References 267

List of Tables

TABLE		PAGE
2.1	Summary of the Smooth Bed Turbulent Mean Velocity Profile Regions	14
2.2	Selected Experimental Studies of Turbulent Plumes and Jets Summary	21
2.3	Summary of Pertinent Navigational Strategies	30
3.1	Summary of Flow Conditions	44
3.2	Summary of Plume Parameters	46
5.1	Summary of the Data Collected to Quantify Crab Response to Plume Structure	134
5.2	Conditions Necessary for a Change in Bias (Δ**BIAS = 1**)	186

List of Figures

FIGURE		PAGE
2.1	Figure 2.1 Overhead view of a continuous passive scalar release (neutrally buoyant red dye) into a developed turbulent boundary layer**.**	7
2.2	Universal smooth-bed mean-velocity relations plotted on wall variables for inner and overlap regions.	11
2.3	Approximate location of crab chemosensory locations. Photograph is a flow visualization of a blue crab tracking an odor source in a laboratory flume. Also visible is the diode backpack used to follow the motion of the crab (Photo courtesy of Marc Weissburg).	38
3.1	Flow visualization images of the (a) continuous plume, (b) pulsed plume, and (c) meandering plume.	42
3.2	Experimental setup for the 3DLIF system, as seen from the side of the flume. The horizontal lines represent the sequential locations of the laser scan.	47
3.3	Arrangement for the 3DLIF system, as seen from above.	48
3.4	Images for the camera (top) black level, (center) gray level, and (bottom) white level. The black level image was created by averaging 200 images collected in darkness with the lens cap on.	56
3.5	(a) Schematic of the sampling zone for determining the base power level for attenuation. The dimensions of the sampling zone are 5 mm by 5 mm. (b) Semi-log plot of pixel intensity levels after radial correction and sensitivity normalization.	59

3.6	Attenuation coefficient plot for an example calibration. Extinction coefficient dependence on concentration is linear for concentrations below about 150 μg/l.	60
3.7	Schematic showing the determination of the distance from the center of the camera sensor to the base grid point with 5.0 cm spacing.	62
3.8	Schematic that explains the calculation of the image distortion at the grid locations.	63
3.9	Comparison between distorted and undistorted grid placed at the floor of flume. The red dots are the known grid point locations and the black dots are the distorted image point locations.	64
3.10	Map of the distortion level for the elevation at the channel substrate.	65
3.11	Laser scan slices (red) and assumed planar sections (green). Deviations of the laser scan locations from the horizontal planes are due to scanning mirror angle, magnification, and refraction at the water surface.	66
3.12	Time records of intensity for two example pixel recordings of the continuous plume, which show the fluctuating noise level. The horizontal lines are the threshold values described in the text and act as a filter. Intensity samples at levels above the threshold values are assumed to be valid concentration bursts.	69
3.13	Raw average plume data for 7400 images at the nozzle centerline for the continuous release prior to filtering and application of the calibration.	71
3.14	Average concentration field corresponding to the intensity field shown in Figure 3.14 after application of the calibration. Contours are of relative concentration.	71
3.15	Photograph of a blindfolded crab prior to a behavioral trial.	75

4.1	Flow visualization of the continuous plume, which is created via a continuous iso-kinetic release into the test section of the saltwater flume. The view is from above, with the flow moving from left to right. The flow and plume parameters are defined in Tables 3.1 and 3.2.	85
4.2	Two examples of instantaneous concentration fields at z = 2.2 cm ($z/H = 0.10$) near the elevation of nozzle centerline.	86
4.3	Fields of average concentration, Θ/Θ_0, for the continuous plume at four elevations above the substrate: (a) 0.5 cm $(z/H = 0.02)$, (b) 2.2 cm $(z/H = 0.10)$, (c) 4.7 cm $(z/H = 0.22)$, and (d) 7.2 cm $(z/H = 0.34)$.	87-88
4.4	Fields of the standard deviation of the concentration fluctuations, θ'/Θ_0, for the continuous plume at four elevations above the substrate: (a) 0.5 cm $(z/H = 0.02)$, (b) 2.2 cm $(z/H = 0.10)$, (c) 4.7 cm $(z/H = 0.22)$, and (d) 7.2 cm $(z/H = 0.34)$.	89-90
4.5	Fields of intermittency factor γ based on a threshold of 1% of the source concentration (i.e., the probability that the concentration exceeds $0.01\Theta_0$) for the continuous plume at four elevations above the substrate: (a) 0.5 cm $(z/H = 0.02)$, (b) 2.2 cm $(z/H = 0.10)$, (c) 4.7 cm $(z/H = 0.22)$, and (d) 7.2 cm $(z/H = 0.34)$.	91-92
4.6	Transverse profiles for the continuous plume. (a) average concentration, and (b) standard deviation of the concentration fluctuations. Both sets of profiles correspond to the measurement plane that is nearest to the nozzle centerline elevation z_0 (z = 2.2 cm, z/H = 0.10).	93

4.7	Profiles for the continuous plume. (a) Streamwise profiles of the average concentration (squares) and standard deviation of the concentration fluctuations (filled circles) along the centerline of the plume, i.e. for $y = 0$ and $z = 2.2$ cm (every third data point shown for clarity), and (b) vertical profiles of average concentration along the plume centerline, i.e. for $y = 0$ and various distances from source.	94
4.8	Transverse plume width for the continuous plume based on the average concentration field. Theoretical curve is equation 4.9 with diffusivity determined from the data.	95
4.9	Flow visualization of the meandering plume, which is created via a continuous iso-kinetic release into the test section of the saltwater flume downstream of a cylindrical obstacle. The view is from above, with the flow moving from left to right. The flow and plume parameters are defined in Tables 3.1 and 3.2.	105
4.10	Two examples of instantaneous concentration fields for the meandering plume at $z = 2.2$ cm ($z/H = 0.10$) near the elevation of nozzle centerline.	106
4.11	Fields of average concentration, Θ/Θ_0, for the meandering plume at four elevations above the substrate: (a) 0.5 cm $(z/H = 0.02)$, (b) 2.2 cm $(z/H = 0.10)$, (c) 4.7 cm $(z/H = 0.22)$, and (d) 7.2 cm $(z/H = 0.34)$.	107-108
4.12	Fields of the standard deviation of the concentration fluctuations, θ'/Θ_0, for the meandering plume at four elevations above the substrate: (a) 0.5 cm $(z/H = 0.02)$, (b) 2.2 cm $(z/H = 0.10)$, (c) 4.7 cm $(z/H = 0.22)$, and (d) 7.2 cm $(z/H = 0.34)$.	109-110

4.13	Fields of intermittency factor γ based on a threshold of 1% of the source concentration (i.e., the probability that the concentration exceeds $0.01\Theta_0$) for the meandering plume at four elevations above the substrate: (a) 0.5 cm $(z/H = 0.02)$, (b) 2.2 cm $(z/H = 0.10)$, (c) 4.7 cm $(z/H = 0.22)$, and (d) 7.2 cm $(z/H = 0.34)$.	111-112
4.14	Sketch of the meandering plume model adapted from Gifford (1959).	113
4.15	Streamwise profiles of the meander width (open squares) and plume width (solid circles) for the meandering plume in the plane nearest the nozzle centerline elevation z_0 (z = 2.2 cm).	113
4.16	Transverse profiles of average concentration for the meandering plume for two distances from the source. The curves in color are profiles based upon equation 4.14 with coefficients determined from the data.	114
4.17	Transverse profiles of the standard deviation of the concentration fluctuations. The solid curve is a Gaussian model assuming two sources located at the transverse boundaries of the upstream cylinder.	115
4.18	Vertical profiles of average concentration along the plume centerline, i.e. for y = 0. The concentration field becomes homogeneously mixed in the vertical direction at approximately $x/H = 6$.	116
4.19	Flow visualization of the pulsed plume, which is created via a pulsed release into the test section of the saltwater flume. The view is from above, with the flow moving from left to right. The flow and plume parameters are defined in Tables 3.1 and 3.2	121
4.20	Two examples of instantaneous concentration fields for the pulsed plume at z = 2.2 cm ($z/H = 0.10$) near the elevation of nozzle centerline.	122

4.21	Fields of average concentration, Θ/Θ_0, for the pulsed plume at four elevations above the substrate: (a) 0.5 cm $(z/H = 0.02)$, (b) 2.2 cm $(z/H = 0.10)$, (c) 4.7 cm $(z/H = 0.22)$, and (d) 7.2 cm $(z/H = 0.34)$.	123-124
4.22	Fields of the standard deviation of the concentration fluctuations, θ'/Θ_0, for the pulsed plume at four elevations above the substrate: (a) 0.5 cm $(z/H = 0.02)$, (b) 2.2 cm $(z/H = 0.10)$, (c) 4.7 cm $(z/H = 0.22)$, and (d) 7.2 cm $(z/H = 0.34)$.	125-126
4.23	Fields of intermittency factor γ based on a threshold of 1% of the source concentration (i.e., the probability that the concentration exceeds $0.01\Theta_0$) for the pulsed plume at four elevations above the substrate: (a) 0.5 cm $(z/H = 0.02)$, (b) 2.2 cm $(z/H = 0.10)$, (c) 4.7 cm $(z/H = 0.22)$, and (d) 7.2 cm $(z/H = 0.34)$.	127-128
4.24	Transverse profiles for the pulsed plume. (a) average concentration, and (b) standard deviation of the concentration fluctuations. Both sets of profiles correspond to the measurement plane that is nearest to the nozzle centerline elevation z_0 (z = 2.2 cm, z/H = 0.10).	129
4.25	Profiles for the pulsed plume. (a) Streamwise profiles of the average concentration (squares) and standard deviation of the concentration fluctuations (filled circles) along the centerline of the plume, i.e. for y = 0 and z = 2.2 cm (every third data point shown for clarity), and (b) vertical profiles of average concentration along the plume centerline, i.e. for y = 0 and various distances from source.	130
4.26	Transverse width for the pulsed plume based on the average concentration field.	131

5.1	Schematic of the vectors used in crab kinematic analysis. The source vector **R** points from the crab to the source. The crab displacement vector **r** is the vector distance traveled by the crab in the time between recorded images, 0.21 s. The mean concentration gradient vector **G** is calculated from a simplified form of equation 2.18, and the mean velocity vector **U** points downstream.	136
5.2	Schematic showing the sign convention for the angle α between the source, displacement, and mean concentration gradient vectors.	138
5.3	Grayscale image of a typical crab track with the light paths shown as blue curves. Reflections off of the crab and the two LED's are visible at the far right. The blue curves trace the center of each LED during the navigation.	140
5.4	Detailed view of the crab displacement vector. Note that the displacement distance and angle α are independent of crab orientation.	141
5.5	Temporal autocorrelation function for crab step length in the *x*-direction. The time scale τ is found by fitting the data to equation 5.4 while forcing $R(0) = 1.0$. The decay time scale τ was 1.1 s, 1.4 s and 0.9 s for the continuous, meandering and pulsed plumes, respectively.	142
5.6	Temporal autocorrelation function for crab step length in the *y*-direction. Transverse step lengths lose correlation more rapidly than streamwise step lengths (shown in Figure 5.5), with the exception of the meandering plume where the crabs' transverse movements followed the plume meander.	144
5.7	Distribution of the angle between the crab displacement vector and the mean flow vector (**-U r** angle) and source vector ($\mathbf{R} \cdot \mathbf{r}$ angle) for the continuous plume. The Gaussian fit curve corresponds to the mean flow-displacement vector alignment.	149

5.8	Distribution in the transverse direction of small angular deviations between the source and displacement vectors (**R r**·angle) for the continuous plume. Shown are angles between -9 and 9 degrees only.	150
5.9	Overlay of crab tracks, shown as black, on the intermittency factor field for the continuous plume. The threshold for the intermittency factor was one percent of the source concentration.	150
5.10	Distribution of normalized dot product (Eq. 5.2) between various vectors for the continuous plume. **R** is the source vector, **G** is the mean concentration gradient vector, and **r** is the crab displacement vector.	151
5.11	Distribution of the angle between the crab displacement vector and the mean flow vector (**-U r** angle) and source vector (**R**·**r** angle) for the meandering plume. The Gaussian fit curve corresponds to the mean flow-displacement vector alignment.	155
5.12	Distribution in the transverse direction of small angular deviations between the source and displacement vectors (**R r**·angle) for the continuous plume. Shown are angles between -9 and 9 degrees only.	156
5.13	Overlay of crab tracks, shown as black, on the intermittency factor field for the meandering plume. The threshold for the intermittency factor was one percent of the source concentration.	157
5.14	Distribution of the normalized dot product (Eq. 5.2) between the source vector **R** and displacement vector **r** for the meandering plume.	158
5.15	Distribution of the angle between the crab displacement vector and the mean flow vector (**-U r**·angle) and source vector (**R r**·angle) for the pulsed plume. The Gaussian fit corresponds to the mean flow-displacement vector alignment for angles between -45 and 45 degrees**.**	162

5.16	Distribution in the transverse direction of small angular deviations between the source and displacement vectors (**R r**·angle) for the pulsed plume. Shown are angles between -9 and 9 degrees only.	163
5.17	Overlay of crab tracks, shown as black, on the intermittency factor field for the pulsed plume. The threshold for the intermittency factor was one percent of the source concentration.	163
5.18	Distribution of the normalized dot product (Eq. 5.2) between the source vector **R** and displacement vector **r** for the pulsed plume.	164
5.19	Overlay of simulated crab tracks (top) and experimental crab tracks (bottom) on the field of intermittency factor defined by a threshold of one percent of the source concentration for the continuous plume.	167
5.20	Location of the sampling zone for the crab antennules region.	169
5.21	Extracted time traces for crab **116O** in the continuous plume. (a) Concentration and elevation data. (b) Streamwise and transverse walking velocities and crab orientation angle data.	172
5.22	Extracted time traces for crab **1352Q** in the continuous plume. (a) Concentration and elevation data. (b) Streamwise and transverse walking velocities and crab orientation angle data.	173
5.23	Extracted time traces for crab **1286Q** in the meandering plume. (a) Concentration and elevation data. (b) Streamwise and transverse walking velocities and crab orientation angle data.	175
5.24	Extracted time traces for crab **1317S** in the meandering plume. (a) Concentration and elevation data. (b) Streamwise and transverse walking velocities and crab orientation angle data.	176

5.25	Extracted time traces for crab **1201M** in the pulsed plume. (a) Concentration and elevation data. (b) Streamwise and transverse walking velocities and crab orientation angle data.	178
5.26	Extracted time traces for crab **1358M** in the pulsed plume. (a) Concentration and elevation data. (b) Streamwise and transverse walking velocities and crab orientation angle data.	179
5.27	The location of the sampling zone for evaluating the signal at the walking appendage chemosensors. Due to shadowing concerns, concentration data are extracted at an earlier upstream location (green box in upper panel) and assumed to be advected to the chemosensory location (orange box in lower panel).	183
5.28	Definition sketch for the analysis of concentration centroid evolution. h_1 and h_2 are the concentration centroids within the sampling volumes at the measurement ($t_0 - \tau_D$) and sampling (t_0) times, respectively. The depth of the sampling volume is along the x_3 axis, which projects into and out of the paper and is not shown.	185
5.29	Location of test sampling boxes shown on the average concentration field for a) the continuous plume, b) the meandering plume, and c) the pulsed plume. The sampling boxes are 3.1 cm by 18.1 cm (in the streamwise and transverse directions, respectively), which is a typical size used in the analysis of the tracking trial data.	187
5.30	The probability of the change in bias being greater than zero for sampling boxes 1 and 2 (labeled in Figure 5.29).	188
5.31	The probability of the change in bias being greater than zero for sampling boxes 3 and 4 (labeled in Figure 5.29).	189

5.32	Evolution of the average and standard deviation of the concentration centroid for the two close sampling boxes labeled 1 and 2 in Figure 5.29 for a) the continuous plume, b) the meandering plume, and c) the pulsed plume.	191
5.33	Figure 5.33 Evolution of the average(equation 5.12) and standard deviation of the concentration centroid (equation 5.13) for the two far sampling boxes labeled 3 and 4 in Figure 5.29 for a) the continuous plume, b) the meandering plume, and c) the pulsed plume	192
5.34	Time traces of concentration centroid location, crab center, and side bias for crab **116O** in the continuous plume.	193
5.35	Time traces of concentration centroid location, crab center, and side bias for crab **1352Q** in the continuous plume.	194
5.36	Time traces of concentration centroid location, crab center, and side bias for crab **1286Q** in the meandering plume.	197
5.37	Time traces of concentration centroid location, crab center, and side bias for crab **1317S** in the meandering plume.	198
5.38	Time traces of concentration centroid location, crab center, and side bias for crab **1201M** in the pulsed plume.	199
5.39	Time traces of concentration centroid location, crab center, and side bias for crab **1358M** in the pulsed plume.	201
6.1	Two crab tracks shown on the field of intermittency factor based on a threshold of one percent of the source concentration. The tracks shown are for crabs 1363N (purple) and 1238Q (blue) in the continuous plume. The tracks consist of movements correlated in time between periodic major track adjustments.	215

6.2	Figure 6.2 Detail of crab track for crab 1363N from Figure 6.1. The track can be broken into short periods where turns occur between longer periods of correlated movement.	215
A1	(A) Crab **1305H** time trace of maximum and average relative concentrations at antennules and body elevation above substrate (cm). (B) Time traces of streamwise V_x velocity, transverse V_y velocity and crab angle with respect to the flow Ψ.	218
A2	(A) Crab **1364L** time trace of maximum and average relative concentrations at antennules and body elevation above substrate (cm). (B) Time traces of streamwise V_x velocity, transverse V_y velocity and crab angle with respect to the flow Ψ.	218
A3	(A) Crab **465L** time trace of maximum and average relative concentrations at antennules and body elevation above substrate (cm). (B) Time traces of streamwise V_x velocity, transverse V_y velocity and crab angle with respect to the flow Ψ.	219
A4	(A) Crab **105N** time trace of maximum and average relative concentrations at antennules and body elevation above substrate (cm). (B) Time traces of streamwise V_x velocity, transverse V_y velocity and crab angle with respect to the flow Ψ.	219
A5	(A) Crab **1305N** time trace of maximum and average relative concentrations at antennules and body elevation above substrate (cm). (B) Time traces of streamwise V_x velocity, transverse V_y velocity and crab angle with respect to the flow Ψ.	220

A6	(A) Crab **1221N** time trace of maximum and average relative concentrations at antennules and body elevation above substrate (cm). (B) Time traces of streamwise V_x velocity, transverse V_y velocity and crab angle with respect to the flow Ψ.	220
A7	(A) Crab **1271O** time trace of maximum and average relative concentrations at antennules and body elevation above substrate (cm). (B) Time traces of streamwise V_x velocity, transverse V_y velocity and crab angle with respect to the flow Ψ.	221
A8	(A) Crab **435O** time trace of maximum and average relative concentrations at antennules and body elevation above substrate (cm). (B) Time traces of streamwise V_x velocity, transverse V_y velocity and crab angle with respect to the flow Ψ.	221
A9	(A) Crab **1238Q** time trace of maximum and average relative concentrations at antennules and body elevation above substrate (cm). (B) Time traces of streamwise V_x velocity, transverse V_y velocity and crab angle with respect to the flow Ψ.	222
A10	(A) Crab **1399R** time trace of maximum and average relative concentrations at antennules and body elevation above substrate (cm). (B) Time traces of streamwise V_x velocity, transverse V_y velocity and crab angle with respect to the flow Ψ.	222
A11	(A) Crab **105R** time trace of maximum and average relative concentrations at antennules and body elevation above substrate (cm). (B) Time traces of streamwise V_x velocity, transverse V_y velocity and crab angle with respect to the flow Ψ.	223

A12	(A) Crab **1394R** time trace of maximum and average relative concentrations at antennules and body elevation above substrate (cm). (B) Time traces of streamwise V_x velocity, transverse V_y velocity and crab angle with respect to the flow Ψ.	223
A13	(A) Crab **1238R** time trace of maximum and average relative concentrations at antennules and body elevation above substrate (cm). (B) Time traces of streamwise V_x velocity, transverse V_y velocity and crab angle with respect to the flow Ψ.	224
B1	Crab **105N** time trace of transverse coordinates (cm) of the center of crab and concentration centroid. Side bias shown to indicate where two transverse coordinates differ by more than 0.5 cm.	226
B2	Crab **105R** time trace of transverse coordinates (cm) of the center of crab and concentration centroid.	226
B3	Crab **435O** time trace of transverse coordinates (cm) of the center of crab and concentration centroid.	227
B4	Crab **465L** time trace of transverse coordinates (cm) of the center of crab and concentration centroid.	227
B5	Crab **1221N** time trace of transverse coordinates (cm) of the center of crab and concentration centroid.	228
B6	Crab **1238Q** time trace of transverse coordinates (cm) of the center of crab and concentration centroid.	228
B7	Crab **1238R** time trace of transverse coordinates (cm) of the center of crab and concentration centroid.	229
B8	Crab **1271O** time trace of transverse coordinates (cm) of the center of crab and concentration centroid.	229
B9	Crab **1305H** time trace of transverse coordinates (cm) of the center of crab and concentration centroid.	230

B10	Crab **1305N** time trace of transverse coordinates (cm) of the center of crab and concentration centroid.	230
B11	Crab **1364L** time trace of transverse coordinates (cm) of the center of crab and concentration centroid.	231
B12	Crab **1394R** time trace of transverse coordinates (cm) of the center of crab and concentration centroid.	231
B13	Crab **1399R** time trace of transverse coordinates (cm) of the center of crab and concentration centroid.	232
B14	Crab **119O** time trace of transverse coordinates (cm) of the center of crab and concentration centroid.	232
B15	Crab **1357N** time trace of transverse coordinates (cm) of the center of crab and concentration centroid.	233
B16	Crab **1363N** time trace of transverse coordinates (cm) of the center of crab and concentration centroid.	233
B17	Crab **1314L** time trace of transverse coordinates (cm) of the center of crab and concentration centroid.	234
B18	Crab **1347L** time trace of transverse coordinates (cm) of the center of crab and concentration centroid.	234
B19	Crab **1331N** time trace of transverse coordinates (cm) of the center of crab and concentration centroid.	235
C1	(A) Crab **417K** time trace of maximum and average relative concentrations at antennules and body elevation above substrate (cm). (B) Time traces of streamwise V_x velocity, transverse V_y velocity and crab angle with respect to the flow, Ψ.	237

C2	(A) Crab **1034P** time trace of maximum and average relative concentrations at antennules and body elevation above substrate (cm). (B) Time traces of streamwise V_x velocity, transverse V_y velocity and crab angle with respect to the flow, Ψ.	237
C3	(A) Crab **1213Q** time trace of maximum and average relative concentrations at antennules and body elevation above substrate (cm). (B) Time traces of streamwise V_x velocity, transverse V_y velocity and crab angle with respect to the flow, Ψ.	238
C4	(A) Crab **1237Q** time trace of maximum and average relative concentrations at antennules and body elevation above substrate (cm). (B) Time traces of streamwise V_x velocity, transverse V_y velocity and crab angle with respect to the flow, Ψ.	238
C5	(A) Crab **1262Q** time trace of maximum and average relative concentrations at antennules and body elevation above substrate (cm). (B) Time traces of streamwise V_x velocity, transverse V_y velocity and crab angle with respect to the flow, Ψ.	239
C6	(A) Crab **1115Q** time trace of maximum and average relative concentrations at antennules and body elevation above substrate (cm). (B) Time traces of streamwise V_x velocity, transverse V_y velocity and crab angle with respect to the flow, Ψ.	239
C7	(A) Crab **1241Q** time trace of maximum and average relative concentrations at antennules and body elevation above substrate (cm). (B) Time traces of streamwise V_x velocity, transverse V_y velocity and crab angle with respect to the flow, Ψ.	240

C8	(A) Crab **1265S** time trace of maximum and average relative concentrations at antennules and body elevation above substrate (cm). (B) Time traces of streamwise V_x velocity, transverse V_y velocity and crab angle with respect to the flow, Ψ.	240
C9	(A) Crab **1351S** time trace of maximum and average relative concentrations at antennules and body elevation above substrate (cm). (B) Time traces of streamwise V_x velocity, transverse V_y velocity and crab angle with respect to the flow, Ψ.	241
C10	(A) Crab **1393S** time trace of maximum and average relative concentrations at antennules and body elevation above substrate (cm). (B) Time traces of streamwise V_x velocity, transverse V_y velocity and crab angle with respect to the flow, Ψ.	241
C11	(A) Crab **1336S** time trace of maximum and average relative concentrations at antennules and body elevation above substrate (cm). (B) Time traces of streamwise V_x velocity, transverse V_y velocity and crab angle with respect to the flow, Ψ.	242
C12	(A) Crab **1306S** time trace of maximum and average relative concentrations at antennules and body elevation above substrate (cm). (B) Time traces of streamwise V_x velocity, transverse V_y velocity and crab angle with respect to the flow, Ψ.	242
D1	Crab **417K** time trace of transverse coordinates (cm) of the center of crab and concentration centroid. Side bias shown to indicate where two transverse coordinates differ by more than 0.5 cm.	244
D2	Crab **1034P** time trace of transverse coordinates (cm) of the center of crab and concentration centroid	244

D3	Crab **1115Q** time trace of transverse coordinates (cm) of the center of crab and concentration centroid	245
D4	Crab **1213Q** time trace of transverse coordinates (cm) of the center of crab and concentration centroid	245
D5	Crab **1237Q** time trace of transverse coordinates (cm) of the center of crab and concentration centroid	246
D6	Crab **1214Q** time trace of transverse coordinates (cm) of the center of crab and concentration centroid	246
D7	Crab **1262Q** time trace of transverse coordinates (cm) of the center of crab and concentration centroid	247
D8	Crab **1265S** time trace of transverse coordinates (cm) of the center of crab and concentration centroid	247
D9	Crab **1306S** time trace of transverse coordinates (cm) of the center of crab and concentration centroid	248
D10	Crab **1336S** time trace of transverse coordinates (cm) of the center of crab and concentration centroid	248
D11	Crab **1351S** time trace of transverse coordinates (cm) of the center of crab and concentration centroid	249
D12	Crab **1393S** time trace of transverse coordinates (cm) of the center of crab and concentration centroid	249
D13	Crab **105O** time trace of transverse coordinates (cm) of the center of crab and concentration centroid	250
D14	Crab **122O** time trace of transverse coordinates (cm) of the center of crab and concentration centroid	250
D15	Crab **1249O** time trace of transverse coordinates (cm) of the center of crab and concentration centroid	251
D16	Crab **1305O** time trace of transverse coordinates (cm) of the center of crab and concentration centroid	251

D17	Crab **1336O** time trace of transverse coordinates (cm) of the center of crab and concentration centroid	252
E1	**(**A) Crab **112M** time trace of maximum and average relative concentrations at antennules and body elevation above substrate (cm). (B) Time traces of streamwise V_x velocity, transverse V_y velocity and crab angle with respect to the flow, Ψ .	254
E2	**(**A) Crab **122T** time trace of maximum and average relative concentrations at antennules and body elevation above substrate (cm). (B) Time traces of streamwise V_x velocity, transverse V_y velocity and crab angle with respect to the flow, Ψ	254
E3	**(**A) Crab **1209T** time trace of maximum and average relative concentrations at antennules and body elevation above substrate (cm). (B) Time traces of streamwise V_x velocity, transverse V_y velocity and crab angle with respect to the flow, Ψ	255
E4	**(**A) Crab **1237T** time trace of maximum and average relative concentrations at antennules and body elevation above substrate (cm). (B) Time traces of streamwise V_x velocity, transverse V_y velocity and crab angle with respect to the flow, Ψ	255
E5	**(**A) Crab **1241T** time trace of maximum and average relative concentrations at antennules and body elevation above substrate (cm). (B) Time traces of streamwise V_x velocity, transverse V_y velocity and crab angle with respect to the flow, Ψ	256
E6	**(**A) Crab **1269T** time trace of maximum and average relative concentrations at antennules and body elevation above substrate (cm). (B) Time traces of streamwise V_x velocity, transverse V_y velocity and crab angle with respect to the flow, Ψ	256

E7	**(**A) Crab **1271M** time trace of maximum and average relative concentrations at antennules and body elevation above substrate (cm). (B) Time traces of streamwise V_x velocity, transverse V_y velocity and crab angle with respect to the flow, Ψ	257
E8	**(**A) Crab **1341T** time trace of maximum and average relative concentrations at antennules and body elevation above substrate (cm). (B) Time traces of streamwise V_x velocity, transverse V_y velocity and crab angle with respect to the flow, Ψ	257
E9	**(**A) Crab **1354T** time trace of maximum and average relative concentrations at antennules and body elevation above substrate (cm). (B) Time traces of streamwise V_x velocity, transverse V_y velocity and crab angle with respect to the flow, Ψ	258
E10	**(**A) Crab **1395T** time trace of maximum and average relative concentrations at antennules and body elevation above substrate (cm). (B) Time traces of streamwise V_x velocity, transverse V_y velocity and crab angle with respect to the flow, Ψ	258
F1	Crab **112M** time trace of transverse coordinates (cm) of the center of crab and concentration centroid. Side bias shown to indicate where two transverse coordinates differ by more than 0.5 cm.	260
F2	Crab **122T** time trace of transverse coordinates (cm) of the center of crab and concentration centroid.	260
F3	Crab **1209T** time trace of transverse coordinates (cm) of the center of crab and concentration centroid.	261
F4	Crab **1237T** time trace of transverse coordinates (cm) of the center of crab and concentration centroid.	261

F5	Crab **1241T** time trace of transverse coordinates (cm) of the center of crab and concentration centroid.	262
F6	Crab **1269T** time trace of transverse coordinates (cm) of the center of crab and concentration centroid.	262
F7	Crab **1271M** time trace of transverse coordinates (cm) of the center of crab and concentration centroid.	263
F8	Crab **1341T** time trace of transverse coordinates (cm) of the center of crab and concentration centroid.	263
F9	Crab **1354T** time trace of transverse coordinates (cm) of the center of crab and concentration centroid.	264
F10	Crab **1395T** time trace of transverse coordinates (cm) of the center of crab and concentration centroid.	264
F11	Crab **105M** time trace of transverse coordinates (cm) of the center of crab and concentration centroid.	265
F12	Crab **461M** time trace of transverse coordinates (cm) of the center of crab and concentration centroid.	265
F13	Crab **471M** time trace of transverse coordinates (cm) of the center of crab and concentration centroid.	266
F14	Crab **1249M** time trace of transverse coordinates (cm) of the center of crab and concentration centroid.	266

List of Symbols

$\mathbf{a}$	drift coefficient in vector-valued Langevin equation
$\mathbf{B}$	diffusion tensor in vector-valued Langevin equation
C	average concentration
C_0	source concentration
C_{avg}	non-zero average concentration within a measurement zone
C_{max}	maximum concentration within a measurement zone
d	plume source size
$d\mathbf{w}$	vector-valued Weiner process (random variable)
D	molecular diffusivity
D_y	maximum meander amplitude
$\mathbf{G}$	mean concentration gradient
h	transverse coordinate of the instantaneous concentration centroid within a given volume
H	average flow depth
H_B	height of concentration centroid measurement zone
I	digital pixel intensity value
k_s	roughness length scale for developed boundary layer
K	eddy diffusivity (scalar form)
L_B	Batchelor length scale ($\eta Sc^{-1/2}$)
L_c	cloud size
ℓ	turbulent integral length scale
M	total release mass within a cloud
p	turbulent pressure fluctuation

$\tilde{P}$	instantaneous pressure
P	average pressure/laser power
q_{nozzle}	source volumetric flow rate
R	radial distance from camera centerline to a given pixel
$R(t)$	autocorrelation function
R'	apparent distance from camera centerline to a given pixel
$\mathbf{r}$	crab displacement vector
$\mathbf{R}$	source vector
Re	Reynolds number
Sc	Schmidt number (ν/D)
t	time
T_m	meander period
u_i	component of turbulent velocity fluctuation
u'	root-mean-square of turbulent velocity
u_*	shear velocity
$\hat{u}$	phase-average velocity fluctuation at phase lag τ_m
U_i	component of average velocity
$\tilde{U}_i$	component of instantaneous velocity
U_m	boundary layer maximum average velocity
$\mathbf{U}$	mean flow vector
V_x	streamwise crab velocity
V_y	transverse crab velocity
w	width of concentration centroid measurement zone
x	longitudinal coordinate

x_c	downstream distance from a cylinder
x_i	Cartesian coordinate
y	transverse coordinate
z	vertical coordinate
z_0	nozzle centerline vertical coordinate
α	angle between two vectors $\mathbf{V}_1$ and $\mathbf{V}_2$.
α_c	pixel calibration coefficient of proportionality
β	attenuation coefficient of Rhodamine 6G in artificial seawater
γ	intermittency of scalar concentration
δ	length scale for developed boundary layer
δ_s	boundary layer displacement thickness
ε	turbulent kinetic energy dissipation rate/eddy diffusivity
ε_{ij}^t	eddy diffusivity (tensor form)
θ	scalar concentration fluctuation
θ'	standard deviation of the concentration fluctuations
θ_t	intermittency γ threshold concentration
$\tilde{\Theta}$	instantaneous scalar concentration
Θ	average scalar concentration
Θ_0	source concentration
ϑ	power-law exponent for developed boundary layer
κ	von Kármán constant for log-law boundary layer
λ	extinction coefficient of laser light through Rhodamine 6G in artificial seawater
η	Kolmogorov length scale $\left(\left(\nu^3 / \varepsilon\right)^{1/4}\right.$

ν	kinematic viscosity
ρ	fluid density
σ	standard deviation of transverse average concentration profile
$\boldsymbol{\tau}$	auto correlation decay time scale for crab movements
$\boldsymbol{\tau_D}$	time advance used in outer chemosensor sampling technique
$\boldsymbol{\tau}_m$	time lag used for calculating phase-average velocity fluctuation
$\boldsymbol{\Psi}$	crab inclination with respect to mean flow vector
χ	scalar variance dissipation rate

Summary

The main focus of this study was to quantify the chemical signals received by a blue crab (*Callinectes sapidus*) while tracking an odorant source in a laboratory flume. To make a direct linkage between tracking behavior and the odorant concentration signal, we developed a measurement system to quantify the instantaneous concentration field surrounding actively tracking blue crabs. A three-dimensional laser-induced fluorescence (3DLIF) system was designed and constructed to measure odorant concentrations around crabs tracking three source types: a continuous release with exit velocity matching the mean local velocity in the flume; a continuous release with a meander created by an upstream cylinder; and a pulsed release switching on and off and with the same mass flow rate as the other two plume types. The meandering and pulsed plumes were introduced to observe the effects of large-scale spatial (meandering) and temporal (pulsed) intermittency on crab tracking. Simultaneous with the chemical concentration measurements, crab position data was recorded for kinematic analysis during post-processing. In addition, concentration measurements were collected for the three plume types without crabs present in order to quantify the statistical characteristics of the plume structure.

The concentration signals arriving at the antennules and outer chemosensory organs, most notably the legs, were targeted due to the hypotheses that concentration bursts at the antennules mediate upstream movement and that spatial contrast at the leg chemosensors mediates turning. A sampling zone was placed in front of the crab's mouth parts and aligned with the crab carapace orientation to extract odorant bursts at the antennules. The

data generally showed an increase in upstream walking speed when high concentration bursts arrive at the antennules location, which agrees with the hypothesis. Measurement of the odorant concentration at the outer chemosensors was less direct and involved placing a box upstream of the crab and sampled earlier in time in order to avoid shadowing interference and reflections. Based on the signal at the upstream sampling box, a general bias for turning was observed. Crabs casted transversely in response to the directional bias extracted from the upstream sampling box. A statistical analysis of crab behavioral response to concentrations at the antennules and outer chemosensors can be found in a (future) companion thesis written by Jennifer Page in the School of Biology.

Statistical measures of the data collected in the absence of blue crabs were calculated for each plume type, including the time-averaged concentration, the standard deviation of the concentration fluctuations, intermittency factor, and the average plume width. For the three plume types, the standard deviation of the concentration fluctuations was greater than the time-averaged concentration, as time records consisted of intermittent high concentration bursts interspersed with concentrations close to zero. For the continuous plume, the time-averaged concentration displayed Gaussian profiles centered on the nozzle centerline. The meandering plume data conformed to the meandering plume model of Gifford (1959) modified for an induced pseudo-periodic meander. The pulsed plume displayed characteristics that were intermediate between the cloud dispersion model (Townsend 1951, Chatwin and Sullivan 1979) and the Gaussian dispersion model for a continuous release.

Chapter 1

Introduction

To investigate behavioral mechanisms used by organisms to find resources in turbulent environments, tracking studies have been conducted for many organisms (reviewed in Weissburg 2000, Vickers 2000, Koehl 2006). Tracking trials generally consist of placing an animal in a controlled environment, releasing an attractant odorant upstream or upwind, and observing subsequent tracking behavior. These studies reveal much about behavioral response and subsequent navigational patterns, i.e. taxis, yet offer little more than a qualitative idea of the olfactory stimulus experienced by the tracking organism.

To determine precisely how a tracking animal is responding to a given stimulus, the instantaneous concentration field of the odorant must be quantified in a non-intrusive manner. Odorant concentration at the location of the olfactory organs needs to be measured at spatial and temporal scales that are consistent with organism sensing abilities. A minimally intrusive measurement technique is required because a physical probe usually disturbs the flow and often can only collect data at a single point. The development of laser-induced fluorescence (LIF) permits a non-intrusive quantitative measurement of instantaneous concentration fields (Koochesfahani and Dimotakis 1985). Laser-induced fluorescence involves the use of low concentrations of a tracer dye, or fluorophore, that excites at a molecular level when exposed to laser light. As long as the odorant and tracer diffuse at the same rate and decay minimally, the odorant plume is identical to that of the fluorophore.

A logical progression is to combine planar laser-induced fluorescence (PLIF) with an actively tracking organism to directly correlate navigational behavior with odorant concentration at olfactory organs. Many factors have restricted combined PLIF-organism studies, however. Shadowing of the laser by portions of the organism body can create gaps in the concentration time record at shaded chemosensors. Animals generally track while shifting the vertical location of olfactory organs through walking, flicking of antennules, or presumed attempts to sample in the vertical direction. Further, the olfactory systems of some arthropods, such as blue crabs, are not limited to a single location, such as the antennules, but are distributed across the animal's body. In addition, the laser light used in PLIF is intense and can disorient animals. For many of these reasons, simultaneous PLIF has been restricted to the analysis of one tracking animal, a stomatopod (*Hemisquilla ensiguera californica*), with a "simple" olfactory system consisting of a pair of antennules, each with a central aesthetasc array (Mead 2002). Planar laser-induced fluorescence enabled the measurement of concentrations along the aesthetasc array for wave-driven and unidirectional flow. Only seven plume tracks (out of ninety) could be used in the analysis due to problems associated with coordinating PLIF with an actively tracking animal. Nevertheless, the measurements showed that navigating stomatopods encountered odor filaments more frequently in the wave-driven compared to unidirectional flow (Mead et al. 2003).

Callinectes sapidus has two types of sensory organs capable of detecting odorant and bulk flow direction. Odorant-detecting organs essentially smear the small scale structure of plumes through movement, such as flicking or walking. Neural pooling of the odorant signal by arrays of setae (Gomez and Atema 1996, Cate and Derby 2001) could also blur

small-scale plume features. The odorant stimulus at the antennules (located near the mouth region) is responsible for maintaining upstream movement (Keller et al. 2003, Jackson et al. 2007). Chemosensors on the legs are spatially separated and allow perception of a contrast between sides of the crab's body. Navigational turns based on the spatial contrast are believed to occur when a bilateral contrast is sensed, a response referred to as tropotaxis. Combined sensory information from the chemosensors and mechanosensory organs permits the crab to track a source using odor-gated rheotaxis, or upstream movement modulated by chemosensory odorant input (Weissburg and Zimmer-Faust 1993). Since sampling occurs at multiple elevations and transverse locations, any attempt to quantify the stimulus patterns experienced by a tracking blue crab would necessarily have to include more than a single measurement plane. In addition, blue crabs can alter the position of their antennules and thereby enable perception of variability in the vertical direction. To adequately resolve the concentration field experienced by a tracking blue crab, a three-dimensional, time-resolved measurement system is needed. Three-dimensional laser-induced fluorescence (3DLIF) is an experimental technique that builds upon PLIF and can be used to measure the pseudo-instantaneous concentration field (Yoda et al. 1994, Tian and Roberts 2003, Van Vliet et al. 2004).

The objective of this thesis is to describe a 3DLIF system for use in a saltwater laboratory flume with an actively tracking blue crab. Three source release types, continuous, meandering and pulsed, will be used to determine the effects of spatial and temporal intermittency upon search behavior. Spatial intermittency was introduced through the creation of a meandering plume induced by a cylinder upstream of the source. Temporal

intermittency was created through alternatively turning on and off the source. The concentration data and stimulus signal will be compared to individual behavior tracks to provide new insights into the odorant tracking behavior of blue crabs. To support the results and conclusions of the simultaneous concentration and behavior measurements, statistical descriptions of the odorant plumes will be provided for the three release types using data collected in the absence of tracking crabs.

Chapter 2

Literature Review

In turbulent environments, organisms release chemicals in the form of clouds or plumes, which are advected downstream by the mean flow, dispersed by the fluid turbulence and diffused molecularly (Figure 1.1 in Moore and Crimaldi 2004). Many animals are able to track chemical signals to a source within these chaotic environments (Weissburg 2000, Vickers 2000). In addition to chemosensory sampling, many tracking organisms use mechanical sensation to determine the mean flow direction, as the source location can be assumed in the upstream direction. Understanding these processes requires a quantification of the signals available to the searcher, in particular the spatial and temporal characteristics of the turbulent concentration field. To lay the foundation for the current research effort, this chapter reviews current knowledge about turbulence mixing, turbulent boundary layers, chemical odor plumes, and olfactory navigation.

2.1 Fundamentals of turbulence

Although the Navier-Stokes equations mathematically describe fluid motion, the non-linear nature of the advective velocity terms and a high dependence upon initial conditions lead to non-unique solutions and what appears to be a random flow field. Despite apparent instantaneous randomness, the statistics of the flow field can be determined and in some cases modeled quite accurately. Osborne Reynolds was the first to approach the problem of turbulence in a statistical manner, through the decomposition of the velocity ($\tilde{U} = U + u$) and pressure ($\tilde{P} = P + p$) variables into an average and a fluctuating component. Inserting the Reynolds decomposition into the incompressible

Navier-Stokes equations and time-averaging each term results in the Reynolds-averaged Navier-Stokes equations (RANS):

$$\frac{\partial U_i}{\partial t} + U_j \frac{\partial U_i}{\partial x_j} = -\frac{1}{\rho}\frac{\partial P}{\partial x_i} + \frac{\partial}{\partial x_j}\left[-\overline{u_i u_j} + \nu \frac{\partial U_i}{\partial x_j} \right] \tag{2.1a}$$

$$\frac{\partial U_i}{\partial x_i} = \frac{\partial u_i}{\partial x_i} = 0 \tag{2.1b}$$

Time- or ensemble-averaging is denoted by an overbar. Reynolds-averaging introduces additional variables, called the Reynolds stress tensor $\overline{u_i u_j}$, which includes six independent terms for which there are no additional equations. This creates an indeterminate situation referred to as the closure problem (Tennekes and Lumley 1972).

The non-linear nature of the Navier-Stokes equations is physically reflected by the wide range of eddy sizes, or scales, present in turbulent flows. Kinetic energy of the mean flow transfers into turbulent kinetic energy through interaction of the mean shear rate with the larger eddy sizes, represented by a characteristic length scale, ℓ. A cascade of energy occurs, where kinetic energy is transferred to progressively smaller eddy sizes through vortex tilting and stretching. Viscosity becomes important at the smallest scales where the turbulent kinetic energy is dissipated as heat at a rate referred to as the dissipation rate, ε. In stationary homogeneous isotropic turbulence, where the statistics of the velocity fluctuations u_i are independent of space and time, the turbulent energy dissipation rate can be estimated by $\varepsilon = u'^3/\ell$, where u' is the root-mean square, or standard deviation, of the velocity fluctuations (Tennekes and Lumley 1972).

Advection leads to the filamentous structure of passive scalars observed in turbulent plumes and shown in Figure 2.1. In analogy with the cascade of turbulent eddies, passive scalar filaments are stretched, compressed and folded until reaching a size sufficiently small for concentration gradients to grow to the point where molecular diffusion dominates. For most naturally-occurring passive chemical species in water, the smallest scales of the scalar structure are much smaller than those of the velocity field. For a passive scalar, the rate of dissipation refers to the destruction of the variance of the scalar fluctuations.

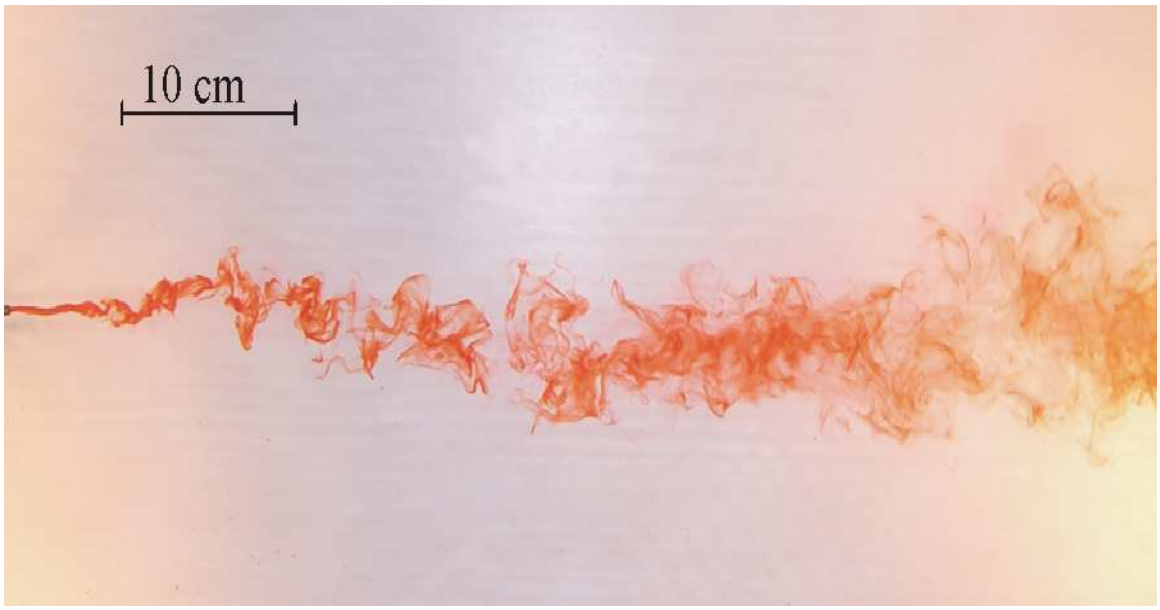

Figure 2.1 Overhead view of a continuous passive scalar release (neutrally buoyant red dye) into a developed turbulent boundary layer (water flow from left to right), flow depth H = 210 mm and average velocity 50 mm/s. Release height at 25 mm above channel bed.

2.1.1 General scaling laws

Building upon turbulent concepts advanced by Taylor, Richardson, and others, Kolmogorov (1941) presented a groundbreaking theory, now referred to as K41, of the turbulent velocity field. K41 consists of a group of scaling arguments based upon

assumed isotropy at the smaller turbulent scales and a consequent statistical theory derived from dimensional considerations. The assumption of isotropy at the smallest scales, or universality, requires a theoretical infinite Reynolds number ($U\ell/\nu$). Presumably, with a sufficiently high Reynolds number, the anisotropy of the larger scales due to boundary conditions becomes lost as energy is transferred to smaller and smaller scales. Using dimensional arguments, K41 defines a scale at which turbulent kinetic energy is dissipated at large Reynolds number, the Kolmogorov scale:

$$\eta = \left(\nu^3 / \varepsilon\right)^{1/4} \tag{2.2}$$

At very large Reynolds number, a range of scales exists that are much smaller than the integral length scale, yet much larger than the Kolmogorov scale (i.e. for wavenumbers in the range $1/\ell << k << 1/\eta$), termed the inertial subrange. Theoretically, the inertial subrange in flows with large Reynolds number simply acts to transfer energy from the large scales of the flow to the dissipative range, close to the Kolmogorov scale. The Reynolds number restriction has been shown to be more limiting on the inertial subrange than for the dissipation range (Batchelor and Townsend 1956).

Similar scaling arguments can be made concerning the statistics of the passive scalar field in isotropic turbulence. Diffusion of a passive scalar quantity differs from that of momentum; consequently, mixing dynamics are dependent upon the molecular diffusivity D of the scalar quantity into the ambient fluid. Scaling arguments thus involve another dimensionless number, the Schmidt number $Sc = \nu / D$, relating the molecular diffusivity of momentum, or kinematic viscosity, to the diffusivity of the chemical species.

Obukhov (1949) and Corrsin (1951) used scaling arguments analogous to those of K41 to describe the statistics of passive scalar fluctuations at high Reynolds numbers with low Schmidt number, or Kolmogorov-Obukhov-Corrsin (KOC) theory. At high Reynolds numbers, the large passive scalar scales are again assumed anisotropic with isotropy approached as scale size decreases. Scalar energy, or the passive scalar concentration variance, is transferred down a cascade towards the smallest filaments where the variance is eliminated through molecular diffusion. Batchelor (1959) extended KOC theory to include solutes or other passive scalars with high Schmidt numbers ($Sc >> 1$) and determined a length scale, since termed the Batchelor scale, for the smallest scalar variance dissipative scales:

$$L_B = \left(\nu D^2 / \varepsilon\right)^{1/4} \tag{2.3}$$

The Batchelor and Kolmogorov length scales are related through the Schmidt number $L_B = \eta Sc^{-1/2}$. The Batchelor scale is smaller than the smallest turbulent eddies, represented by the Kolmogorov scale η, and leads to a second convective range of wavenumbers. Within the viscous-convective range, the scales are small enough to dissipate kinetic energy through viscosity, yet are larger than the diffusive scales of the scalar variance. Dispersion occurs through viscous motion at scale sizes much larger than the Batchelor scale yet smaller than the Kolmogorov scale. Batchelor derived a second scaling law for the scalar variance spectrum in the viscous-convective range, or what he termed "convection subrange B", for wavenumbers $1/L_B >> k >> 1/\eta$. Batchelor's viscous-convective range relationship depends upon a persistent local strain rate, the scalar dissipation rate, and the Schmidt number:

$$G(k) = A_0 \chi (\nu/\varepsilon)^{1/2} k^{-1} \exp\left[-A_0 (kL_B)^2 \right] \quad (2.4)$$

Where A_0 is a dimensionless constant that depends upon the minimal strain-rate and is assumed locally constant (persistent). For wavenumbers $k << 1/L_B$, the exponential term approaches one and equation 2.4 reduces to $G(k) = A_0 \chi (\nu/\varepsilon)^{1/2} k^{-1}$. Thus, in the viscous-convective range, the spectrum is expected to follow an inverse relationship with the wavenumber. Unlike for KOC or RSH, the assumption of high Reynolds number is not required for the existence of a universal viscous-convective range. Experimental and numerical validation of Batchelor's power law for his relationship in the viscous-convective range has been inconclusive (Warhaft 2000, Dasi 2004), partly due to resolution requirements for measurements and simulations.

2.2 Boundary layers

In boundary layers, organisms with size much larger than the Kolmogorov scale contend with fluctuating flow fields with mean velocity gradients. The mean characteristics of developed boundary layers within channels or in the atmosphere are often homogeneous in the transverse and longitudinal directions, yet inhomogeneous vertically. For a boundary layer with a smooth bed, the mean velocity profile can be broken into two distinct regions: an inner region where viscosity has a dominant influence and an outer region where free-stream variables dominate. An overlap occurs between the inner and outer regions, where both viscosity and inertia are important.

Together, the model for the inner and overlap regions is called the law-of-the-wall and includes the viscous sublayer, buffer zone, and overlap region, usually referred to as the log-law layer (see Figure 2.3). The viscous sublayer velocity profile can be derived

simply by assuming laminar flow within a constant shear stress region very close to the wall. Dimensional analysis for the viscous sublayer results in the following velocity distribution:

$$u^+ = \frac{U}{u_*} = y^+ = \frac{u_* y}{\nu} \tag{2.5}$$

Experiments have shown that equation 2.5 is valid for $y^+ < 5$.

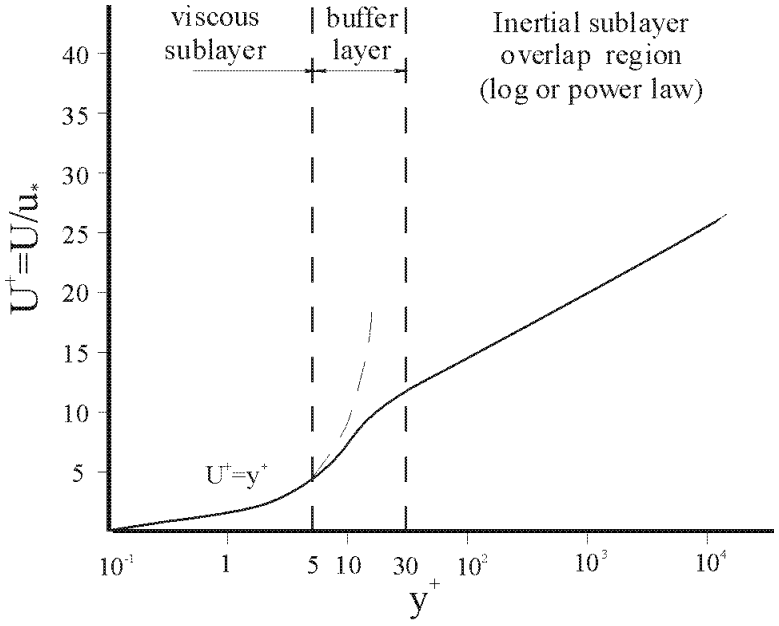

Figure 2.2 Universal smooth-bed mean-velocity relations plotted on wall variables for inner and overlap regions.

Likewise, a mathematical description of the overlap region can be determined through dimensional considerations by assuming the velocity gradient to be a function of inner wall variables and a universal function Φ of y^+ along with Reynolds number:

$$\frac{\partial U}{\partial y} = \left(u_* / y\right)\Phi\left(y^+, Re\right) \tag{2.6}$$

Using an eddy-viscosity model, von Kármán and Prandtl (see Chapt. 6 of White 2005) proposed a length scale termed the mixing length. The mixing length assumption yields a universal, compact mathematical form for the velocity profile:

$$U^+ = \frac{1}{\kappa}\ln y^+ + B \tag{2.7}$$

Although the eddy-viscosity concept is flawed except for the simplest flows (Tennekes and Lumley 1972), subsequent experimental results over the past 70 years have supported the law-of-the-wall for two-dimensional boundary layers.

Despite strong empirical evidence supporting the log law, debate has occurred in recent years whether the overlap layer is best fit by the log law or a power law (Pope 2000, Buschmann and Gad-el-Hak 2003). Another valid form of the velocity profile between the viscous sublayer and the outer region can be derived through the assumption of a power law for the universal function Φ:

$$\Phi\left(y^+\right) = A\left(y^+\right)^{\vartheta} \tag{2.8}$$

with both A and ϑ depending on the Reynolds number. Barenblatt (1993) proposed an asymptotic expansion for the coefficient ϑ:

$$\vartheta = a_1\xi + a_2\xi^2 + \ldots \tag{2.9}$$

Based upon the fractal properties of vortex dissipative structures in fully developed turbulent flows, Barenblatt assumed $\xi = 1/\left(\ln(Re)\right)$ to derive:

$$\vartheta = 3/\left(2\ln\left(Re\right)\right) \tag{2.10}$$

Equation 2.10 with the coefficient A determined by least squares (Barenblatt and Prostokishin 1993) results in the following power law for the overlap region:

$$\Phi\left(y^{+}\right) = \left(\frac{1}{\sqrt{3}}\ln\left(Re\right) + 2.5\right) y^{+\left[3/\left(2\ln Re\right)\right]} \tag{2.11}$$

Barenblatt (1993) determined a value of 0.425 for the von Kármán constant by taking the limit of equation 2.11 as Reynolds number and y^{+} approach infinity. Zagarola et al. (1997) determined the coefficient to the second power on ξ:

$$\vartheta = \frac{1.085}{\ln Re} + \frac{6.535}{\left(\ln Re\right)^{2}}$$

From experiments performed in a smooth pipe, Zagarola and Smits (1998) found more restrictive limits than are generally accepted for the logarithmic layer and no evidence of a logarithmic layer for pipe Reynolds numbers below 400 x 10^3. A power law for a portion of the overlap region with universal coefficients (ϑ being equal to 0.137) was proposed between the buffer layer and the logarithmic layer or outer region. Their value of the von Kármán constant was 0.436. Using a smaller diameter Pitot tube, McKeon et al. (2004) found the presence of a logarithmic layer for Reynolds numbers in excess of 230 x 10^3, a von Kármán constant of approximately 0.421 and a wider logarithmic zone.

Table 2.1 Summary of the Smooth Bed Turbulent Mean Velocity Profile Regions

Region	Sublayer	Velocity Profile	Equation Notes
Inner (Constant Shear Stress)	Viscous	$\frac{U(y)}{u_*} = U^+ = y^+ = \frac{u_* y}{\nu}$	Valid for $y^+ < 5$
	Buffer Zone	Intermediate	No theoretical equation – best-fit between viscous and log-law sublayers
Overlap	Inertial (Log Law)	$\frac{U}{u_*} = \frac{1}{\kappa}\ln\left(\frac{y u_*}{\nu}\right) + B$	κ = 0.40 - 0.44 = constant relating a local length scale to distance from the wall, y $B = 5.2$ - constant of integration Restricted to $Re > 230{,}000$ in circular pipe flow (McKeon et al. 2004)
	Inertial (Power Law)	$\frac{U}{u_*} = \left(\frac{1}{\sqrt{3}}\ln \mathrm{Re} + \frac{5}{2}\right)\left(y^+\right)^{3/2\ln \mathrm{Re}}$	Form taken from Barenblatt (1993)
Outer	Wake	$\frac{U_m - U}{u_*} = -\frac{1}{\kappa}\ln\left(\frac{y}{\delta}\right) + \frac{\Pi}{\kappa} 2\cos^2\left(\frac{\pi y}{2\delta}\right)$	Form proposed by Coles (1956)

Buschmann and Gad-el-Hak (2003) compared the log and power law representations of the overlap region and found inconclusive evidence to support one theory over the other. Both assumptions matched experimental and DNS profiles well within a core of the

overlap layer. The log law fit the profiles better closer to the wall, while the power law performed better towards the outer region. Though debate over this topic continues, a compelling reason to favor either law is currently lacking.

In the outer region, also termed the wake region, the law-of-the-wall variables are replaced by the velocity defect ($U_m - U$) and a boundary layer length scale δ. The velocity defect can be expressed in the following functional form:

$$\frac{U_m - U}{u_o} = f_o(y/\delta) \tag{2.12}$$

where f_o is a universal function. Several velocity scales have been proposed for the outer region, including the shear velocity u_*, the maximum velocity U_m, and a "mixed outer" scale proposed by Zagarola and Smits (1998): $U_m\delta^*/\delta$ with δ^* being the displacement thickness (Akinlade et al. 2004).

For the outer region, a relationship for the mean velocity can be derived through modifying the log law (equation 2.7) with a wake function (Coles 1956):

$$\frac{U}{u_*} = \frac{1}{\kappa}\ln\left(y^+\right) + \frac{2\Pi}{\kappa}W\left(\frac{y}{\delta}\right) + B' \tag{2.13}$$

Equation 2.13 is equally valid for the overlap and outer flow regions and can be expressed in terms of the velocity defect:

$$\frac{U_m - U}{u_*} = -\frac{1}{\kappa}\ln\left(\frac{y}{\delta}\right) + \frac{2\Pi}{\kappa}W\left(\frac{y}{\delta}\right) \tag{2.14}$$

Mathematical relationships for the two boundary layer regions and the overlap for the smooth bed case are summarized in Table 2.1.

2.3 Passive scalar plumes

Passive scalars are quantities, such as miscible chemicals and temperature, which move with the flow field yet have no significant effect on flow dynamics. For the purposes of this document, passive scalars are mass-conservative and are introduced into the flow from an idealized point source. The mixing process of a passive scalar into the surrounding fluid medium depends upon many parameters, including a measure of the source size d, the molecular diffusivity of the scalar D, and the range of turbulent scales or eddy sizes, i.e., the Reynolds number. A scalar filament with size significantly smaller than the larger eddy sizes initially meanders within a turbulent boundary layer and mixing is minimal due to interactions being limited to the less energetic smaller turbulent eddies. The smaller scales eventually spread the plume sufficiently for successively larger eddy sizes to become effective in mixing and the plume rapidly disperses. The turbulent kinetic energy within a given size range of small eddies increases with Reynolds number corresponding to more rapid mixing. Molecular motion ultimately diffuses the scalar into the surrounding fluid through high scalar gradients generated by the fluctuating velocity field (Monin and Yaglom 1975, Fischer et al. 1979).

The scalar field $\tilde{\Theta}(\mathbf{x},t)$ can be modeled in an incompressible environment through the transport (advection-diffusion) equation:

$$\frac{\partial \tilde{\Theta}}{\partial t} + \tilde{U}_i \frac{\partial \tilde{\Theta}}{\partial x_i} = D \frac{\partial^2 \tilde{\Theta}}{\partial x_i \partial x_i} \tag{2.15}$$

For a conservative passive scalar, the transport equation 2.15 is linear with respect to scalar concentration $\tilde{\Theta}$. Performing a Reynolds decomposition of the scalar ($\tilde{\Theta} = \Theta + \theta$) and velocity fields with subsequent Reynolds-averaging results in:

$$\frac{\partial \Theta}{\partial t} + U_i \frac{\partial \Theta}{\partial x_i} = \frac{\partial}{\partial x_i}\left[D \frac{\partial \Theta}{\partial x_i} - \overline{u_i \theta} \right] \tag{2.16}$$

As with the RANS equations (2.1), an additional term, the turbulent scalar flux, appears and corresponds to a correlation between the velocity and scalar fluctuations $\overline{u_i \theta}$. This term physically corresponds to the mean transport of the scalar quantity by the turbulent fluctuations. Since the fluctuating concentration field θ is unknown, the turbulent scalar flux introduces an unclosed term into equation 2.16.

A simple, practical means of closing equation 2.16 is with an eddy-diffusivity model analogous to the eddy-viscosity, or mixing length, models used in two-dimensional boundary layers. The eddy-diffusivity model is an empirical relationship introduced by Boussinesq in the 1880's that relates turbulent scalar flux to the mean concentration gradient:

$$\overline{u_i \theta} = -\varepsilon_{ij}^{t} \frac{\partial \Theta}{\partial x_j}$$

Eddy diffusivity in a dispersing cloud or plume is not constant, but varies with time, or distance downstream of the source in a moving fluid. While the plume width remains below the larger eddy sizes of the flow, the eddy diffusivity varies with the 4/3-power of the plume size for the simplified assumption of homogeneous turbulence (Richardson

1926). In bounded homogeneous systems, the plume or cloud eventually reaches the size of the larger flow scales and eddy diffusivity reaches a constant scalar value $\varepsilon^t = \ell\left(\overline{u_i u_i}\right)^{1/2}$ (Fischer et al. 1979). Substitution of an eddy-diffusivity model into equation 2.16 with known mean velocity profile and boundary conditions results in an analytical solution for the mean scalar concentration field.

The eddy diffusivity model has been used to derive the familiar Gaussian distribution of mean concentration for a continuous release into a homogeneous flow. Given a constant mean flow velocity U_i and a Galilean transformation of the coordinate system, with the spatial coordinates transformed by $x_i' = x_i - U_i t$, reduces the advection-diffusion equation to a partial differential equation for the mean concentration field called the heat, or diffusion, equation:

$$\frac{\partial \Theta}{\partial t} = \frac{\partial}{\partial x_i'}\left(\varepsilon_{ij}^t \frac{\partial \Theta}{\partial x_j'}\right) = K \frac{\partial}{\partial x'_i}\frac{\partial}{\partial x'_i}\Theta \tag{2.17}$$

Closed-form solutions to equation 2.20 exist for a variety of boundary and initial conditions (Carslaw and Jaeger 1959, Fischer et al. 1979). Neglecting diffusion in the longitudinal direction, the resulting mean concentration profile for an iso-kinetic release into a fluid flowing at uniform speed U is the Gaussian profile (Sutton 1953, Fischer et al. 1979):

$$\Theta(x,y,z) = \frac{\dot{M}}{4\pi K x} exp\left(-\frac{\left(y^2 + z^2\right)U}{4Kx}\right) \tag{2.18}$$

Equation 2.18 assumes that the plume is dispersing into an infinite medium, a generally valid approximation when the plume width, defined by four times the standard deviation $4\sigma = 4\sqrt{2Kx/U}$, has not reached the channel boundaries.

2.3.1 Time-averaged concentration and basic scaling arguments

The time-averaged scalar concentration exhibits self-similar Gaussian behavior where the plume is not influenced by a boundary or the source geometry. The zone of flow establishment (ZFE) refers to the distance from a finite source where the "top hat" shaped concentration profiles transitions to a Gaussian form. The Gaussian time-averaged shape for turbulent jets and plumes beyond the ZFE has been confirmed by many researchers. Fackrell and Robins (1982) showed approximate Gaussian forms in the vertical direction for elevated sources in a wind tunnel. Bara et al. (1992), Crimaldi and Koseff (2001), and Rahman and Webster (2005) found a Gaussian profile for mean concentrations beyond the ZFE in the transverse direction for various iso-kinetic releases.

Due to dynamic similarity beyond the ZFE, scaling relationships can be derived for plume releases into turbulent boundary layers. The maximum average concentration occurs along the plume centerline with distance downstream ($y = z = 0$) and decreases according to x^{-1} as predicted by equation 2.18. The derivation of equation 2.18 assumes a point source, an obvious inconsistency with the physical world because plume sources have finite size. Turbulent plumes have been shown to display self-similar behavior conforming to the theoretical results of dimensional analysis beyond the ZFE. The ZFE is dependent upon source geometry with the diameter d being the pertinent length scale for circular releases. Based upon experimental data, Fischer et al. (1979) define the ZFE for a turbulent circular jet to begin at a distance of $6d$ from the source. For an iso-

kinetic elevated circular release in a channel, Rahman and Webster (2005) found the ZFE to begin approximately two channel depths downstream $(x/H > 2)$. Experimental data validate the approximate x^{-1} relationship for centerline concentration beyond the ZFE for iso-kinetic elevated releases (Rahman and Webster 2005), buoyant jets (Tian and Roberts 2003), and turbulent jets (Shaughnessy and Morton 1977, Webster et al. 2001a). Experimental data of Fackrell and Robins (1982) and Jones (1983) displayed similar dilution rates, though their data were limited in the longitudinal direction.

With the assumption of constant eddy diffusivity, a power-law relationship exists between plume width and downstream distance, as measured by the standard deviation of the mean concentration profiles $\sigma = 4\sqrt{2Kx/U}$, and the distance from the source $\sigma \propto x^{0.5}$ beyond the ZFE. Fackrell and Robins (1982) found the plume-width growth rate to agree well with the expected $x^{0.5}$ relationship for an elevated release and a $x^{0.75}$ relationship for a ground-level release. In contrast, Jones (1983) determined a power-law exponent of about 0.6 for data taken with ionized air in an atmospheric release. For an iso-kinetic release into a laboratory flume, Webster et al. (2003) found the plume width to increase as $x^{0.75}$, similar to the ground-level release of Fackrell and Robins. The theoretical power law exponent of 0.5 has been confirmed beyond the ZFE by Rahman and Webster (2005) for iso-kinetic elevated releases and Crimaldi and Koseff (2001) for flush-bed releases.

Table 2.2 Selected Experimental Studies of Turbulent Plumes and Jets Summary

Investigators	Fluid Medium	Scalar Release	Experimental Motivation
Shaughnessy and Morton (1977)	Rectangular wind tunnel 0.215 m × 0.305 m	Jet of dioctyl phthalate smoke $Sc = 4 \times 10^4$ released from 6.35-mm nozzle at centerline.	Demonstration of optical procedure
Fackrell and Robins (1982)	Rectangular wind tunnel 24 m × 9.1 m × 2.7 m	Neutrally buoyant mixture of propane and helium with 3- to 35-mm nozzles placed just above roughness elements and elevated.	Plume characteristics, statistical analysis and flux calculations
Jones (1983)	Atmospheric boundary layer	Ionized air release from 1.3-cm diameter tube placed 1 m above the ground.	Atmospheric contaminant dispersion
Dinar et al. (1988)	Atmospheric boundary layer	Oil fog with optical detectors. 20-cm diameter tube 1 m above ground.	Atmospheric contaminant dispersion models
Bara et al. (1992)	Open channel	Neutrally buoyant mixture of saltwater and ethanol from flush-bed release from 0.536-cm diameter nozzle.	Comparison with meandering plume models
Yee et al. (1992)	Open channel	Iso-kinetic release of neutrally buoyant mixture of saltwater and ethanol. 4.2-mm diameter nozzle with source height of 52 mm above bed.	Comparison of statistics of fluctuations with various known statistical distributions
Mylne (1993)	Atmospheric boundary layer	Propylene tracer with photoionization detectors with 1-cm diameter release with heights of 0 to 4 m above ground.	Atmospheric contaminant dispersion
Crimaldi et al. (2002)	Open channel	Release of water dyed with Rhodamine 6G. 1-cm diameter flush-bed release	Scalar statistics and interactions with viscous sublayer.
Webster et al. (2003)	Open channel	Iso-kinetic release of water dyed with Rhodamine 6G from 4.7-mm nozzle 25 mm above the bed.	Turbulent plume measurements using LIF
Tian and Roberts (2003)	Open tank both stratified and unstratified	Saltwater mixture with Rhodamine 6G dye released from 4-mm diameter nozzle.	Plume dynamics in stratified and unstratified environments
Rahman and Webster (2005)	Open channel	Iso-kinetic release of water dyed with Rhodamine 6G from 4.7-mm diameter nozzle located 25 mm from the bed.	Effects of roughness on plume characteristics
Crimaldi and Koseff (2006)	Open channel	Release of water dyed with Rhodamine 6G. 1-cm diameter flush-bed release.	Effects of flow inhomogeneity on plume statistics

2.3.2 Fluctuating concentration – instantaneous plume information

An animal sensing odor within a turbulent boundary layer does not experience chemical stimulus in a time-averaged sense, but as a highly variable intermittent signal. The mean concentration field provides little information concerning the instantaneous spatial structure that animals experience and there is significant doubt over an animal's ability to generate such averages (Webster and Weissburg 2001). Turbulent plumes are characterized by concentration fluctuations as filaments of relatively undiluted fluid pass a stationary point. Intermittency occurs as filaments of relatively high concentration are followed by entrained ambient fluid with concentration levels approaching zero. Fluctuations and intermittency eventually approach zero at sufficient distances downstream as the scalar quantity becomes uniformly mixed across the channel cross section.

The standard measure for scalar fluctuations in turbulence is the scalar variance defined as $\overline{\theta^2}$. An evolution equation for the scalar variance can be derived by subtracting the time-averaged equation (2.16) from the instantaneous equation (2.15), multiplying by θ, and Reynolds averaging:

$$\frac{\partial \overline{\theta^2}}{\partial t} + U_i \frac{\partial \overline{\theta^2}}{\partial x_i} = \underbrace{\frac{\partial}{\partial x_i}\left(D\frac{\partial \overline{\theta^2}}{\partial x_i} - 2\overline{u_i \theta^2} \right)}_{\text{Turbulent and Diffusive Transport}} - \underbrace{2\overline{u_i \theta}\frac{\partial \Theta}{\partial x_i}}_{\text{Production}} - \underbrace{2D\left(\overline{\frac{\partial \theta}{\partial x_i}\frac{\partial \theta}{\partial x_i}} \right)}_{\text{Dissipation}} \tag{2.19}$$

The last two terms are referred to as the production of scalar variance ($-2\overline{u_i \theta}\partial\Theta / \partial x_i$) and the dissipation rate of the scalar variance χ, respectively. The first two terms on the RHS are transport terms that distribute scalar variance within the field. The production of

scalar variance occurs through interaction of the turbulent flux with gradients in the mean concentration field. In the absence of a production term, the scalar variance strictly decays. Equation 2.19 illustrates the eventual decay of scalar variance to zero far from a source as scalar variance dissipation is always negative while production decreases to zero due to the mean gradient term $\partial\Theta / \partial x_i$ approaching zero. Decay to zero indicates a complete smoothing of the fluctuations of the scalar quantity within a region of the flow field.

As with mean concentration, passive scalar fluctuations for turbulent plumes are source-size and Reynolds-number dependent. Quite a number of experiments have been conducted on passive scalar plumes released into two-dimensional boundary layers typical of the atmosphere or natural stream channels with a general summary found in Table 2.2. Self-similar forms for the average concentration and concentration variance profiles were found in the plume measurements. One interesting aspect of the plume data was the presence of off-center peaks in normalized concentration fluctuation profiles in the transverse directions. Plume experiments by Shaughnessy and Morton (1977), Fackrell and Robins (1982), Bara et al. (1992), and Rahman and Webster (2005) displayed off-centerline peaks of scalar fluctuations for sufficient distances downstream of the source. Bara et al. (1992) suggested plume meandering to be the mechanism maintaining a unimodal fluctuation distribution and that off-centerline peaks were the result of small-scale eddies. Crimaldi and Koseff (2001) did not find off-centerline maxima in concentration fluctuations and attributed their presence to plume release characteristics. Rahman and Webster (2005) found Gaussian profiles of standard deviation of scalar fluctuations close to the source, while a bimodal distribution profile

appeared farther downstream. They argued that close to the source, the longitudinal production term $2\overline{u_i\theta}\partial\Theta/\partial x_i$ is large due to high mean concentration gradients and creates most of the scalar variance. Scalar variance generally decays in the downstream direction as production terms become much smaller relative to the turbulent flux terms. At sufficient distances downstream, a transverse production term $2\overline{v\theta}\partial\Theta/\partial y$ begins to dominate in equation 2.19, leading to off-centerline maxima located approximately at the inflection points on the transverse mean scalar concentration profile (Fackrell and Robins 1982, Rahman and Webster 2005).

The shape of the probability density function (PDF) for the variable $\tilde{\theta} = \left(\tilde{\Theta} - \Theta\right)/\theta'$, where θ' is the standard deviation of the scalar fluctuations, shows a strong dependence on distance from the source. In the near-field region for the elevated release, the PDF for $\tilde{\theta}$ is strongly skewed towards positive values (Rahman and Webster 2005, Dasi 2004). In the near field the standard deviation is greater than the time-averaged value, hence high concentration fluctuations occur with higher frequency close to the source and corresponding negative fluctuations are obviously impossible due to the lower bound at zero. Further downstream, the plume becomes more uniform and the PDF, though still skewed towards the larger fluctuations, displays an approximate Gaussian form. Yee et al. (1993) observed large deviations from Gaussian behavior for their data on scalar variance for a saline tracer in water. They attempted to fit several known probability distributions to their data and found a conjugate beta distribution to best fit their data. The distribution shape is likely to be a function of location within the plume, however.

Intermittency is another inherent characteristic of the concentration field associated with turbulent chemical plumes. The scalar time-record at a particular point within a plume is discontinuous, with periods of relatively high concentration followed by those at or close to zero. In quantitative terms, intermittency γ is defined as the probability that a threshold concentration is exceeded $\gamma_I = \text{Prob}(\theta \geq \theta_t)$, where θ_t is the threshold value (Chatwin and Sullivan 1989). Crimaldi et al. (2002) found the intermittency parameter to follow a Gaussian profile in the transverse direction far downstream from a flush-bed source. Close to the source, the intermittency variable displayed a "top hat" profile in the transverse direction. Fackrell and Robins (1982) used a threshold value of zero and found intermittency to correspondingly decrease with distance from the source. Their results showed intermittency to depend on the source size.

Of potential utility to foraging organisms is the burst strength or ramp and cliff structures quantified by the scalar gradient $\partial\theta/\partial x_i$. Experimental measurements and DNS have revealed rapid onsets of passive scalar bursts, where the scalar magnitudes increase rapidly in time (Warhaft 2000). The presence of ramp and cliff structures has been observed in a variety of passive scalar releases, including isotropic grid-generated turbulence (Mydlarski and Warhaft 1998), the atmospheric boundary layer (Mylne 1993), and iso-kinetic turbulent plumes in water channels (Yee et al. 1993, Webster and Weissburg 2001). Passive scalar gradients display non-Gaussian behavior and possess PDF's with exponential tails. Dasi (2004), in his measurements of high-Schmidt-number flows in an open channel, found longitudinal and vertical gradients at the distribution tails 40 to 50 times the expected value, a clear departure from Gaussian shape. Skewness values for scalar gradient PDF's depart from the Gaussian value of 0. Mydlarski and

Warhaft (1998) reported skewness values of 0.6 to 1.6 for fluctuations in a mean temperature gradient in grid turbulence of a wind tunnel. Dasi (2004) reports skewness values of order of 1 with no apparent Reynolds-number dependence. Using DNS, Yeung et al. (2004) showed skewness to decrease with increasing Schmidt number for simulations in a locally isotropic field. The differences between the results of Dasi (2004) and DNS experiments of Yeung et al. (2004) were attributed to anisotropy of the velocity field. Anisotropy, as measured by a positive skewness, indicates high positive scalar spatial gradients to be more frequent than corresponding negative gradients of identical magnitude.

2.4 Olfactory navigation

Animals within turbulent environments sense odor stimuli carried by the ambient fluid within what has been termed “a chemical landscape” (Atema 1996). Turbulent odor plumes are ephemeral and non-reproducible in time and space. In a laminar environment with a single source, spatial concentration gradients can be measured and essentially “climbed” to locate the source. Such a strategy in a turbulent environment would lead trackers on spurious searches (see Weissburg and Dusenbery 2002), as instantaneous concentration gradients can point in any direction. The challenge of locating a source in a turbulent environment based upon chemical signals alone is to find some means of using the instantaneous plume characteristics as general guides towards a source.

The fluid environment, whether laminar or turbulent, experienced by a particular organism is dependent on scales of the flow relative to the size of the organism. For macroscopic organisms much larger than the Kolmogorov length scale, turbulent dispersion dominates and the chemical stimulus carried by fluid currents is intermittent

and spatially variable. The Schmidt number of most dispersing natural chemicals in aqueous environments is on the order of 1000 (Moore and Crimaldi 2004); thus, the Batchelor scale is about 30 times smaller than the Kolmogorov length scale (see equations 2.2 and 2.3). Sampling times and the sensory resolution of macroscopic animals are believed to be much coarser than the time and length scales of scalar diffusion and turbulent dissipation. Hence, animals are effectively sensing "smeared" chemical concentration filaments measured at intervals determined by chemosensory response rate or sampling method, such as sniffing or the flicking time of sensory appendages (Koehl et al. 2001). Experimental evidence seems to indicate that the temporal response rate of crustacean receptor cells is insufficient to resolve time-dependent plume characteristics such as burst strength (Weissburg et al. 2002). Gomez and Atema (1996) determined a stimulus integration time of 200 ms for olfactory receptor cells of the American lobster (*Homarus americanus*). To gather detailed temporal information of the filamentous structure of a turbulent plume requires sampling frequencies much greater than the 5-Hz capability reported for lobsters. Of the available plume characteristics, foraging blue crabs seem to rely on spatial aspects, such as bilateral comparison, and mean flow sensation, rather than temporal plume information in making tracking decisions.

2.4.1 Orientation Strategies

Macroscopic animals in their natural environments generally respond to stimulus by moving in a preferred direction in a process referred to as taxis. Taxis strategies (see Table 2.3) use chemical, mechanical, optical, and other sensory stimuli to locate food, escape predators, and engage in social interactions. Chemotaxis depends upon chemical

gradient cues and is particularly effective in a diffusive (microscopic) environment where flow conditions are laminar (Dusenbery 2001, Moore and Crimaldi 2004). In diffusive environments, tracking is straightforward as sources can be located simply by heading up the concentration gradient. More specifically, chemotaxis involves sampling at a particular location, moving and resampling the chemical information (this sequential comparison strategy is also called klinotaxis). Chemotaxis is limited to bacteria and other small organisms that live in environments where diffusion is the dominant transport mechanism. Turbulent flows involve dispersive processes unrelated to molecular diffusion and create chemical gradients which may not point towards the source in an instantaneous sense (reviewed in previous sections). In such an environment, chemotaxis is an ineffective search strategy and is probably not useful to rapidly moving macroscopic animals (Weissburg 1997). Rheotaxis and anemotaxis are oriented responses to flow direction in water and air, respectively, and may be mediated by visual cues or mechanical sensation.

A tracking strategy differing from directed movement towards a source involves using a Brownian-type search mechanism, or kinesis. Upon encountering an odorant plume, motion is initiated in a random direction. After a certain amount of time, another chemical sample is taken and random change in direction undertaken. The source is located after a succession of random movements.

Scale is important in the navigational strategy employed, especially the relative size of the animal with respect to that of the tracked odor plume. Fluid dynamical and chemical plume properties perceived by whales are much different than those for plankton found in

the same habitat. One theory for organisms with a sensor distribution larger than those of a typical tracked odor plume (macroscopic organisms) postulates bilateral or multi-point comparison of stimulus information (tropotaxis) to be an important part of successful plume navigation (Webster et al. 2001). Weissburg (2000) accounts for the relative size of an animal to the odor plume by a spatial integration factor (SIF), calculated by the distance between chemosensory receptors. Animals with an SIF larger than that of the plume width are presumed capable of detecting the edges of the odor plume and using bilateral comparison to adjust their heading. Animals with large SIF can use a bilateral comparison, or chemo-tropotaxis, to improve orientation when a contrast is present across distal chemosensors (Weissburg et al. 2002, Webster et al. 2001).

Terrestrial and aquatic arthropods use a variety of strategies, depending upon the ambient fluid medium, their size, and other considerations. For example, moths use a combination of chemical and visual cues in what is termed odor-modulated optomotor anemotaxis (Vickers 2000). Moths compensate for drift by using visual information of the ground to verify upstream movement and a casting behavior determined by an internal guided motor program (Willis and Cardé 1990, Vickers and Baker 1994). Larvae of the parasitic barnacle *Heterosaccus dollfusi* in a laminar laboratory flume tracked a host using a combination of rheotaxis and chemotaxis (Pasternak et al. 2004). The barnacle larvae swam upstream when tracking host metabolites and displayed casting behavior similar to moths when losing contact with the plume. Bilateral comparison, i.e. tropotaxis, has been observed in North American lobsters in combination with rheotaxis in a process referred to as chemotropotactic orientation (Moore et al. 1991). Freshwater crayfish display tracking behaviors similar to those of lobsters (Wolf et al. 2004). Blue

crabs have demonstrated an odor-conditioned rheotactic response supplemented by spatial comparison, or tropotaxis, to successfully track odor plumes (Keller et al. 2003).

Table 2.3 Summary of Pertinent Navigational Strategies

Taxis	Orientation	Environments
Mechanism: Taxis – Directional movement in response to environmental cue.		
klinotaxis	sequential sampling based upon one sensor	various
tropotaxis	spatial sampling using more than one sensor	"larger" arthropods, such as crabs and lobsters
chemotaxis	following a chemical gradient	laminar (diffusive) environments
rheotaxis	sensing of flow direction	aquatic environments
anemotaxis	sensing of flow direction	atmospheric environments
Mechanism: Kinesis – Random movement in response to environmental cue.		
Kinesis	**Orientation**	**Environments**
Orthokinesis	change in animal speed with increasing stimulus	various

2.4.2 Animal tracking studies

The tracking of chemical plumes by male moths in wind tunnels and the atmospheric boundary layer has been a focus of intense study, mainly involving the use of pheromone attractants for pest control. Moths perform a casting behavior while tracking in efforts at maintaining olfactory contact with plumes that are generally quite narrow and meandering. Motion relative to the ground is determined visually to assist in maintaining

an upwind tack (Murlis et al. 1992). Tracking moths experience a highly discontinuous signal due to intermittency and plume meander and respond to concentration peaks (Murlis 1986). Vickers and Baker (1994) proposed a model for plume tracking in moths broken into response by two neurological systems: the first phasic with moths surging upwind after contact with a plume filament (pheromones in this case), and the second tonic, in which moths cast side to side after reaching a pocket of clean (low or zero concentration) air. The casting process is important for tracking moths, as the plumes they track are of low concentration and meander significantly due to small source size.

Gypsy moths (*Lymantria dispar*) responded to intermittent pheromone plumes in a field experiment in a deciduous forest where various Gaussian plume models failed to predict concentrations above perceptible levels (Elkinton et al. 1984). Gypsy moths responded to pheromone plumes at spatial locations where the average concentration using a Gaussian plume model was several orders of magnitude below detectable levels. The gypsy moth experiments demonstrated the highly intermittent character of pheromone plumes in the atmosphere. Experiments conducted by Mafra-Neto and Cardé (1994) on the almond moth (*Cadra cautella*) used pheromone sources in a wind tunnel. Almond moths were most efficient at tracking when the source was pulsed rather than continuous. A refractory period was defined during which a moth maintained its course after entering a pocket of odor-free air before the initiation of casting. For relatively straight upwind flight to occur, cues due to signal intermittency had to be shorter than the refractory period in order to supersede the internal counterturning program for casting behavior, or the tonic response. Vickers and Baker (1994) evaluated the response of flying male

Heliothis virescens to strands of pheromone in upwind surging and crosswind casting and proposed the reiterative phasic/tonic response to odor plumes mentioned earlier.

In the aquatic environment, stomatopods, or mantis shrimp, have rather simple chemosensory organs and sense chemical odor through flicking of their antennae (Mead 2002). Stomatopods use chemical signals in foraging, reproduction, burrow investigation and social interactions. Mead et al. (2003) used planar laser-induced fluorescence (PLIF) in the laboratory to determine concentration levels experienced by the flicking antennules of the stomatopod *Hemisquilla ensiguera californica*. Their PLIF setup recorded concentrations at the approximate level of the chemosensors with a transverse and longitudinal resolution of 180 μm, intermediate between the Kolmogorov and Batchelor scales. The width of the laser determined the vertical resolution, 2.5 mm, set to correspond to the approximate thickness of the stomatopod antennules. Filament width, a measure of filament sharpness and concentration variance, was calculated from PLIF data in two flow situations, wave-driven and unidirectional. The available signal, as measured by filament parameters, was highest in wave-driven flow, the natural habitat of *H. ensiguera californica.*

Tracking patterns of the American lobster (*Homarus americanus*) in a laboratory flume performed by Moore et al. (1991) indicated a comparison of sensory information from the legs and antennules to be the primary tracking mechanism, termed a chemotropotactic response (a chemically modulated response based upon comparison between chemosensors). Heading angles, defined as the angle between the animal heading and a straight line to the source, displayed a decrease followed by a slight increase as the source

was approached, indicating a deviation from rheotactic behavior. A lobster starting within the odor plume would have heading values about 0 degrees if using odor-modulated rheotaxis. Plume navigation was broken into three stages. Initially, lobsters determined a heading based upon the flow direction and chemosensory information collected by sampling an area of the plume. During the second stage, the fastest walking speeds were recorded, relative to the initial and terminal phase, and only minor heading adjustments were made. Close to the source, walking speeds declined significantly. The decrease was attributed to a switch in chemosensory receptor dominance from the legs relative to that of the antennules. Moore et al. (1991) suggested that the primary stimulus in the final approach to the source was received from the legs.

Crayfish tracking odor sources in flume studies have demonstrated tactic behavior similar to that of lobsters. Kozlowski et al. (2003) found crayfish (*Orconectes rusticus*) to cease motion when losing contact with a pulsed chemical release. A minimum exposure rate of about 1 Hz was necessary for successful tracking of the chemical plume. In continuous plumes, crayfish navigated to the source more rapidly relative to high frequency pulsed sources at the same mass flow rate. Intermittency of the odor source controlled the temporal aspects of the search, such as walking speed, a process called orthokinesis. Bilateral-comparison-mediated steering indicated an additional tropotactic response. Kozlowski et al. (2003) suggested both orthokinesis and tropotaxis to be used by foraging crayfish due to the intermittent nature of the chemical plume.

The tracking efficiency of crayfish is high relative to other crustaceans, based upon data taken from various flume experiments. Two North American crayfish species, *O.*

rusticus and *O. virilis*, were able to track odor sources located greater than 1 m away with a higher success rate than other studied crustaceans (Keller et al. 2001). Moore and Grills (1999) observed faster walking speeds and higher success rates for cobble substrate relative to sand substrate under identical flow velocities. The study suggested increased levels of turbulence, as measured by the roughness Reynolds number $Re_* = u_* k_s / \nu$, led to higher successful tracking rates for *O. rusticus*. Similar to the lobster tracking phases of Moore et al. (1991), crayfish odor tracking consisted of three stages: an initial stage with first contact with the plume, a tracking phase, and a final approach where other cues, such as visual or tactile, became important (Wolf et al. 2004).

Current experimental data suggest blue crabs use odor-modulated rheotaxis with turns modulated by information from chemosensors and bilateral comparison (Weissburg et al. 2003). Blue crabs move upstream when sensing appropriate chemical stimulus and have difficulty locating prey in quiescent environments (Weissburg and Zimmer-Faust 1994). Flow direction information was found to be necessary for a successful search, indicating a rheotactic component to crab navigation. Contrary to the results of Moore and Grills (1999) with crayfish, Weissburg and Zimmer-Faust (1994) found blue crabs to have increasing difficulty in locating odor sources with increased levels of turbulence, i.e., higher Re_*. With increasing roughness Reynolds number, higher turbulent intensity increased dispersion and decreased crab performance presumably because bilateral comparison of receptor information became less distinct. Data taken from LIF and behavioral experiments for substrates with increasing roughness Reynolds number were analyzed by Jackson et al. (2007). Blue crabs exhibited a decrease in search efficiency for the rougher substrates. Increasing roughness had the most effect on tracking speeds

in response to a decrease in scalar fluctuations at the level of the antennules. Steering and turning angles appeared to be independent of increasing turbulence levels as measured by the roughness Reynolds number.

A behavioral response of blue crabs with increases in flow velocity is a tendency to shift their carapace orientation during tracking in apparent attempts at reducing drag. At low flow speeds, orientation angle remains approximately constant and perpendicular to the flow. Increasing flow speed leads to a skewed orientation, with the upstream portions of the body creating a wake flowing over the carapace. Weissburg et al. (2003) demonstrated a reduction in drag to occur with increasing angular orientation, which consequently leads to a corresponding loss of plume definition for chemosensors influenced by vortices shed upstream through increased mixing. Keller and Weissburg (2004) looked at the effects of large-scale properties of scalar releases through tracking studies with pulsed sources and different release rates. Search efficiency decreased with decreasing pulse-rate frequency, indicating large-scale temporal features of turbulent plumes to have an effect on search success. Crabs tracked most successfully in plumes with high flux rates and concentrations, while those subject to discontinuous, pulsed sources displayed degraded tracking ability.

Moths have shown similar characteristics when tracking pulsed plumes (Mafra-Neto and Cardé 1994). Inter-pulse rates reducing tracking success were 2.5 and 0.25 to 1 seconds for blue crabs and moths, respectively. The difference was attributed to a higher temporal resolution of stimuli by moths and greater turbulent intensity in aquatic versus terrestrial habitats in the portion of the boundary layer in which moths and crabs track.

Simulations of crab behavior have been performed on PLIF plume data using a computer model for source tracking (Weissburg and Dusenbery 2002). The algorithm used weighted contributions of chemo-tropotaxis and rheotaxis, two behavioral responses demonstrated by tracking blue crabs (Keller et al. 2003). Crab data was taken from behavioral studies performed in a laboratory flume. Using PLIF data taken from plumes of an iso-kinetic release under similar flow conditions, searches were conducted with a tropotactic model described by Dusenbery (2001). Crab behavior was similar to that of the computer model for rheotactic and tropotactic weightings of 0.5 each. Complicated sampling procedures did not improve search efficiency compared to simply turning in the direction of the sensor with the highest level of stimulation. A proper balance between rheotaxis and tropotaxis was necessary for a successful search, as some weightings actually led the simulated searcher downstream chasing packets of advected chemicals. The study suggested that the spatial distribution of chemosensors is important more for the greater likelihood of one or more receptors contacting the plume than for an ability to sense a gradient across the receptor spacing.

The role of the various blue crab chemoreceptors was investigated by Keller et al. (2003) via the deafferentation of particular sensory organs. Chemical receptors on the crab body were broken into two groups, cephalic, which included the antennules and antennae, and thoracic, associated with the walking legs and claws. Crabs with deafferented cephalic sensors had difficulty locating a source and spent more time stationary relative to control and deafferented leg treatments. The results suggest that antennae and antennules, cephalic sensors, are important for the rheotactic aspect of the search. Thoracic chemosensory receptors were found to mediate turning with respect to the plume,

although deficiencies in search behavior were more apparent close to the source. The difficulties that crabs displayed in maintaining contact with the plume with deafferented thoracic receptors validated the role of tropotaxis.

The behavioral studies and PLIF data analysis of Jackson et al. (2007) showed blue crabs to wander farther from mean plume centerline with increasing bed roughness, or Re_*. Spreading and homogenization of the plume increased with increasing bed roughness. The sensor spacing available to a crab is relatively fixed at about 10 cm. When the plume width exceeds maximum sensor spacing, crabs can also detect a signal contrast by moving to the edge of the instantaneous plume. PLIF data showed the transverse correlation for searchers with sensor spacing of 10 cm to provide a greater signal contrast when located to the side of the plume. Though behavioral and PLIF data were taken separately, Jackson et al. illustrates the general focus of this study of linking the characteristics of the physical environment to organism behavioral observations.

2.5 Contributions of current research

The studies discussed in the previous sections reveal much about behavioral response and subsequent navigational patterns, i.e. taxis, yet offer little more than a qualitative idea of the olfactory stimulus experienced by the tracking organism. The aims of the current study are to increase understanding of what turbulent plume aspects blue crabs use during successful navigation towards a source. A logical progression would be to combine PLIF with an actively tracking organism to directly correlate navigational behavior with odorant concentration at olfactory organs. Turbulent passive scalar plumes can be quantified through means other than PLIF. Point measurements with a probe, such as an ion sensor, can be taken within a turbulent odor plume though measurements cannot be

simultaneous with animal tracking. The presence of probes within the flow field introduces an additional limitation, where downstream measurements could be affected by upstream probes. Planar laser-induced fluorescence offers a non-intrusive means of measuring a passive scalar field at multiple locations.

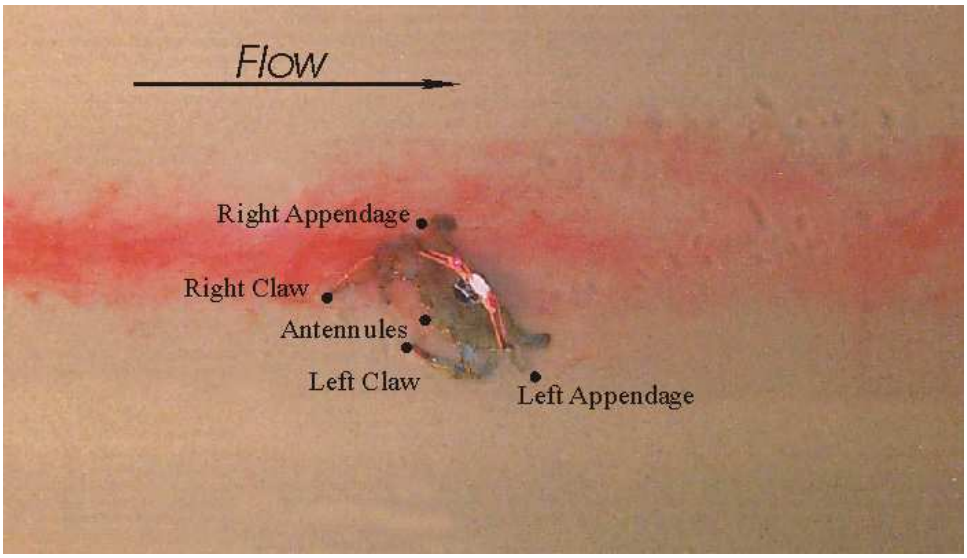

Figure 2.3 Approximate location of crab chemosensory locations. Photograph is a flow visualization of a blue crab tracking an odor source in a laboratory flume. Also visible is the diode backpack used to follow the motion of the crab (Photo courtesy of Marc Weissburg).

Many factors have restricted combined PLIF-organism studies, however. Shadowing of the laser by portions of the organism body can create gaps in the concentration time record at shaded chemosensors. Animals generally track while shifting the vertical location of olfactory organs through walking, antennule flicking, or presumed attempts to sample in the vertical direction. Further, the olfactory systems of some arthropods, such as blue crabs, are not limited to a single location, such as the antennules, but are distributed across the animal's body (see Figure 2.3). In addition, the laser light used in PLIF is intense and can disorient animals. For many of these reasons, simultaneous PLIF

has been restricted to the analysis of one tracking animal, a stomatopod (*Hemisquilla ensiguera californica*), with a "simple" olfactory system consisting of a pair of antennules, each with a central aesthetasc array (Mead 2002). Only seven plume tracks (out of ninety) could be used in the analysis due to problems associated with coordinating PLIF with an actively tracking animal.

The process of combining behavioral studies with direct quantification of odorant stimulus is not limited to PLIF. Electrodes or other sensors can be connected to tracking organisms either externally or internally. Leonard et al. (1994) implanted electrodes capable of detecting odorant concentrations at the tips of the antennules of lobsters. A concentration-time record was generated through recording data via an amplifier-transmitter backpack attached to the lobster. Vickers and Baker (1994) attached an excised antenna connected to an electroantennogram to a moth with unaltered antennae. The attached antenna required a small wire lead which traveled with the moth as it tracked a pheromone plume in a wind tunnel. Time records of electroantennogram output versus tracking coordinates for several moths can be found in Vickers et al. (2001).

To gather time-records at the chemosensory organs of a blue crab would require multiple sensors and some means of transmitting the data, i.e., wires, to an amplifier and recorder. Attachment of multiple sensors to a blue crab, particularly on the legs, would likely impair movement and tracking abilities significantly. Laser-induced fluorescence avoids the wires or backpacks required for external or internal sensors. Therefore, for this study, LIF was chosen as it both minimizes the physical limitations imposed on the tracking crab while providing a non-intrusive sampling method.

Since sampling occurs at multiple elevations and transverse locations, any attempt to quantify the stimulus patterns experienced by a tracking blue crab would necessarily have to include more than a single measurement plane. In addition, blue crabs can alter the position of their antennules and thereby enable perception of variability in the vertical direction. To adequately resolve the concentration field experienced by a tracking blue crab, a three-dimensional, time-resolved measurement system is needed. The focus of this study is to develop a concentration measurement system to map the three-dimensional instantaneous odorant field around a tracking blue crab. With physical concentration measurements, the behavior of *C. sapidus* can be correlated with a quantifiable signal structure. The experimental setup allows earlier behavioral studies, which were limited to only a qualitative idea of the tracked odor plume, to be linked with quantitative measures.

Chapter 3

Experimental Description

The passive scalar fields were quantified using three-dimensional laser-induced fluorescence (3DLIF), a non-intrusive technique. As described in this chapter, a unique 3DLIF system was designed, constructed, and validated. Three plume types were generated, a continuous release, a continuous release with an induced meander, and a pulsed release. Measurements were recorded for successful searches by blue crabs in the three plume environments. 3DLIF was also used to gather concentration fields for three plume types in the absence of crabs to determine their statistical structure. The three plume types were chosen to approximately mimic odorant plumes created by blue crab prey in a natural tidal channel. In this chapter, the apparatus and procedures for the 3DLIF technique and crab-tracking trials are described in detail along with the methods for processing the resulting data.

3.1 Flow facility

The experimental apparatus was a biological-grade seawater flume located in the Georgia Tech Environmental Fluid Mechanics Laboratory. The seawater flume dimensions were 0.76 m wide by 13.5 m long with a level bed. Flow depth was controlled via changeable weir boards at the downstream end of the flume and flow rate was determined by rectangular weir formulas (Brater and King 1976). Artificial seawater was recirculated through the flume by a centrifugal pump. The flume had clear polyacrylic sidewalls in the test section, allowing the use of scanning laser illumination.

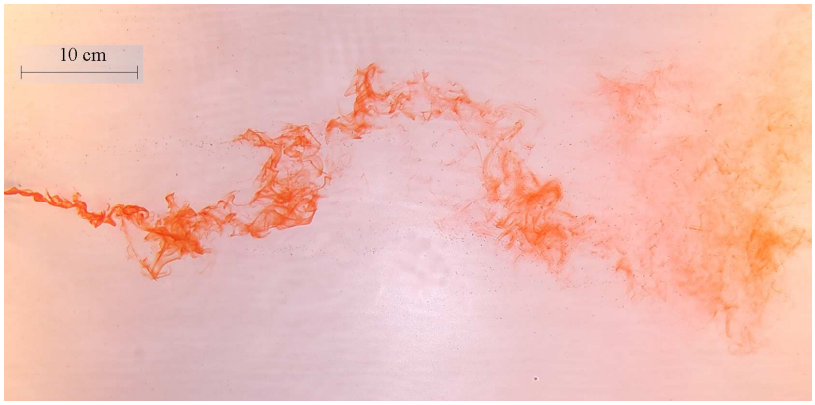

Figure 3.1 Flow visualization images of the (a) continuous plume, (b) meandering plume, and (c) pulsed plume.

3.2 Flow and plume parameters

3.2.1 Flow conditions

Flow conditions replicated those typically found in blue crab tidal habitats (Finelli et al. 1999, Smee and Weissburg 2006). An open channel boundary layer was established upstream of the seawater flume test section, which is located roughly 10 m downstream of the headbox. The flow velocity and depth were 50 ± 2.5 mm/s and 212 ± 1 mm, respectively. A naturally occurring fine sand, with a median diameter (d_{50}) of 1.1 mm, was used upstream of the test section. Slightly coarser black sand was placed within the test section to limit potential laser light reflection (and subsequent data noise) to the overhead CMOS camera. The corresponding boundary layer was transitional between hydraulically smooth and rough, with a roughness Reynolds number of around 3. Table 3.1 summarizes flow conditions with the values for shear velocity calculated from equations for the friction factor in smooth boundary layers (Rahman 2002, White 2005). Jackson et al. (2007) obtained a wall shear velocity of 3.01 mm/s using acoustic Doppler velocimetry for a boundary layer over fine sand in the same flume. The Kolmogorov and Batchelor scales were estimated from inertial scaling (equations 2.2 and 2.3 with the dissipation rate estimated as $\varepsilon = u'^3 / \ell$ where ℓ is approximated as half of the channel depth and u' is approximated as equal to u_*). The molecular diffusivity of Rhodamine 6G in seawater was taken to be 8 x 10^{-10} m^2/s (Barrett 1989).

Table 3.1 Summary of Flow Conditions

Average velocity (mm/s)	**50**
Flow depth (mm)	**212**
Substrate d_{50} (mm)	**1.1 (fine sand)**
Wall shear velocity u_* (mm/s)	**3.0**
Re_*	**3 (transitional)**
Kolmogorov scale (mm)	**1.2**
Batchelor scale (mm)	**0.03**

3.2.2 Plume parameters

The released passive scalar consisted of a mixture of prey exudates and a trace amount of Rhodamine 6G. The source concentration of Rhodamine 6G for behavioral trials varied depending upon plume type, but was generally equal to 2000 μg/l (4.2×10^{-6} M). Previously frozen shrimp (2.21 g) was soaked in 1 liter of flume seawater for 1 hour prior to experiments to create an odorant stimulus that crabs have actively tracked in previous studies. The scalar mixture was created from flume sump water and had neutral buoyancy. The diffusivities of Rhodamine 6G (Schmidt number is approximately 1250) and the chemical exudates were approximately equal in seawater and did not chemically interact. Hence, the scalar filaments of dye and odorant were assumed identical. The point-source nozzle was streamlined in the downstream direction to limit the wake perturbation.

Figure 3.1 shows flow visualization of the three plumes. For the continuous and meandering plume cases, the scalar was released iso-kinetically through a 4.2-mm diameter nozzle located approximately 9 m downstream of the flume inlet. The pulsed plume was released with the same nozzle setup, and the frequency of the pulsing was 0.1 Hz with a 50-50 duty cycle (i.e., 5 seconds on and 5 seconds off). The resulting plume had a slight amount of momentum relative to the flow as the scalar mass release rate matched those of the continuous and meandering plumes (i.e. for the 5 second on period, the flow rate was twice a large and hence not iso-kinetic). In all cases, the center of the nozzle was positioned 2.5 cm above the channel floor, within the inertial, or overlap, region of the turbulent boundary layer.

Experimental plume parameters are summarized in Table 3.2. One objective of the study is to determine how large scale changes to the plume structure affect blue crab tracking success. Plume intermittency and spatial variability have been shown to affect the foraging behavior of crustaceans (Keller et al. 2003, Jackson et al. 2007). Pulsed releases introduce substantial intermittency to an odorant plume and blue crabs have decreased success rates and increased tracking times with increasing pulse frequency (Keller and Weissburg 2004). In the current experiments, spatial variability is introduced by placing a 10.1-cm cylinder (axis aligned vertically) at a distance of 50.8 cm upstream of the nozzle to induce a quasi-periodic vortex street. The Reynolds number of the cylinder is approximately 5100 and the wake weakly displays the periodicity found in a classic von Karman vortex street. Turbulence generated in the cylinder wake enhances mixing and vertical transport while causing significant plume meander.

Table 3.2 Summary of Plume Parameters

Type	Experimental Setup	Objectives
Continuous	Iso-kinetic release	Correlation of tracking behavior and odorant concentration signal at various chemosensory organs
Pulsed	Weak jet - 5 s on followed by 5 s off	Effects of large-scale temporal intermittency on tracking efficiency and plume characteristics
Meandering	Iso-kinetic release with a 10.1-cm cylinder placed 50.8 cm upstream	Effects of large-scale spatial meander, misalignment of bulk flow direction and local chemical flux, and enhanced mixing

3.3 Measurement system

A 3DLIF system has been developed for three-dimensional recording of the odorant concentration field. The system works by collecting consecutive planar LIF images separated by small vertical distances. For small separation distances and collection rates that are much faster than time scales of the flow, the resulting PLIF images can be considered frozen and a virtual three-dimensional representation of the concentration field can be reconstructed. Similar 3DLIF systems have been constructed by other investigators, including Tian and Roberts (2003).

3.3.1 Laser-induced fluorescence

Laser-induced fluorescence is a technique developed in the 1980's used to measure concentration at a specific point in a flow in a relatively non-intrusive manner (e.g., Koochesfahani and Dimotakis 1985, 1986). The technique has been used extensively and the rotating mirror system for this study is similar to those developed by previous investigators (Yoda et al. 1994, Crimaldi and Koseff 2001, Webster et al. 2003, Tian and Roberts 2003). Perturbations to the flow due to the energy introduced by the laser beam can be minimized through the use of suitable fluorophores and lasers to reduce

quenching, photobleaching, and thermal blooming effects (Lozano et al. 1992, Crimaldi 1997, Wang and Fiedler 2003, Larsen and Crimaldi 2006). The fluorescent intensity is collected on a photosensitive device with discrete pixel size and output. With suitable calibration, the recorded intensity can be converted to local concentration.

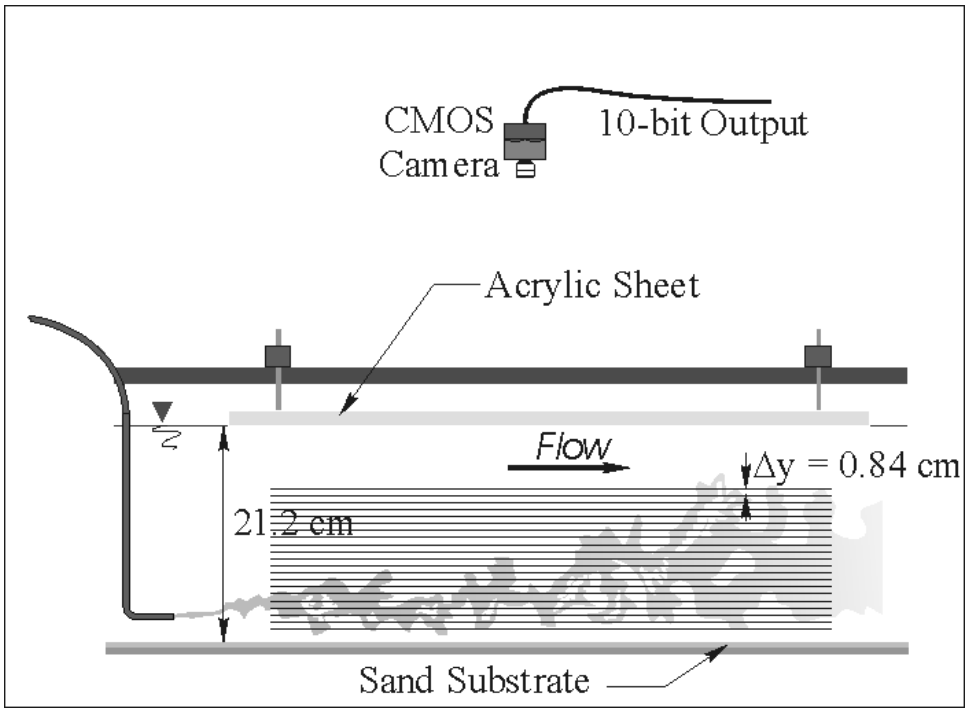

Figure 3.2 Experimental setup for the 3DLIF system, as seen from the side of the flume. The horizontal lines represent the sequential locations of the laser scan.

The 3DLIF system has been developed beside the test section of the seawater flume described previously (Figures 3.2 and 3.3). An Argon-ion laser (Innova 100-10) beam scans across the measurement section using a pair of mirrors attached to galvanometers. The mirrors progressively advance the laser beam in the horizontal and vertical directions. The horizontal-direction mirror moves the laser beam across the measurement section at a slight angle to horizontal. Once the horizontal scan is complete, the vertical-

direction mirror shifts the beam a small distance and horizontal movement commences in the opposite direction. For this particular experimental setup, the separation distance between PLIF illumination planes is approximately 0.84 cm with the lowest scan elevation at 0.5 cm above the sand substrate (at flume centerline). Each 3DLIF sequence includes 20 sheets with the highest plane located approximately 17 cm above the channel substrate. The vertical limits were chosen to ensure plume filaments remained within the 3DLIF collection area with the exception of extreme events.

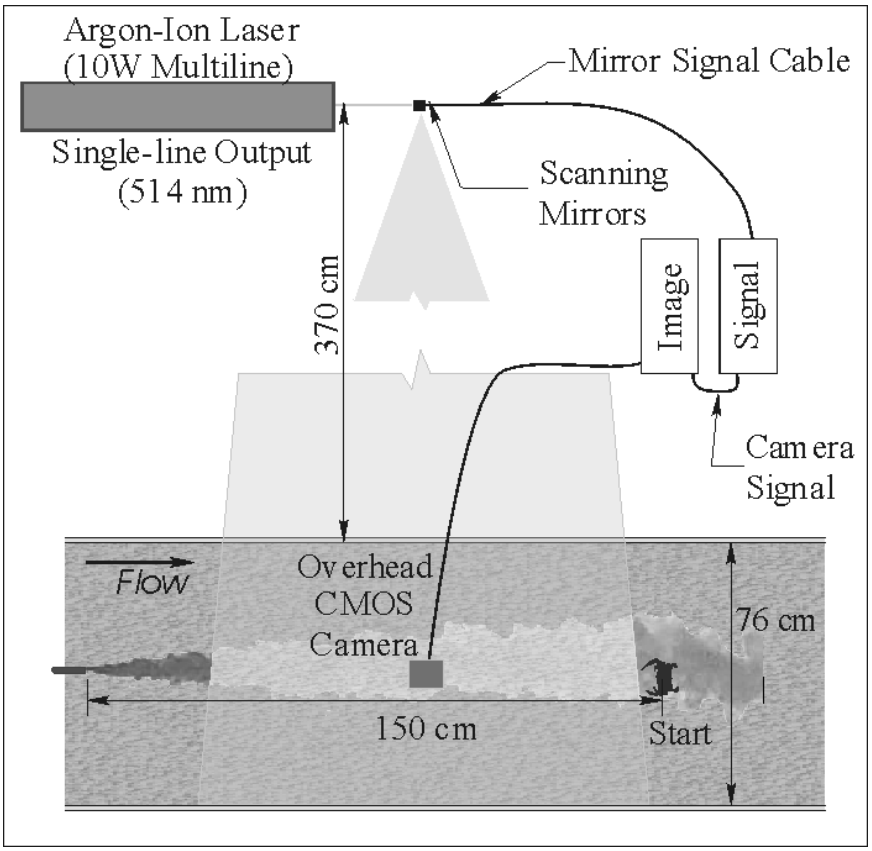

Figure 3.3 Arrangement for the 3DLIF system, as seen from above.

3.3.1.1 3DLIF Resolution

Resolution parameters were chosen to balance two conflicting scale issues. The smallest scales of the plume structure are on the order of the Batchelor scale. To fully resolve the smallest scales of the concentration field with a single camera would limit the test area to approximately 2 cm by 2 cm (Dasi 2004). To gather meaningful information about blue crab behavioral response necessitates test areas that are much larger.

The 3DLIF resolution (approximately 1 mm) for this study was chosen to be greater than the Batchelor scale as a compromise between matching the sensor resolution of blue crabs and maximizing the size of the field of view. Blue crab chemosensory organs at the distal tip of the antennules are on the order of 1 to 2 mm in length (Gleeson 1980) and are assumed to sample at scales closer to the Kolmogorov scale in natural environments (on the order of 1 mm in aquatic environments for blue crabs). Detailed studies on the effective scalar-detecting resolution of aquatic crustaceans are generally lacking (Weissburg and Dusenbery 2002).

Crustaceans bodies are covered with setae, small hair-like structures termed sensillum, used to gather mechanical and chemical information from their environment. Sensilla are concentrated at certain locations, such as along the antennules and on portions of the legs. In the Caribbean spiny lobster (*Panulirus argus*), chemosensory sensilla are composed of tufts, or aesthetascs, and non-tufted setae (Cate and Derby 2001). Through flicking of antennules, crustaceans sample odors in their environment by forcing ambient fluid through the aesthetascs and past other setae (Koehl 2006). Although the size of individual aesthetasc is smaller than the Batchelor scale, chemical information is believed to be effectively smeared as antennule motion enhances mixing and the neurological

signal is supposedly pooled (Keller and Weissburg 2004). The chemosensory response rate for crustaceans is believed to be in the range of 5 Hz (Gomez and Atema 1996), which is too low to resolve the smallest concentration fluctuations (Webster and Weissburg 2001). Further, Crimaldi et al. (2002a) examined the influence of sensor size and sampling frequency on the signal pattern gathered by a virtual antennule in a turbulent odorant plume in the laboratory. Their results showed signal intermittency to be nearly independent of sensor size for sampling frequencies in the range of 5 Hz.

3.3.2 3DLIF system setup

The camera was positioned over the test section to achieve a 1 mm by 1 mm resolution per pixel (at an elevation of 5 cm above the channel substrate). The selected pixel resolution was approximately the size of the Kolmogorov length scale, and was much greater than the Batchelor scale. A 4-m focal length lens reduced the laser beam $1/e^2$ diameter to approximately 1 mm at the flume centerline. Laser power emission was set to 5.0 W at the single line wavelength of 514 nm, which is close to the peak absorption of 530 nm of the chosen fluorophore, Rhodamine 6G. The peak spectral emission of fluoresced Rhodamine 6G occurs at a wavelength of approximately 560 nm (Arcoumanis et al. 1990).

A 1280 × 1024 complementary metal oxide semiconductor (CMOS) camera with a Fujinon 12.5-mm focal length lens collected emitted fluoresced light above the measurement section. The camera was a Mikrotron model MC 1302 with a pixel depth of 10 bits (0 to 1023 grayscale value), peak monochrome quantum efficiency at roughly 530 nm, and maximum frame rate of 100 frames per second. Lens aperture was set at the maximum (f-stop of 1.4). Most PLIF experiments involve the use of charge-coupled

device (CCD) cameras which generally have a higher signal-to-noise ratio. To accomplish the high frame rate required for the 3DLIF experiments of this study, a CMOS camera was chosen, because contemporary CCD cameras could not match these frame rates. Techniques to handle the decreased signal to noise ratio for the CMOS camera are discussed below.

The measurement region for 3DLIF, or region of interest (ROI), varied from 470 to 480 pixels in the transverse direction and 900 to 1030 pixels in the streamwise direction. Crabs successfully tracking odorant sources within the seawater flume did not wander beyond the ROI. The full range of the camera's sensor area was not used for two primary reasons. First, laser light attenuation due to Rhodamine 6G during calibration limited the transverse extent of the ROI. Section 3.3.4 gives more detail about attenuation. A second reason for limiting the ROI was the logistics of data storage. A ROI of 480 by 1030 pixels requires approximately 38% of the uncompressed storage space compared to the full camera range of 1024 by 1280.

An optical filter (Tiffen orange 21 with a cutoff wavelength of 560 nm) and a standard hot mirror were placed over the camera lens to pass fluoresced light while eliminating scattered laser light and protecting the camera sensors. The camera ran at 100 frames per second and was coordinated with the scanning mirrors through a National Instruments multifunction input/output (I/O) board (PCI-MIO-16E-4) programmed with LabView software. Scanning was initiated after a transistor-to-transistor logic (TTL) signal was transmitted from the camera to the I/O board (i.e., the camera acts as the timing master). A proprietary computer system developed by IO Industries collected the camera data via

Video Savant software with an array of six 36.6-gigabyte hard drives through a CameraLink cable with a maximum data rate of 85 MHz. The maximum data rate used for the system was around 66 MHz (two 10-bit signals per clock cycle). As configured, the recording system had the capacity to collect continuous data for 14 minutes.

Due to differences in clock speeds between the camera, the I/O board, and the signal computer, a blank frame was included within the recorded images after each three-dimensional set (i.e., 21 frames are captured to image 20 slices). During this exposure the laser beam sat stationary at one end of the sampling area while the I/O board re-synchronized to the camera. A computer program identified and removed the spurious frames through a comparison algorithm prior to data calibration and analysis. The resulting sampling rate of the 3D volume, roughly 4.76 Hz, was slightly less than the ideal rate of 5 Hz.

For momentumless plumes released into an infinite moving turbulent fluid, the time-averaged concentration C along the centerline in the downstream direction follows a theoretical decay that is inversely proportional to distance from the point source $C \propto x^{-1}$, where x is the distance downstream (Albertson et al. 1950). The inverse power law decay assumes that the turbulence is isotropic and that x is sufficiently downstream of the source for all turbulent eddy sizes to be involved in mixing. Despite the fact that most plumes do not disperse in isotropic turbulence, the power law relationship for the average concentration has been validated experimentally, although the power coefficient may deviate from -1 (Fisher et al. 1979).

For a uniform sweep rate of the laser beam, the inverse power law suggests that fluorescent intensity will decrease significantly with distance from the source. PLIF images covering 1 meter or more of a dispersing plume therefore become significantly dimmer downstream and consequently the signal-to-noise ratio decreases. To increase the uniformity of the image contrast and the signal-to-noise ratio, a power-law control signal to the mirrors was used to increase the beam residence time in the downstream region relative to that in the upstream region. Webster et al. (2003) describe the use of non-uniform angular speeds of the horizontal mirror in PLIF experiments for flow and release conditions similar to this study. The voltage signal sent to the mirror was:

$$E = E_o + \left(E_1 - E_o\right)\left(\frac{t}{T}\right)^{1/(n+1)} \tag{3.1}$$

where n is the power law exponent and E_o and E_1 correspond to the start and end voltages, respectively, and T is the total sweep time period. A power-law exponent of n = 0.75 was chosen for the measurements described in this thesis because it yielded the most uniform images.

3.3.3 LIF Calibration

System calibration is necessary to generate meaningful concentration data from LIF images. Calibration consisted of scanning the laser through artificial seawater with fixed uniform concentrations of Rhodamine 6G. A transparent polyacrylic tank was centered in the flume and filled with a known volume of seawater (taken from the flume sump). Flow depth in the flume was set to the depth used in subsequent experiments (21.2 cm) to include attenuation effects due to seawater between the flume and calibration tank walls. A small amount of Rhodamine 6G was added to the seawater in the tank and uniformly

mixed. Laser scanning was initiated with identical scan positions for calibration and data collection. The fluorescent signal was collected for 100 frames at each 3DLIF level (a total of 2000 images). The process was repeated for 10 to 12 uniform concentration levels. For concentration levels below 60 to 80 μg/l, a linear relationship between the camera pixel intensity and concentration (Ferrier et al. 1993) was found:

$$C = \alpha_c I \tag{3.2}$$

where C is the local concentration, I is the grayscale value of the camera pixel, and α_c is a constant of proportionality including effects of laser power, sweep rate, and pixel nonuniformity. Assuming that α_c is actually a *constant* of proportionality leads to a straightforward calibration process.

3.3.4 Lens vignette, pixel sensitivity and laser light attenuation

Systematic errors can lead to nonlinear pixel response curves during PLIF calibration. Systematic errors due to these and other effects are minimized by performing a pixel by pixel calibration curve for each PLIF layer with constant laser power just prior to collecting experimental data and ensuring a linear relationship between pixel intensity and fluorophore concentration. Thermal blooming occurs when laser intensities are high enough to increase the temperature of the fluid around excited fluorophore molecules. Increased temperature around packets of high concentration increases the index of refraction of the ambient fluid and creates areas of optical distortion. Camera lenses do not transmit light perfectly, leading to higher intensity at the center of the image relative to the edges, an effect referred to as lens vignette (Tian and Roberts 2003). Photobleaching is a process where a fluorophore reaches a saturation state and can no

longer absorb laser light leading to decreased pixel response with increasing fluorophore concentration or laser intensity (Speiser and Shakkour 1985, Crimaldi 1997, Larsen and Crimaldi 2006). Local pH or the interaction of the fluorophore with other chemical species within the ambient fluid, especially dissolved chlorine in the case of Rhodamine 6G, can also significantly affect fluorescent response.

Figure 3.4 demonstrates the spatial variability of the base pixel sensitivity for images taken with the cap on the camera lens in a dark room. The effects of lens vignette can be isolated by collecting data of uniform images (shown in Figure 3.4 center and bottom). The response of each pixel and the influence of lens inhomogeneities can be determined by subtracting the black level from the gray and white level images. Assuming the lens-camera system responds linearly to increasing light intensity, pixel response can be normalized to the most sensitive pixel. The effects of lens vignette and pixel response can be removed from images by applying a correction factor to the data values (Tian and Roberts 2003):

$$p_{cor} = \frac{I_{WL}^{\max} - I_{GL}^{\max}}{I_{WL} - I_{GL}} \tag{3.3}$$

where I_{WL} and I_{GL} are the white and gray level values, respectively. To normalize an image, each pixel is adjusted to the most sensitive pixel as follows:

$$I_{cor} = p_{cor} \cdot \left(I_{uncor} - I_{BL}\right) + I_{BL} \tag{3.4}$$

where I_{cor}, I_{uncor} and I_{BL} are the corrected, uncorrected, and black level values, respectively.

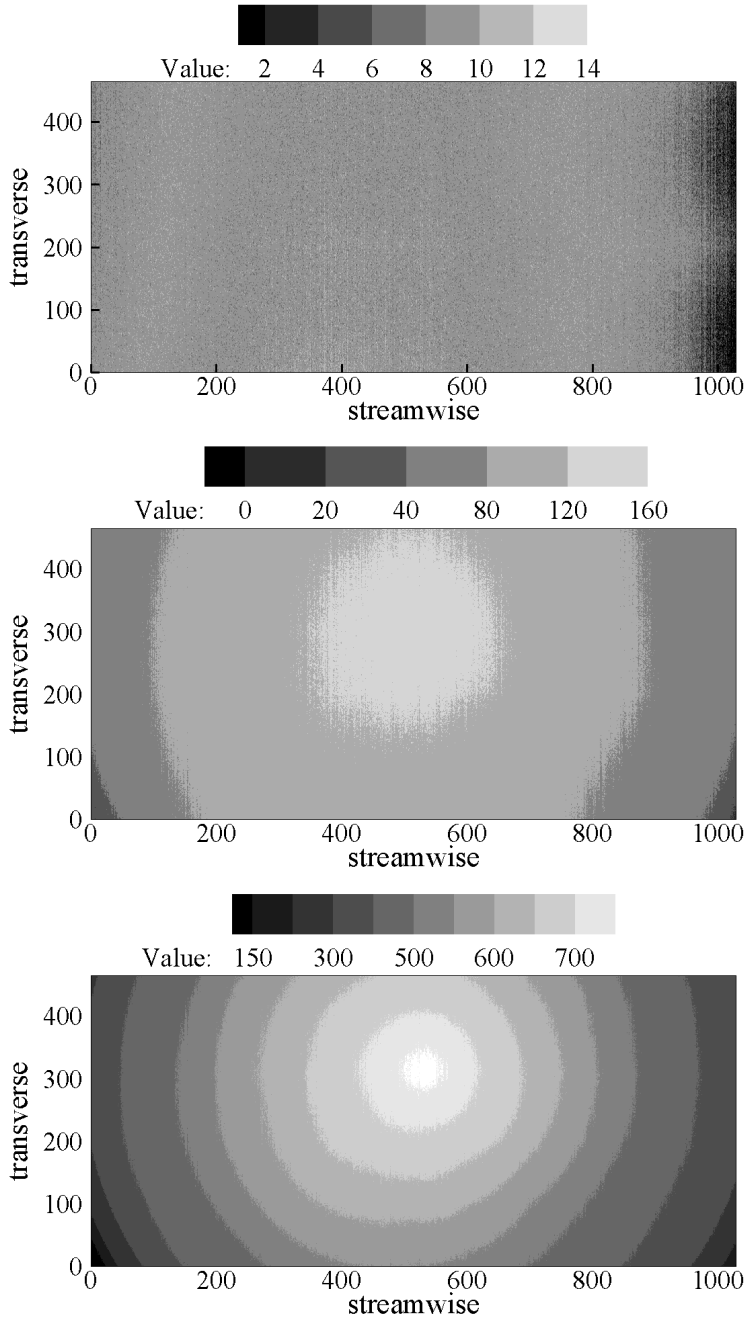

Figure 3.4 Images for the camera (top) black level, (center) gray level, and (bottom) white level. The black level image was created by averaging 200 images collected in darkness with the lens cap on. The gray and white level images were created by averaging 200 images of a uniform background. Fixed pattern noise (FPN) is evident in all three images as vertical lines. The effects of lens vignette are evident in the two gray level images (center and bottom) as concentric rings.

Further, the presence of fluorescent dyes, impurities, and the ambient fluid causes a decrease in laser intensity with distance through a medium. The loss of laser power with distance follows the Bouguer-Lambert-Beer Law:

$$P(x) = P_0 e^{-\beta x} \tag{3.5}$$

where $P(x)$ is the laser power at a distance x within the medium, P_0 is the initial laser power at $x = 0$, and β is an attenuation coefficient. The attenuation coefficient is not generally constant with varying concentration and can be assumed to be composed of two independent parts $\beta = \beta_{SW} + \lambda C$, where β_{SW} is a base attenuation coefficient due to attenuation from seawater and other effects, λ is the extinction coefficient, and C is the concentration of Rhodamine 6G. The extinction coefficient for Rhodamine 6G to laser light at 514 nm has been reported as 0.00023 cm^{-1} $(\mu g/l)^{-1}$ by Ferrier et al. (1993) and 0.00021 cm^{-1} $(\mu g/l)^{-1}$ by Brackmann (2000). Rhodamine 6G is available in different forms from various commercial vendors and the extinction coefficient is likely to vary.

An in-situ attenuation coefficient was calculated from the calibration images by examining the decrease in beam power as indicated by decreasing pixel intensity (10-bit value). A 5-pixel-wide column aligned collinearly with the beam and perpendicular to the flume centerline was analyzed where residence times are greatest and geometric corrections are minimal. The intensity values within the 5-pixel wide column were averaged and corrected for beam residence time. When using scanning mirrors, laser light passes through the integration area of an individual camera sensor at speeds

dependent upon distance from the reflecting mirror and angular deflection. The residence time correction for a given pixel location is (Crimaldi and Koseff 2001):

$$I_{cor}^{(x,y)} \Big/ I^{(X,Y)} = \frac{r\cos^2\varphi}{Rt\dfrac{\partial\varphi}{\partial t}} \tag{3.6}$$

where $r = \sqrt{x^2 + y^2}$ is the radial distance from the mirrors to the pixel location and $R = \sqrt{X^2 + Y^2}$ is the radial distance to a reference point along the same beam path (i.e., with the identical horizontal angular deflection φ). Although the scan rate in the current measurements varied according to equation 3.1, for a small sweep arc, the rate $\partial\varphi/\partial t$ and resultant angular displacement $t\,\partial\varphi/\partial t$ both can be assumed constant. For the column of pixels selected ($\varphi = 0$), the residence time correction reduced to a ratio of the radial distance of a given pixel to the radial distance of a reference location, the front of the calibration tank for this study. The correction coefficient normalizing to the most sensitive pixel using equations 3.3 and 3.4 was applied. The normalization and radial correction procedure isolated the observed power decrease with distance into the tank, or the recorded fluorescence decrease, to be directly attributable to attenuation effects.

Calculating the extinction coefficient requires a measure of beam power at the front of the fluid medium. The procedure assumed a linear relationship between local laser power at the front of the calibration tank, P_0, and resultant recorded intensity I_0. The value of I_0 was the average pixel intensity for the 5 by 5 group of pixels at the front of the calibration tank (covering an area of 5 mm by 5 mm) (Figure 3.5a). Plots of pixel intensity versus distance through the calibration tank displayed an exponential decay as

expected (see Figure 3.5b). The extinction and base attenuation coefficients were calculated by fitting the log-transformed data to a least-squares fit line (see Figure 3.6). Several calibrations were performed with resulting extinction coefficients around 0.00024 cm^{-1} $(\mu g/l)^{-1}$. The resulting base attenuation coefficient β_{SW} due to the seawater medium was 0.004 cm^{-1}. The in-situ extinction coefficients found for this study were slightly higher than those reported by Ferrier et al. (1993) and Brackmann (2000) for Rhodamine 6G. The discrepancy is assumed to be due to the relatively high laser intensity and Rhodamine 6G concentrations used in this study.

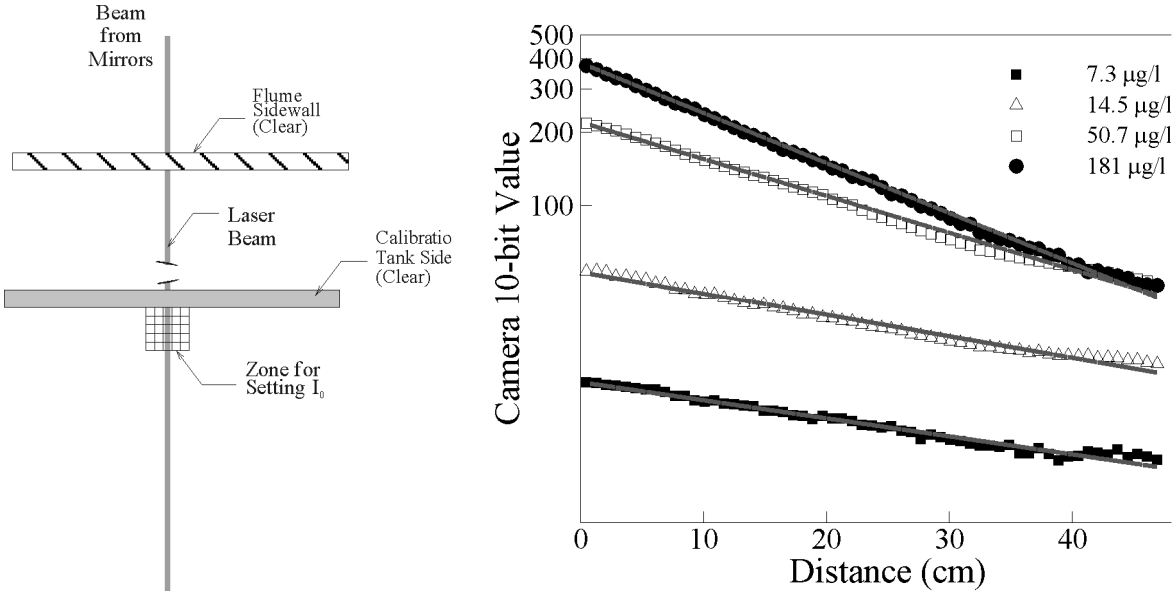

(a) (b)

Figure 3.5 (a) Schematic of the sampling zone for determining the base power-level for attenuation. The dimensions of the sampling zone are 5 mm by 5 mm. (b) Semi-log plot of pixel intensity levels after radial correction and sensitivity normalization. Every tenth data point and best-fit lines are shown. The location denoted as zero corresponds to the front of the calibration tank as shown in panel (a).

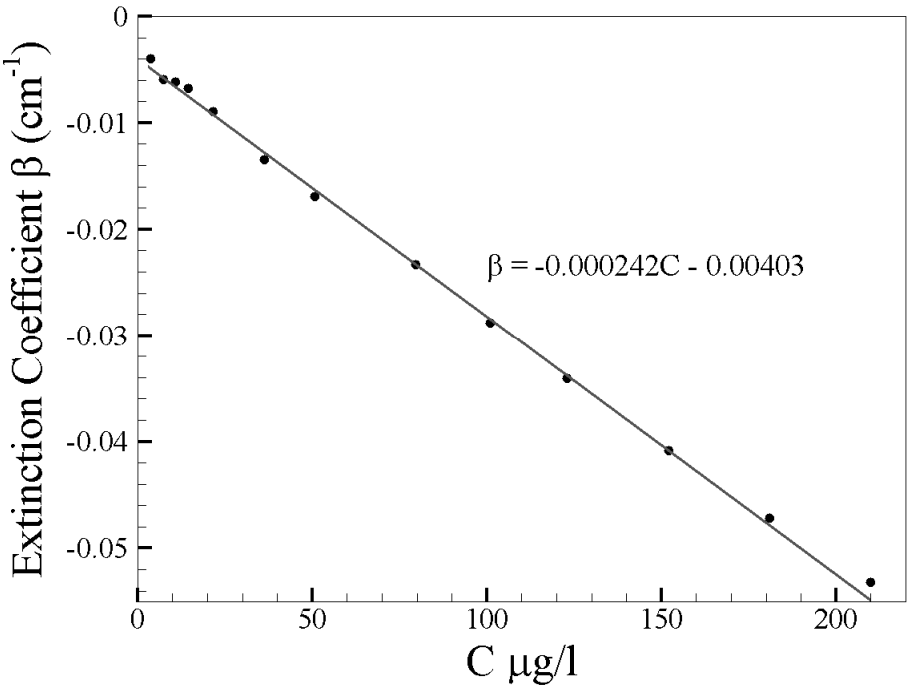

Figure 3.6 Attenuation coefficient plot for an example calibration. Extinction coefficient dependence on concentration is linear for concentrations below about 150 μg/l.

3.3.4.1 Magnification and optical distortion

Refraction of laser light at the water surface influences the apparent pixel location. Light passing from one medium to another bends at the boundary between mediums with the incident and refractive rays following Snell's law:

$$n_1 \sin(\theta_1) = n_2 \sin(\theta_2) \tag{3.7}$$

with n being the medium index of refraction, or the ratio of the speed of light in the medium with that of a vacuum, and θ is the respective incident or refractive angle. An increasing difference in refractive index indicates increasing bending of light at the

medium boundary. Water has a refractive index of 1.33, which introduces significant beam deflection with increasing angle of incidence. The 3DLIF fluorescent light passed through two refractive boundaries. The first was at the boundary between the seawater and the acrylic plate placed at the surface to remove distortion effects from small waves. The second was at the top of the acrylic plate at the boundary with the ambient air. The refractive effects due to the acrylic plate could be assumed small as the medium was thin.

The effects of both refraction and lens magnification can be accounted for by evaluating an image collected for a grid with known spacing. A grid was constructed by placing 1 mm by 1 mm printed squares in an array with spacing of 5 cm by 5 cm. The grid was physically placed in the flume and centered at the approximate centerline of the camera sensors. Flow depth was set at that used during experiments and the acrylic plate was placed over the water surface. An image was taken of the grid located at the level of the substrate with the overhead camera. A second image was taken with the grid located at the level of the water surface, at the bottom of the acrylic sheet. Each 1 mm by 1 mm grid square was located within the pixel grid to sub-pixel accuracy using Gaussian interpolation.

The distortion at the centerline of the camera sensor was determined by using the surrounding 4 grid pixels as follows:

1. The center of the camera sensor was assumed coincident with lens centerline and the consequent center of distortion, or the optical centerline. The optical centerline was placed at the center of the total sensor array, with dimensions of 1280 streamwise by 1024 transverse.

2. The four grid nodes surrounding the sensor center were located and the distance between the four pixels calculated from the sub-pixel locations (see Figure 3.7).

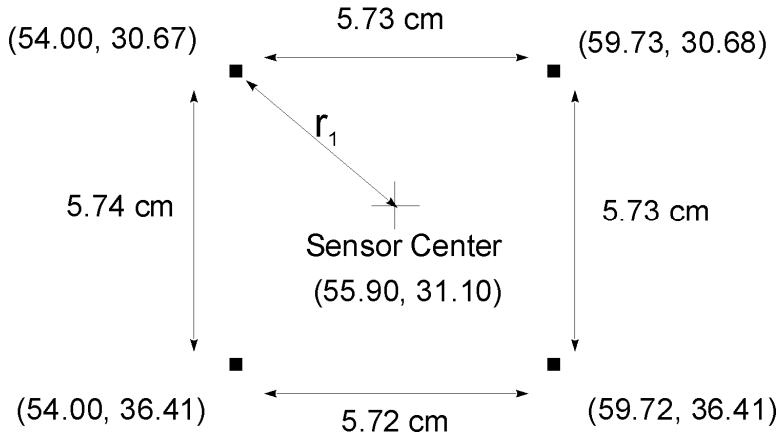

Figure 3.7 Schematic showing the determination of the distance from the center of the camera sensor to the base grid point with 5.0 cm spacing. In this case, the base distortion is $m_B \cong \frac{5.73}{5} = 1.146$. Hence, for a measured distance of r_1' = 1.95 cm, the actual distance is $r_1 = \frac{r_1'}{m_B} = \frac{1.95\,\text{cm}}{1.146} = 1.70\,\text{cm}$.

3. A base distortion value was calculated in the vicinity of the sensor center. This was done by dividing the average distance between the 1 mm by 1 mm grid nodes in the image by the known physical distance.

4. The top left square was chosen as the base point for subsequent distortion calculations. The distance from the camera sensor to the base point, r_1, was calculated using the base distortion value.

5. The distance from the base point to each grid node, R', was calculated from the sub-pixel values (Figure 3.8). The actual distance, R, was calculated from the known physical spacing between grid points and r_1.

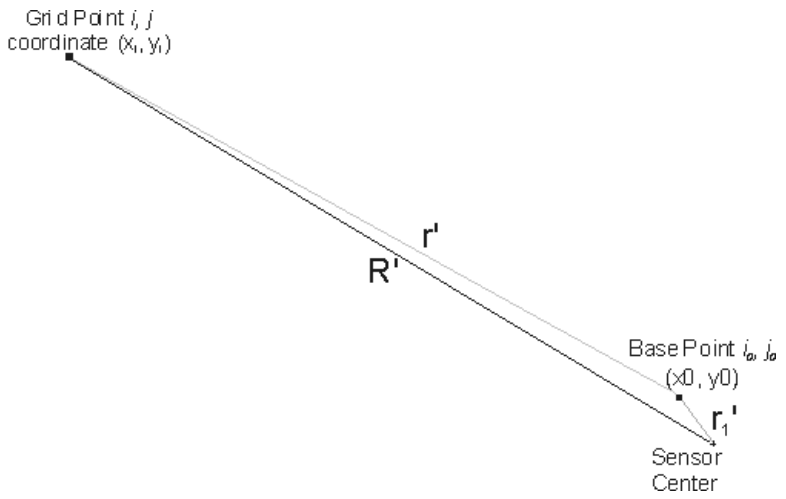

Distorted distance $\vec{R}' = \vec{r}_1' + \vec{r}'$ with $|r'| = \sqrt{(x_i - x_0)^2 + (y_i - y_0)^2}$

Actual grid distance $\vec{R} = \vec{r}_1 + \vec{r}$ with $|r| = d\sqrt{(i - i_0)^2 + (j - j_0)^2}$ where d is the known grid spacing (50 mm).

Resultant distortion at (x_i, y_j) is the ratio of the respective radii $m_{ij} = \dfrac{|\vec{R}'|}{|\vec{R}|}$

Figure 3.8 Schematic that explains the calculation of the image distortion at the grid locations.

6. With the physical and imaged distances, the distortion at each grid point was calculated as the ratio of *R/R'*. Distortion of the remainder of the camera field was determined on a pixel-by-pixel basis using a 4-point bilinear interpolation with the grid points as corners (Castleman 1996).

Figure 3.9 is a plot of the corrected and uncorrected grid for the image corresponding to the lowest plane. Distortion values are shown in Figure 3.10 for the image corresponding to the lowest plane. The resulting distortion varied from pixel to pixel and took into consideration lens magnification and refraction effects.

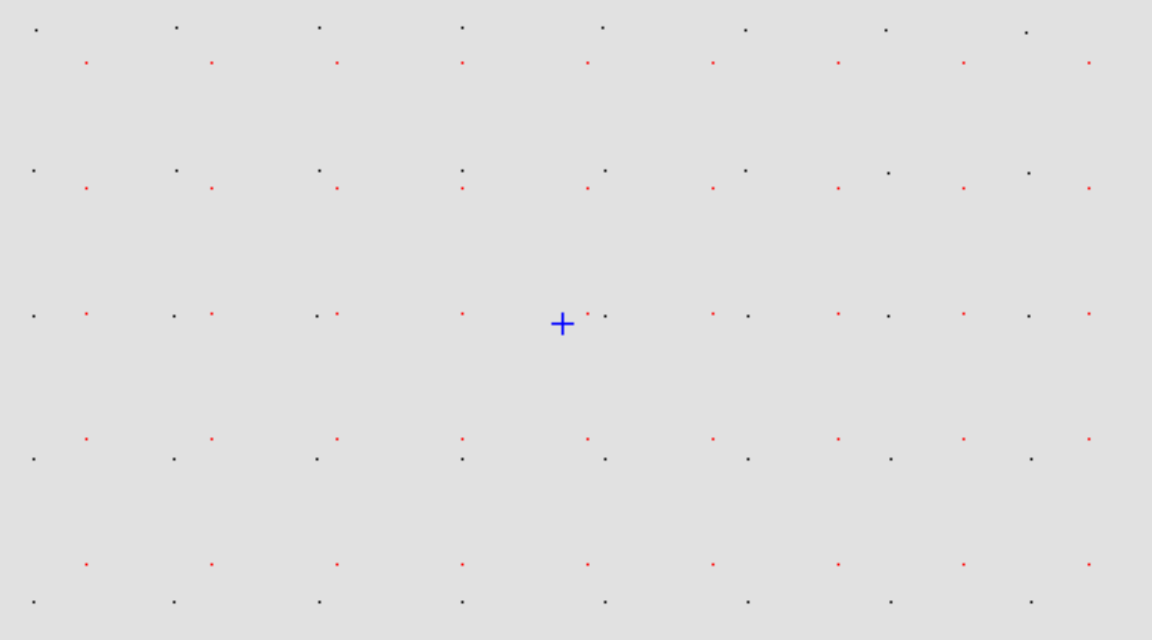

Figure 3.9 Comparison between distorted and undistorted grid placed at the floor of flume. The red dots are the known grid point locations and the black dots are the distorted image point locations. The blue cross is located at the center of the camera sensor, and the dots are shown relative to the grid point to the left of the blue cross. Note that only a portion of the field is shown in this image for clarity.

3.3.4.2 Coordinate determination

The 3DLIF system used scanning mirrors which directed the beam at small angles relative to horizontal. For larger scan areas, the beam angles introduced a non-trivial error to the horizontal plane assumption, especially close to the boundaries. For the 3DLIF setup of this study, the laser scans could differ from the horizontal plane assumption by several centimeters at the edges of the region of interest. The error could

introduce significant error to subsequent calculations pertaining to crab kinematics and plume statistical parameters.

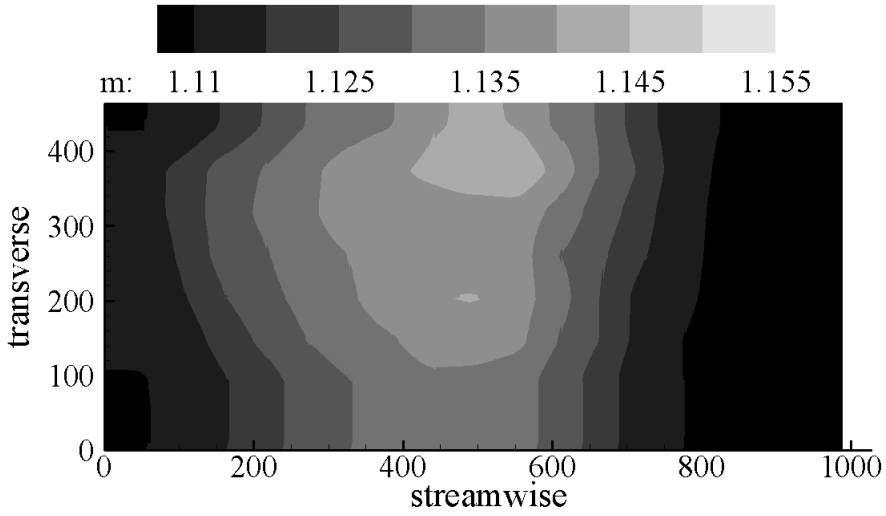

Figure 3.10 Map of the distortion level for the elevation at the channel substrate. Contours shown are magnification.

With the distortion level determined at the channel substrate and water surface, the actual coordinates of the laser beam could be determined. The mirrors were programmed to reflect the beam at set distances above the substrate at the flume centerline. The resulting laser scans were not horizontal, but inclined at small angles (Figure 3.11). From the calibration images, the magnified distance to each point from the center of the camera sensor, R', was known. The vertical coordinate, z, depended on the mirror angle and the radial distance from the mirror. Using R', the radial distance from the mirrors, the consequent difference from the horizontal assumption was estimated.

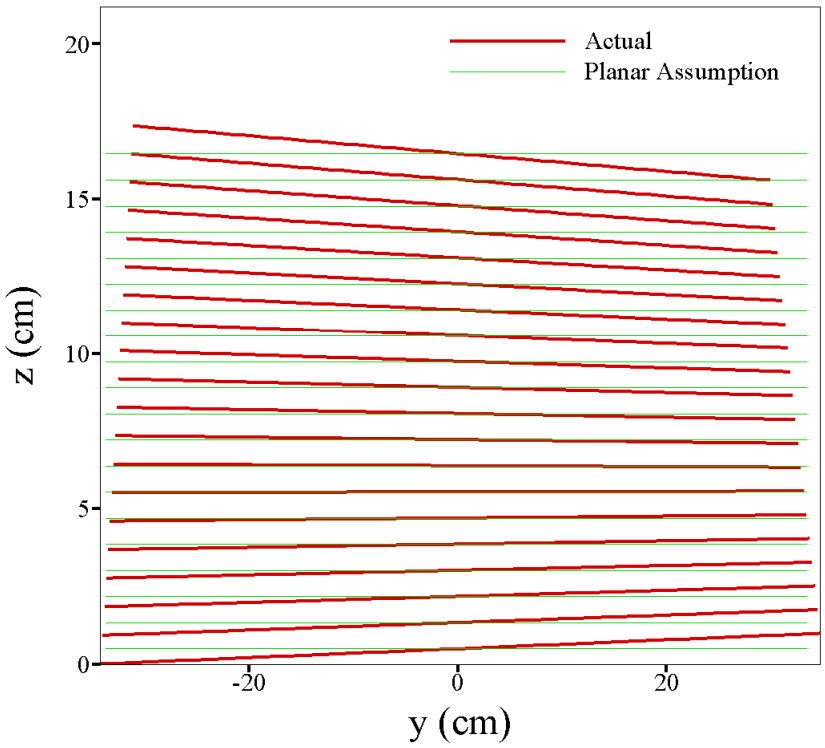

Figure 3.11 Laser scan slices (red) and assumed planar sections (green). Deviations of the laser scan locations from the horizontal planes are due to scanning mirror angle, magnification, and refraction at the water surface.

The distortion of R' used to determine the actual distance R varied with distance from the camera lens. A simple relationship between distortion and distance from the camera lens was assumed. For a given pixel location, the distortion was determined by linearly interpolating in the vertical direction between grid images collected at the bed and water surface. The value of R' was corrected to R and a new vertical coordinate generated. An error was introduced by using unshifted pixel values in place of actual coordinates in the linear interpolation of the distortion level and resultant magnification. A second error occurred by using the uncorrected radial distance R' instead of the correct distance R

when determining pixel vertical location for calculating the magnification. With the mirror angles and radial distances from the mirror used, the error in magnification due to using uncorrected pixel elevations was estimated to be very small and assumed negligible.

3.3.4.3 Pixel-by-pixel calibration procedure

With the in-situ laser-power decay coefficients and coordinate locations known, the calibration procedure could be completed. The raw intensity values of the calibration images were adjusted through the use of the Bouguer-Lambert-Beer Law (equation 3.5) with the travel distance through Rhodamine 6G calculated from the difference in the radial distance from the individual pixel location to the mirror and radial distance from the mirror to the front of the calibration tank. The corrected pixel values followed the linear response predicted by equation 3.2 for concentration values below approximately 80 μg/l. The result was linear regression coefficients (i.e. slope and intercept) for each pixel location in each imaging plane.

3.3.4.4 Quantifying the black level

For the camera used in this study, the black level was unsteady, possessing both a mean and a fluctuating part. In contrast to a charge-coupled device (CCD), each CMOS sensor has an individual analog-digital converter, which enables high data throughput with the tradeoff of greater noise level. To get reliable concentration data, the individual pixel noise fluctuations for the black level had to be quantified and filtered.

The noise in the black level signal could be reduced to zero through various camera settings. The problem with reducing the black level instability to zero was that it made the camera increasingly insensitive to light, even with high Rhodamine 6G

concentrations. Modifying the camera gain and white level resulted in better sensitivity to light but at the expense of increasing noise levels. The predominant manifestation of pixel noise was in the form of fixed pattern noise (FPN), which appeared as vertical or horizontal lines on images depending on individual pixel A-D converter sensitivity and the method of data transmission (see FPN on figures 3.4a and 3.4b). Several combinations of source fluorophore concentration and camera settings were attempted prior to finding a balance between pixel noise and sensitivity. Figure 3.12 shows a trace of the output from two pixels during LIF image collections and demonstrates the fluctuating recorded black level. A further complication was nonstationarity in the noise itself between image recordings, i.e., the traces shown on Figure 3.12 change in both the average and the amount of fluctuation between video recordings. Thus, the method of removing the base pixel noise was unique to each image set collected.

The noise in the signals shown on Figure 3.12 is evident. Several methods were evaluated in order to filter the background noise from the image signal. The first technique involved simply finding the minimum pixel output from a time record and adding a fixed amount:

$$I_{ij}^{BL} = I_{ij}^{MIN} + I^{C} \tag{3.9}$$

where I_{ij}^{MIN} is the minimum digital output at pixel ij and I^{C} is a constant. Intensity values below I_{ij}^{BL} were assumed to be noise and filtered (i.e., the intensity was set to I_{ij}^{BL}, which corresponded to a concentration of zero). Adding a fixed amount to the minimum

intensity worked well for values of I^C in the range 8 to 10, although the noise level in the time-averaged values still showed significant FPN.

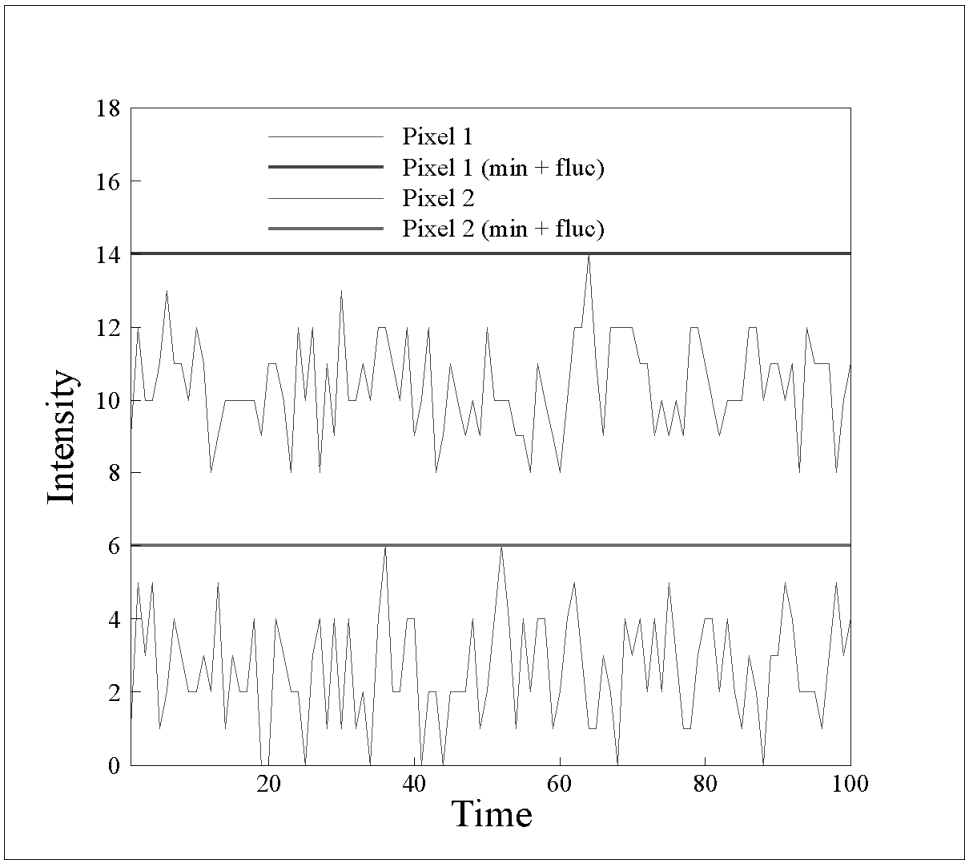

Figure 3.12 Time records of intensity for two example pixel recordings of the continuous plume, which show the fluctuating noise level. The horizontal lines are the threshold values described in the text and act as a filter. Intensity samples at levels above the threshold values are assumed to be valid concentration bursts.

A second technique for removing pixel noise involved finding the average and standard deviation for the intensity at each pixel for a moderately long time record, usually 500 ensembles. Since noise characterization was required for image sets with concentration data, not all fluctuations could be considered noise. Consequently, a second pass through the time record was performed whereby pixel intensities above the average plus three

times the standard deviation were not included. The process was repeated using the second generation average and standard deviation, with the upper pixel limit reduced to the average plus two times the standard deviation. The third pass set the final threshold, I_{ij}^{BL}, to the third generation average plus two times the third generation standard deviation. For a normal distribution, the average plus twice the standard deviation removes approximately 98 percent of the noise. Whereas this technique may be the most defensible from a statistical perspective, it did not improve the results relative to adding a pixel-dependent constant to the minimum digital value.

For the current study, the noise filtering technique minimizing FPN on concentration images was similar to the first technique described above. From a black level image, the amount of pixel noise was calculated by subtracting the minimum intensity from the maximum over a record of 1000 frames. The constant of equation 3.9 now varied:

$$I_{ij}^{BL} = I_{ij}^{MIN} + I_{ij}^{BLN} \tag{3.10}$$

where I_{ij}^{BLN} is the black level noise for the given pixel. A map of the value of black level noise at each pixel location is shown at the top of Figure 3.4. Most values are in the range of 6 to 10, close to the assumed values used in the first technique.

3.3.5 Data Processing

Once the calibration was completed, concentration data can be calculated from images collected by the overhead CMOS camera. In most cases, the process was simple; concentration was calculated through the calibration slope and intercept:

$$C_{ij} = m_{ij}\left(I - I_{ij}^{BL}\right) + b_{ij} \tag{3.11}$$

with C_{ij}, m_{ij}, I_{ij}^{BL} and b_{ij} as the respective concentration, calibration slope, black level intensity, and calibration intercept at pixel ij. In the event that equation 3.11 yielded a negative concentration, the value was set to zero.

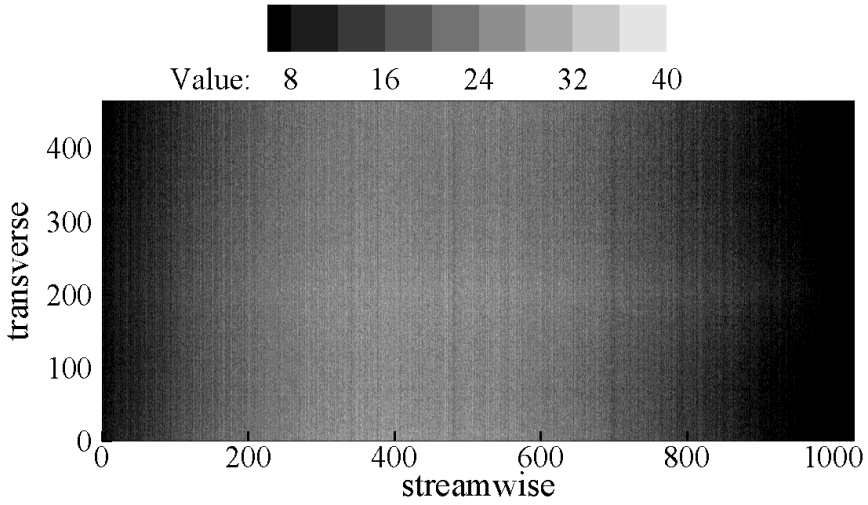

Figure 3.13 Raw average plume data for 7400 images at the nozzle centerline for the continuous release prior to filtering and application of the calibration

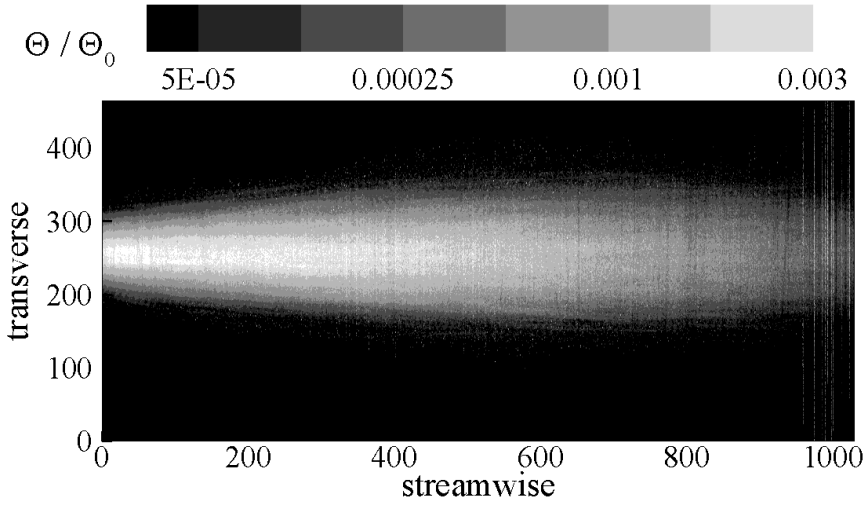

Figure 3.14 Average concentration field corresponding to the intensity field shown in Figure 3.13 after application of the calibration. Contours are of relative concentration.

Shown in Figure 3.13 is an average of 7400 images of the continuous plume in the plane near the elevation of the nozzle centerline. The average plume shape should be centered transversely (i.e., around 220 pixels) and is barely discernible. Background noise is significant and is mostly removed during application of the calibration. An example concentration field is shown in Figure 3.14 and corresponds to the data shown in Figure 3.13 after application of the calibration.

3.4 Behavioral trials

Blue crabs used in the 3DLIF trials were either collected from Wassaw Sound in Georgia or purchased from Gulf Specimen Marine Laboratory in Panacea, Florida. The animals were stored in artificial seawater tanks interconnected through a filtered recirculating system and were fed a diet of previously frozen shrimp. Blue crabs were permitted to acclimate for 48 hours prior to blindfolding in the procedure described below.

3.4.1 Blindfolding of the crab specimens

The purpose of performing 3DLIF experiments in conjunction with animal behavior trials was to determine the instantaneous concentration field experienced by the tracking organism as it approached a source. Blue crabs demonstrated an adverse reaction to intense laser light at frequencies of 514 nm. After several unfruitful attempts at developing a blindfolding procedure, a technique involving electrical heat-shrink wrap was found to be effective. After applying the blindfolds, the crabs were allowed to acclimate for a minimum of 48 hours before performing trials. Earlier trials comparing blindfolded with unaltered crabs showed the blindfolds to have no effect on tracking behavior (Jackson, unpublished data). Crabs typically were able to remove the blindfolds within a week after application with no noticeable adverse affects.

3.4.2 Kinematic data and physical limitations

Crab kinematic data were calculated by following two light-emitting diodes (LEDs) in a small backpack temporarily attached to the crab. During trials, the flume area was darkened to minimize visual distractions to the crab and to increase the contrast of the emitted light from the LIF dye and the backpack lights compared to the background. Crabs were held in a cage at the downstream end of the test arena for a 10-minute acclimation period. Once the cage door was raised, crabs were given 10 minutes to initiate tracking by exiting the cage and an additional 10 minutes to complete their motion across the test section. Within this time period, crabs either moved across the test section and missed or found the odorant source, or remained stationary for the entire time period. No animals were in the process of tracking at the end of the 10-minute observation period.

The coordinates of the light locations were determined by following the centroid location through the image frames. The diode center was located on each image by a computer algorithm that sampled a small moving area for the pixel surrounded by the highest recorded light intensities. The light locations were verified visually by plotting a trace for each crab light position and overlaying it onto the raw image data. Velocity in each coordinate direction, crab angle with respect to flume centerline, and acceleration in each coordinate direction were calculated based on the average of the two light locations for each 3DLIF set (i.e., average of the 20 images) at approximately every 0.2 s. The time differential of approximately 0.2 s was chosen to calculate the time derivatives because it roughly corresponds to the presumed neurological response of aquatic arthropods (Gomez and Atema 1996) and led to some smoothing of the resulting acceleration data.

The presence of the animal within the PLIF measurement area created shadows where the laser beam hit the crab body. When traveling upstream against a current, blue crabs generally oriented themselves at an acute angle with respect to the flow vector (Weissburg and Zimmer-Faust 1993, Weissburg et al. 2003). Depending upon the direction chosen to align with the flow, the crab antennules region either faced the laser or was obscured in shadows. Behavioral studies have suggested the antennules region to be pivotal in the maintenance of upstream movement towards a source (Keller et al. 2003). Little useful concentration-related information could be extracted from trials where the antennules region was shaded. The determination of the concentration field and behavioral correlations were limited to those crab tracks which faced the laser. In the experimental setup shown in Figure 3.3, this corresponded to crabs leading upstream with their left claw.

Despite placing optical filters on the camera lens, laser light reflected from the surface of the crab was intense enough for the camera sensors to record. Light reflected from the crab and shadowing effects prevented precisely extracting the odorant concentration impinging upon the crab's outer chemosensors. Mead et al. (2003) encountered similar limitations on their PLIF data with tracking mantis shrimp. The techniques developed in this study to extract meaningful concentration field data near the chemosensory organs are described in Chapter 5.

Figure 3.15 Photograph of a blindfolded crab prior to a behavioral trial.

Chapter 4

Physical Characteristics of the Plumes

To complement the concentration fields collected around actively tracking blue crabs described in the next Chapter, experimental data was collected for the three plumes in the absence of crabs and without odorant in order to gain a quantitative understanding of plume structure in each case. The plume and flow parameters are identical to the conditions employed in the plume tracking trials. Data collected for the continuous plume are similar to those collected by Rahman (2002) using traditional PLIF. The data collected for the meandering plume and pulsed plume are unique to this thesis. The measurement area (region of interest, ROI) extends in the streamwise direction approximately from $x = 1.6H$ (0.34 m) to $x = 6H$ (1.27 m). The total distance from the source location to the starting point for the blue crabs was 1.5 m. Hence, the selected ROI focused on the region that corresponded to the early and mid-stage periods of the tracking paths and was generally within the region beyond the zone of flow establishment.

The concentration data reported are for the fluorophore, Rhodamine 6G. Concentrations of Rhodamine 6G and odorant when used together are proportional as both tracers are conservative, though the proportionality is unknown. By non-dimensionalizing the data by the source concentration, the proportionality is removed thereby enabling a direct comparison with the odorant used in behavioral trials of the previous chapter.

4.1 Continuous plume

Figure 4.1 shows flow visualization images of the continuous plume release of a neutrally buoyant red dye. In the zone of flow establishment ($x/H < 2$, Rahman 2002), the plume is narrow and meanders slightly as the larger energetic eddies are not yet effective in mixing. Due to the iso-kinetic nature of the release, ambient turbulence within the boundary layer is primarily responsible for the dispersion of the dye into the filamentous structure shown. The downstream decrease in concentration is pronounced in all three images. The photograph at the top of Figure 4.1 shows the plume as wider compared to the lower images, which demonstrates the variability of the plume structure and suggests that the plume was briefly influenced by a large vortex structure.

Two example instantaneous concentration fields are shown in Figure 4.2. The fields consist of sparse regions of high concentration surrounded by an ambient condition of zero or near-zero concentration. The high concentration regions correspond to the intersections of odorant filaments with the plane of measurement. Note that the gradient of concentration is very large at the edge of the filaments; the concentration rises from near zero to a large value within a millimeter or less. The concentration of the filaments decreases rapidly in the streamwise direction due to the mixing and dilution of individual filaments.

The source concentration in this case was 600 µg/l and the averaging calculation included 7800 fields at each 3DLIF level (i.e. a total of 152,000 images). The time period required to collect the images was approximately 25 minutes with the camera running at 100 frames per second. The large number of samples and long sample period were required

because of the sparse and intermittent nature of the plume structure. Average concentration data are the result of simple ensemble averaging:

$$\Theta = \frac{1}{T}\sum_{1}^{T}\tilde{\Theta} \tag{4.1}$$

where T is the number of fields, 7800 in this case. Figure 4.3 shows the average concentration field for four elevations above the substrate. For the four fields shown in Figure 4.3, the contours are symmetric about the nozzle centerline (i.e., y = 0). The nozzle is located nearest to the plane labeled z = 2.2 cm in Figure 4.3b and the average concentration along the centerline decreases from the high value near the source. For planes above the nozzle elevation (Figures 4.3c and 4.3d), the location of the peak in the average concentration is found downstream of the source because dye must be transported upward to these regions. The antennules of tracking blue crabs were generally found between measurement levels 6 and 8, corresponding to 4.7 to 7.2 cm above the substrate ($z/H = 0.22 - 0.34$). Figures 4.3c and 4.3d show that the location of the peak average concentration is in the range of x/H between 3 and 4.5. Although statistical averages are a poor indicator of the signal that a blue crab encounters during tracking (Webster and Weissburg 2001), the changes in the average concentration fields with elevation reflect the contrasting olfactory environments experienced by sensors closer to the substrate and those higher in the water column.

The magnitude of the concentration fluctuations was quantified by calculating the standard deviation using the ensemble of fields:

$$\theta' = \left[\frac{1}{(T-1)} \sum_{1}^{T} \left(\tilde{\Theta} - \Theta \right)^2 \right]^{1/2} \tag{4.2}$$

Plots of the standard deviation of the concentration fluctuations are shown in Figure 4.4 at four 3DLIF elevations. Note that the magnitude of the standard deviation is greater than the average shown in Figure 4.3. Hence, the time records consist of large fluctuations in concentration above a relatively small average value. The standard deviation therefore describes the sparse and intermittent plume structure observed in the instantaneous fields (Figure 4.2). The fluctuation intensity does not vary significantly among elevations for x/H greater than approximately 4.5.

The standard deviation of the concentration fluctuations reaches a maximum at the nozzle centerline with a given distance from the source. The centerline maximum occurs due to the interaction of the mean concentration gradient with the turbulent mass flux, both of which peak at the centerline when using the eddy-diffusivity hypothesis. An eddy-diffusivity allows the production of concentration variance in equation 2.19 to be related solely to the mean concentration gradient:

$$-2\overline{u_i \theta} \frac{\partial \Theta}{\partial x_i} = 2\varepsilon_{ij} \frac{\partial \Theta}{\partial x_j} \frac{\partial \Theta}{\partial x_i} = 2\left(\varepsilon_x \frac{\partial \Theta}{\partial x} \frac{\partial \Theta}{\partial x} + \varepsilon_y \frac{\partial \Theta}{\partial y} \frac{\partial \Theta}{\partial y} + \varepsilon_z \frac{\partial \Theta}{\partial z} \frac{\partial \Theta}{\partial z} \right) \tag{4.3}$$

In gravity-driven, two-dimensional shear flow, statistical characteristics of the turbulence depend solely upon the z-coordinate. When Schmidt and Reynolds number are high, turbulent diffusion dominates and the eddy-diffusivity tensor ε_{ij} can be assumed aligned with the mean flow, i.e., with the x-axis, and the z-axis (Monin and Yaglom 1972, page 613). As with the eddy-viscosity, the eddy-diffusivity becomes diagonal in a Cartesian

coordinate system aligned with the flow, yet is not necessarily isotropic. As the source is approached, the streamwise mean concentration gradient term dominates in equation 4.3 and the production of the variance of the scalar fluctuations reduces to:

$$-2\overline{u_i\theta}\frac{\partial\Theta}{\partial x_i} \cong -2\overline{u\theta}\frac{\partial\Theta}{\partial x} = 2\varepsilon_x \frac{\partial\Theta}{\partial x}\frac{\partial\Theta}{\partial x} \tag{4.4}$$

The mean streamwise concentration gradient is maximum along nozzle centerline ($y = 0, z = z_0$), which is reflected in the centerline peaks in the standard deviation of the concentration fluctuations shown in figures 4.4a and 4.4b.

As observed with the average concentration fields (Figure 4.3), the location of peak fluctuations occurs away from the source for layers above the plume centerline. The plume requires time to expand sufficiently to reach elevations above the nozzle height; hence near the source the fluctuations are near zero because the plume structure is not present and the peak in fluctuation intensity is located away from the source as the plume structure expands to that elevation.

Crimaldi et al. (2002) noted that the combination of the average, standard deviation, and intermittency factor provides a meaningful measure of the instantaneous plume structure, whereas they fail individually. Field plots of intermittency factor are shown in Figure 4.5. The intermittency factor γ is defined as the probability of a local concentration exceeding a given threshold as proposed by Chatwin and Sullivan (1989):

$$\gamma = \mathbf{prob}\left(\tilde{\Theta} > \Theta_t\right) \tag{4.5}$$

During combined 3DLIF/behavioral trials, successfully tracking blue crabs appeared to react to threshold concentrations of approximately one percent of the source concentration, $\Theta_t = 0.01\Theta_0$. Consequently, the intermittency factor plotted in Figure 4.5 corresponds to a threshold of one percent of the source concentration. Beyond approximately $4.5H$ from the source, the intermittency factor becomes vertically uniform for elevations below $z/H = 0.22$ as the plume becomes homogenized. For this release type, the shift in the characteristics of the intermittency factor suggests that a change of search strategy by blue crabs may be necessary at $x/H \approx 4.5$.

Transverse profiles of average concentration and the standard deviation of the concentration fluctuations for four distances from the source are shown in Figure 4.6. The transverse coordinate is normalized by the respective standard deviation, σ, of the profile shape, which is found by fitting the log-transformed transverse profiles to the Gaussian profile form of equation 2.18:

$$C(y)/C(0) = \exp\left(-\frac{y^2}{2\sigma^2}\right) \tag{4.6}$$

where $C = \Theta$ for the average concentration and $C = \theta'$ for the standard deviation of the concentration fluctuations. Because the flume walls are far away and do not bound the plume development, the plume is free to expand transversely and the transverse profiles of the average concentration follow a self-similar form. Explanation of the profiles of standard deviation of concentration fluctuations requires more effort. The freedom of the plume to disperse in an unrestricted manner allows equation 2.19 to be closed using a K-model (Csanady 1967), similar to those developed for modeling the turbulent kinetic

energy equation. K-models require the average concentration field to be known, and the turbulent transport and production terms are modeled via x-dependent eddy-diffusivities $K_{\theta'}$ in the y- and z-directions. The dissipation term is modeled through the use of a decay time-scale. Provided that the production terms become small far from the source and that the eddy-diffusivities $K_{\theta'}$ are isotropic, the resulting transverse profile for the standard deviation of the fluctuations is a Gaussian shape in the *y*- and *z*-directions (Hanna 1982). Consistently, the profiles of standard deviation of the concentration fluctuations (Figure 4.6b) appear to follow a self-similar Gaussian form, although it should be noted that dispersion is anisotropic due to the proximity of the nozzle to the substrate.

Streamwise profiles along the nozzle centerline for the average concentration and standard deviation of the concentration fluctuations are shown in Figure 4.7a. For a point source released into an isotropic turbulent stream with minimal boundary effects, the Gaussian plume model (equation 2.18) along the nozzle centerline (i.e., $z = z_0$; $y = 0$) reduces to:

$$\Theta(x)/\Theta_0 = \frac{q_{nozzle}}{4\pi\varepsilon x} \tag{4.7}$$

The theoretical decay of centerline mean concentration follows a x^{-1} power law. Vertical profiles of the average concentration are shown in Figure 4.7b. Average concentration levels are smaller than those of Webster et al. (2003) for a similar continuous release. Beyond $x/H = 6$ the average concentration is fairly constant below mid-depth. The vertical profiles do not follow the Gaussian shape predicted by equation

2.18 (for $y = 0$) as the boundaries limit plume development in the vertical direction. Due to the linear nature of the simplified advection-diffusion equation (equation 2.17), the presence of the bed can be taken into consideration by adding a mirror source located at $z = -z_0$, effectively adding a vertical length scale z_0. Hence, the presence of the vertical length scale prevents a Gaussian profile shape from forming.

Elder (1959) derived an analytical expression for ε_z by assuming that momentum and mass disperse at the same rate and the log-law for the vertical velocity profile:

$$\varepsilon_z = 0.067 H u_* \tag{4.8}$$

An analysis similar to Elder's cannot be derived in the transverse direction as the mean velocity lacks a theoretical profile and is usually assumed uniform. Experimental data suggest transverse dispersion coefficients follow the form of equation 4.8 with leading constants varying from 0.1 to 0.2 (Fischer et al. 1979). Equation 4.7 can be used to estimate the turbulent dispersion coefficient by longitudinal curve-fitting as the nozzle flow rate is known. The resulting turbulent dispersion coefficient ε was found to be $0.074 H u_*$ by fitting the centerline data to an equation of the form 4.8 in the range of x/H from 2.5 to 5.

Figure 4.8 shows the development of the plume width, defined as 4σ, at the nozzle centerline elevation. Plume width was calculated by fitting the transverse average concentration profiles to equation 4.6 using linear least-squares on the log-transformed data. The curve shown on Figure 4.8 is the theoretical evolution of average plume width using an eddy-diffusivity of $\varepsilon = 0.074 u_* H$ from the analysis above:

$$\sigma_{\Theta} = 4\sqrt{2\varepsilon x / U} \tag{4.9}$$

As shown, the profile of plume width based on the average concentration field agrees very well with equation 4.9, except where $x/H < 2.5$. Effects of the source influence mixing for $x/H < 2.5$, the zone of flow establishment where the average concentration field differs from theory due to finite source size.

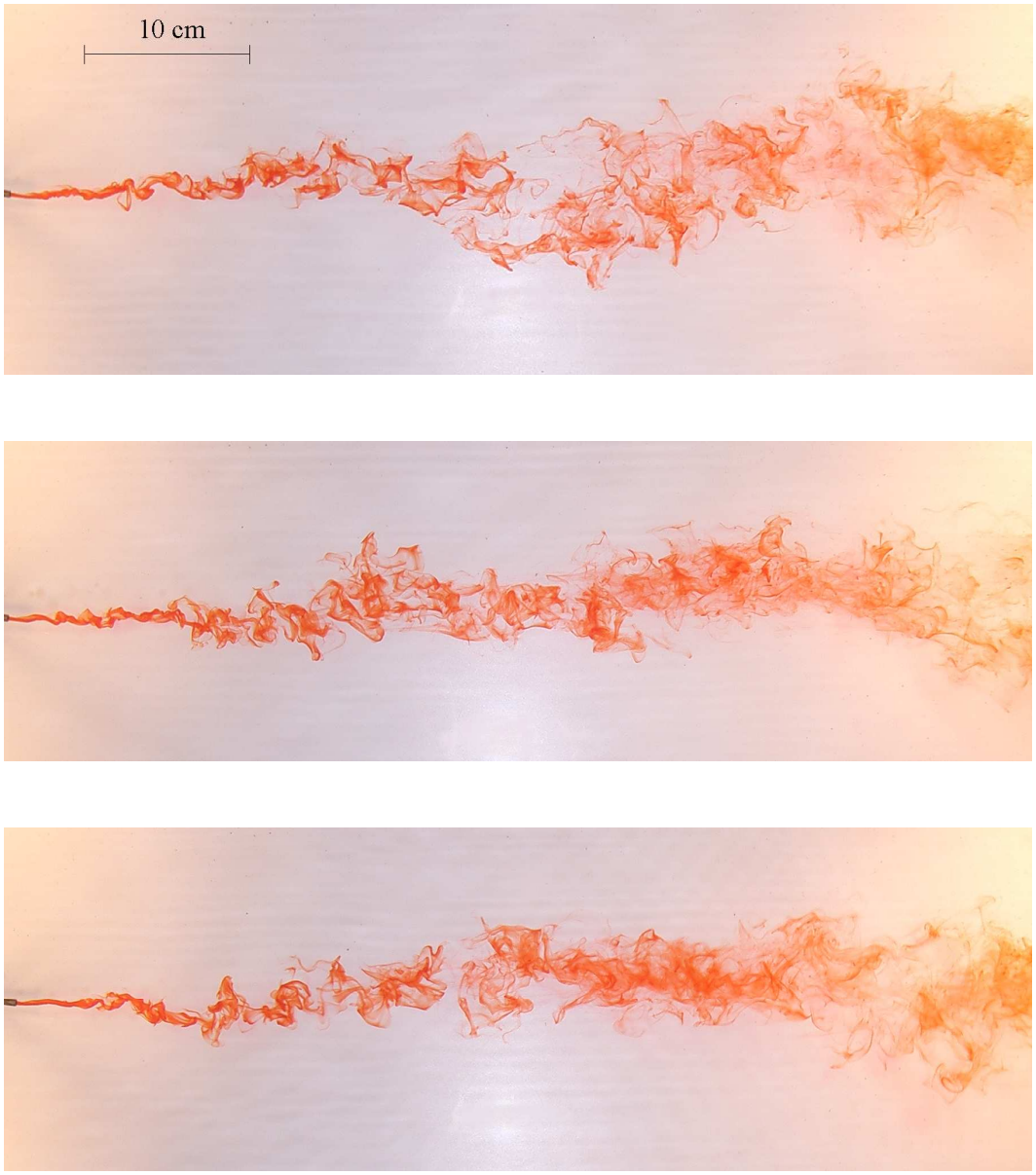

Figure 4.1 Flow visualization of the continuous plume, which is created via a continuous iso-kinetic release into the test section of the saltwater flume. The view is from above, with the flow moving from left to right. The flow and plume parameters are defined in Tables 3.1 and 3.2.

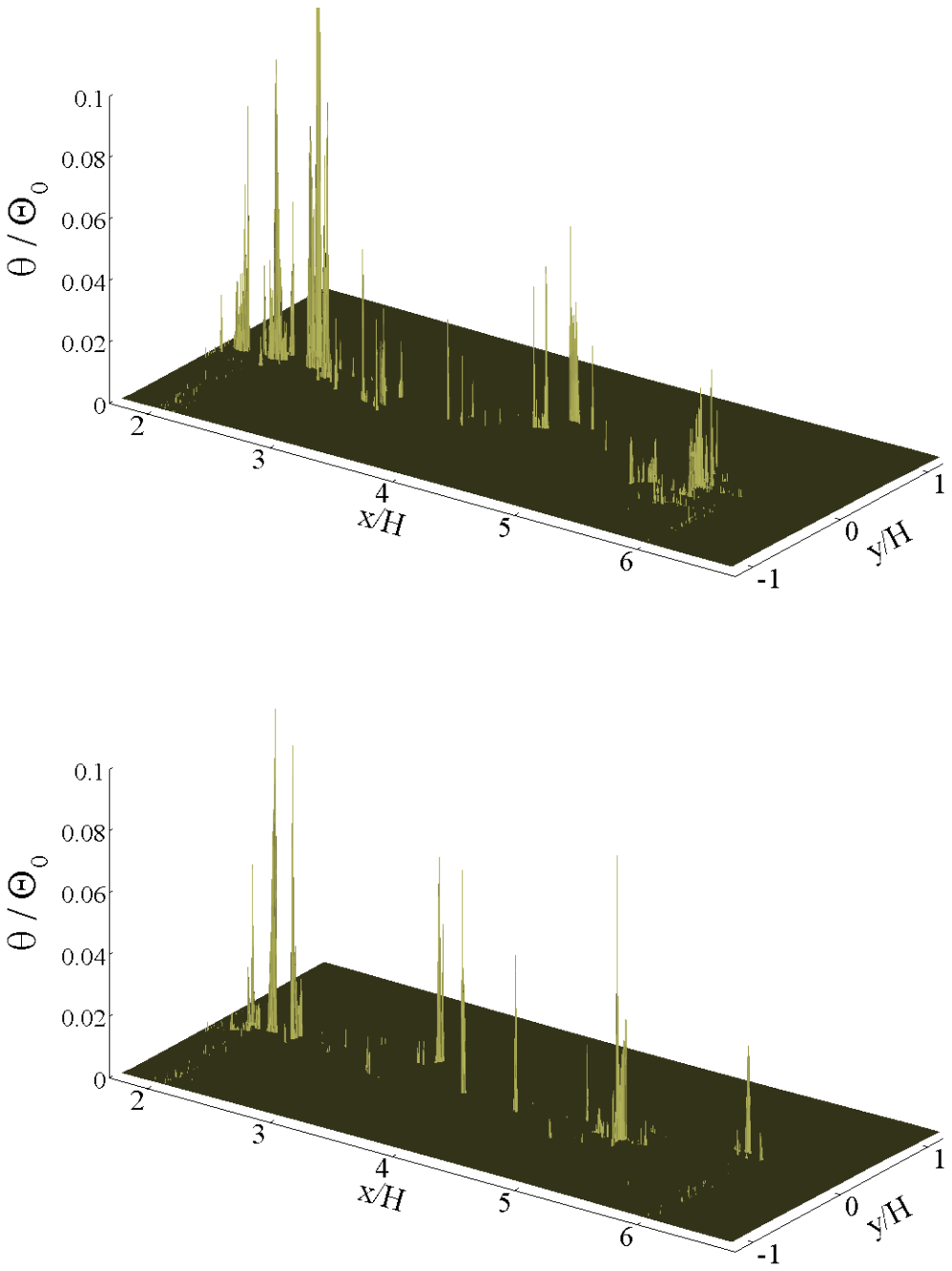

Figure 4.2 Two examples of instantaneous concentration fields at z = 2.2 cm ($z / H = 0.10$) near the elevation of nozzle centerline.

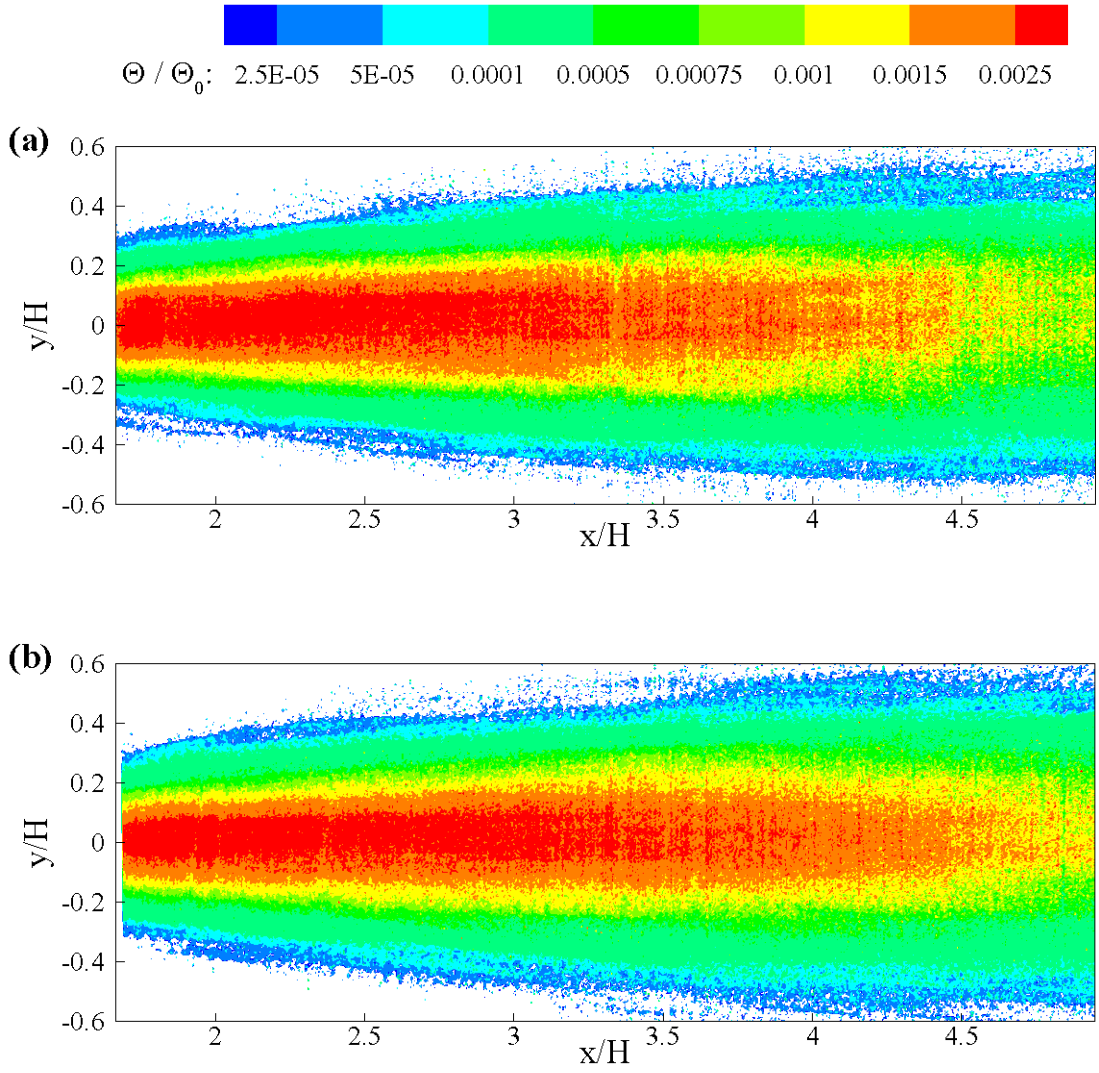

Figure 4.3 Fields of average concentration, Θ/Θ_0, for the continuous plume at four elevations above the substrate: (a) 0.5 cm $(z/H = 0.02)$, (b) 2.2 cm $(z/H = 0.10)$, (c) 4.7 cm $(z/H = 0.22)$, and (d) 7.2 cm $(z/H = 0.34)$.

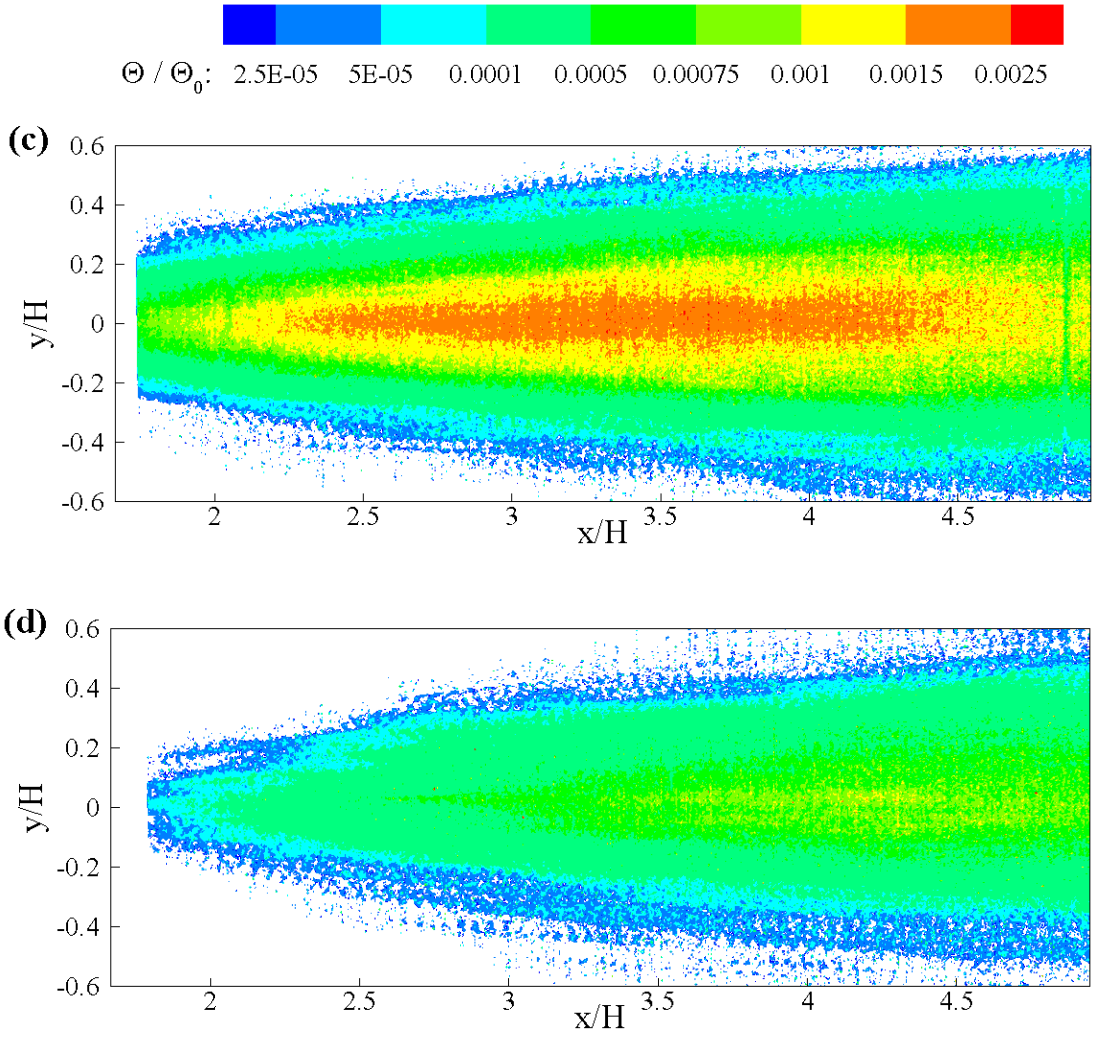

Figure 4.3 Continued.

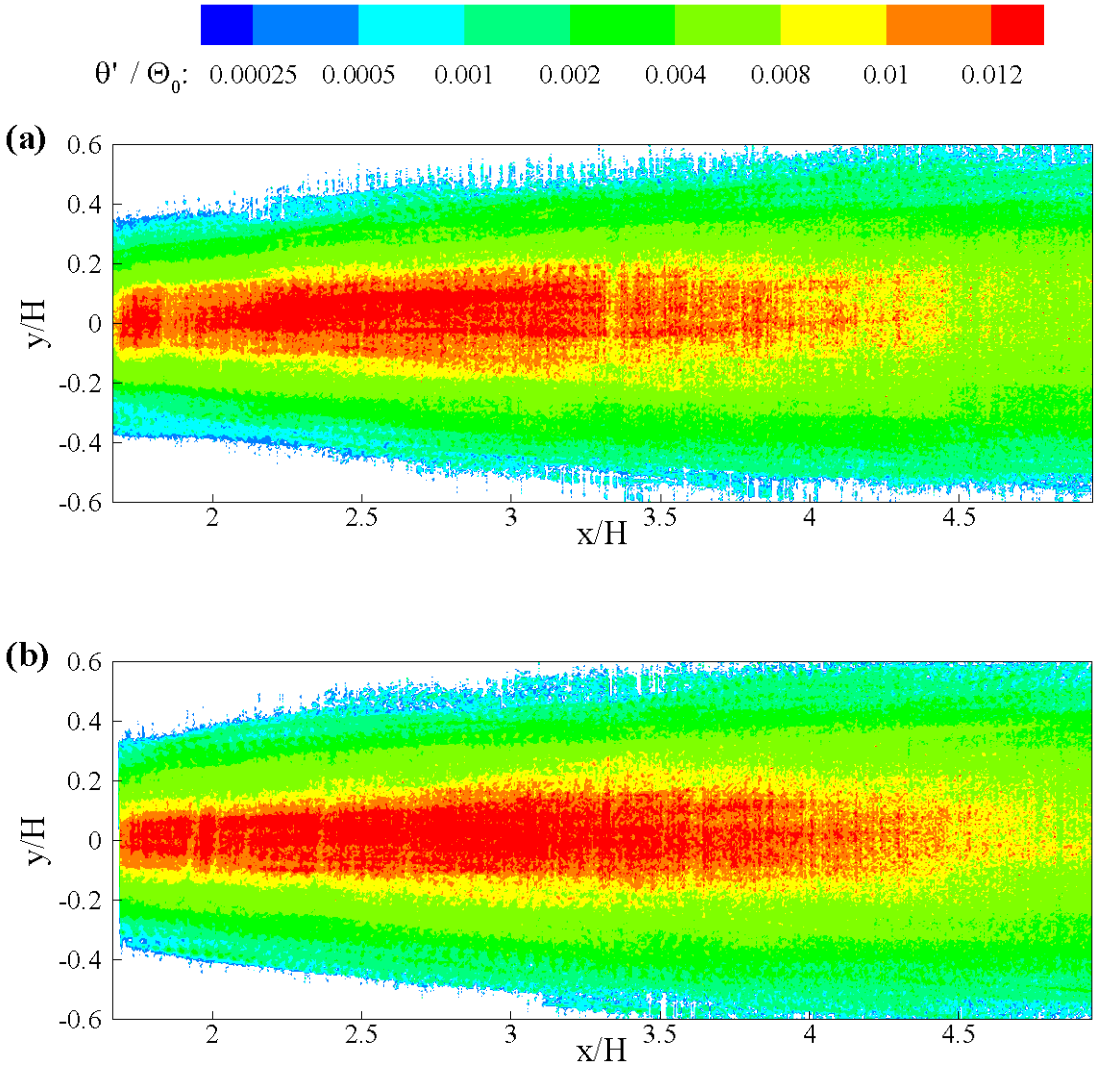

Figure 4.4 Fields of the standard deviation of the concentration fluctuations, θ'/Θ_0, for the continuous plume at four elevations above the substrate: (a) 0.5 cm $(z/H = 0.02)$, (b) 2.2 cm $(z/H = 0.10)$, (c) 4.7 cm $(z/H = 0.22)$, and (d) 7.2 cm $(z/H = 0.34)$.

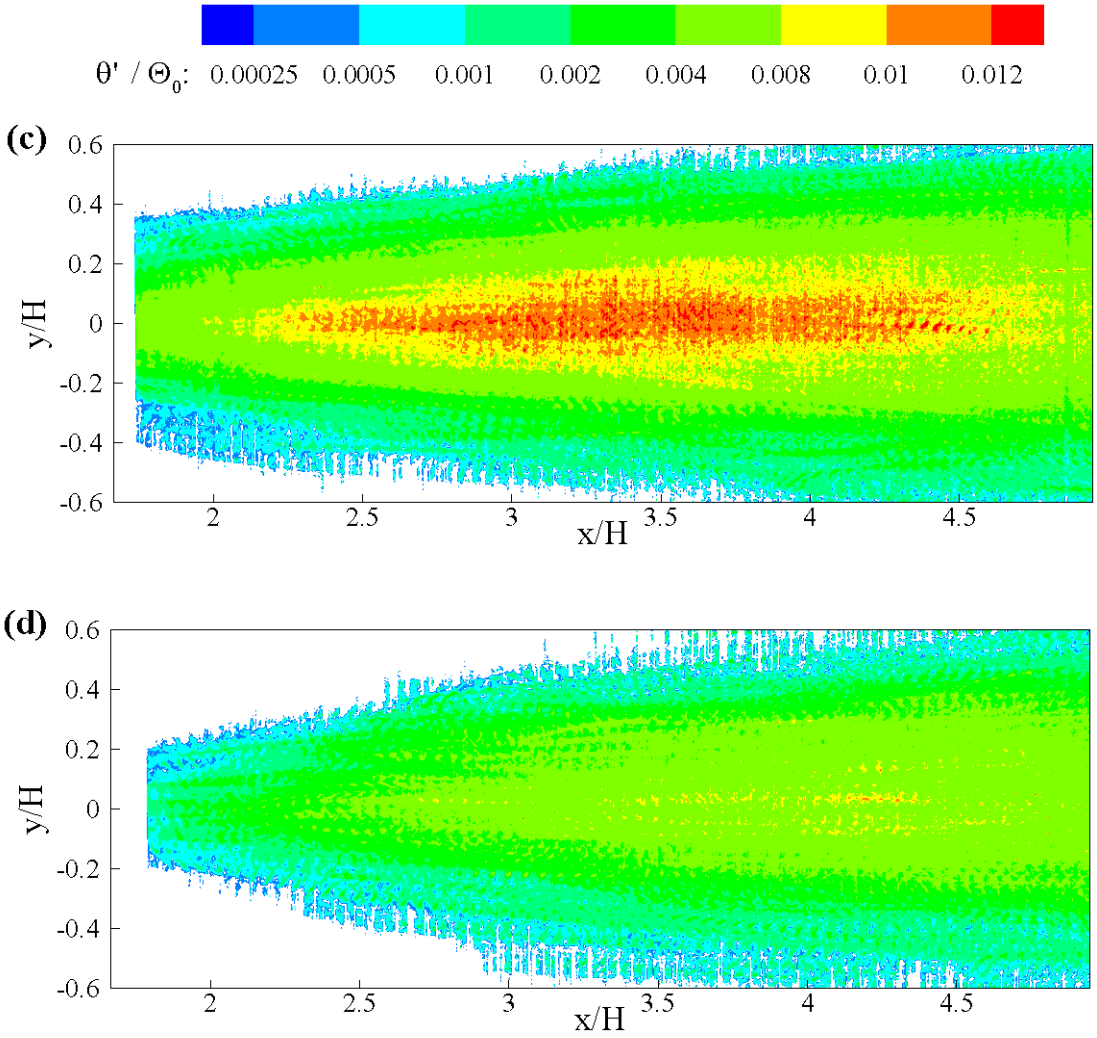

Figure 4.4 Continued.

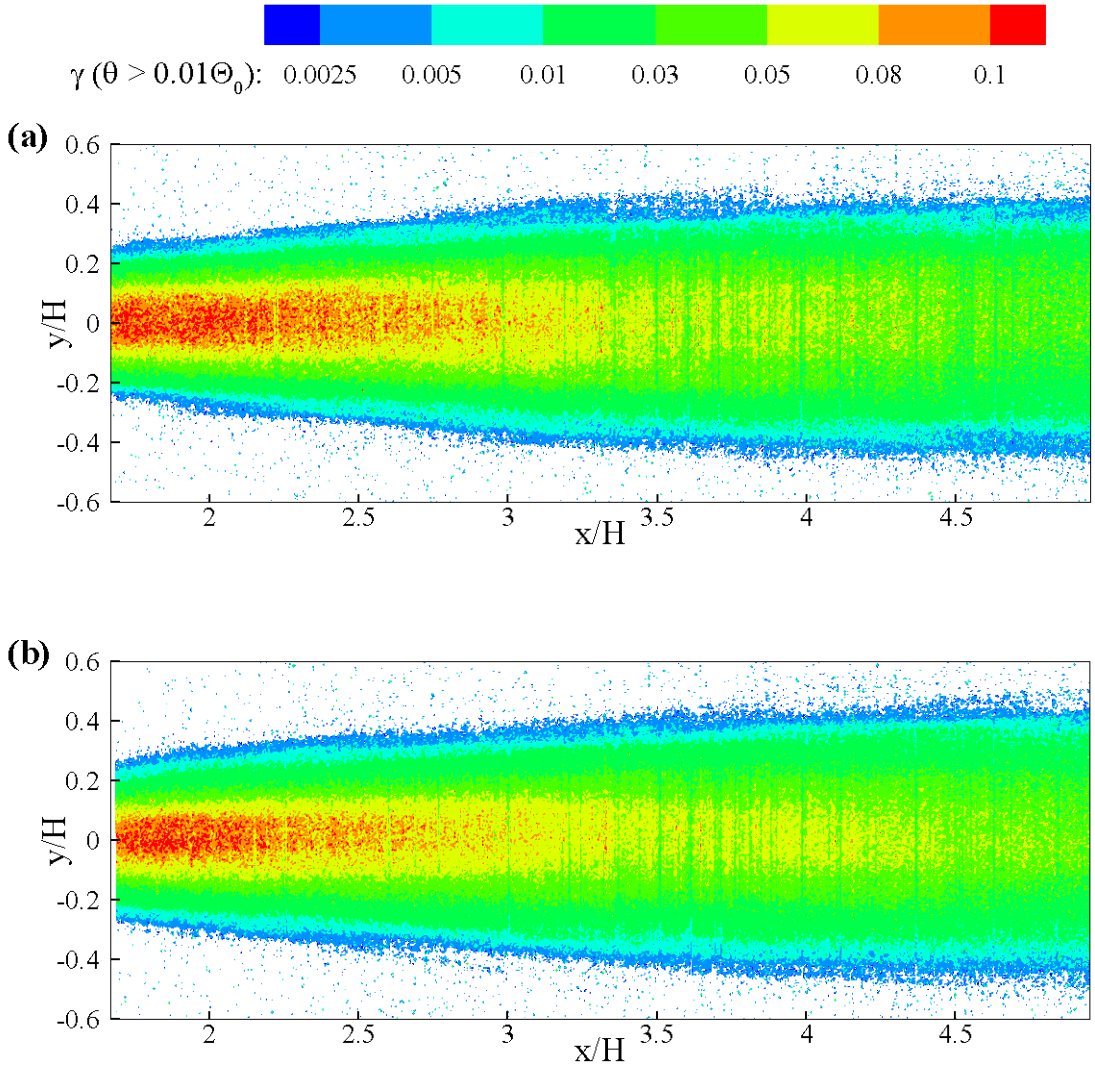

Figure 4.5 Fields of intermittency factor γ based on a threshold of 1% of the source concentration (i.e., the probability that the concentration exceeds $0.01\Theta_0$) for the continuous plume at four elevations above the substrate: (a) 0.5 cm $(z/H = 0.02)$, (b) 2.2 cm $(z/H = 0.10)$, (c) 4.7 cm $(z/H = 0.22)$, and (d) 7.2 cm $(z/H = 0.34)$.

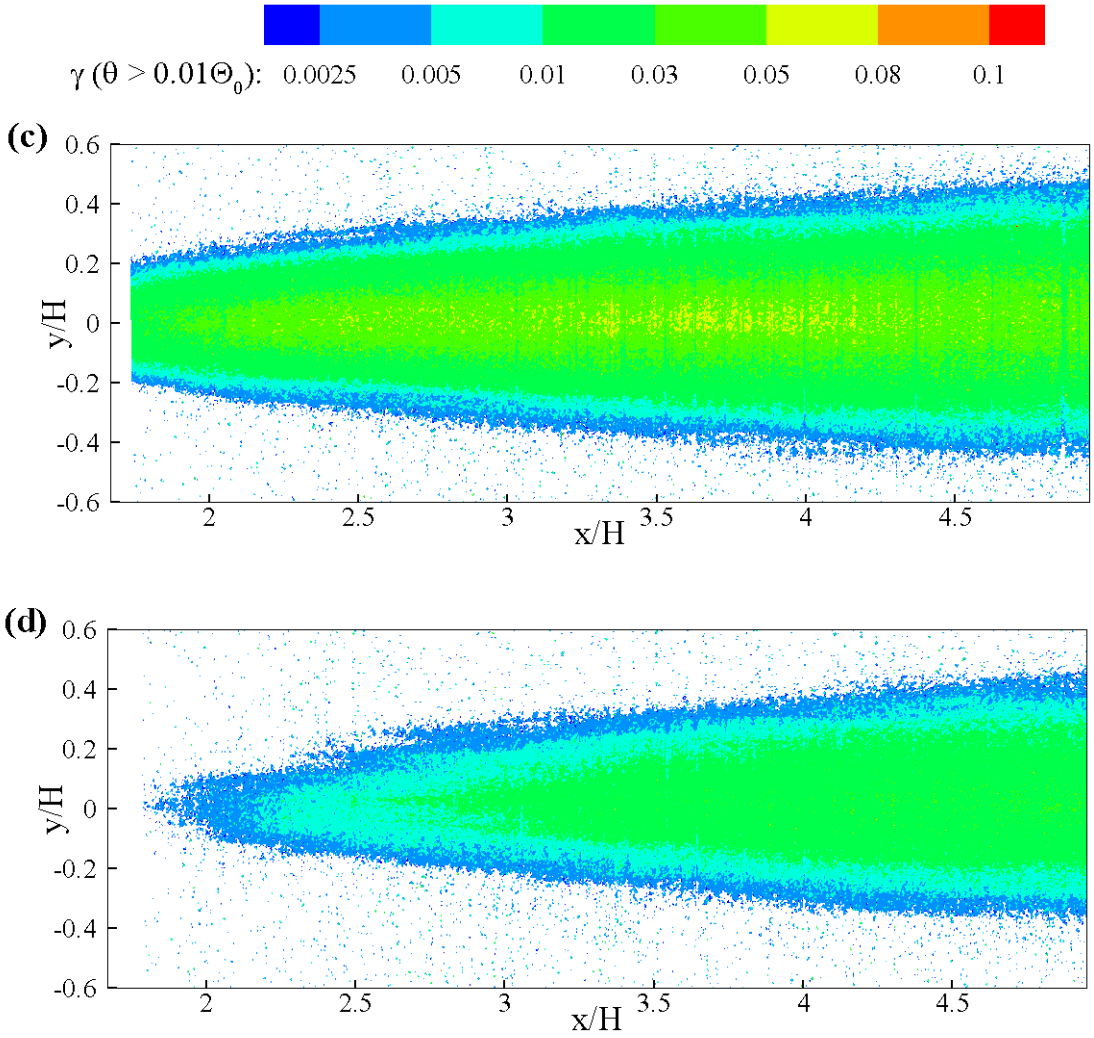

Figure 4.5 Continued.

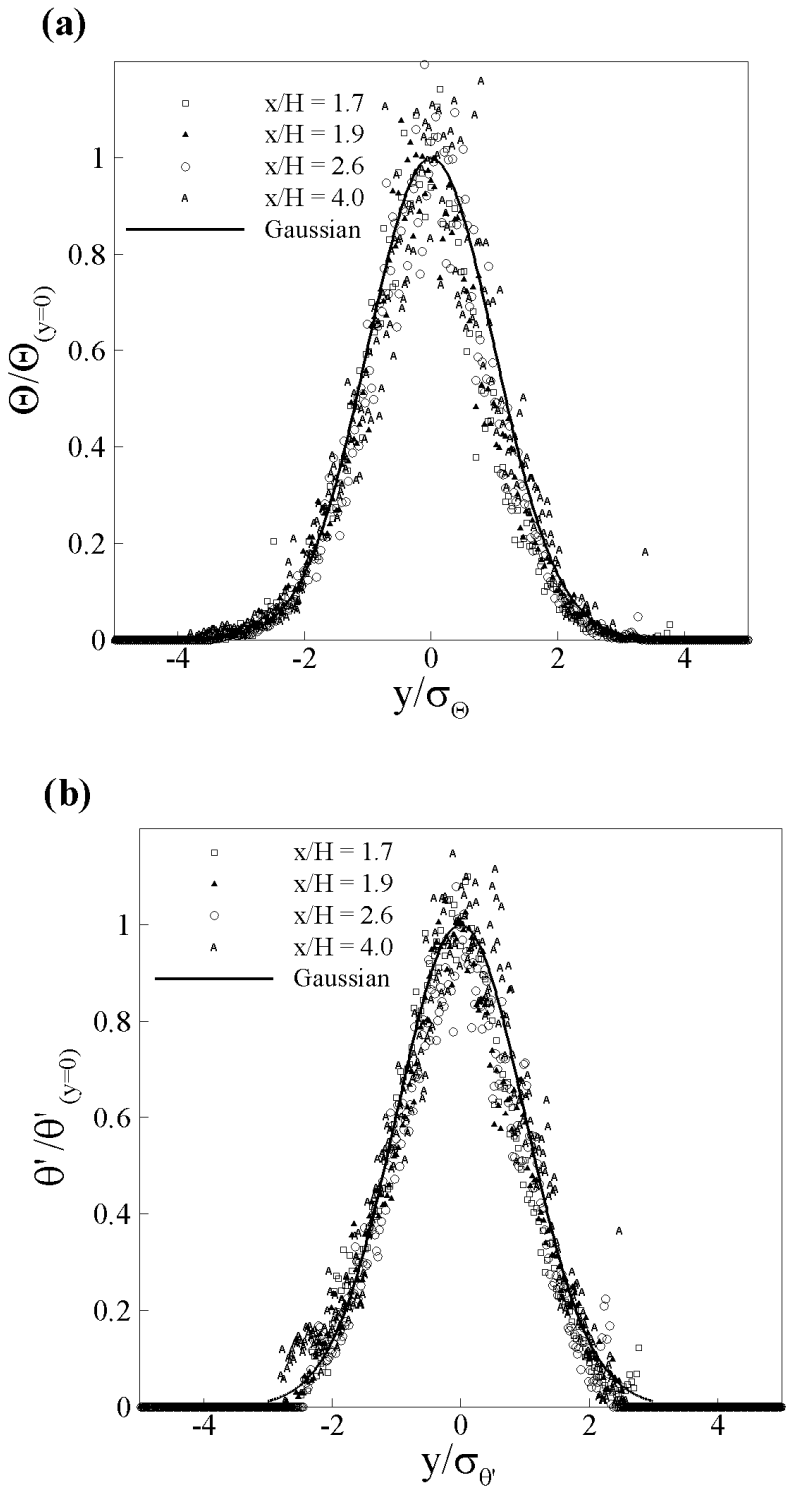

Figure 4.6 Transverse profiles for the continuous plume. (a) average concentration, and (b) standard deviation of the concentration fluctuations. Both sets of profiles correspond to the measurement plane that is nearest to the nozzle centerline elevation z_0 (z = 2.2 cm, z / H = 0.10).

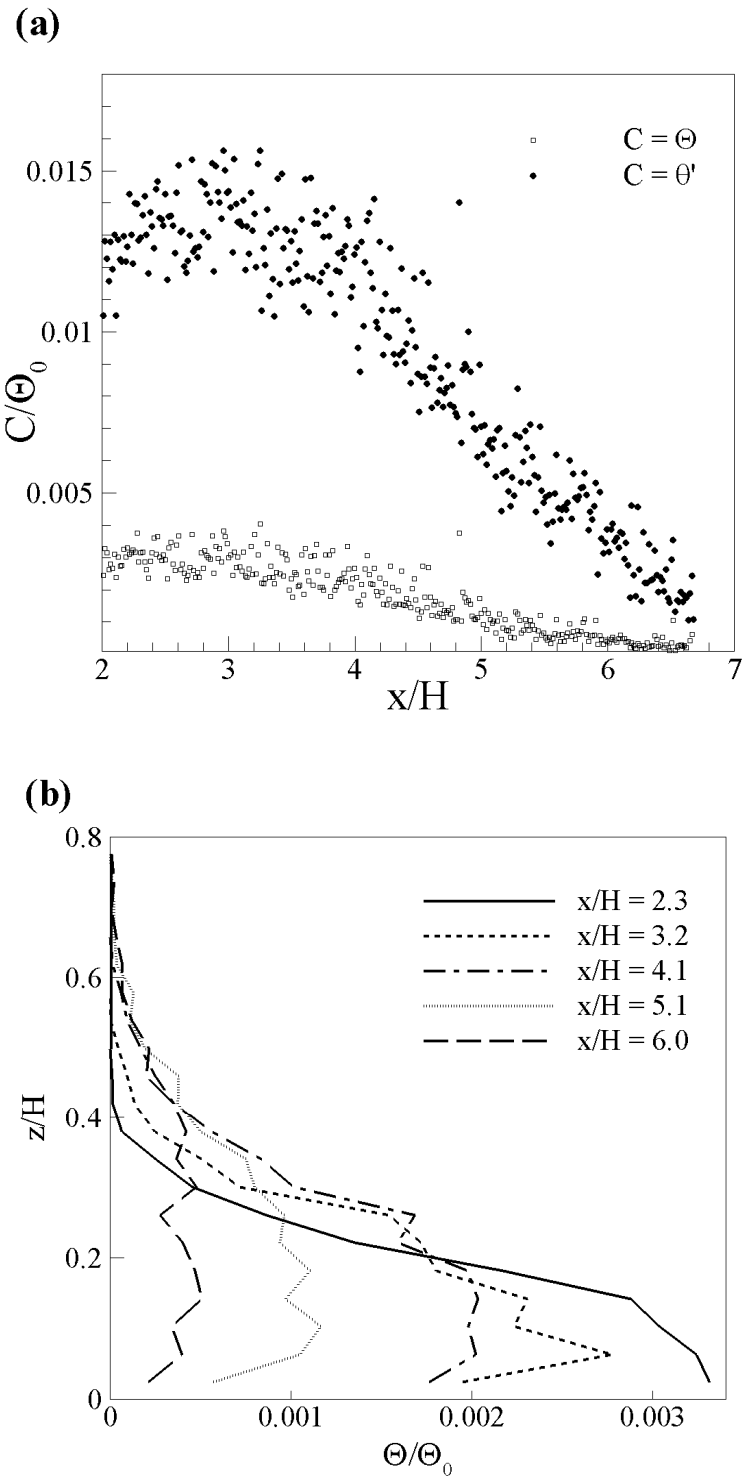

Figure 4.7 Profiles for the continuous plume. (a) Streamwise profiles of the average concentration (squares) and standard deviation of the concentration fluctuations (filled circles) along the centerline of the plume, i.e. for $y = 0$ and $z = 2.2$ cm (every third data point shown for clarity), and (b) vertical profiles of average concentration along the plume centerline, i.e. for $y = 0$ and various distances from source.

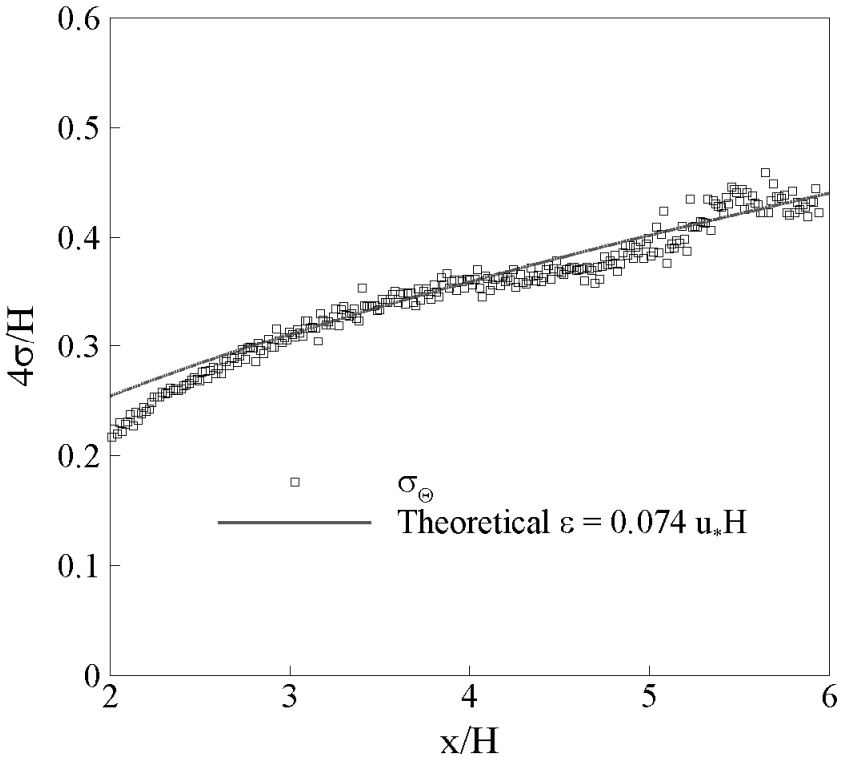

Figure 4.8 Transverse plume width for the continuous plume based on the average concentration field. Theoretical curve is equation 4.9 with turbulent diffusion coefficient determined from the data. Every third point shown for clarity

4.2 Meandering plume

Figure 4.9 shows flow visualization images of the meandering plume using neutrally buoyant red dye. The flow induced by the upstream cylinder is quasi-cyclical as the cylinder has a Reynolds number of approximately 5100 and Strouhal number of approximately 0.20 (Roshko 1954). The resulting wake has a frequency of about 0.1 cycles per second. For cylinder Reynolds numbers above 5000, the downstream wake loses the defined periodicity of the von Karman vortex street although some periodicity is retained (Cantwell and Coles 1983). Hence, for the meandering plume, turbulence is

generated both by the boundary layer flow and the wake flow of the upstream cylinder. The plume images shown in Figure 4.9 display large-scale quasi-periodicity due to the vorticies shed at the boundary layer separation points on the cylinder. The dye visualization images also suggest more rapid dilution of the filaments in the meandering plume compared to the continuous plume.

Two example instantaneous concentration fields for the meandering plume are shown in Figure 4.10. The concentrations are much lower than those shown for the continuous plume in Figure 4.2. The fields consist of sparse regions of high concentration surrounded by an ambient condition of zero or near-zero concentration. The meander induced by the upstream cylinder is difficult to discern. Instantaneous concentrations decrease much more quickly than with the continuous release

The decrease in concentration is quantified in the average concentration fields plotted in Figure 4.11. The source concentration in this case was 2000 µg/l and the average consists of an ensemble of 18,400 images at each 3DLIF level (i.e., 368,000 total images). The total time required to collect the images was approximately 62 minutes with the camera running at 100 frames per second. The slight asymmetry about the nozzle centerline (i.e., $y = 0$) in the field plots of average concentration is due either to a small deviation from centerline in the upstream cylinder placement or to small calibration errors as the concentration is very small.

The standard deviation of the concentration fluctuations, θ', is shown in Figure 4.12 at four 3DLIF levels. The concentration fluctuation is greatest near the bed and the plume becomes nearly homogeneous in the vertical direction by approximately four flow depths

downstream of the source. Compared to the continuous plume case described in the last section, the average and fluctuation fields are wider in the horizontal (y) direction due to increased turbulent transport introduced by the upstream cylinder.

The intermittency factor was calculated by equation 4.5 with a threshold of one percent of the source concentration and is shown in Figures 4.13. Intermittent bursts of concentration that exceed the threshold occur throughout the measurement area. The intermittency factor for the meandering plume is smaller than that for the continuous plume as the centerline of the plume is approached. Near the source $(x/H < 2.5)$, regions of high values of the intermittency factor are a good indicator of coincidence with the plume centerline for the continuous plume (see Figure 4.5b). However, concentration bursts occur at greater distances from the plume centerline for the meandering plume case and regions of high values of the intermittency factor do not provide a good indicator of coincidence with the plume centerline. The wider intermittency field of the meandering plume suggests increased difficulty in source location for a tracking blue crab because high concentration bursts do not necessarily indicate good coincidence of the crab position with the plume centerline. In addition, the width of the meandering plume exceeds the maximum sensor spacing of a blue crab throughout the recorded region. Hence, a contrast between distal chemosensors would not always be a reliable indicator of plume centerline due to meander.

Turbulent wakes behind bodies approach self-similarity with large distances from the body. For circular cylinders, experimental evidence has shown that velocity and concentration profiles become self-similar at distances of approximately

$x_C / D \approx 180 - 200$ (Rehab et al. 2001). The meandering plume data was recorded in the region of $x_C / D = 4.0 - 8.6$, which corresponds to the intermediate wake region (where the Karman vortex street appears for suitable Reynolds numbers). Hence, under suitable coordinate transformation, transverse profiles of concentration data do not collapse onto a single curve, i.e., self-similarity is not achieved.

Several theoretical models of meandering plumes have been introduced in order to address the dilution and spread of the plume within the inertial range of turbulent length scales. The meandering plume model introduced by Gifford (1959) breaks the plume into transverse disks in which longitudinal dispersion is neglected. Within each transverse disk, the plume disperses about an instantaneous centroid located at a meandering distance D_y from the plume centerline (see Figure 4.14). Gifford's model assumes that dispersion, reflected by the plume width σ_y, occurs solely in the transverse direction and independently of the meander. The meandering process is attributed to larger scale eddies that are not involved in mixing yet are capable of physically shifting the instantaneous plume centerline location. The Gifford model was developed for plumes dispersing into the atmosphere where the plume size remains within the inertial range and does not approach that of the largest eddy sizes. The meandering plume described in the current study differs from the classic description in that the bulk plume movement is due to quasi-periodic vorticies in the wake of a cylinder. A second difference is that longitudinal dispersion cannot be entirely neglected, as longitudinal velocity fluctuations in the wake are on the order of the mean flow velocity.

Reynolds and Hussain (1972) introduced a phase-averaged component to the Reynolds decomposition described in Chapter 2. The total instantaneous velocity can be broken into three contributions, a time-averaged U and fluctuating u component from conventional Reynolds decomposition, and a third periodic, or phase-averaged, component $\hat{u}$:

$$\tilde{u} = U + u + \hat{u} \tag{4.10}$$

Concentration, pressure, and other flow scalars can be decomposed similarly. Time-averaging of a phase-averaged component $\hat{u}$ is zero. Phase-averaging involves averaging at specific time lags or phases:

$$\hat{u}(\tau_m) = \frac{1}{N}\sum_{j=1}^{N}\left(\tilde{u}(j\,\tau_m) - U\right) \tag{4.11}$$

where j is an integer sufficiently large to ensure $\overline{u} = \frac{1}{N}\sum_{j=1}^{N} u(j\tau_m)$ converges to zero. Ensemble-averaged correlations between fluctuating and phase-averaged components, i.e., $\overline{\hat{u}u}$, are also zero. Substitution of velocity and concentration decompositions into the advection-diffusion equation (equation 2.15) and time averaging results in an additional term:

$$\frac{\mathrm{D}\Theta}{\mathrm{D}t} = \frac{\partial}{\partial x_i}\left(K\frac{\partial\Theta}{\partial x_i} - \overline{u_i\theta} - \overline{\hat{u}_i\hat{\theta}}\right) \tag{4.12}$$

The assumptions used in defining an eddy-diffusivity for $\overline{u_i\theta}$ in the closure of equation 2.15, namely the eventual decay of the fluctuating velocity autocorrelation function to zero, cannot be applied to the term $\overline{\hat{u}_i\hat{\theta}}$. The phase-averaged quantity $\overline{\hat{u}_i\hat{\theta}}$ is application-specific in most cases.

A straightforward way to estimate the average concentration field for the meandering plume based upon equation 4.12 is to use the model introduced by Gifford (1959). Assuming negligible longitudinal dispersion, transverse and vertical dispersion within the plume occurs independently of plume meander. Ensemble-averaging the plume at a given phase lag τ_m results in equation 2.18 in the coordinate frame of the primed axes in Figure 4.14. Each phase has a unique average concentration field similar to the sketch shown in Figure 4.14. The overall time-averaged concentration $\Theta(x, y, z)$ at a given distance is the average over all phase lags from 0 to mean plume meander period T_m. Assuming meander in the y-direction only, the primed and unprimed axes differ only in the transverse coordinate:

$$y' = y - D_y\left(x, \tau_m\right)\sin\left(2\pi\tau_m/\mathrm{T}_m\right) \tag{4.13}$$

Substitution of equation 4.13 into equation 2.18 results in the ensemble-averaged concentration along plume centerline $(z = z_0)$ at a give phase lag τ_m.

$$\frac{\Theta\left(x, y, z_{0,}\tau_m\right)}{\Theta_0} = \frac{1}{\sqrt{\pi}}\exp\frac{-\left[y - D_y\left(x, \tau_m\right)\sin\left(2\pi\tau_m/\mathrm{T}_m\right)\right]^2}{2\left(\sigma_y\left(x\right)\right)^2} \tag{4.14}$$

The time-averaged concentration is found by integrating equation 4.14 over all phase lags from zero to T_m:

$$\frac{\Theta(x,y)}{\Theta_0} = \frac{1}{T_m\sqrt{\pi}} \int_0^{Tm} \exp \frac{-\left[y - D_y(x,\tau_m)\sin\left(2\pi\tau_m / T_m\right)\right]^2}{2\left(\sigma_y(x)\right)^2}\, d\tau_m \tag{4.15}$$

A theoretical profile can be developed if the period T_m is known and a relationship can be found between the meandering distance D_y and the plume width σ_y. The variance of the meandering distance can be found by integrating

$$\left\langle D_y(x)^2 \right\rangle = D_y'^2 = \frac{1}{T_m} \int_0^{Tm} \left[D_y \sin\left(2\pi\tau_m / T_m\right)\right]^2 d\tau_m = \frac{D_y^{\,2}}{2} \tag{4.16}$$

Following Gifford (1959), the standard deviation of the meandering distance can be found from the transverse concentration profiles at the $z = z_0$ plane (nozzle centerline elevation):

$$\frac{D_y}{\sqrt{2}} = D_y' = \left(\frac{1}{T-1} \sum_1^T \left\{ \frac{\sum_{y=h\max}^{y=h\max} \left[y\tilde{\Theta}(y) \right]}{\sum_{y=-h\max}^{y=h\max} \tilde{\Theta}(y)} \right\}^2 \right)^{1/2} \tag{4.17}$$

The plume width σ_y within each slice is found relative to the meandering distance at the same plane:

$$\sigma_y = \left(\frac{1}{T-1} \sum_{1}^{T} \left\{ \frac{\sum_{y=-h\max}^{y=h\max} \left[(y - D'_y)\tilde{\Theta}(y) \right]}{\sum_{y=-h\max}^{y=h\max} \tilde{\Theta}(y)} \right\}^2 \right)^{1/2} \tag{4.18}$$

Figure 4.15 shows the evolution of the meander distance standard deviation and plume width with distance from the source. Within the measurement region, the plume width σ_y grows according to a power law (i.e., $\propto x^{0.6}$), with an exponent that is larger than the $\sigma \propto x^{0.5}$ relationship predicted by the Gaussian plume model (equation 4.6). The form of equation 4.18, which only approximates actual phase-averaging and the influences of longitudinal dispersion, likely creates the discrepancies between the theoretical meandering plume growth and the experimental data.

In the zone of self-similarity $x_C / D \approx 180 - 200$, the widths of a turbulent wake and a turbulent plume theoretically evolve in isotropic environments according to power laws with identical exponent (Rehab et al. 2001). A transverse average concentration profile can be generated from equation 4.15 using simplifications to the evolution of plume width and meander distance taken from similarity theory. As with similarity theory, power laws of the form $\propto x^n$ for the growth of D_y and σ_y can be substituted into equation 4.15. Numerical integration at a given distance x over a full cycle T at each transverse value of y/σ_y leads to a transverse average concentration profile. The ratio $D_y / \sigma_y \propto x^{-0.4}$ is estimated from the power-law fits shown in Figure 4.15. Transverse profiles of average concentration are shown in Figure 4.16, where the theoretical profiles are distributions calculated from numerical integration of equation 4.15. To reduce the

effects of noise, the data are normalized by the average of the five consecutive points with the highest mean concentrations, which does not occur at nozzle centerline. The theoretical and data profiles are not self-similar, as would be expected due to proximity to the upstream cylinder. Figure 4.16 demonstrates very good agreement between the data and the model profiles.

Transverse profiles of the standard deviation of the concentration fluctuations are shown in Figure 4.17. In lieu of developing a model similar to equation 4.15 for the concentration fluctuations, a simplified dual-source model is used. The transverse profiles are modeled by two point-sources positioned equidistantly from the plume centerline. Equation 4.6 can be modified for the standard deviation to include two sources:

$$\theta'(y)\Big/\theta'(0) = \exp\left(-\frac{(y-b)^2}{2\sigma^2}\right) + \exp\left(-\frac{(y+b)^2}{2\sigma^2}\right) \tag{4.19}$$

At each transverse location on one limb of the profile, i.e. $(\infty < y < b)$, shown in Figure 4.17, a value of σ was found by solving equation 4.19 using Newton's method in the transverse y direction. Unlike a simple Gaussian profile, such as equation 4.6, the value of σ in equation 4.19 cannot be determined by a log-transformed fit, instead requires a root-finding method at each transverse coordinate (Newton's method in this case). The profile standard deviation $\sigma_{\theta'}$ was calculated as an average of the σ values over the range $\infty < y < b$. The resulting theoretical transverse profile matches the fringes of the plume ($|y/\sigma_{\theta'}| > 2$, Figure 4.17) for $x/H = 2.6$. The data appear to follow the model

along the rising limbs of the 2-source curve. Though not expected due to proximity to the upstream cylinder, self-similarity is difficult to discern due to noise levels. Near the plume centerline, the data scatter is large and similarity with equation 4.19 is hard to evaluate.

Vertical average profiles are shown in Figure 4.18. Dilution occurs rapidly and the vertical distribution becomes homogeneous by approximately $x/H = 5$. Average concentration levels are an order of magnitude lower than those of the continuous plume (compare to Figure 4.7). Vertical profile shape in the meandering case increase monotonically as the bed is approached, which contrasts the continuous plume profiles that approximate a reflected Gaussian model.

The wider transverse extent of the meandering plume compared to the continuous plume introduces factors that potentially complicate the successful tracking of a point source. As discussed above, the likelihood of encountering a relatively high concentration burst at locations away from plume centerline increases significantly. In addition, the spatial structure of the meandering plume creates cases where a strict bilateral comparison could direct an animal away from the centerline or leave the animal with no signal at any chemosensor. The increasing complexity of the meandering plume would imply that crabs would likely have more convoluted navigational paths relative to a continuous release.

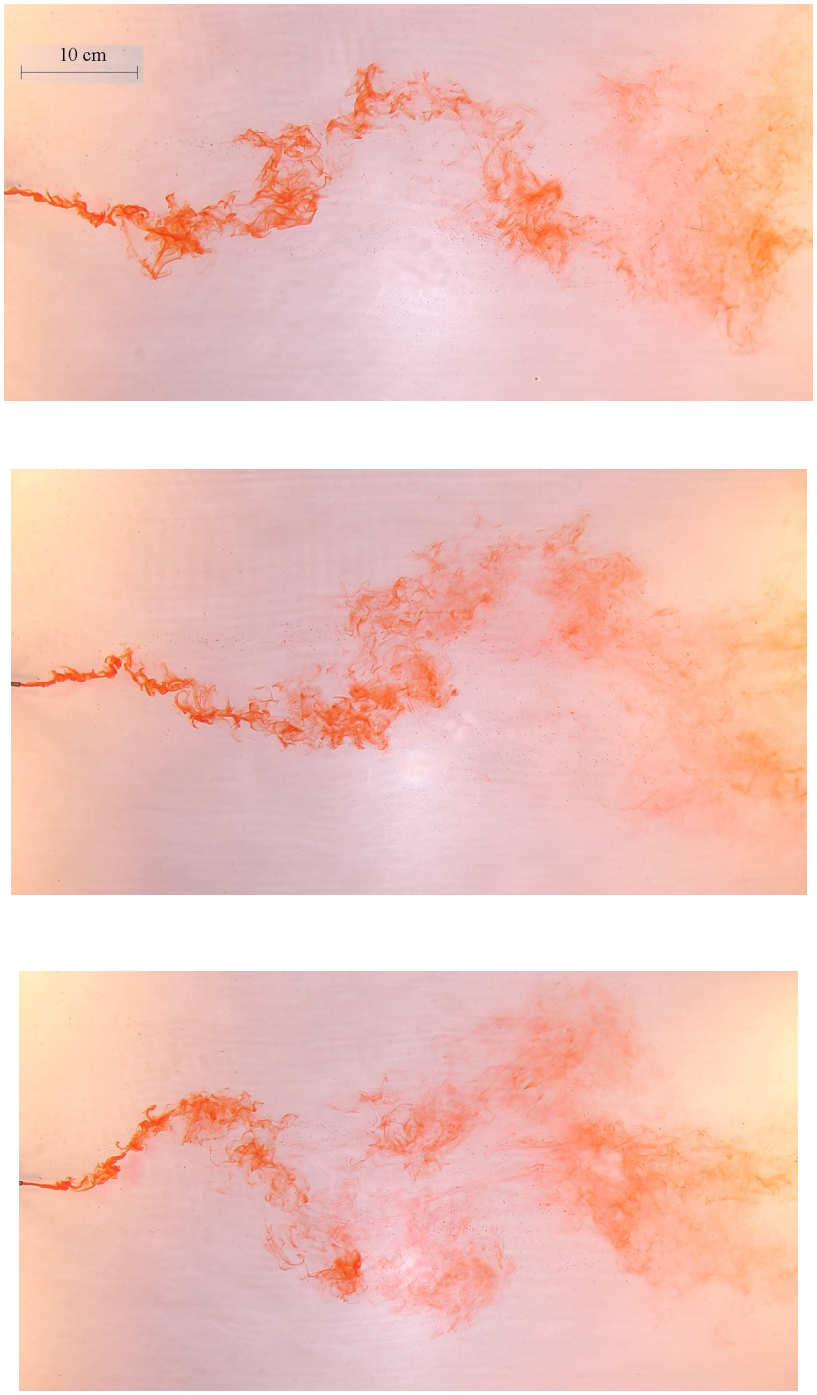

Figure 4.9 Flow visualization of the meandering plume, which is created via a continuous iso-kinetic release into the test section of the saltwater flume downstream of a cylindrical obstacle. The view is from above, with the flow moving from left to right. The flow and plume parameters are defined in Tables 3.1 and 3.2.

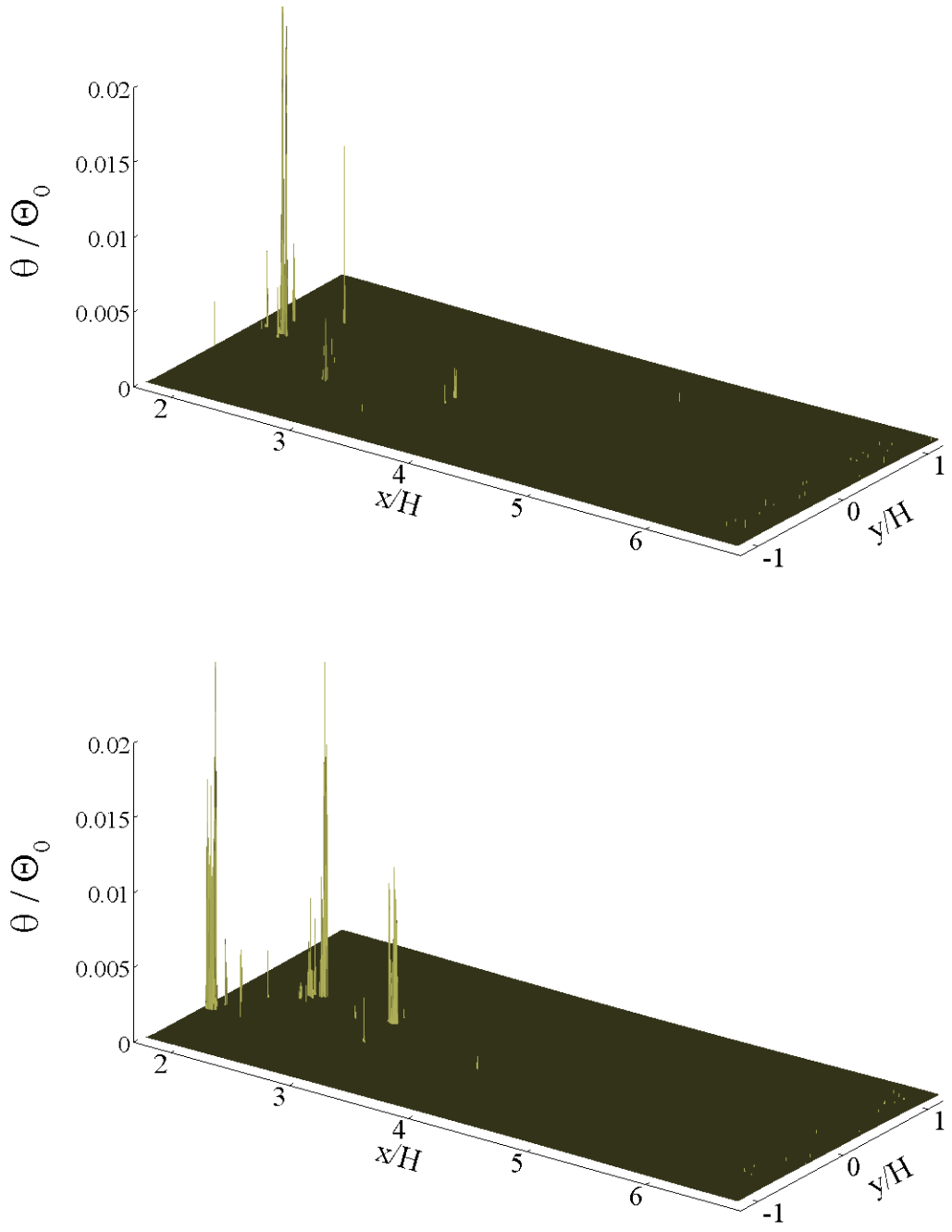

Figure 4.10 Two examples of instantaneous concentration fields for the meandering plume at z = 2.2 cm ($z / H = 0.10$) near the elevation of nozzle centerline.

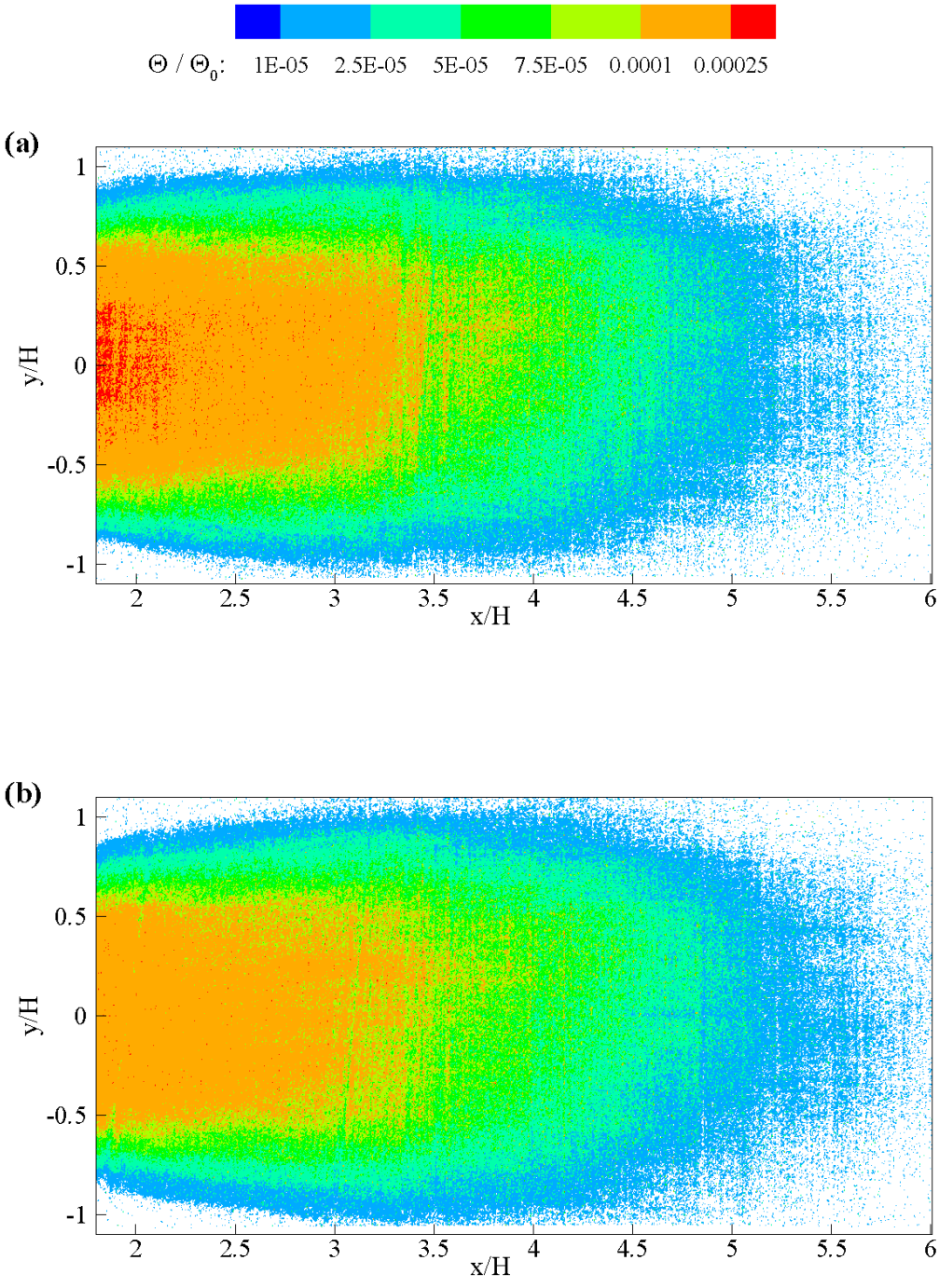

Figure 4.11 Fields of average concentration, Θ/Θ_0, for the meandering plume at four elevations above the substrate: (a) 0.5 cm $(z/H = 0.02)$, (b) 2.2 cm $(z/H = 0.10)$, (c) 4.7 cm $(z/H = 0.22)$, and (d) 7.2 cm $(z/H = 0.34)$.

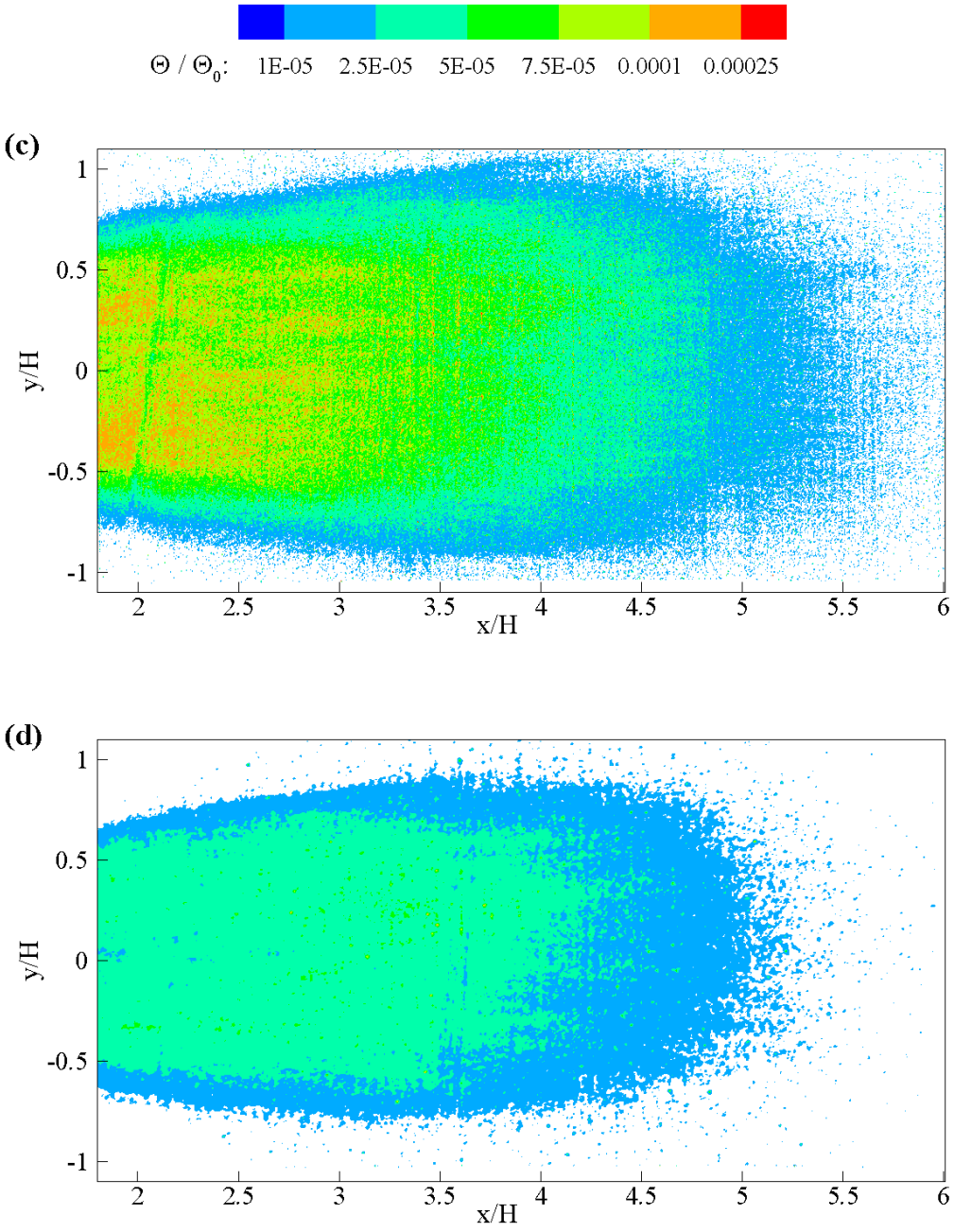

Figure 4.11 Continued.

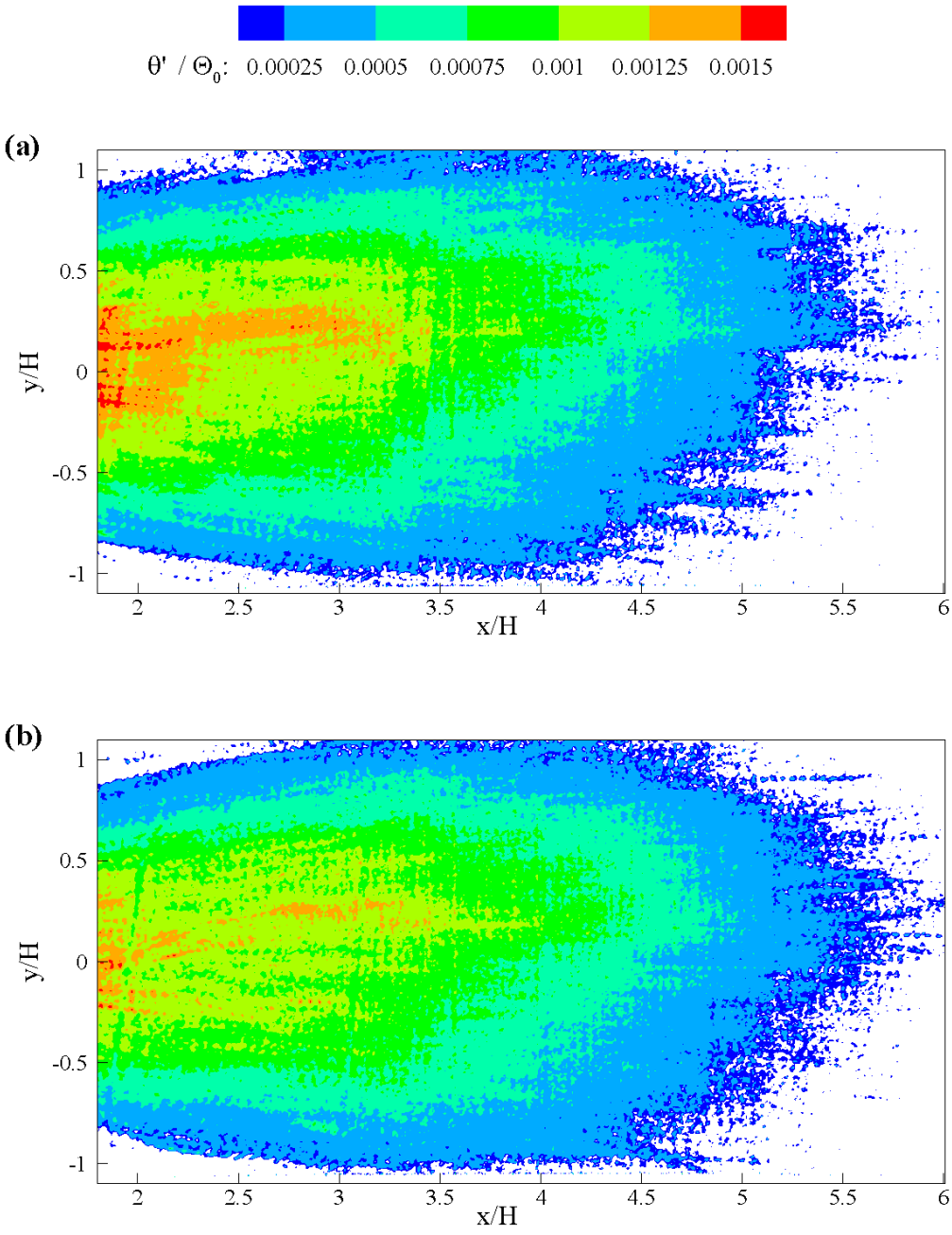

Figure 4.12 Fields of the standard deviation of the concentration fluctuations, θ'/Θ_0, for the meandering plume at four elevations above the substrate: (a) 0.5 cm $(z/H = 0.02)$, (b) 2.2 cm $(z/H = 0.10)$, (c) 4.7 cm $(z/H = 0.22)$, and (d) 7.2 cm $(z/H = 0.34)$.

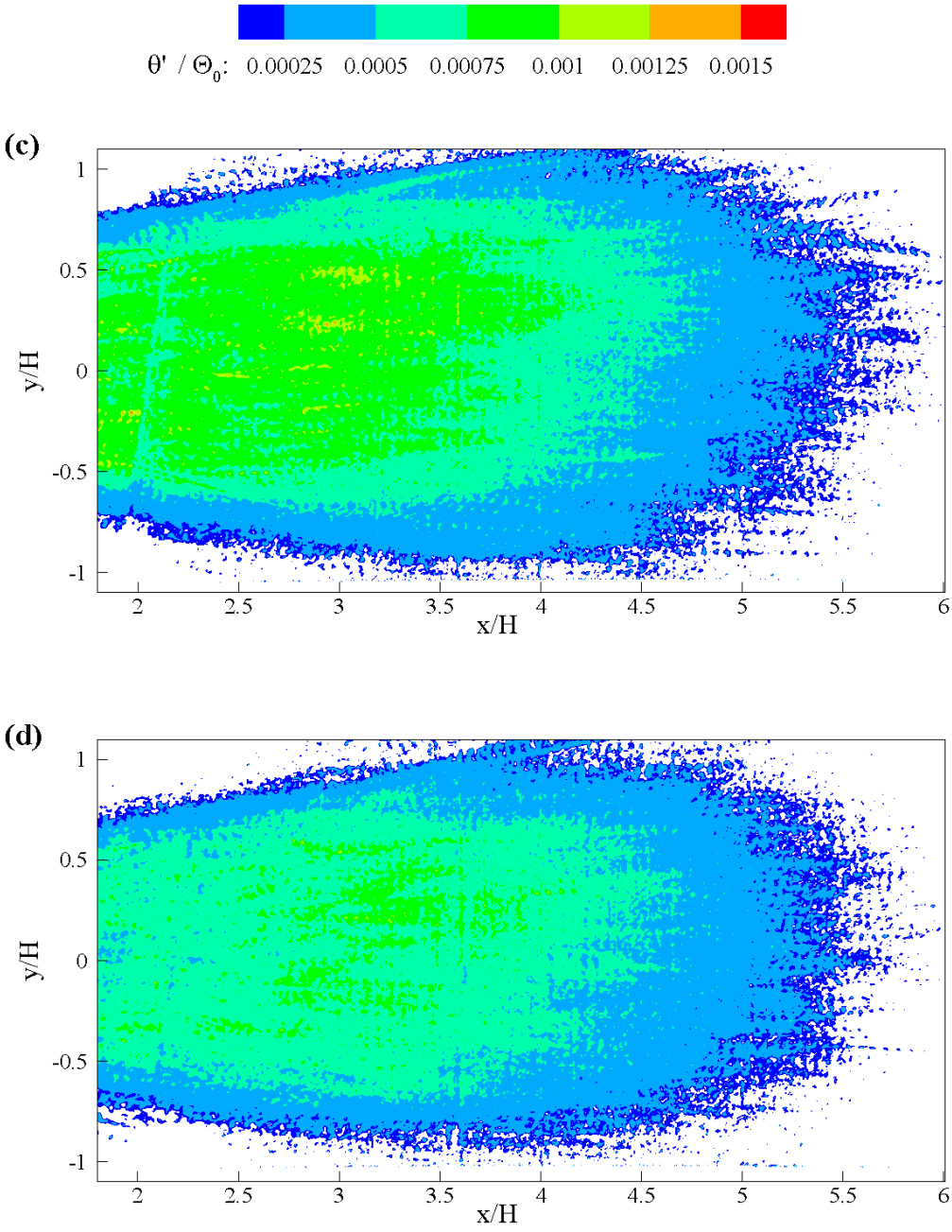

Figure 4.12 Continued.

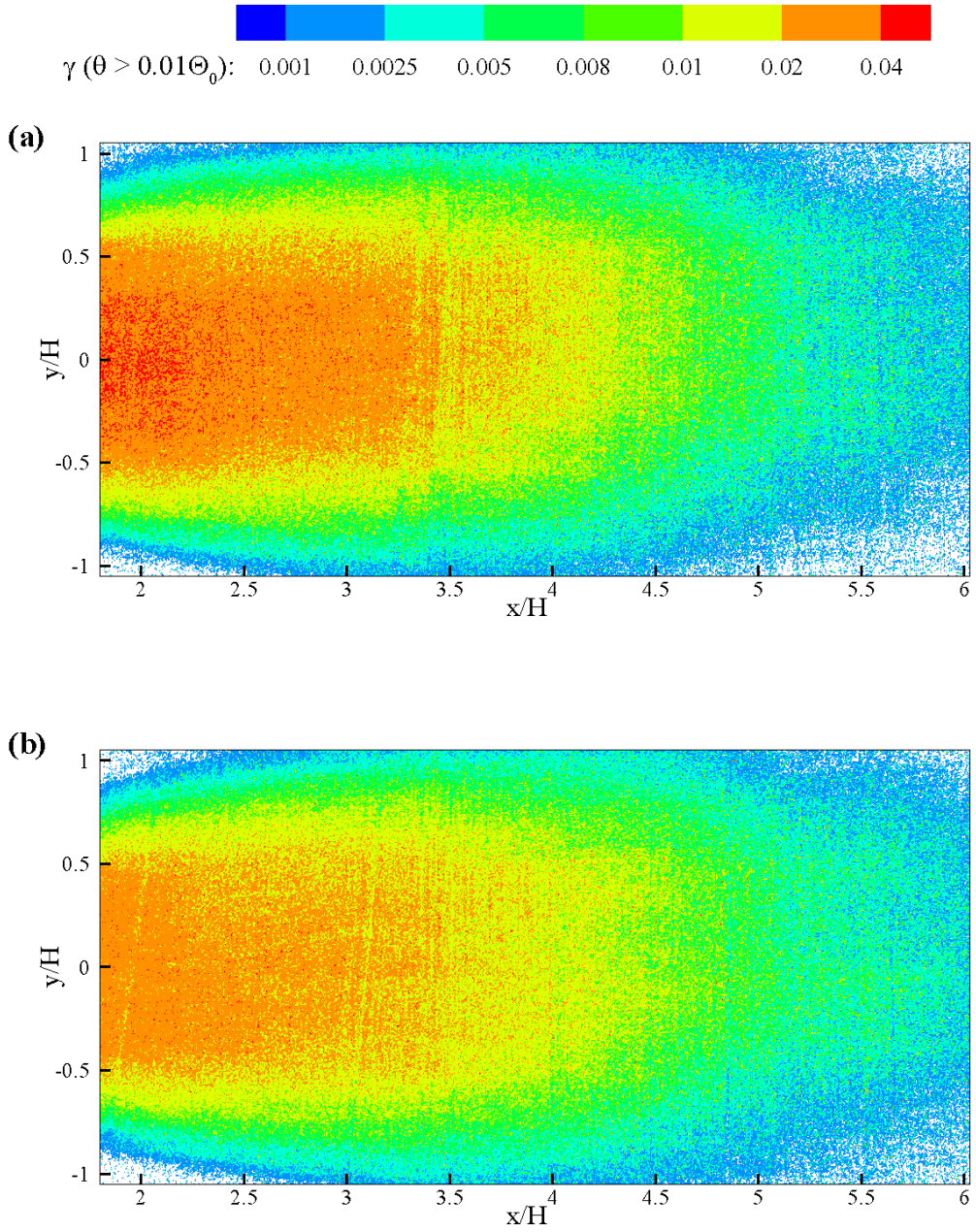

Figure 4.13 Fields of intermittency factor γ based on a threshold of 1% of the source concentration (i.e., the probability that the concentration exceeds $0.01\Theta_0$) for the meandering plume at four elevations above the substrate: (a) 0.5 cm $(z/H = 0.02)$, (b) 2.2 cm $(z/H = 0.10)$, (c) 4.7 cm $(z/H = 0.22)$, and (d) 7.2 cm $(z/H = 0.34)$.

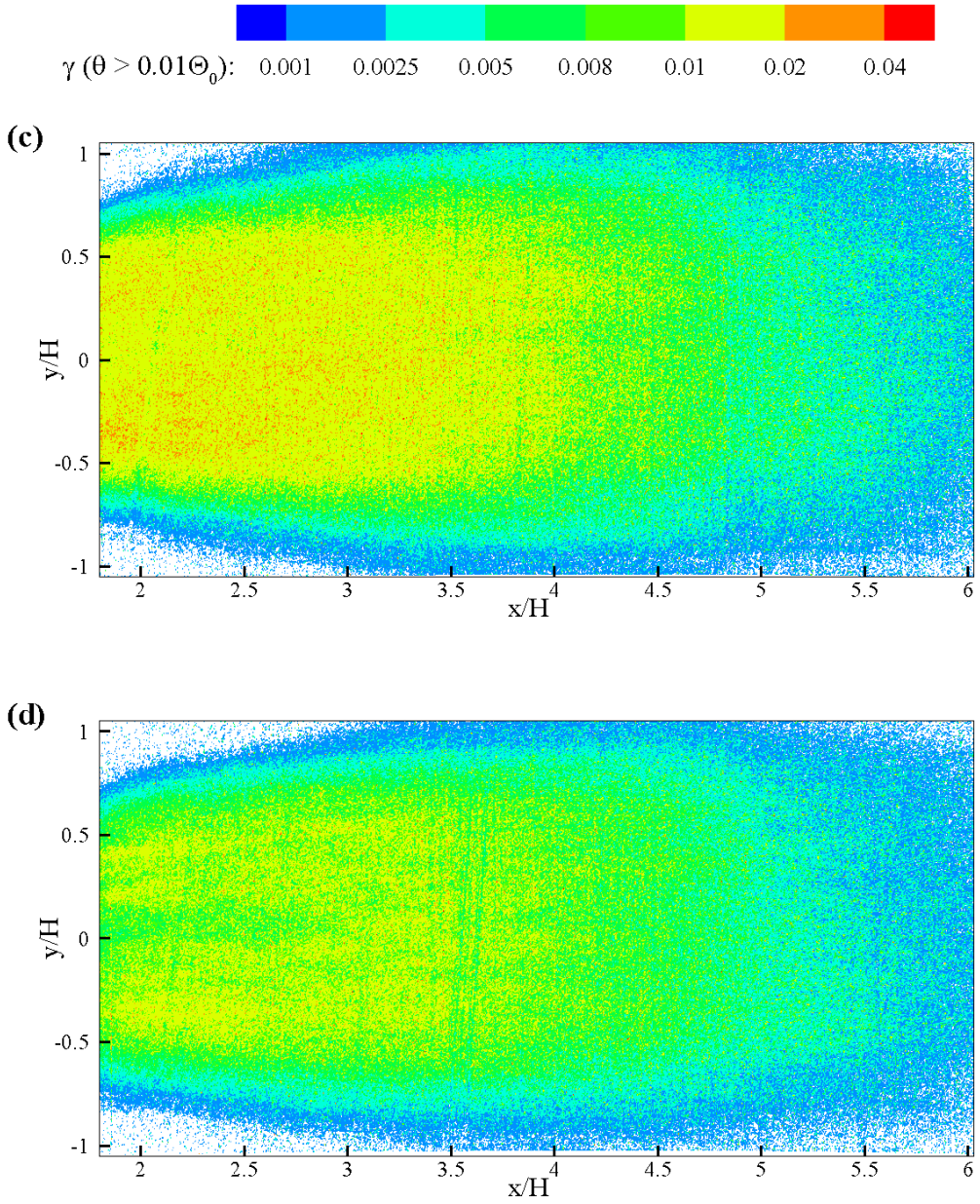

Figure 4.13 Continued.

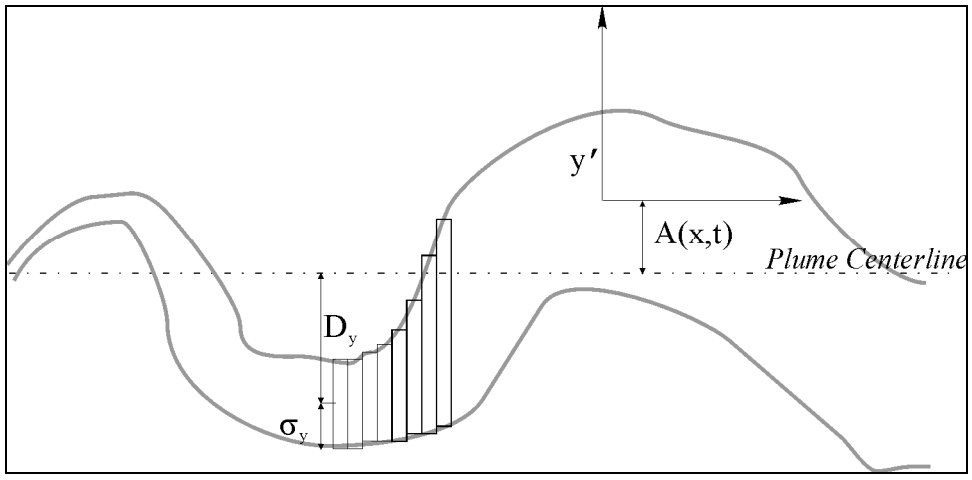

Figure 4.14. Sketch of the meandering plume model adapted from Gifford (1959). Dispersion occurs within each longitudinal disk according to the Gaussian model, equation 2.18. The plume meanders back and forth with amplitude $A(x,t)$.

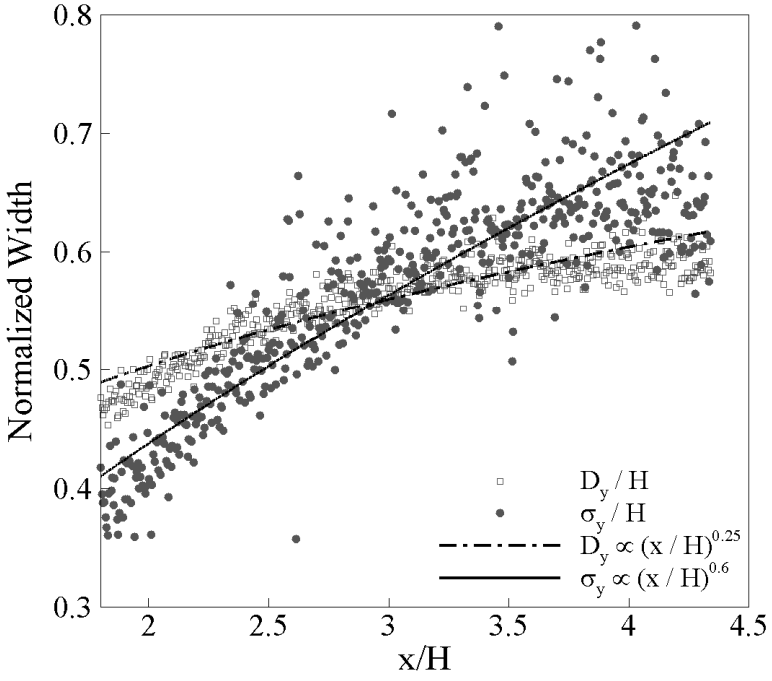

Figure 4.15 Streamwise profiles of the meander width (open squares) and plume width (solid circles) for the meandering plume in the plane nearest the nozzle centerline elevation z_0 (z = 2.2 cm).

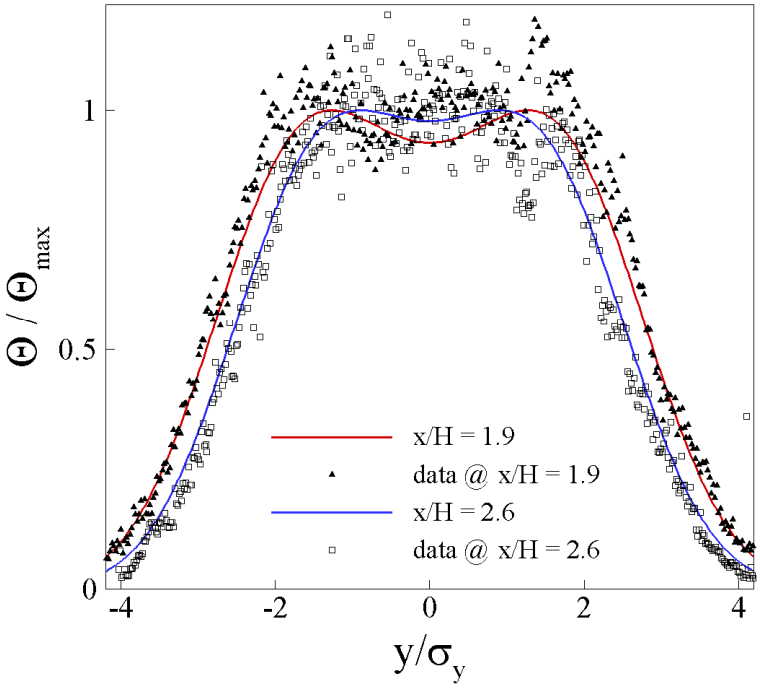

Figure 4.16 Transverse profiles of average concentration for the meandering plume for two distances from the source. The curves in color are profiles based upon equation 4.14 with coefficients determined from the data.

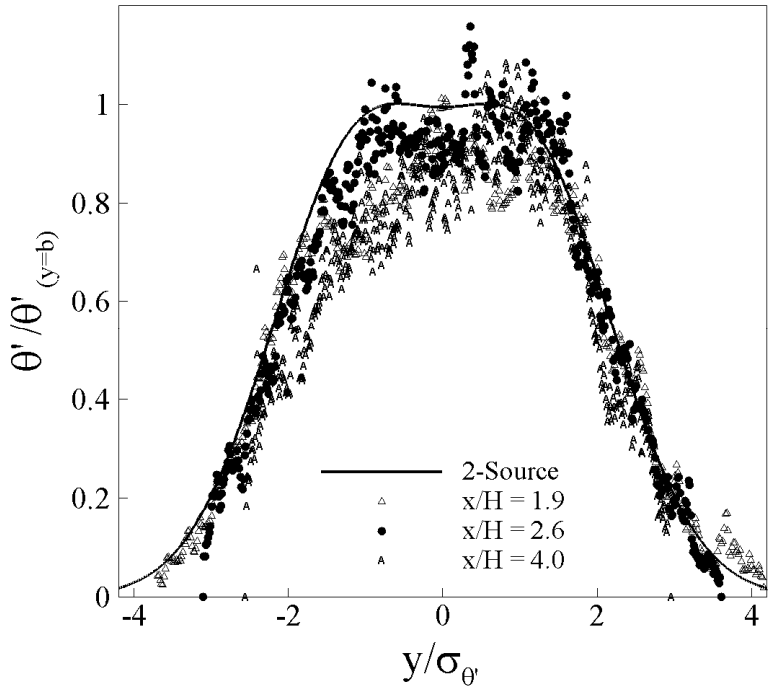

Figure 4.17 Transverse profiles of the standard deviation of the concentration fluctuations. The solid curve is a Gaussian model assuming two sources located at the transverse boundaries of the upstream cylinder.

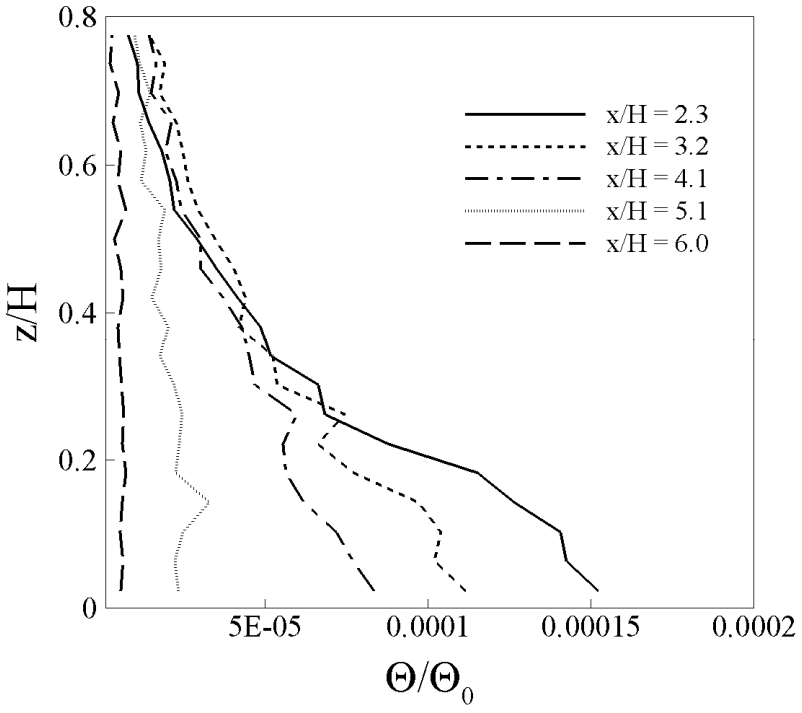

Figure 4.18 Vertical profiles of average concentration along the plume centerline, i.e. for $y = 0$. The concentration field becomes homogeneously mixed in the vertical direction at approximately $x / H = 6$.

4.3 Pulsed plume

Figure 4.19 shows flow visualization images of the pulsed plume of a neutrally buoyant red dye. The plume was not released iso-kinetically; the jet had a mean velocity relative to that of the flume flow. Flow from the nozzle was zero when not releasing dye-water mixture. The mass delivery of the continuous plume (Section 4.1) and the pulsed plume were matched over one 10-s cycle (i.e., the pulsed plume released the same amount of mass during the 5 s "on" period as the continuous plume released over 10 s). Hence, the average jet velocity was approximately twice that of the ambient flow, which leads to a mild velocity gradient between the jet and ambient flows. The flow visualization images

reveal a plume consisting of discrete patches (or “clouds”) of dye separated by regions of clear fluid. Each patch advects downstream and turbulent mixing acts to expand the patch and dilute the filaments.

Two example instantaneous concentration fields are shown in Figure 4.20. The fields consist of sparse regions of high concentration surrounded by an ambient condition of zero or near-zero concentration. Gaps between the individual clouds moving downstream are apparent when compared to the instantaneous plots of the continuous plume in Figure 4.2. Decreases in concentrations with distance downstream are similar to those of the continuous release.

Fields of average concentration contours are plotted in Figure 4.21 at four heights above the substrate. The source concentration in this case was 600 µg/l and the ensemble average includes 24,000 images at each 3DLIF level (i.e. a total of 480,000 images). The time required to take the images was approximately 80 minutes with the camera collecting at 100 frames per second. The concentration scales for Figures 4.21 and 4.3 are the same for comparison. The average concentration levels in the pulse plume case are roughly half those of the continuous plume and the average plume structure is narrower. The average concentration fields appear to approach a constant width at approximately $x/H = 3.5$.

Fields of the standard deviation of the concentration fluctuations are shown in Figure 4.22 at four 3DLIF elevation levels. The contour levels for Figures 4.4 (for the continuous case) and 4.22 are the same for comparison purposes. The general shape of the contours of the standard deviation is similar to the continuous plume, although the

contour levels are much lower in the pulsed case. The lower level of standard deviation is due to instantaneous concentrations falling to zero (and hence not fluctuating) for significant periods of time between passing patches. The fluctuation fields of the continuous and pulsed plumes spread to similar transverse distances due to similar ambient turbulent conditions.

Fields of intermittency factor are shown in Figure 4.23 for a threshold of one percent of the source concentration. The source character of the pulsed plume becomes most evident in the intermittency plots where the instantaneous signal falls below the threshold more frequently than the continuous release. The transverse widths of the contour pattern for the pulsed and continuous plumes are similar. For transverse distances beyond approximately $y = 0.4H$, the probability of encountering a odorant burst exceeding $0.01\,C_o$ is low for both release types. The intermittency factor plots suggest a crab tracking a pulsed source may hesitate after passing through a patch due to lack of concentration bursts, but the crab is not likely to wander far from plume centerline.

Transverse profiles of the average concentration and standard deviation of the concentration fluctuations are shown in Figure 4.24. The transverse coordinate is normalized by the widths σ_Θ and $\sigma_{\theta'}$, respectively, which were calculated by fitting log-transformed data to equation 4.6. As shown, the profiles approximately match the Gaussian shape predicted by equation 4.6. Scatter in the data is observed near the plume centerline due to fixed pattern noise of the camera and potential off-center maximums. A closed-form solution of the advection-diffusion equation for a jet release, similar to

equation 2.18, does not exist, although extensive empirical evidence shows average concentration profiles to follow a Gaussian form (Fisher et al. 1979).

Centerline profiles of average concentration and standard deviation of the concentration fluctuations are shown in Figure 4.25a. A best-fit line through the average concentration data reveals a decay proportional to $x^{-1.3}$ for $2 < x/H < 4.5$. Using scaling relationships and assuming self-similarity, the decrease in average concentration for a continuous jet follows the same x^{-1} relationship as an iso-kinetic release (Fischer et al. 1979, Tennekes and Lumley 1972). The pulsed plume is not a continuous jet but a train of clouds released from the source. The dispersion of a cloud into an isotropic environment leads to a decrease in average concentration following (Townsend 1951, Chatwin and Sullivan 1979):

$$\Theta \propto \frac{M}{L_c^{\,3}} \tag{4.20}$$

Assuming a Gaussian shape for the transverse profile of average concentration, the cloud size L_c is proportional to $t^{1/2}$. Using the Galilean transformation of equation 2.18, the average concentration scales as:

$$\Theta \propto t^{-3/2} \propto x^{-3/2} \tag{4.21}$$

Average concentration at a fixed point would not strictly follow the decay predicted by equation 4.21 as the cloud continues to disperse as it passes. Further, the turbulence in the boundary layer is not isotropic as assumed in the scaling arguments leading to equation 4.21. Nevertheless, the decay shown in Figure 4.25 for the average

concentration follows a power law $\Theta \propto x^{-1.3}$ with an exponent close to that of equation 4.21.

Vertical profiles of average concentrations at four distances from the source are shown in Figure 4.25b. The general shapes of the vertical profiles and trends are similar to those of the continuous release, although the average concentration levels are roughly half compared to the continuous plume case (compare to Figure 4.7b). Phase-averaging of the pulsed release results in a sequence of discontinuous distorted cones, which when averaged over all phases approximates a reflected Gaussian shape in the vertical direction.

Figure 4.26 shows the development of transverse plume width for the profiles of average concentration. The average concentration width grows according to $x^{0.6}$, hence spreading more rapidly than the continuous release plume ($\sigma_\Theta \propto x^{0.50}$, shown in Figure 4.8). Since the average concentration decays more rapidly than for the continuous plume (see Figure 4.25a), the plume width must correspondingly increase more rapidly as the tracer is conservative.

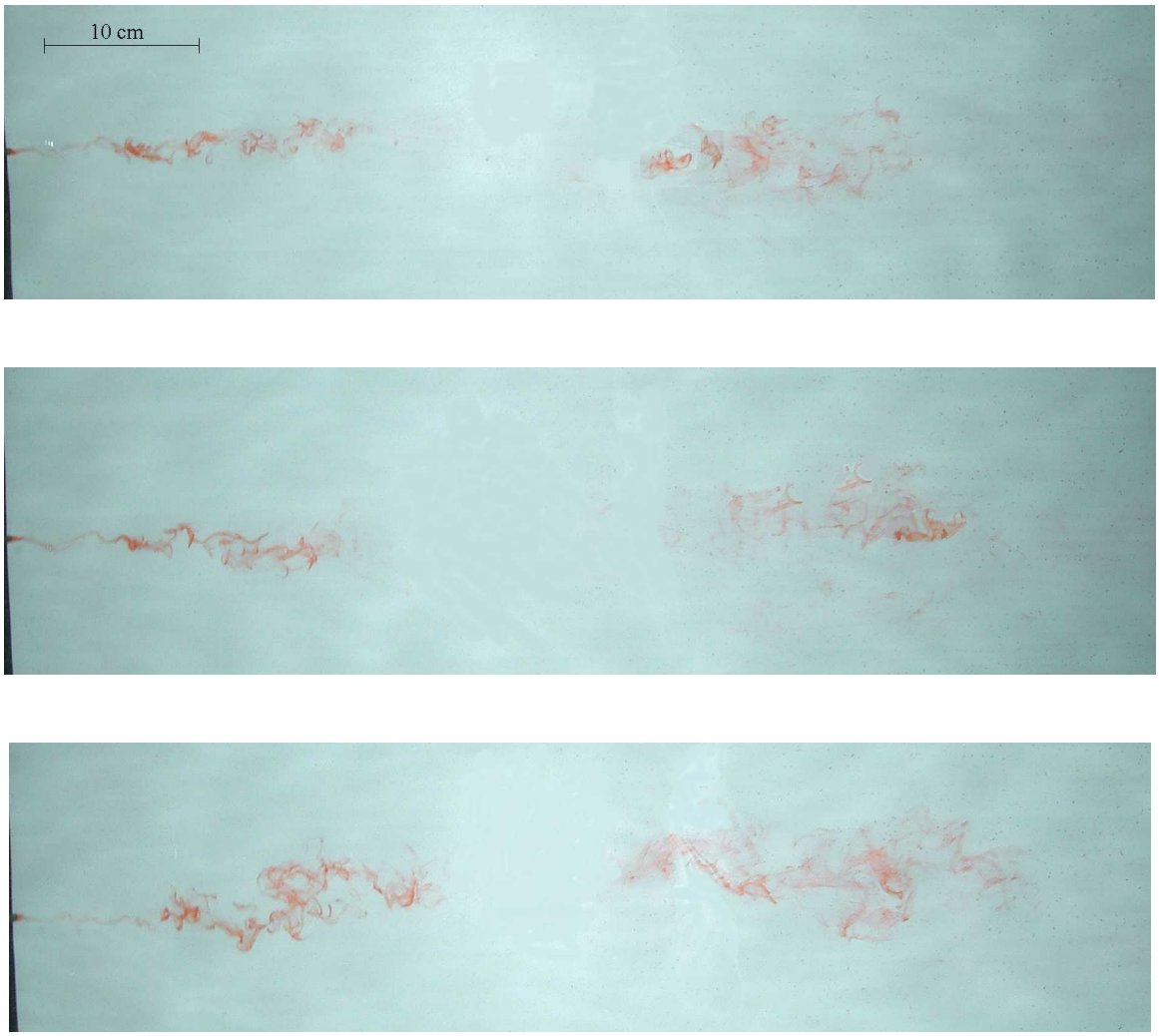

Figure 4.19 Flow visualization of the pulsed plume, which is created via a pulsed release into the test section of the saltwater flume. The view is from above, with the flow moving from left to right. The flow and plume parameters are defined in Tables 3.1 and 3.2.

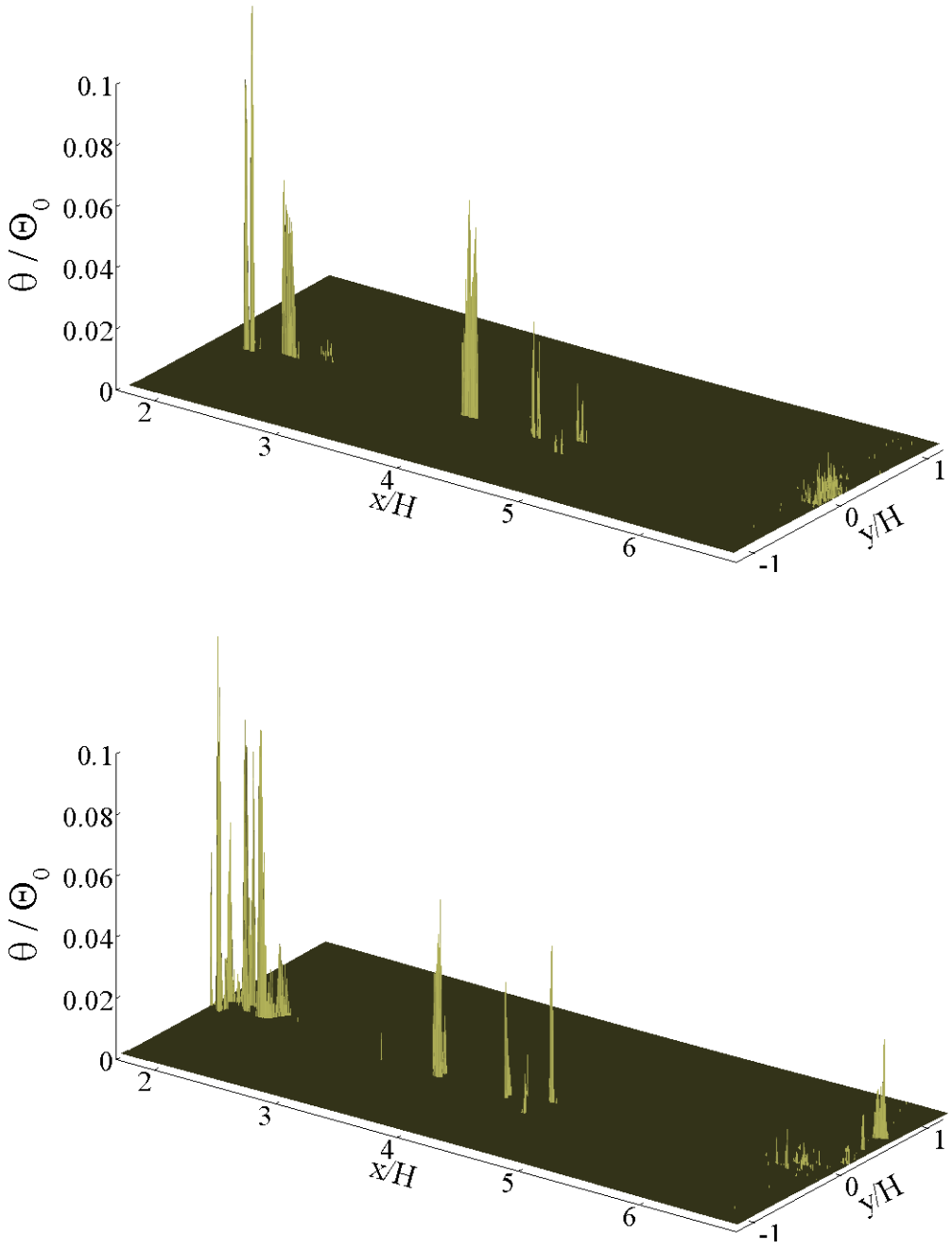

Figure 4.20 Two examples of instantaneous concentration fields for the pulsed plume at z = 2.2 cm ($z / H = 0.10$) near the elevation of nozzle centerline.

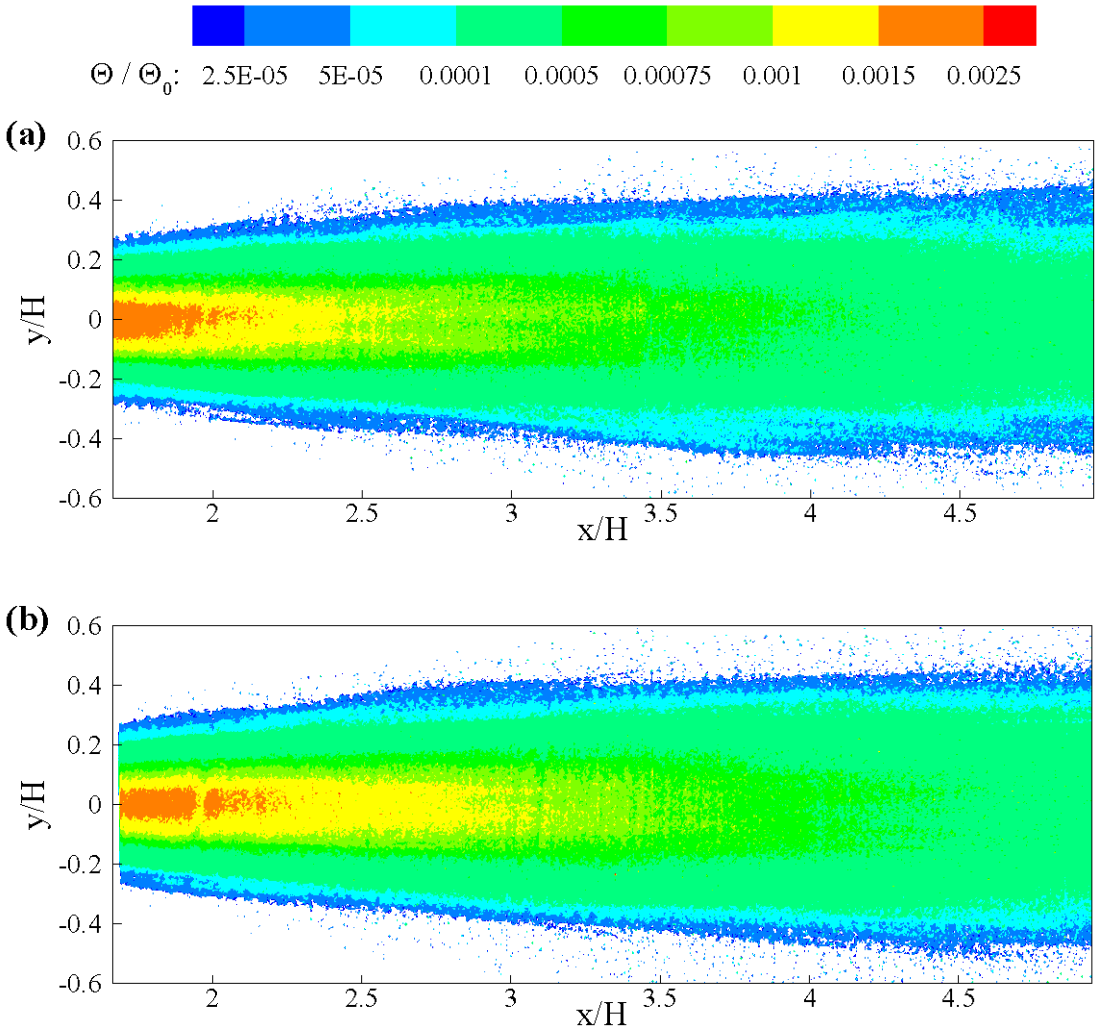

Figure 4.21 Fields of average concentration, Θ/Θ_0, for the pulsed plume at four elevations above the substrate: (a) 0.5 cm $(z/H = 0.02)$, (b) 2.2 cm $(z/H = 0.10)$, (c) 4.7 cm $(z/H = 0.22)$, and (d) 7.2 cm $(z/H = 0.34)$.

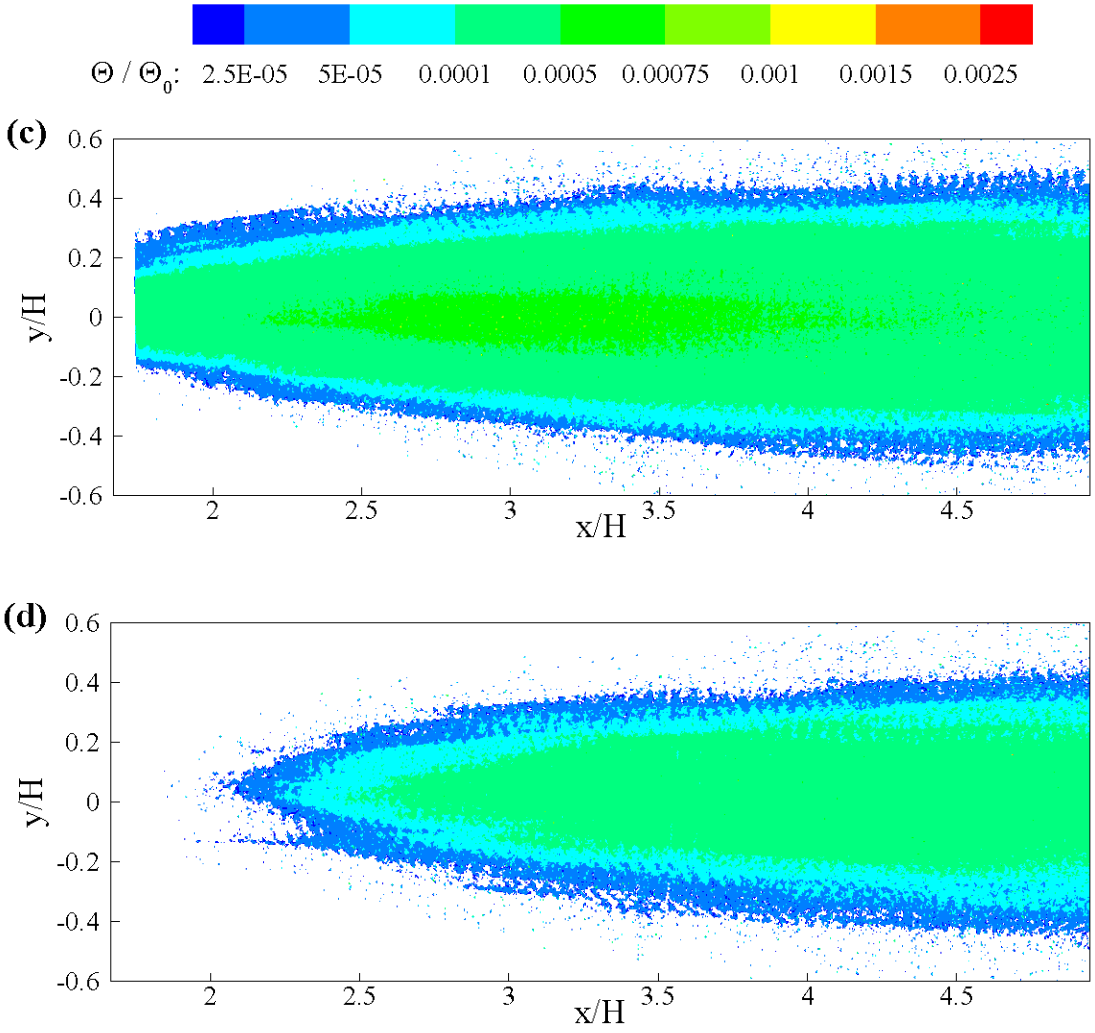

Figure 4.21 Continued.

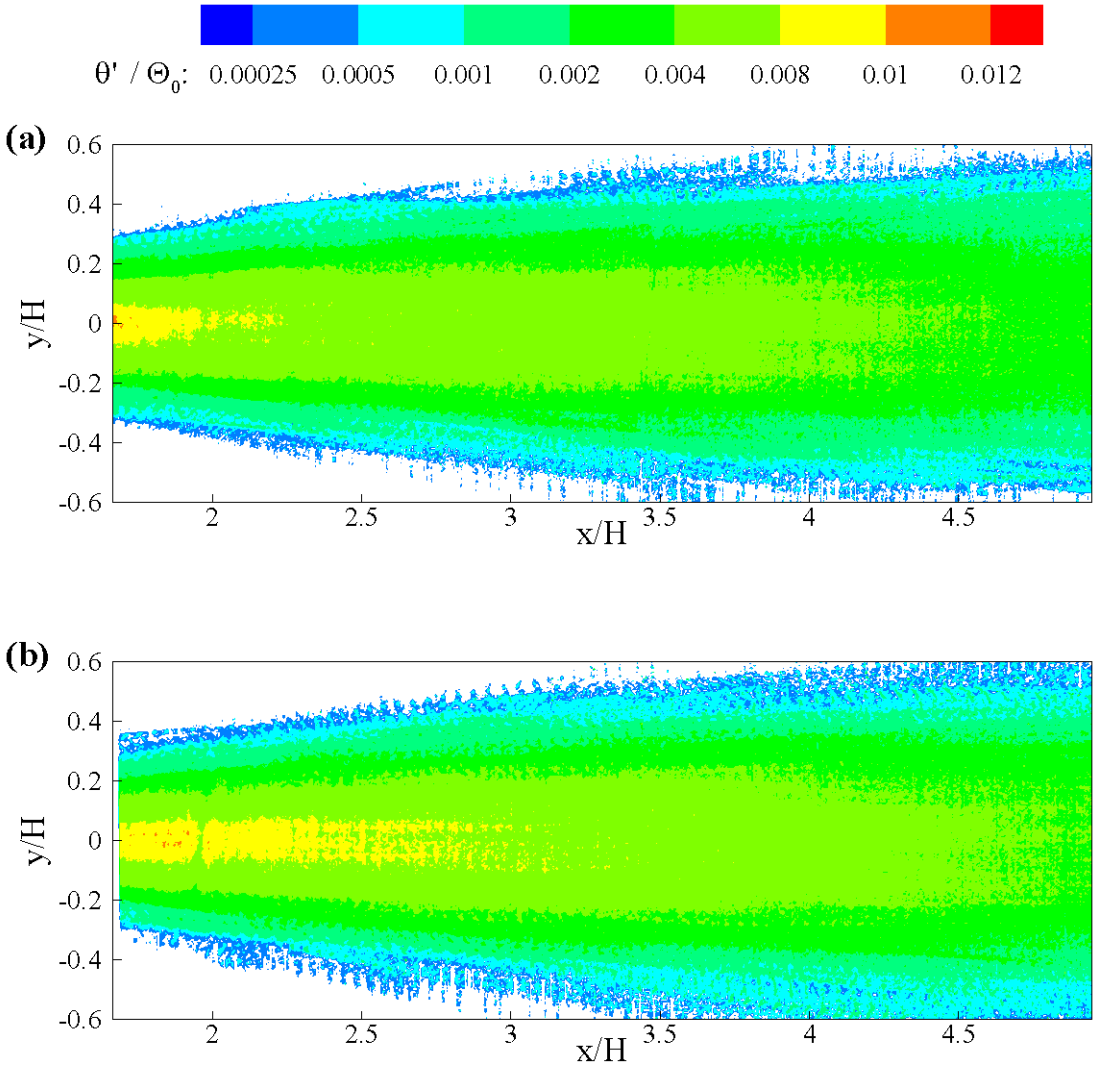

Figure 4.22 Fields of the standard deviation of the concentration fluctuations, θ'/Θ_0, for the pulsed plume at four elevations above the substrate: (a) 0.5 cm $(z/H = 0.02)$, (b) 2.2 cm $(z/H = 0.10)$, (c) 4.7 cm $(z/H = 0.22)$, and (d) 7.2 cm $(z/H = 0.34)$.

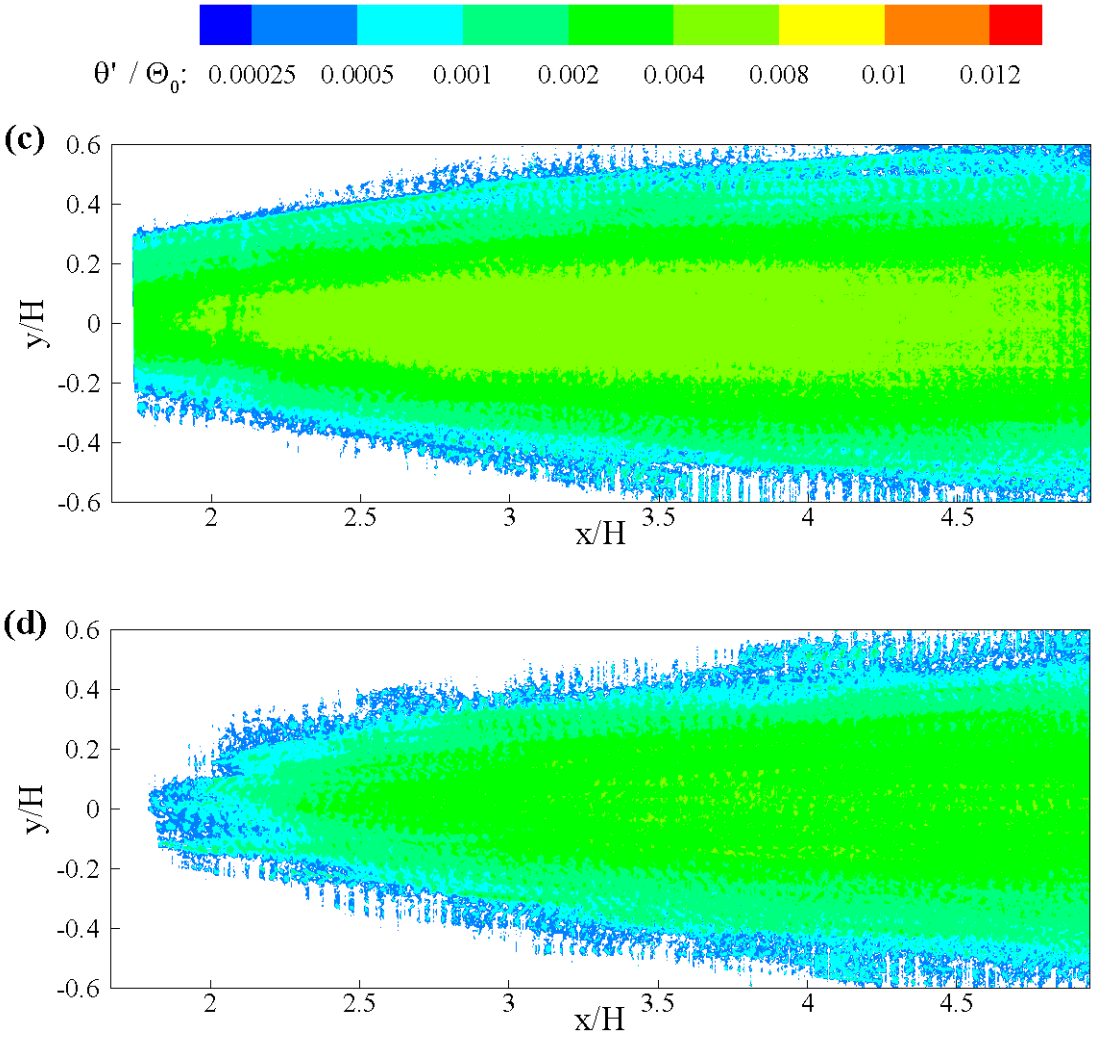

Figure 4.22 Continued.

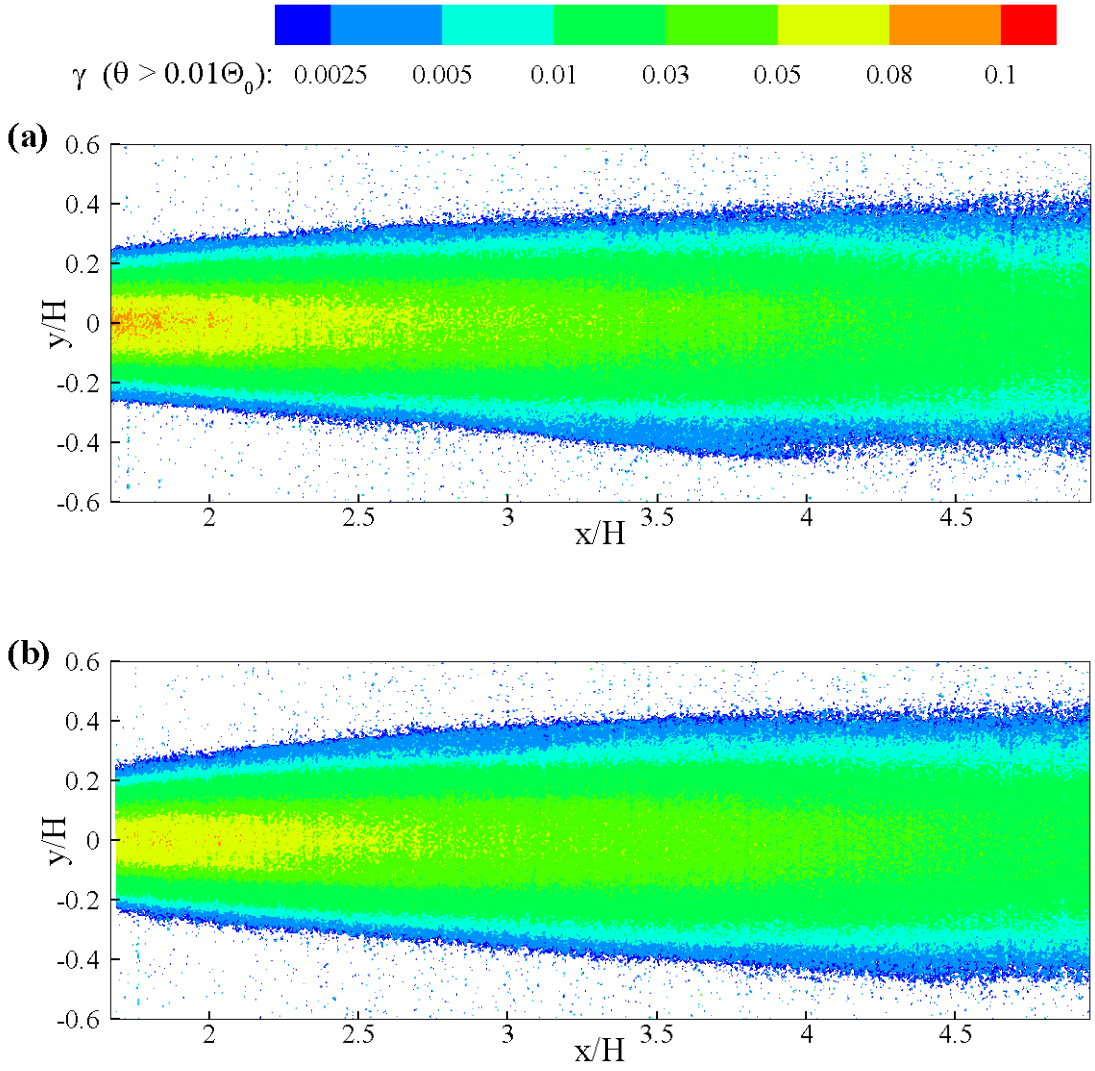

Figure 4.23 Fields of intermittency factor γ based on a threshold of 1% of the source concentration (i.e., the probability that the concentration exceeds $0.01\Theta_0$) for the pulsed plume at four elevations above the substrate: (a) 0.5 cm $(z/H = 0.02)$, (b) 2.2 cm $(z/H = 0.10)$, (c) 4.7 cm $(z/H = 0.22)$, and (d) 7.2 cm $(z/H = 0.34)$.

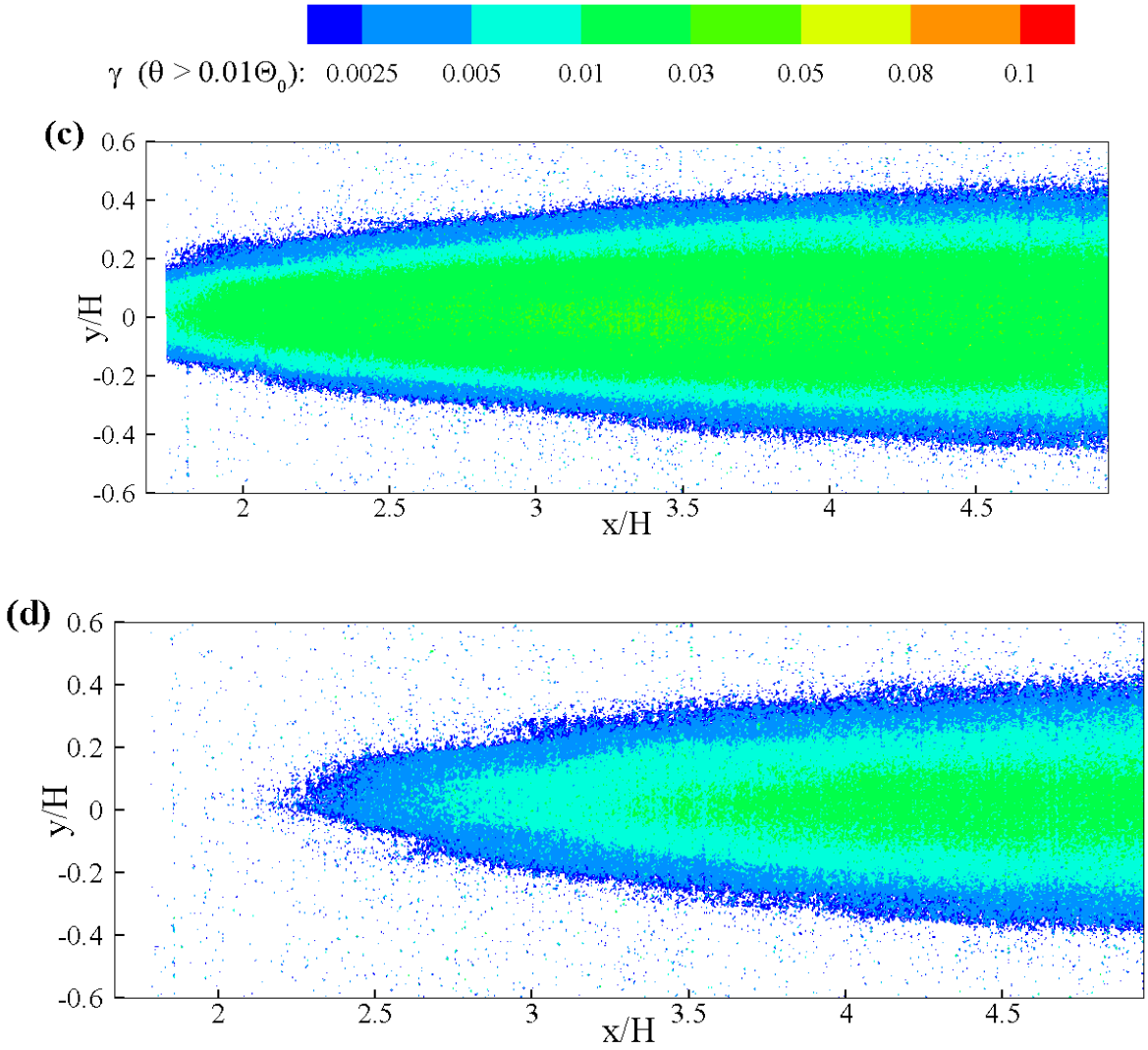

Figure 4.23 Continued.

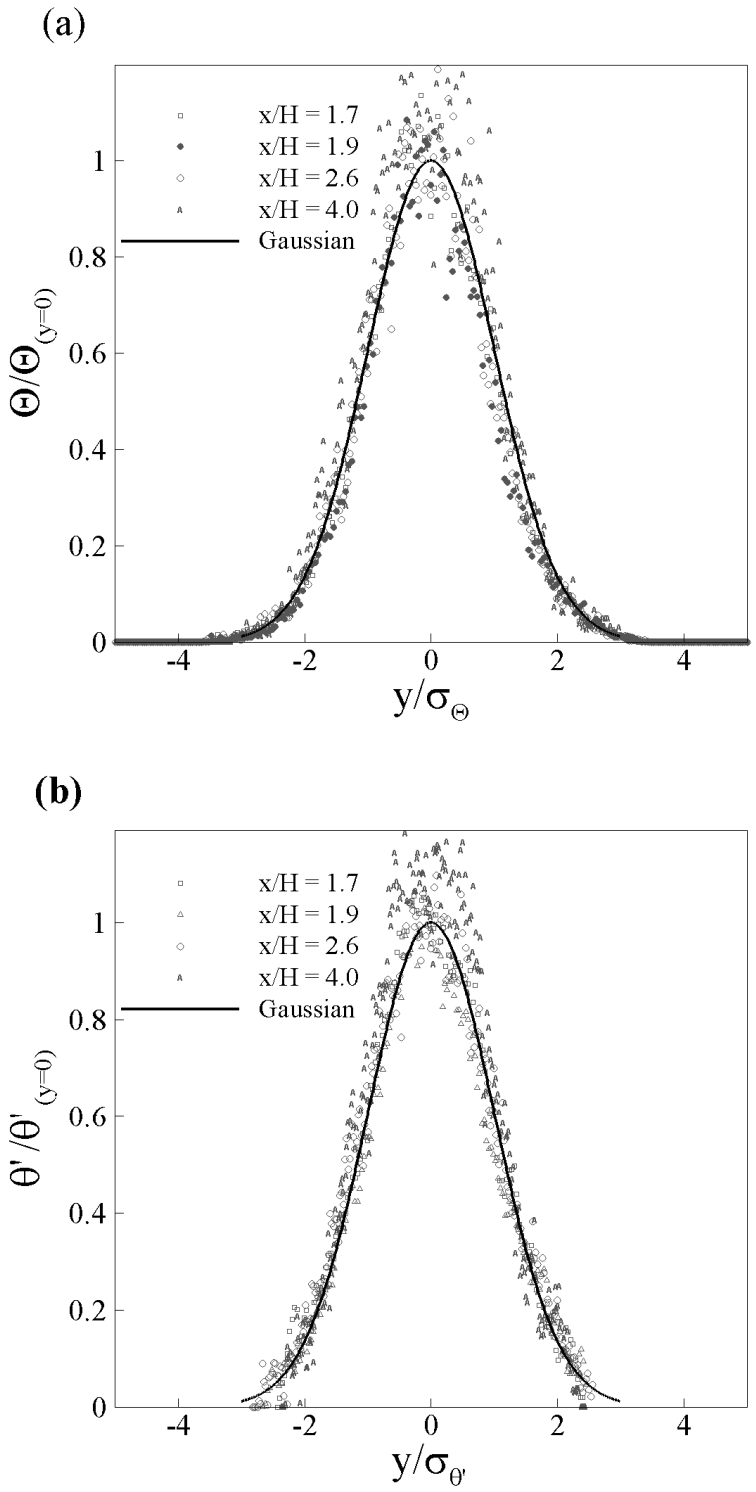

Figure 4.24 Transverse profiles for the pulsed plume. (a) average concentration, and (b) standard deviation of the concentration fluctuations. Both sets of profiles correspond to the measurement plane that is nearest to the nozzle centerline elevation z_0 (z = 2.2 cm, z/H = 0.10).

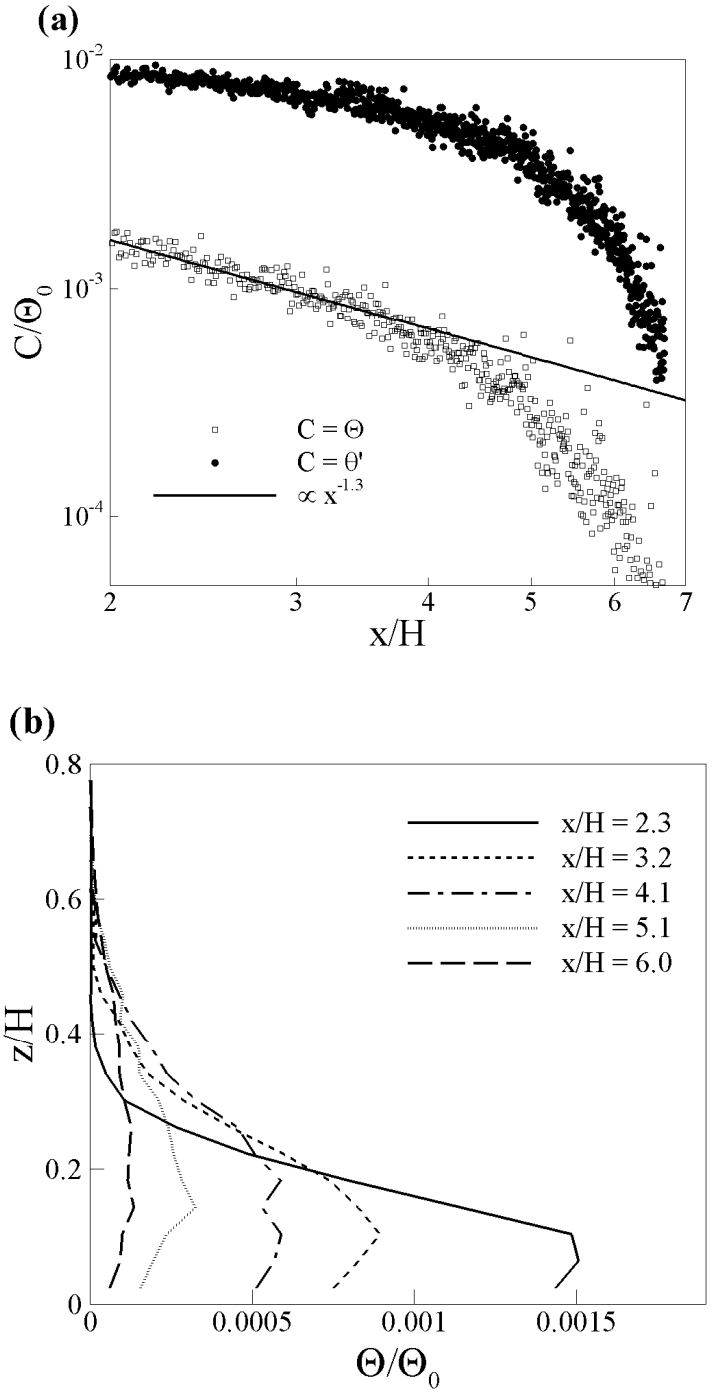

Figure 4.25 Profiles for the pulsed plume. (a) Streamwise profiles of the average concentration (squares) and standard deviation of the concentration fluctuations (filled circles) along the centerline of the plume, i.e. for $y = 0$ and $z = 2.2$ cm (every third data point shown for clarity), and (b) vertical profiles of average concentration along the plume centerline, i.e. for $y = 0$ and various distances from source.

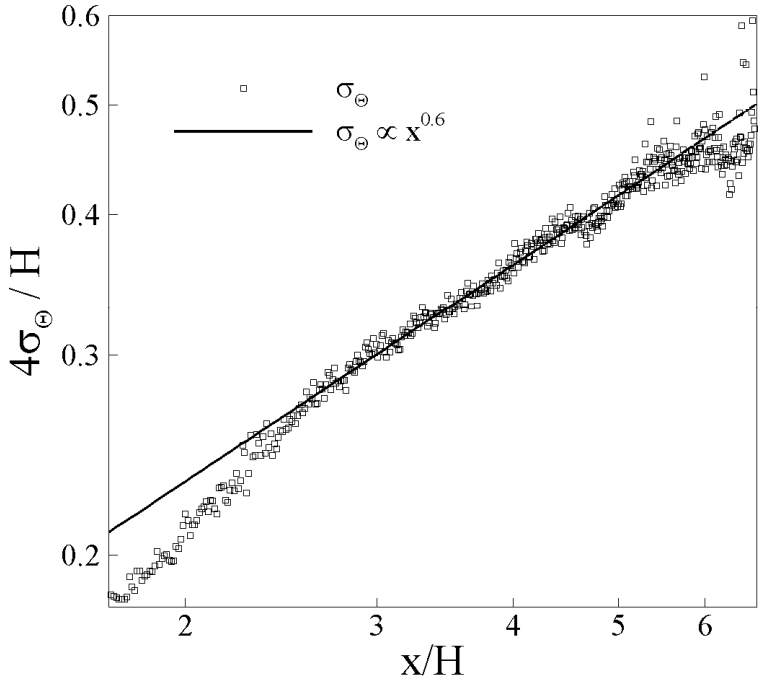

Figure 4.26 Transverse width for the pulsed plume based on the average concentration field.

4.4 Conclusions

Data taken from 3DLIF was used to determine some of the physical characteristics for the three plume types. Due to signal intermittency and noise levels on the CMOS camera, convergence to statistical measures required between 26 (continuous plume) and 84 (pulsed plume) minutes of image recording. Although imperceptible to tracking animals, the statistical measures presented in this chapter do provide some insight into the instantaneous character of turbulent plumes and the signal environment encountered in each plume type. One example is the decrease in average concentration as the source is approached for elevations above plume centerline. Chemosensors that are located higher

in the boundary layer, such as the antennules on a blue crab, generally receive an increasingly intermittent signal closer than approximately $x/H < 3.5$ to the source.

The continuous plume average concentration data generally agreed with previous data reported by Rahman (2002). The transverse profiles followed the Gaussian plume model, and the standard deviations of the concentration fluctuations supported a K-model with isotropic eddy-diffusivities. The growth of the average plume width conformed to the Gaussian model with an eddy-diffusivity of $\varepsilon = 0.074 u_* H$ in the range of x/H from 2.5 to 5.

For the meandering plume, the instantaneous plume centerline followed a serpentine pattern in the downstream direction and continuously varied. The concentration distribution in meandering plume data is wider compared to the continuous plume case. The transverse distribution of the average concentration supported the meandering plume model proposed by Gifford (1959). The average amplitude of the plume meander D_y followed a power law, i.e. proportional to $x^{0.25}$. Plume width grew at a faster rate ($\propto x^{0.6}$) than the $x^{0.5}$ power law predicted by the meandering plume model. Transverse average concentration profiles were not self-similar and had symmetric off-center peaks. At large distances from the source, the model achieves self-similarity as the meander amplitude becomes negligible with respect to plume width.

Transverse profiles for the pulsed plume data followed the Gaussian plume model in agreement with a continuous plume. The instantaneous structure is more intermittent compared to the continuous plume and include regions of very low concentration between clouds of odorant. Profiles of the average concentration and the standard

deviation of the concentration fluctuations followed a self-similar shape, again in agreement with the continuous plume. Average centerline concentrations decreased according to a power law $\propto x^{-1.3}$, which was smaller than the $x^{-1.5}$ predicted by Townsend (1951) and Chatwin and Sullivan (1979) through scaling arguments and passive scalar conservation analysis in a dispersing cloud. Plume width growth followed a power law $\propto x^{0.6}$, which was greater than that predicted by the Gaussian plume model.

Chapter 5

Odorant Plume Tracking by Blue Crabs

The main focus of this study was to physically measure the instantaneous concentration field experienced by a blue crab during a successful search. Included in the trials were three plumes types – continuous, meandering, and pulsed – the characteristics of which are described in Chapter 4. Blue crabs were released 1.5 m downstream of the source and the analysis that follows includes only crabs that successfully located the source. The pulsed and meandering plumes were included in order to determine blue crab response to large-scale temporal and spatial intermittency, respectively. As will be discussed below, crabs that were tracking meandering plumes wandered the most and spent the longest amounts of time locating the source. The stimulus environment of the continuous plume resulted in the most direct paths towards the source.

Table 5.1 Summary of the Data Collected to Quantify Crab Response to Plume Structure

Plume Type	Number of Tracks		Average Non-Zero Walking Velocity (cm/s)	Average Source Vector Angle (deg)
	Kinematics/Outer Chemosensors	Antennules Analysis[1]		
Continuous	22	15	8.4	33
Meandering	19	14	7.4	50
Pulsed	16	12	8.5	45
Totals	57	41		

1 – Analysis of the antennules was limited to crabs facing the laser. This is described in more detail in Section 5.3.1.

Tracking characteristics for the three plume types are summarized in Table 5.1. The number of tracks refers to the number of successful crab tracks used in each analysis. The restrictions on chemical analysis were stricter than those of kinematics as only crabs facing the laser gave useable information regarding odorant concentration at the antennules. The restrictions will be described in more detail in the following sections. Average velocity is the mean non-zero walking speed of the valid tracks within the recorded region. Average source vector angle is the mean angle between the instantaneous crab direction and a vector pointing towards the source. Thus, a crab moving directly towards the source would have a source vector angle of zero, with the displacement and source vectors aligned collinearly. Detailed information about successful crab tracks is provided in the following sections: vector analysis of crab tracks, statistics of crab kinematics, and extraction of chemical data from successful tracks.

5.1 Vector analysis of crab tracks

Coordinate data extracted from the crab backpack LED's provides the instantaneous alignment of the crab compared with various vector quantities deemed important for navigation. When animals perform olfactory searches in a moving stream, they generally proceed in the upstream direction (rheotaxis and anemotaxis described in Chapter 2). The reasons for upstream movement are obvious as the odorant must be advected by the ambient fluid. Alignment of the crab track with the mean flow vector, which is parallel with the positive x-axis for this study, supplies information about crab rheotactic response. Another important vector quantity is the source vector, which extends from the animal to the source. Comparing the crab displacement vector to the source vector provides information about the directness of the tracking maneuvers. Also, the alignment

of the displacement vector with the mean concentration gradient vector is of interest, although it is clear that rapidly tracking animals do not experience the mean concentration profile during their searches (Murlis et al. 1992, Webster and Weissburg 2001, Moore and Crimaldi 2004). However, experimental (Gulitski et al. 2007) and DNS (Brethouwer et al. 2003) evidence suggests that the instantaneous concentration gradient vector aligns preferentially with the mean concentration gradient vector.

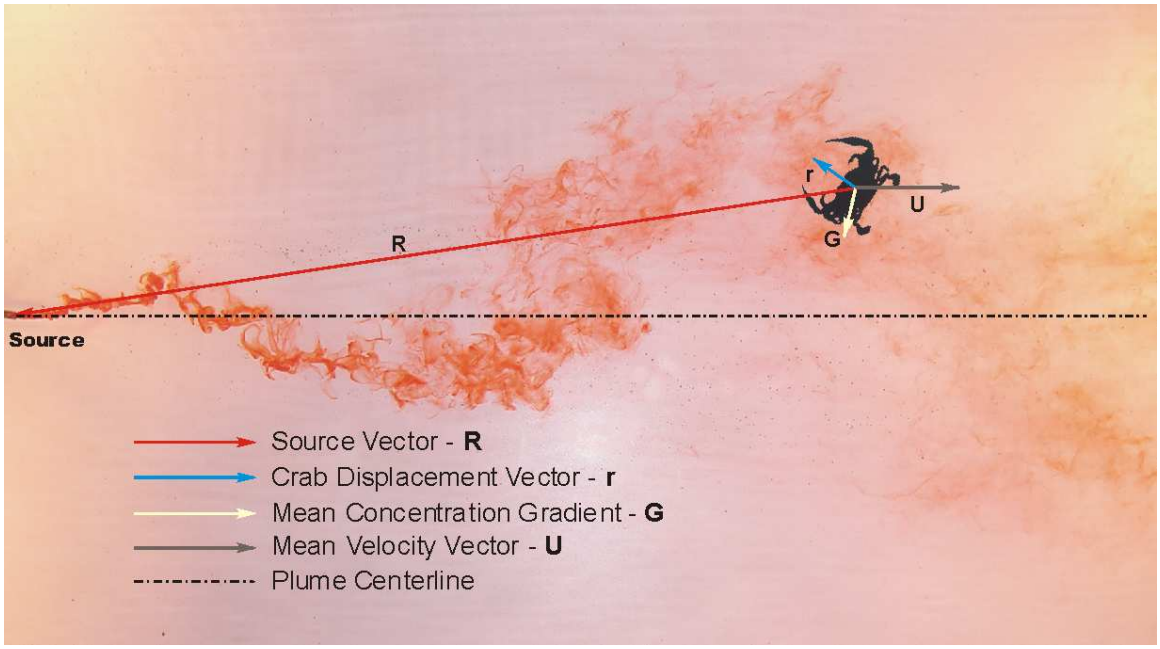

Figure 5.1 Schematic of the vectors used in crab kinematic analysis. The source vector **R** points from the crab to the source. The crab displacement vector **r** is the vector distance traveled by the crab in the time between recorded images, 0.21 s. The mean concentration gradient vector **G** is calculated from a simplified form of equation 2.18, and the mean velocity vector **U** points downstream.

Figure 5.1 defines the various vectors. The source vector **R** is the position vector of the source relative to the crab. The crab displacement vector **r** is the distance and direction traveled during a set time interval, i.e. the 3DLIF measurement time interval of 0.21 s. The time interval was chosen as it corresponds to what is generally known about

arthropod neurological response (Gomez and Atema 1996) and was used in the calculations of velocity and acceleration. The mean velocity vector **U** is the flow direction parallel to the x-axis and is fixed. The mean concentration gradient vector **G** is the local mean concentration gradient assuming the Gaussian distribution of equation 2.18. The gradient was assumed two-dimensional, with $z = z_0$, and calculated by taking the x and y derivatives of equation 2.18.

$$\frac{\partial \Theta}{\partial x} = G_x = \frac{\dot{M}}{4\pi\varepsilon x} \exp\left(\frac{-Uy^2}{4\varepsilon x}\right)\left[\frac{Uy^2}{4\varepsilon x^2} - \frac{1}{x}\right] \tag{5.1a}$$

$$\frac{\partial \Theta}{\partial y} = G_y = \frac{\dot{M}}{4\pi\varepsilon x} \exp\left(\frac{-Uy^2}{4\varepsilon x}\right)\left(\frac{-Uy}{2\varepsilon x}\right) \tag{5.1b}$$

where $\mathbf{G} = G_x\mathbf{i} + G_y\mathbf{j}$. The vector **G** is a rough estimate of the mean concentration gradient vector as the plumes analyzed do not conform strictly to equation 2.18 and the crab chemosensors are not always aligned with the elevation of the nozzle $(z = z_0)$. Nevertheless, the mean concentration gradient vector calculated from equations 5.1 can be used to obtain general information about the alignment of the crab displacement vectors with the mean concentration gradient vector.

Vectors facilitate the quantification of blue crab tracking directness and are a simple means of characterizing rheotactic behavior and other alignment characteristics. The normalized dot product can be seen as a correlation coefficient between two vectors:

$$R = \frac{\mathbf{V_1} \cdot \mathbf{V_2}}{|\mathbf{V_1}||\mathbf{V_2}|} = \cos\alpha \tag{5.2}$$

where $\mathbf{V_1}$ and $\mathbf{V_2}$ are two vectors. The product of equation 5.2 varies from -1 to 1, as does a correlation coefficient, and is equivalent to the Cauchy-Schwarz Inequality.

The angle between the two vectors is the inverse cosine of equation 5.2 $\left(\alpha = \cos^{-1} R\right)$. The inverse cosine of the dot product provides insufficient information about which side of plume centerline the angle deflection lies. An angle between the source vector and the crab displacement vector might be small, yet the crab may be wandering away from mean plume centerline. Consequently, the magnitude of the angle α does not give a complete picture of progression towards the source. An angle convention was developed to take into account whether a given displacement vector was tending away or towards the mean plume centerline. For crab displacement vectors $\mathbf{r}$ between the plume centerline and the source vector $\mathbf{R}$, the angle α was defined as positive. Conversely, for displacement vectors outside the source vector, the angle was defined as negative. Figure 5.2 is a schematic of the angle sign convention. For the dot product calculations with the mean flow vector and the mean concentration gradient vector, the angles were defined similarly.

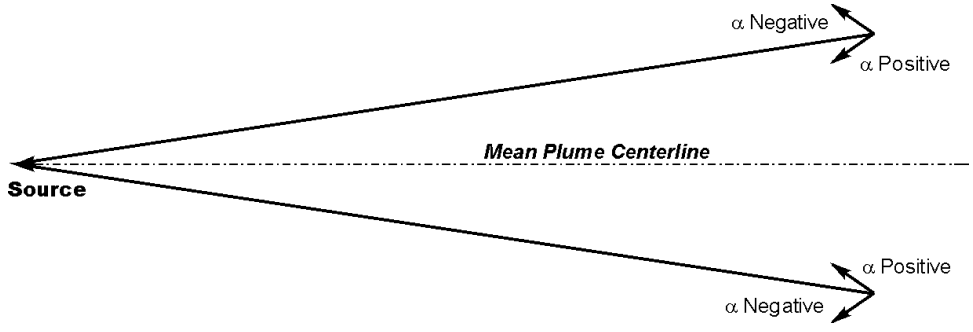

Figure 5.2 Schematic showing the sign convention for the angle α between the source, displacement, and mean concentration gradient vectors.

5.2 Kinematic analysis of successful blue crab searches

Kinematic data from successful crab tracks were extracted from the image sequences based on the position of the two light-emitting diodes (LED's) temporarily attached to the back of the crab. The diode lights were located on each image through the area-search algorithm described in Section 3.4.2. The intensity of the LED's exceeded the capability of the camera CMOS sensors as sensitivity was adjusted to maximize the recorded fluorescence signal. Thus, several pixels generally saturated around each LED on the resulting 3DLIF images. The accuracy of the LED locations could be improved beyond the pixel resolution of approximately 1 mm by assuming a two-dimensional Gaussian distribution of the resulting LED image signal, or improved to sub-pixel accuracy. Since the saturated LED-signal sometimes covered several pixels, any assumed light intensity distribution would be truncated, in this case to a maximum of 1023 (10-bit). Location of the LED's to sub-pixel accuracy could introduce error on the order of the image resolution. Therefore, the location of each LED and consequently the crab was determined to pixel resolution with a maximum error of ±0.5 mm.

Using the light locations, a time record of the crab coordinates and inclination angle with respect to the flow vector was generated. Velocity and acceleration in the streamwise (x-direction) and transverse (y-direction) and angular turning rates were calculated from the time record using a central difference scheme with a time step of 0.21 seconds (i.e., the time delay between consecutive 3DLIF volumes). A typical crab track is shown in Figure 5.3 with a trace of the crab lights. The blue curves are a trace of the path of each LED during the crab's time within the measurement arena. Underlying the curve is

a grayscale image of one 3DLIF volume with the seven lower layers superposed. The crab LED's are visible at the far right of the grayscale image. Only a single instant of the concentration field is shown, hence the field is obviously different when the lights are located at different positions along the path.

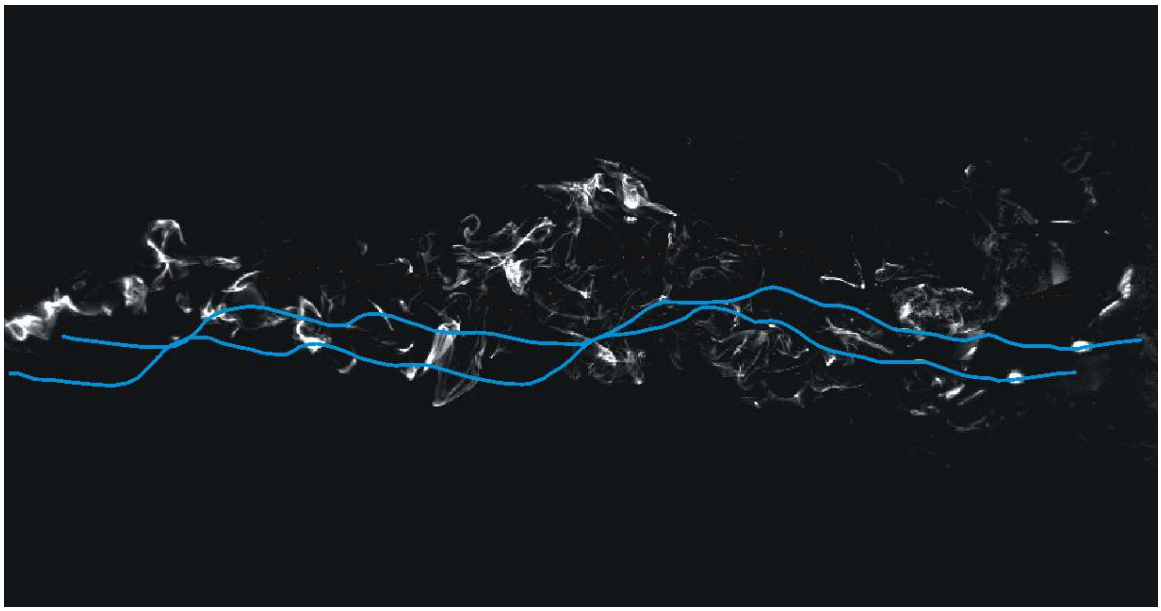

Figure 5.3 Grayscale image of a typical crab track with the light paths shown as blue curves. Reflections off of the crab and the two LED's are visible at the far right. The blue curves trace the center of each LED during the navigation.

Crabs frequently stopped during experimental trials, particularly while tracking the pulsed and meandering plumes. The displacement vector $\mathbf{r}$ is zero for a stationary crab and the resulting dot product of equation 5.2 is also zero. Mathematically, the resulting angle α is a multiple of 90 degrees. Counting a motionless crab as being aligned perpendicularly with a particular vector leads to spurious correlations when lumped with measureable perpendicular displacement vectors. Thus, for periods when crabs remained motionless, the angles between the displacement and other vectors were considered

invalid and were not included in the analysis of the angular distributions. In contrast, the zero-displacement vectors were included in the autocorrelation analysis.

5.2.1 Displacement vector correlations

Figure 5.4 is a schematic of the crab displacement vector broken into transverse and streamwise components. In Figure 5.4, the angle α defines the orientation of the displacement vector with respect to the streamwise direction and is independent of the orientation of the crab body. The vertical coordinate (z) was neglected in the analysis, as adjustments in the height of the crab body were generally small during one time step Δt and could only be resolved in discrete steps of approximately 8 mm. Resolution in the transverse and streamwise directions was on the order of 1 mm.

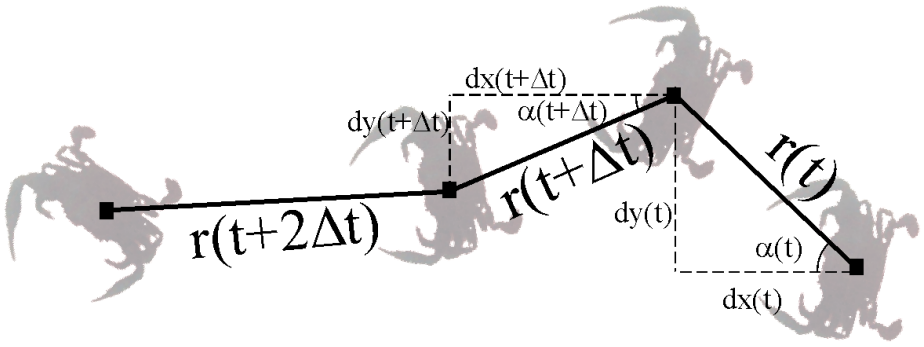

Figure 5.4 Detailed view of the crab displacement vector. Note that the displacement distance and angle α are independent of crab orientation.

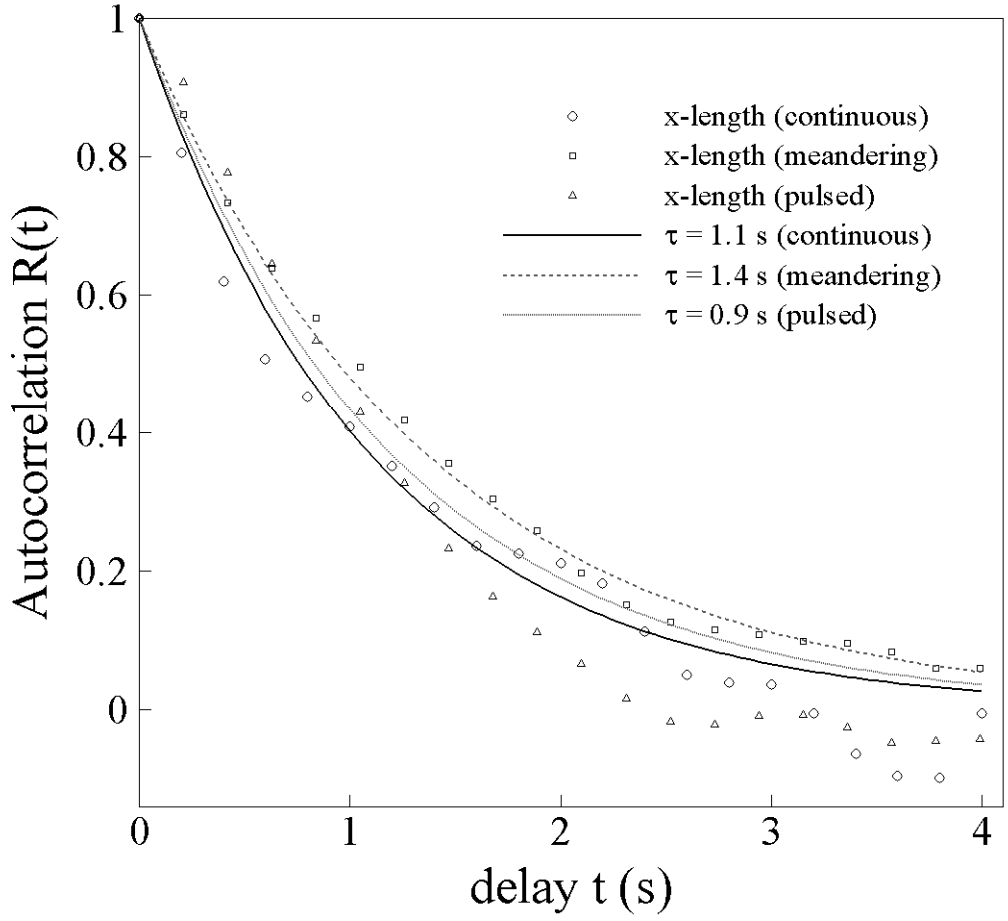

Figure 5.5 Temporal autocorrelation function for crab step length in the x-direction. The time scale τ is found by fitting the data to equation 5.4 while forcing $R(0)=1$. The decay time scale τ was 1.1 s, 1.4 s and 0.9 s for the continuous, meandering and pulsed plumes, respectively.

Figure 5.5 shows the autocorrelation function $R(t)$ of the crab x-displacement data,

$$R(t)=\frac{\left\langle \left(dx(t_0)-\overline{dx}\right)\left(dx(t_0+t)-\overline{dx}\right)\right\rangle}{\left\langle \left(dx-\overline{dx}\right)^2\right\rangle} \tag{5.3}$$

where $dx(t)$ is defined in Figure 5.4 and $\overline{dx}$ is the mean x-displacement value. The autocorrelation function curves shown in Figure 5.5 demonstrate exponential decay with a time scale τ:

$$R(t) = e^{-t/\tau} \tag{5.4}$$

The time scales for each plume type were found by fitting equation 5.4 to the data for delays less than 2 s while forcing $R(0) = 1$. The time scales for the continuous and meandering plumes were 1.1 s (R^2 = 0.97) and 1.4 s (R^2 = 0.99), respectively. Upstream movements remained correlated for longer time periods for crabs tracking the meandering plume relative to the continuous plume. The autocorrelation function for the pulsed plume decays the most rapidly with a time scale of 0.9 s (R^2 = 0.92). Crabs tracking the pulsed plume were much more likely to remain stationary or move away from the source, accounting for the more rapid decay in the upstream displacement autocorrelation function. The autocorrelation function for all plume types decays to near zero within 2 to 3 s.

Figure 5.6 is the autocorrelation function for the y-direction step length calculated using a modified version of equation 5.3 with a zero mean displacement. The streamwise displacement $dx(t)$ has a negative mean value, otherwise the crabs would never reach the source, whereas $\overline{dy}$ calculated from the data is approximately zero. A comparison of Figures 5.5 and 5.6 shows that the streamwise step lengths are more correlated in time than transverse movements. As with the streamwise displacement autocorrelation function, transverse motions remain correlated for longer periods for the meandering case

relative to the pulsed and continuous plumes. The transverse autocorrelation function decays to zero within 1 to 2 s, more rapidly than the streamwise autocorrelation function. Further, the covariance of $dx(t)$ and $dy(t)$ is approximately zero indicating that the transverse and streamwise displacement vectors are uncorrelated.

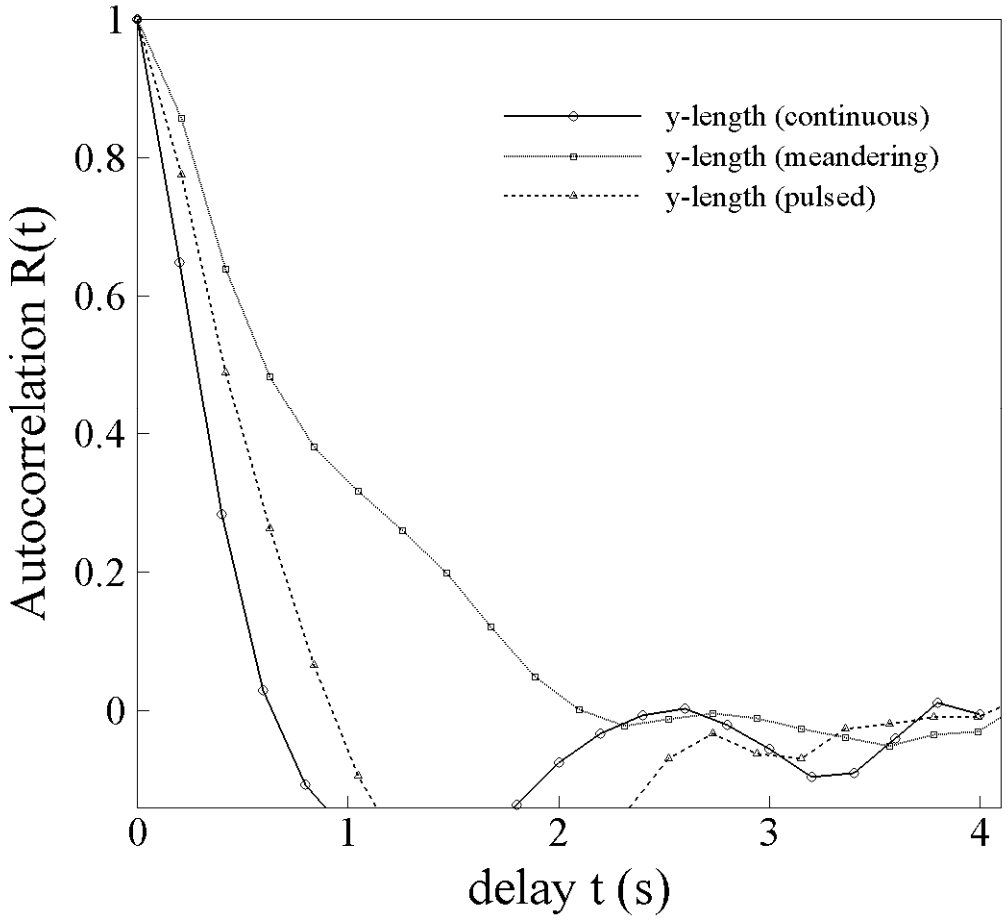

Figure 5.6 Temporal autocorrelation function for crab step length in the *y*-direction. Transverse step lengths lose correlation more rapidly than streamwise step lengths (shown in Figure 5.5), with the exception of the meandering plume where the crabs' transverse movements followed the plume meander.

5.2.2 Displacement vector alignments and distributions

5.2.2.1 Continuous plume

Figure 5.7 shows the distributions of the α angle data for the 22 successful tracks of the continuous plume. Bins of six angular degrees were used to create the histograms shown. The Gaussian fit is a least-squares regression for the angle between the mean flow vector and displacement vector ($-\mathbf{U}\cdot\mathbf{r}$ angle) (the dash-dot line in Figure 5.7) for angles between -90 and 90 degrees. Occurrences of angles outside of the range of -90 to 90 degrees are infrequent. Blue crabs appear to rely strongly upon the flow direction during navigation of the continuous plume (based on the near Gaussian distribution around 0 degrees), although the influence of the chemosensory input may be obscured in Figure 5.7. For the continuous plume, successful blue crabs did not wander far from centerline where the instantaneous plume tended to remain.

Weissburg and Zimmer-Faust (1994) observed angular distributions between the displacement and flow vectors similar to the distribution in Figure 5.7 for their crabs tracking in flow with a mean velocity of 1 cm/s. For a flow velocity closer to that used in this study, 3.8 cm/s, similarity with Figure 5.7 is not apparent although the distance tracked by the crabs was less (0.5 – 1.0 m). Discrepancies could also be attributed to a more dilute attractant used by Weissburg and Zimmer-Faust (1994). Almond moths (*Cadra cautella*) displayed similar angular distributions for continuous pheromone plumes in behavioral experiments by Mafra-Neto and Cardé (1998). Moore et al. (1991) performed behavioral experiments on lobsters in a flume with a relatively low velocity of

1 cm/s. The distributions of heading angles for lobsters tracking a source had a distribution similar to Figure 5.7.

The distributions for the angle between the displacement vector $\mathbf{r}$ and the source $\mathbf{R}$ and flow $-\mathbf{U}$ vectors have a slight skew towards positive angular displacements (see the bump in the distribution from approximately 45 to 90 degrees in Figure 5.7). The skew towards positive angles indicates that crabs preferentially make angular adjustments towards plume centerline, presumably as a result of bilateral comparison. The bimodal peak in the distribution for the angle between the source and displacement vectors around zero degrees is non-Gaussian. Blue crabs making adjustments in alignment with the flow vector results in the negative peak between -12 and -6 degrees. The positive peak at angles between 6 and 12 degrees indicates crab headings towards plume centerline.

When crab displacement vectors lie very close to the plume centerline, a small error in the exact location of the plume centerline could result in a skewed distribution at small angles due to the sign convention used. Despite this conjecture, the small angles between the source and displacement vectors show no tendency to occur in close proximity with the mean plume centerline. Figure 5.8 shows the angle between the source and displacement vectors ($\mathbf{R} \cdot \mathbf{r}$ angle) versus distance from the mean plume centerline for the angles close to zero (i.e., -9 to 0 degrees and 0 to 9 degrees). The tendency of blue crabs to navigate at a slightly askew angle and to navigate to both sides of the source vector is apparent, and the data are apparently independent of the distance from the mean plume centerline. Positive angles less than 2 degrees are infrequent and independent of the transverse coordinate. Small heading adjustments in the direction of the mean flow

vector, resulting in small negative angles between $\mathbf{r}$ and $\mathbf{R}$, suggests that blue crabs possess a remarkable mechanosensory ability.

Figure 5.9 shows a composite of 22 successful crab tracks of the continuous plume superposed on the one-percent intermittency factor field (see Chapter 4 for a definition and more details regarding the intermittency factor). The tracks shown are traces of the center position of the crab as it navigates upstream. The larger heading adjustments tend to occur beyond the contour that indicates an intermittency factor of approximately 0.02. Once within the region where the intermittency factor exceeds approximately 0.06, the crab tracks become nearly straight and begin to converge towards the plume centerline.

The normalized dot products among the displacement vector, source vector and mean concentration gradient vector are shown in Figure 5.10. The displacement vector is predominantly aligned with the source vector, due to limited wandering from the centerline for the continuous plume. The correlation between the mean concentration gradient vector and the displacement vector is nearly uniform, indicating that the vectors $\mathbf{G}$ and $\mathbf{r}$ are uncorrelated. The nearly uniform character of the dot product between the mean concentration gradient vector and the displacement vector corroborates the accepted theory that the mean concentration data are imperceptible to a tracking blue crab (Webster and Weissburg 2001).

The distribution of the dot product between the source vector $\mathbf{R}$ and the mean concentration gradient vector $\mathbf{G}$ is not uniform, with a pronounced peak at approximately 0.15, or at an angle of approximately 80 degrees between the vectors. Spatial limits for positive angles between the mean concentration gradient and the source

vector can be found from equation 5.1(a) and 5.1(b). The mean gradient vector points into the triangular region defined by the source vector and the plume centerline (see Figures 5.1 and 5.2) when the following ratio is satisfied:

$$-\frac{G_y}{G_x} > -\frac{y}{x} \tag{5.5}$$

Substitution of equations 5.1(a) and 5.1(b) into equation 5.5 leads to a limit on the transverse and streamwise coordinates to insure a positive angle between the mean concentration gradient and source vectors:

$$\left|\sqrt{2x^2 + 4\varepsilon/U\,x}\right| > |y| \tag{5.6}$$

From equation 5.6 it becomes clear that the angle between the source and mean gradient vectors remains positive for all but unrealistic values of y within the measurement region. Thus, the mean gradient vector points towards the centerline and could provide information to a searcher about the location of a source provided the mean concentration could be sensed. Despite having directional content, employing the mean concentration gradient vector would be an inefficient means of source location because the mean concentration vector is not well-aligned with the source vector.

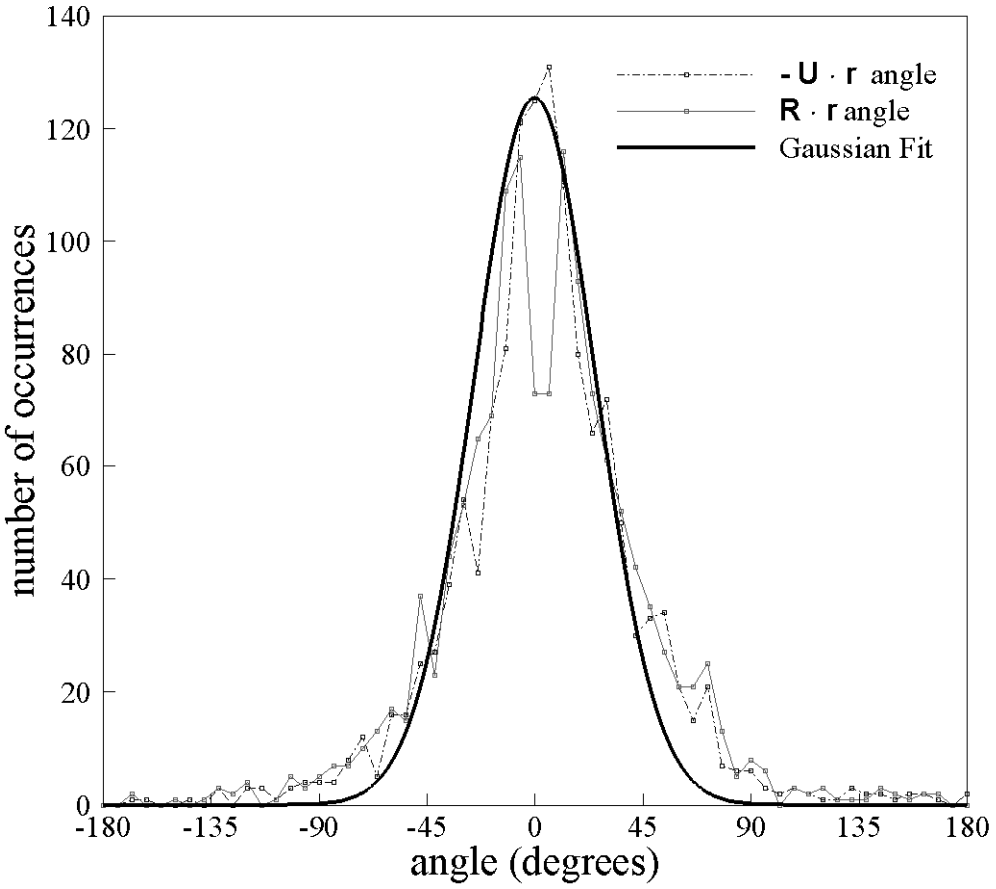

Figure 5.7 Distribution of the angle between the crab displacement vector and the mean flow vector ($-\mathbf{U}\cdot\mathbf{r}$ angle) and source vector ($\mathbf{R}\cdot\mathbf{r}$ angle) for the continuous plume. The Gaussian fit curve corresponds to the mean flow-displacement vector alignment.

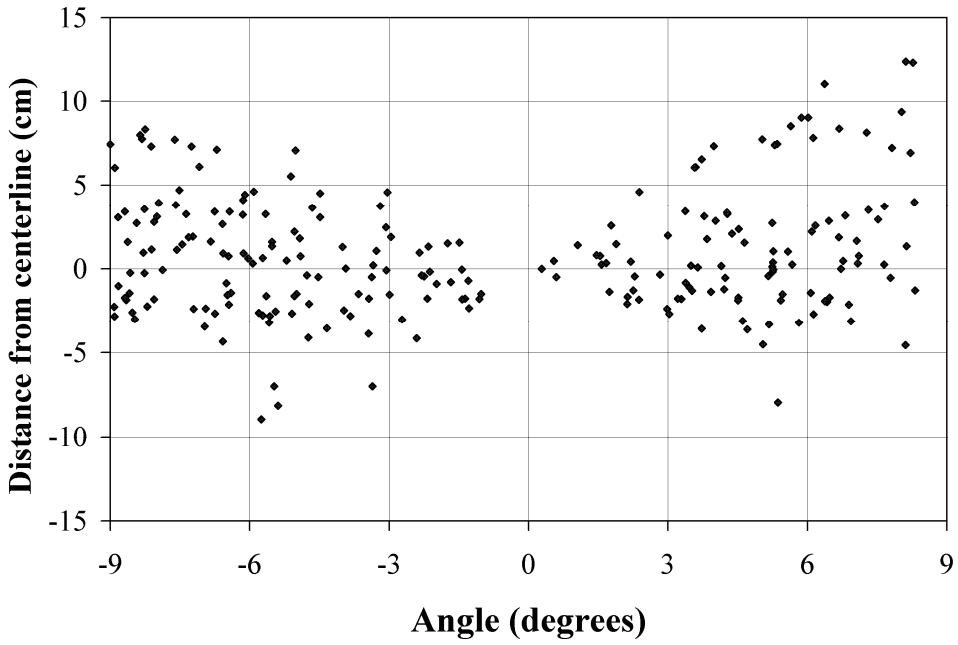

Figure 5.8 Distribution in the transverse direction of small angular deviations between the source and displacement vectors ($\mathbf{R} \cdot \mathbf{r}$ angle) for the continuous plume. Shown are angles between -9 and 9 degrees only. Small navigational corrections are not limited to close proximity to the plume centerline. The skewed distribution towards small negative angles suggests that crabs made small heading adjustments based on the mean flow vector in the continuous plume.

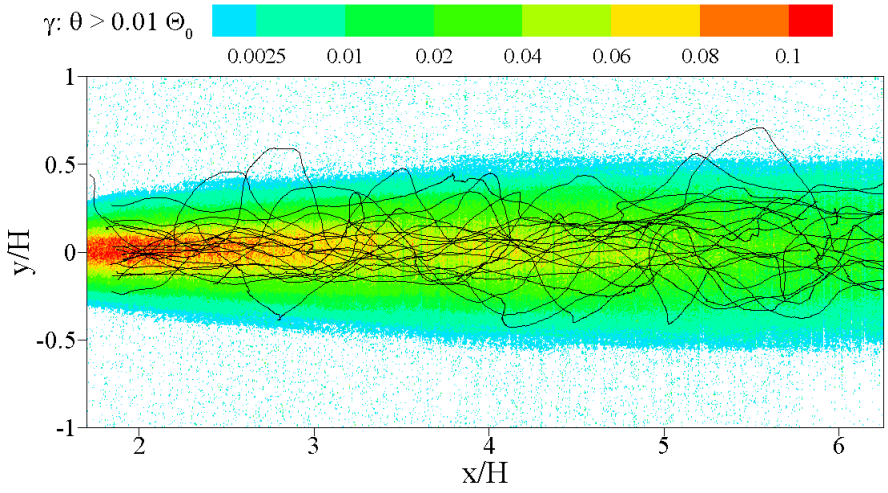

Figure 5.9 Overlay of crab tracks, shown as black, on the intermittency factor field for the continuous plume. The threshold for the intermittency factor was one percent of the source concentration. Crabs casted from side to side, but rarely moved beyond the location of the lowest contour.

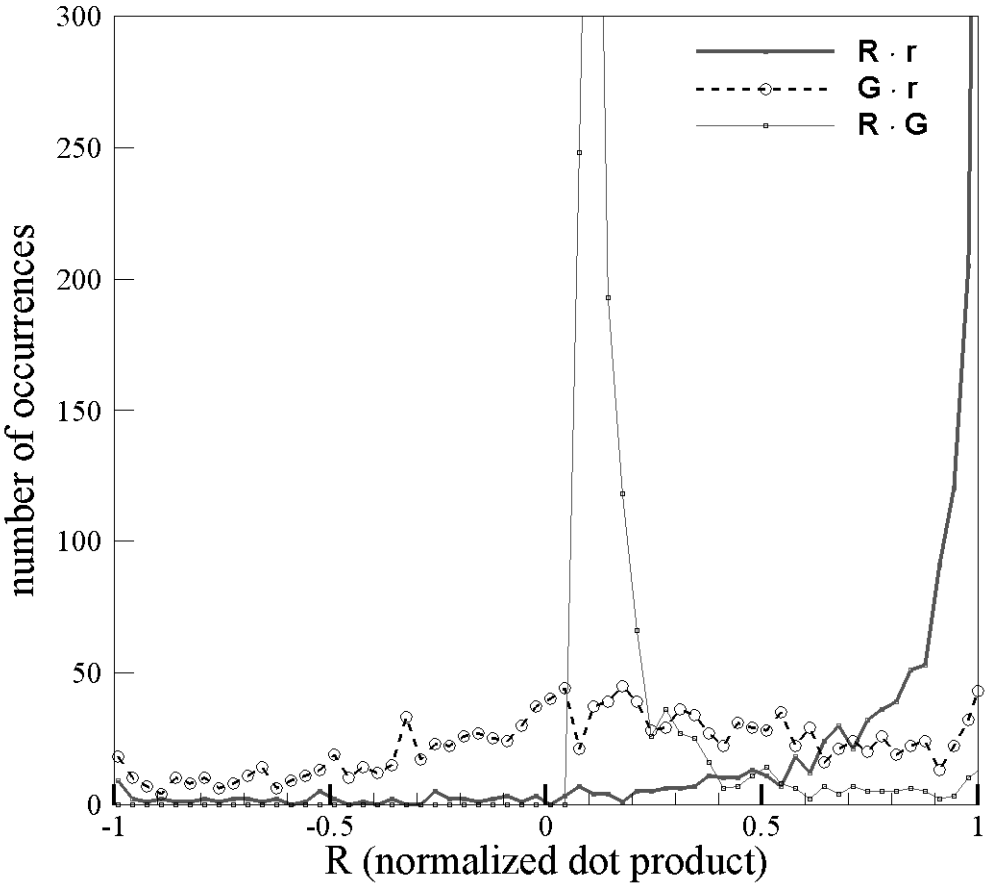

Figure 5.10 Distribution of normalized dot product (Eq. 5.2) between various vectors for the continuous plume. **R** is the source vector, **G** is the mean concentration gradient vector, and **r** is the crab displacement vector. For this plume type, successfully navigating crabs consistently moved toward the source (i.e., the normalized dot product between **R** and **r** is often near one). Although not well-correlated (i.e., the normalized dot product between **R** and **G** peaks near zero), the mean concentration gradient vector did provide a directional, although inefficient, cue towards the source in most circumstances.

5.2.2.2 Meandering plume

Figure 5.11 shows the angle distributions for the 19 successful kinematic tracks for the meandering plume. The number of occurrences is calculated based on bins that are six degrees in width. The Gaussian fit is based on the angle between the mean flow vector

$-\mathbf{U}$ and the displacement vector $\mathbf{r}$ for data between -90 and 90 degrees. The angular distribution is skewed towards positive angles greater than about 45 degrees and has a pronounced peak around zero as with the continuous case (Figure 5.7). The distribution and Gaussian fit are wider than the continuous plume case as crabs were more likely to make large heading adjustments when tracking the meandering plume. Crabs tracking the meandering plume frequently headed downstream, which corresponds to angles with absolute value greater than about 90 degrees. The downstream movements were particularly noticeable on the raw video files. In contrast, downstream movements for crabs tracking the continuous plume were rare.

When making source alignment adjustments greater than about 45 degrees, crabs moving upstream were more likely to turn towards the plume centerline than away. The skew towards positive angles has two possible explanations. First, the crabs could be using a bilateral comparison and preferentially turned at positive angles due to input from chemosensors closer to plume centerline. Second, the skew could be masking a stochastic process similar to Brownian motion whereby turns follow a simple Bernoulli distribution (Chandrasekhar 1943), in which turns to the left or right were equally probable and independent of the chemosensory environment. Successful crab tracks would then necessarily be skewed towards those fortunate enough to choose the correct angular adjustments. Whether the skew towards positive angles shown in figures 5.7 and 5.11 is a statistical artifact or a result of a bilateral comparison cannot be determined from the kinematic data as only successful searchers were included.

The angle between the source and displacement vectors displays a bimodal distribution similar to the continuous case. The absolute value of the angles at the peaks are twice that of the continuous case, suggesting a balance between the flow vector and chemosensory input. Angular adjustments are again skewed when absolute values exceed about 24 degrees. The distribution has a local minimum around zero degrees. The separation between peaks is wider than the continuous distribution as the crabs casted from side to side presumably following the meandering signal. Crabs tracking the meandering plume generally proceeded upstream at angles that were not well-aligned with the source vector.

Figure 5.12 shows the angle between the source and displacement vectors versus distance from the mean plume centerline for data close to zero (i.e., -9 to 0 degrees and 0 to 9 degrees). Crabs made fewer small heading adjustments relative to their counterparts in the continuous plume. The decreased number of points in Figure 5.12 relative to the continuous case, Figure 5.8, indicates a declining effect of rheotaxis in crab navigation upon introduction of a plume meander. Angular adjustments are generally larger as crabs followed an instantaneous plume with a pseudo-sinusoidal shape (see Chapter 4 for physical description of the meandering plume).

Figure 5.13 shows a composite of the 19 successful kinematic crab tracks for the meandering plume superposed on the intermittency factor field. The contour levels for the one-percent intermittency factor are the same as for the continuous case (Figure 5.9) and the intermittency factor data is described in more detail in Chapter 4. The field of intermittency factor is wider than that of the continuous plume, although the values are

lower. As with the continuous plume, the tracks for the most part remain within the boundaries of the intermittency factor field, although significant wander from the plume centerline is evident. Abrupt changes in direction occurred throughout the field in contrast to the tracks for the continuous plume, in which significant track adjustments were generally limited to regions of lower intermittency. Several crabs moved to locations outside of the boundaries of lowest intermittency factor contour shown prior to lateral movements toward the plume centerline. The crab tracks do not converge towards plume centerline at the upstream limit of the measurement region.

The distribution of the normalized dot product between the source vector and displacement vector is shown in Figure 5.14 for the meandering plume crab trials. Crabs tracking the meandering plume were not aligned with the source vector as well as for the continuous plume case. Normalized dot product values of less than an absolute value of approximately 0.8 between the displacement and source vectors occur infrequently and are nearly uniform in distribution. Correlations with the mean concentration gradient vector $\mathbf{G}$ are not shown as the meandering plume does not possess the mean concentration profile given by equation 2.18.

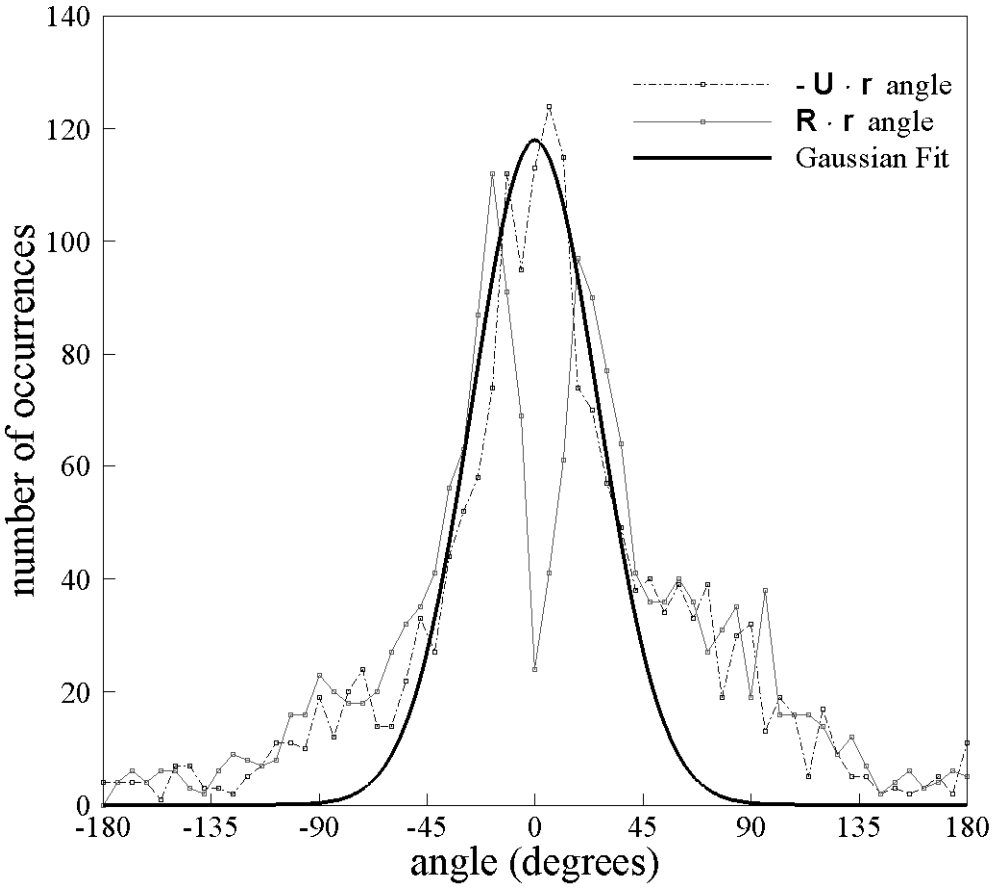

Figure 5.11 Distribution of the angle between the crab displacement vector and the mean flow vector (**-U** ·**r** angle) and source vector (**R** ·**r** angle) for the meandering plume. The Gaussian fit curve corresponds to the mean flow-displacement vector alignment.

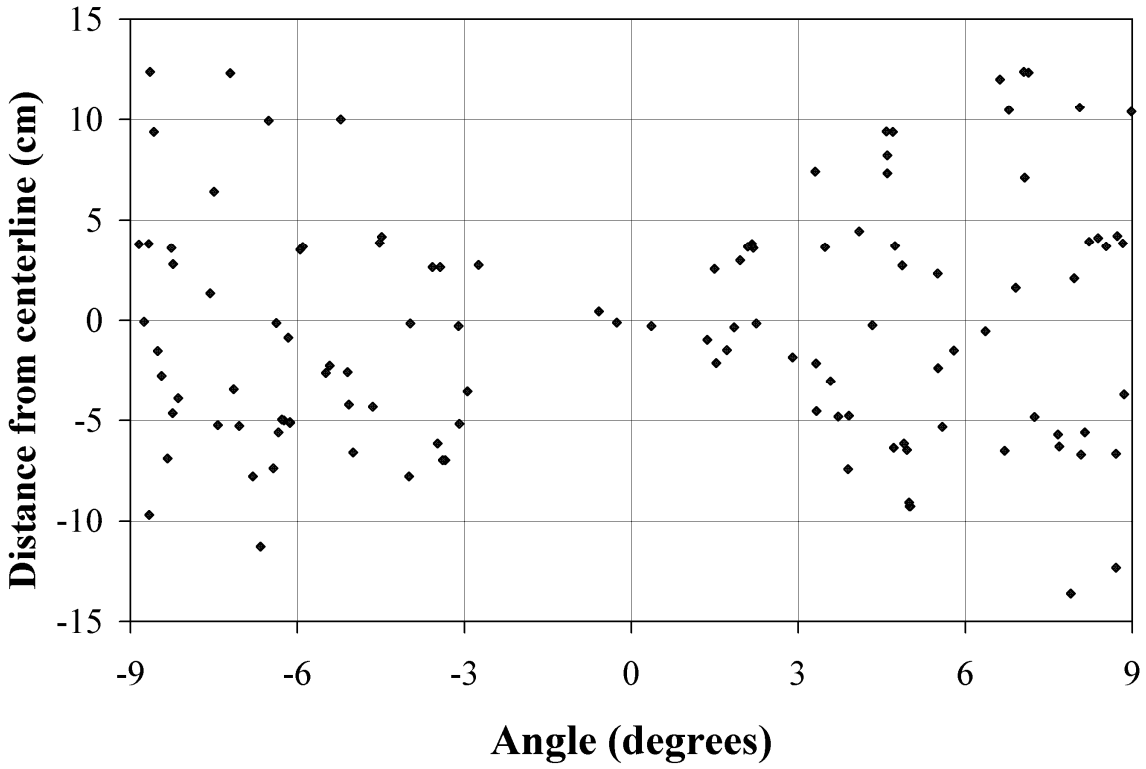

Figure 5.12 Distribution in the transverse direction of small angular deviations between the source and displacement vectors ($\mathbf{R} \cdot \mathbf{r}$ angle) for the meandering plume. Shown are angles between -9 and 9 degrees only. Compared with Figure 5.8 for the continuous plume, crabs tracking the meandering plume made fewer small angular adjustments to their heading.

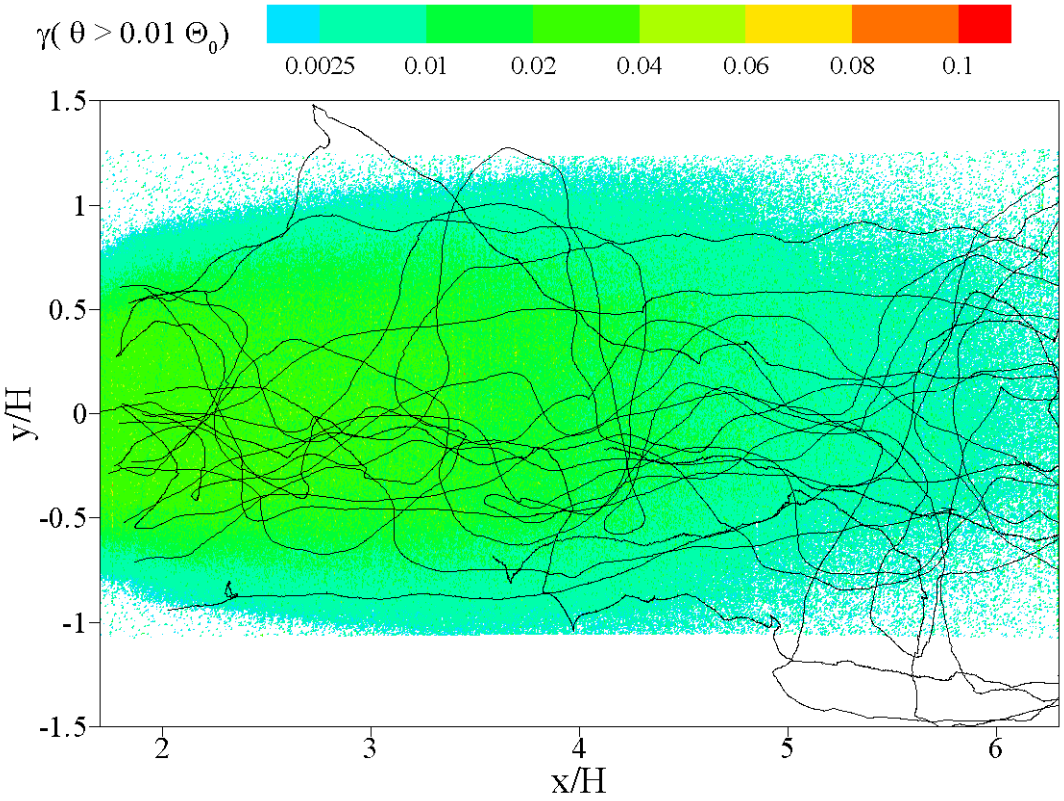

Figure 5.13 Overlay of crab tracks, shown as black, on the intermittency factor field for the meandering plume. The threshold for the intermittency factor was one percent of the source concentration. Crabs casted with greater amplitude than for the continuous case, but generally remained within the boundaries of the lowest contour of the intermittency factor field.

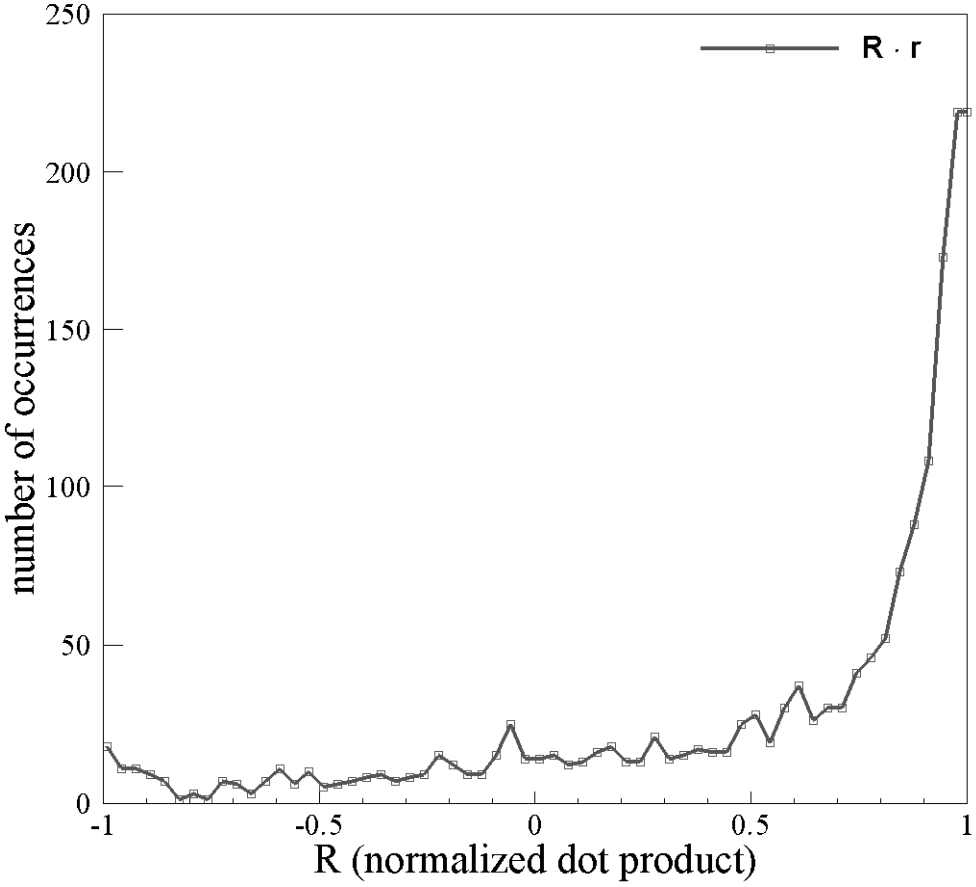

Figure 5.14 Distribution of the normalized dot product (Eq. 5.2) between the source vector **R** and displacement vector **r** for the meandering plume.

5.2.2.3 Pulsed plume

Figure 5.15 shows the angle distributions for the 16 successful kinematic tracks for the pulsed plume. The number of occurrences is calculated based on bins that are six degrees in width. The Gaussian fit is based on the angle between the mean flow vector -**U** and the displacement vector **r** for data between -45 and 45 degrees. As with the meandering and continuous cases, the angular distribution for the mean flow and displacement vectors is skewed towards larger positive angles (greater than about 45 degrees) and has a pronounced peak around zero. The distribution follows the Gaussian fit for angles

between -45 and 45 degrees fairly well. When crabs were headed downstream, movements were much more likely to be towards the plume centerline (angles between 90 and 180 degrees) than away (angles between -180 and -90 degrees). Crabs exhibited a similar tactic response for the meandering plume. As noted in the previous section on the meandering plume, the skew towards positive angles could be explained by bilateral comparison or simple Brownian-type motion.

The distribution of the angles between the source vector **R** and the displacement vector **r** is similar in shape to that of the displacement and mean flow vectors except for angles close to zero. A skew towards negative values occurs for angles less than an absolute value of 90 degrees and is most evident at angles between -18 and 18 degrees. Crabs tracking the pulsed plume moved perpendicular or directly away (angles less than -90 or greater than 90 degrees) from the source more frequently than the other two release types. In the pulsed plume, crabs passed through a sequence of odorant clouds as they navigated upstream. Upon moving through a cloud, crabs frequently stopped or reversed direction briefly following the cloud downstream. Downstream displacement vectors generally included a transverse component pointing towards plume centerline. The increased frequency of downstream movements relative to the other two plume types leads to the higher frequency of angular adjustments greater than an absolute value of 90 degrees. As in the meandering case, the increased proclivity towards downstream motion in the pulsed plume was evident in the raw video files.

Figure 5.16 shows the transverse distribution of small angular adjustments between -9 and 9 degrees. The distribution looks similar to that of the continuous plume (Figure

5.8), although the number of small angular adjustments is reduced from 284 in the continuous case for 22 crabs to 157 for the pulsed plume for 16 crabs. While tracking within a passing cloud, the pulsed and continuous plumes are similar, which is reflected in the distribution of small angular adjustments. Plume intermittency leads to a reduction in the number of small angular adjustments and a higher frequency of movements away from plume centerline or the source.

Figure 5.17 shows a composite of the 16 successful kinematic crab tracks for the pulsed plume superposed on the one-percent intermittency factor field. The contour levels for the intermittency factor are the same as for the continuous case (Figure 5.9) and the intermittency factor data is described in more detail in Chapter 4. The field of intermittency factor defined by a threshold of one percent of the source concentration is similar to that of the continuous plume, although the values are lower due to large-scale temporal intermittency resulting from the passing clouds. Unlike the continuous plume, the tracks wander beyond the boundaries of the intermittency factor field shown. Abrupt changes in direction occur throughout the field. Several crabs moved to locations outside of the boundaries of lowest intermittency factor contour shown and remained there for a significant portion of the track. The tracks do not converge toward the plume centerline, with 4 of the 19 tracks remaining outside the intermittency factor field at the upstream boundary of the measurement region.

The distribution of the normalized dot product between the source vector and displacement vector is shown in Figure 5.18 for the pulsed plume crab trials. The displacement vector is predominantly aligned with the source vector as observed in the

continuous plume case. Normalized dot product values of less than an absolute value of approximately 0.9 between the displacement and source vectors occur infrequently and are nearly uniform in distribution. The mean concentration gradient vector **G** was assumed to follow the form of equations 5.1(a) and 5.1(b) as the mean transverse profiles appear to follow a Gaussian form (see Chapter 4). The displacement and mean concentration gradient vectors are not correlated, with a nearly constant distribution. As with the continuous plume, the mean concentration gradient is nearly perpendicular to the displacement vector about 95 percent of the time. As with the continuous plume case, the mean concentration gradient vector could be used to locate a source, though such a tracking mechanism would require extremely long sampling periods to resolve the mean concentration field and require a calibration to relate the local mean concentration gradient vector to the source vector.

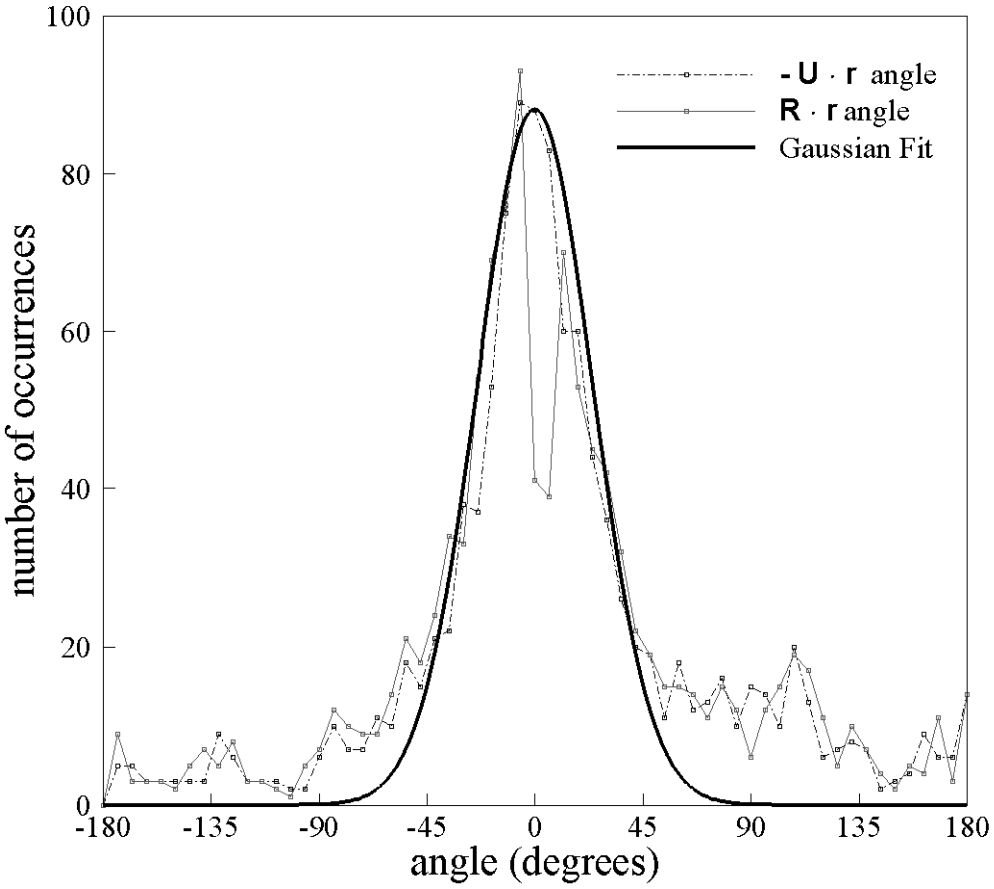

Figure 5.15 Distribution of the angle between the crab displacement vector and the mean flow vector ($-\mathbf{U}\cdot\mathbf{r}$ angle) and source vector ($\mathbf{R}\cdot\mathbf{r}$ angle) for the pulsed plume. The Gaussian fit corresponds to the mean flow-displacement vector alignment for angles between -45 and 45 degrees.

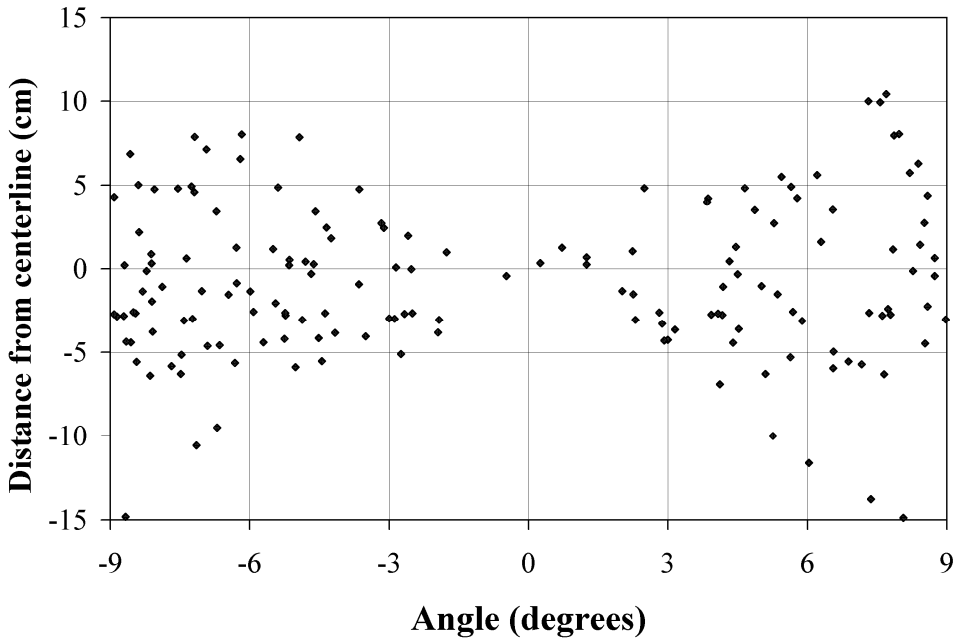

Figure 5.16 Distribution in the transverse direction of small angular deviations between the source and displacement vectors (**R** · **r** angle) for the pulsed plume. Shown are angles between -9 and 9 degrees only.

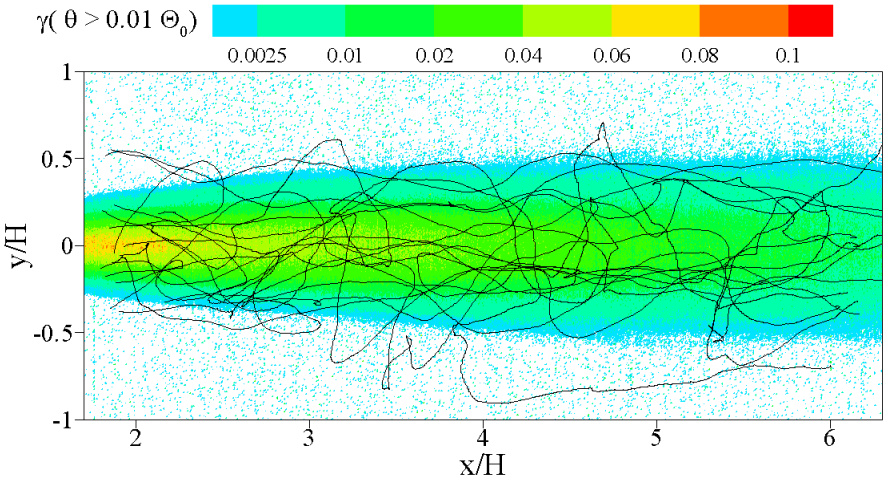

Figure 5.17 Overlay of crab tracks, shown as black, on the intermittency factor field for the pulsed plume. The threshold for the intermittency factor was one percent of the source concentration. Crab movements do not converge towards the center of the intermittency field, which differs from the tracks in the continuous plume.

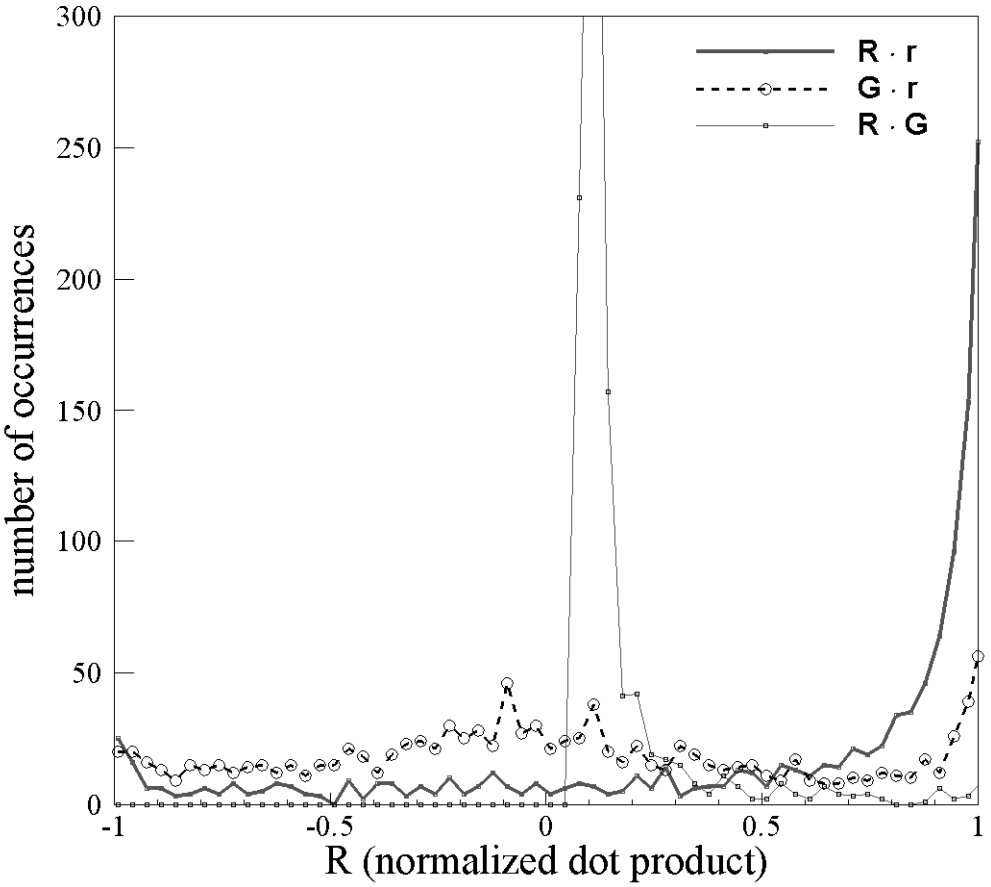

Figure 5.18 Distribution of normalized dot product (Eq. 5.2) between various vectors for the pulsed plume. **R** is the source vector, **G** is the mean concentration gradient vector, and **r** is the crab displacement vector. For this plume type, successfully navigating crabs consistently moved toward the source (i.e., the normalized dot product between **R** and **r** is often near one). The mean concentration gradient vector and source vector are relatively oriented at nearly 90 degrees (i.e., the normalized dot product between **R** and **G** peaks near zero) as with the continuous plume.

5.2.3 Stochastic nature of blue crab navigation

The exponential decay of the autocorrelation functions shown in figures 5.5 and 5.6 indicates that crabs follow a tracking strategy that could be modeled by an Ornstein-Uhlenbeck (OU) process (Pope 2003, Visser 2008). OU processes can be modeled through the Langevin equation:

$$\mathbf{x}(t+\Delta t) = \mathbf{a}(\mathbf{x}(t),t) + \mathbf{B}(\mathbf{x}(t),t)\, d\mathbf{w}(t) \tag{5.7}$$

where $d\mathbf{w}(t)$ is a vector-valued Weiner process. The drift coefficient is constant and equal to the mean distance traveled during the time step Δt,

$$\mathbf{a}(\mathbf{x}(t),t) = \overline{d\mathbf{x}} \tag{5.8}$$

and the diffusion tensor equals the co-variance of the distance travelled,

$$\mathbf{B}_{ij}(\mathbf{x}(t),t) = \left\langle \left(d\mathbf{x}_i - \overline{d\mathbf{x}_i}\right)\left(d\mathbf{x}_j - \overline{d\mathbf{x}_j}\right)\right\rangle^{1/2} \tag{5.9}$$

The mean displacement vector $\overline{d\mathbf{x}}$ for the crab trials only has a streamwise component, i.e. the average upstream displacement in the 3DLIF time interval. Further, the transverse and streamwise displacements are uncorrelated for the three plume types, and therefore the diffusion tensor is diagonal and reduces to a Cartesian vector:

$$\mathbf{B}_{ij}(\mathbf{x}(t),t) = \mathbf{b}(\mathbf{x}(t),t) = \left\langle \left(dx - \overline{dx}\right)^2 \right\rangle^{1/2} \mathbf{i} + \left\langle (dy)^2 \right\rangle^{1/2} \mathbf{j} \tag{5.10}$$

for two-dimensional crab displacements assumed independent of spatial location.

Simplified simulations of blue crab tracking for the continuous plume were performed using the Langevin equation (equation 5.7). A random number generator provided input which was converted to a normal variate for $d\mathbf{w}(t)$. The resulting simulations and experimental tracks overlaying the intermittency factor field are shown in Figure 5.19. The experimental data are a set of 22 successful crab tracks of the continuous plume superposed on the intermittency factor field (i.e., identical to Figure 5.9).

Tracking success for the OU simulations was approximately 32 percent when starting 1.5 m downstream of the source. The transverse starting coordinate at $x = 150$ cm was placed randomly using a normal distribution based upon the total displacement vector length $|\mathbf{r}|$ and varied from 2 to 5 cm. A successful track was declared when the simulation came within 4 cm (y/H =0.19) of the source at $x = 0$. Success of the simulation was less than the 40 and 65 percent reported by Jackson et al. (2007) for behavior trials performed under similar flow and substrate conditions with low and high odorant concentration, respectively. The simulations are not as smooth as the actual crab navigational tracks because the time step Δt of 0.21 s is of the order of the autocorrelation time scale τ of 1.1 s. Behavioral tracks begin to converge towards plume centerline at the upstream edge of the measurement arena whereas the simulations show no such trend. The constant diffusion coefficient in the transverse direction, equation 5.8, precludes convergence of the form shown by the behavioral trials as the source is approached. Reducing the time step and spatial resolution of the data collection system and developing a transverse diffusion coefficient that depends on distance from the source would likely improve the simulation performance. However, a tracker in a continuous plume would find a spatially-dependent transverse diffusion coefficient of limited use as the distance to the source is unknown.

Despite the clear exponential decay of the correlation of streamwise and transverse crab movements shown in figures 5.5 and 5.6, the decreased navigational success of the simulations versus actual tracking behavior indicate crabs do not strictly follow an OU process. The larger track adjustments during crab navigation (see bottom of Figure 5.19) tended to occur at the fringes of the one-percent intermittency factor field and were

associated with burst of odorant concentration or periods where the crab lied beyond the instantaneous plume. Away from the larger track adjustments, crabs generally proceeded upstream for several seconds while maintaining a consistent bearing. Thus, crabs appear to follow a tracking mechanism, where filament contact induces upstream movement and casting initiates upon encountering a signal contrast. For a stochastic process to model a surge-casting behavior, equation 5.7 would require coupling the random arrival of odorant bursts with concentration-dependent drift and diffusion terms.

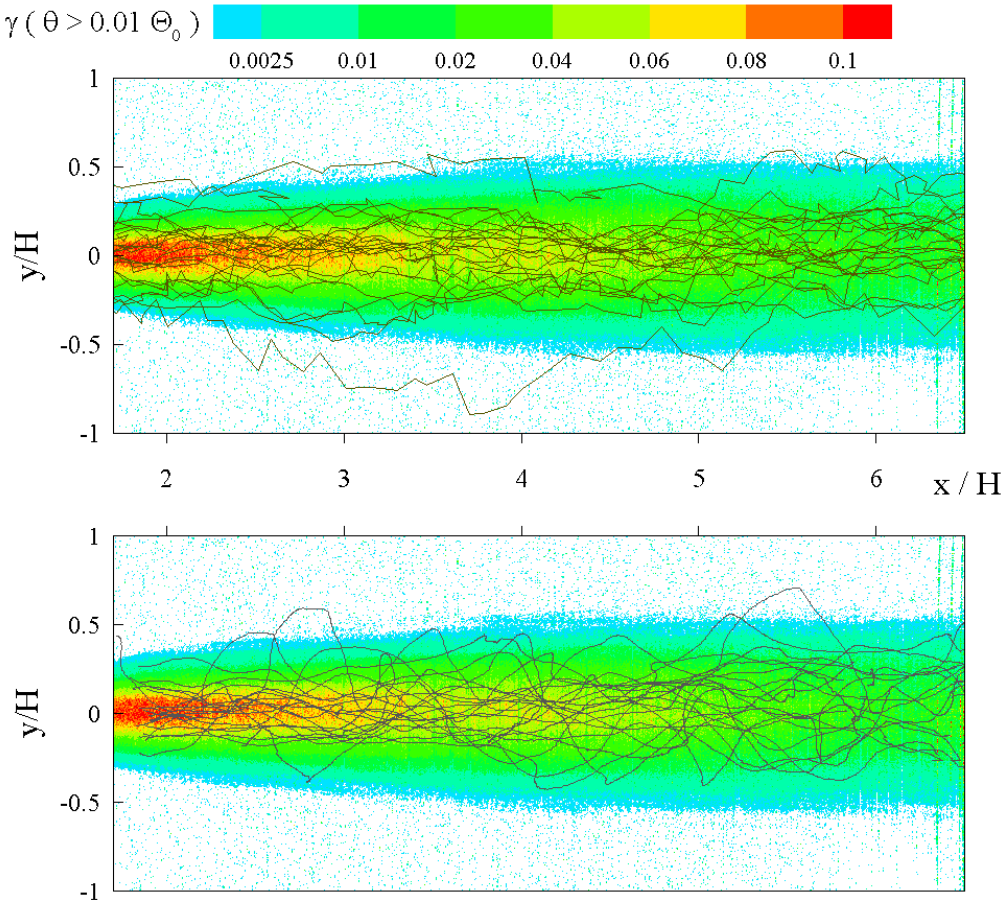

Figure 5.19 Overlay of simulated crab tracks (top) and experimental crab tracks (bottom) on the field of intermittency factor defined by a threshold of one percent of the source concentration for the continuous plume.

5.3 Extraction of concentration data for successful blue crab searches

Keller et al. (2003) developed the hypothesis that blue crabs rely on cephalic chemosensors, the antennules, to mediate upstream speed and to remain within the odorant plume. Further, the outer chemosensors, primarily on the legs, provide steering guidance through signal contrast across the body. Movement is towards the stimulated chemosensor, ostensibly in the plume centerline direction (Weissburg and Dusenbery 2002). 3DLIF data taken for this study focused on obtaining concentration data around the antennules region close to the mouth and the outer chemosensors in general.

For the time traces shown in the figures, the time axis does not always start at zero. Recording of the concentration and kinematic data started after the crab exited the temporary holding tank located 1.5 m downstream of the source (see Chapter 3 for experimental setup details). The amount of time between crab release and entering the measurement region varied, resulting in the different starting times shown in the traces.

The sampling procedures and accompanying experimental challenges are described in the following subsections.

5.3.1 Antennules zones

The elevation of the antennules generally varied as a crab moved upstream through lifting or lowering its body. For each 3DLIF set, the elevation of the antennules was estimated through visual inspection of the recorded frames. Each block of images corresponding to the 20 LIF elevations was manually examined, and the image containing reflections from the mouth region was identified to determine the height of the antennules during that period.

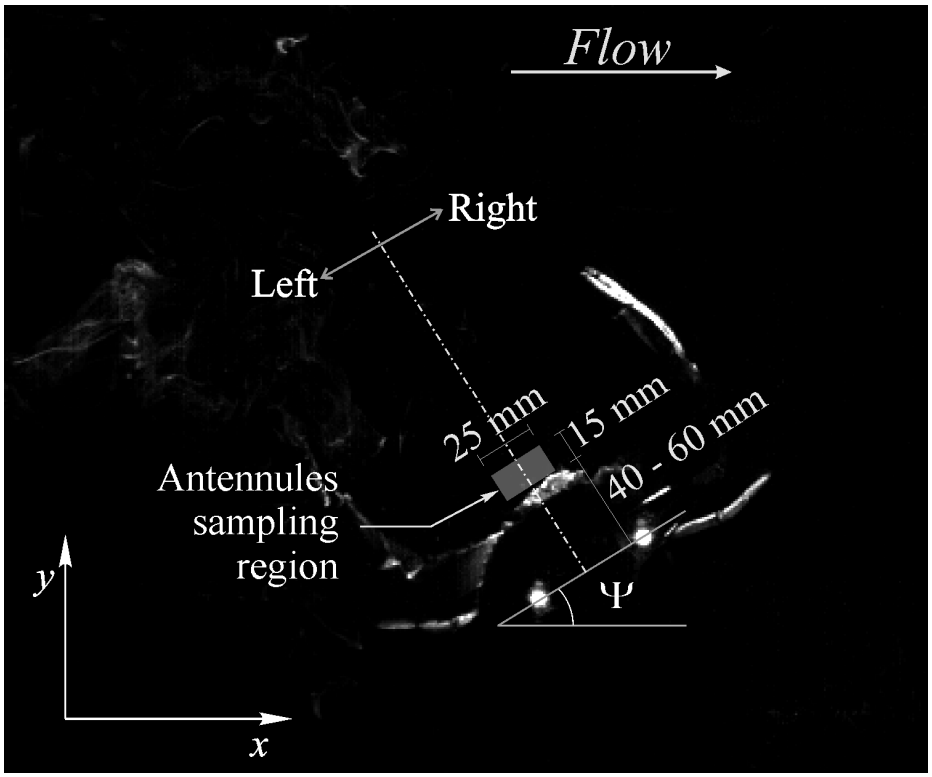

Figure 5.20 Location of the sampling zone for the crab antennules region. Reflected laser light from the right claw can be seen in the upper right region of the image. Similarly, reflected light from the left claw (although dimmer) is seen in the lower left region of the image. The two bright dots in the lower right region of the image are the light-emitting diodes (LED's) used to quantify the crab position. Light reflecting from the carapace and mouth parts is observed in the space between the bright dots and antennules sampling region. Ψ is the crab orientation angle with respect to the x-axis (and mean flow direction). The sampling box is 25 mm by 15 mm oriented at the angle Ψ.

The region used to extract chemosensory data near the antennules was located in the identified plane by projecting a line a given distance from the center of the two LED's at the current angle of the crab (see Figure 5.20). The distance of the projection varied from 40 to 60 mm, depending on the size of the crab. The distance from the center of the diode lights to the mouth region was adjusted by trial-and-error until the measurement region fell sufficiently far from the mouth to avoid false positives from reflections yet

close enough to not miss potential concentration bursts. A sampling region 25 mm by 15 mm and aligned with the crab carapace was placed to determine odorant concentrations at the region of the antennules. The size of the sampling region was chosen to cover the potential reach of the antennules and to include concentration filaments that could advect past the region between sampling periods, approximately 0.21 s. The sampling volume included more than a single plane at the level of the antennules as the exact elevation of the mouthparts was not precise. The analysis included concentration data within the sampling region at three elevations: at the identified level of the antennules, one 3DLIF level above, and one below. The resulting sampling volume for the antennules was approximately 25 mm by 15 mm by 16 mm in the vertical direction. The sampling volume is discontinuous vertically, with only about 3 mm of the 16 mm illuminated by the laser. Data extracted from the region are the maximum concentration and the non-zero average value, which solely accounts for samples greater than zero concentration.

5.3.1.1 Continuous Plume Tracks

Two example traces of crab kinematics and concentrations within the antennules sampling region are shown in figures 5.21 and 5.22 for the continuous plume. The upper plot (a) shows time records of the non-zero average and maximum concentration and the approximate elevation of the antennules. The concentration values, maximum and non-zero average, have been normalized to the source concentration C_0. The lower plot (b) shows time records, with the same time axis as (a), of streamwise and transverse walking velocities and crab orientation angle.

The crab shown in Figure 5.21 (label 116O) frequently adjusted its height in the boundary layer but without a discernible trend. Upstream crab speed varied from zero to

12 cm/s with two short periods with little movement (shown in red). Transverse velocities varied between -5 and 5 cm/s, indicating a low-amplitude casting behavior. A several second time sequence of low concentrations occurred prior to the beginning of movement to the left (shown in green). The crab intercepted an odorant burst during transverse motion, shown in blue, and resumed upstream motion at a relatively high velocity. The concentration burst sequence eventually ended and the crab decelerated to zero upstream velocity. One interesting aspect of the track is the general decrease in the angle Ψ as the crab approached the source. Decreasing orientation angle with upstream progress enabled the crab to span the instantaneous plume throughout the track. As the source is approached, plume width decreases and smaller orientation angles have the dual benefit of decreasing hydrodynamic drag (Weissburg et al. 2003) while still allowing the organism body to span the instantaneous plume width.

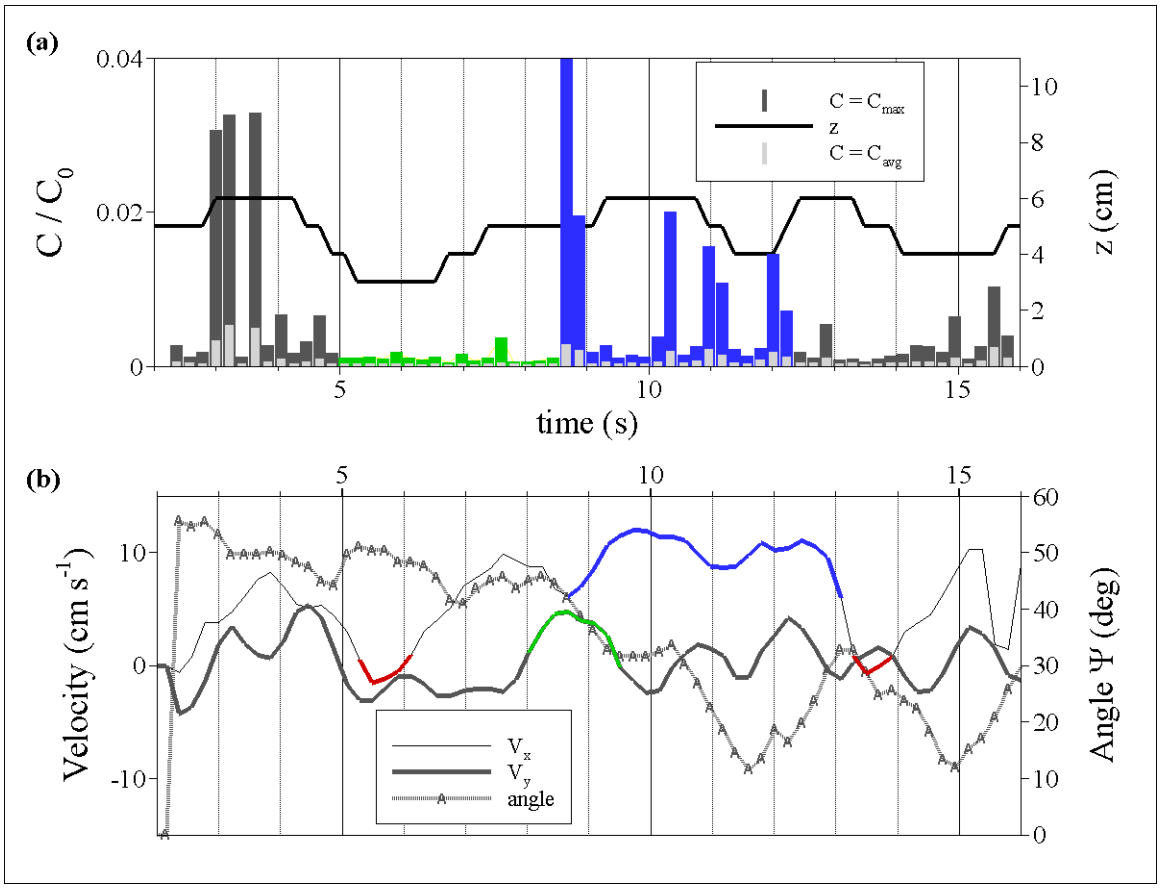

Figure 5.21 Extracted time traces for crab **116O** in the continuous plume. (a) Concentration and elevation data. (b) Streamwise and transverse walking velocities and crab orientation angle data. C_{max} is defined as the maximum concentration present in the sampling box, and C_{avg} is defined as the average of the non-zero values of concentration in the sampling box. Two brief periods with downstream velocity are shown in red. The sequence of low concentrations highlighted with green initiated a casting movement, also green. The crab subsequently received a series of odorant bursts and the upstream walking velocity increased (shown as blue).

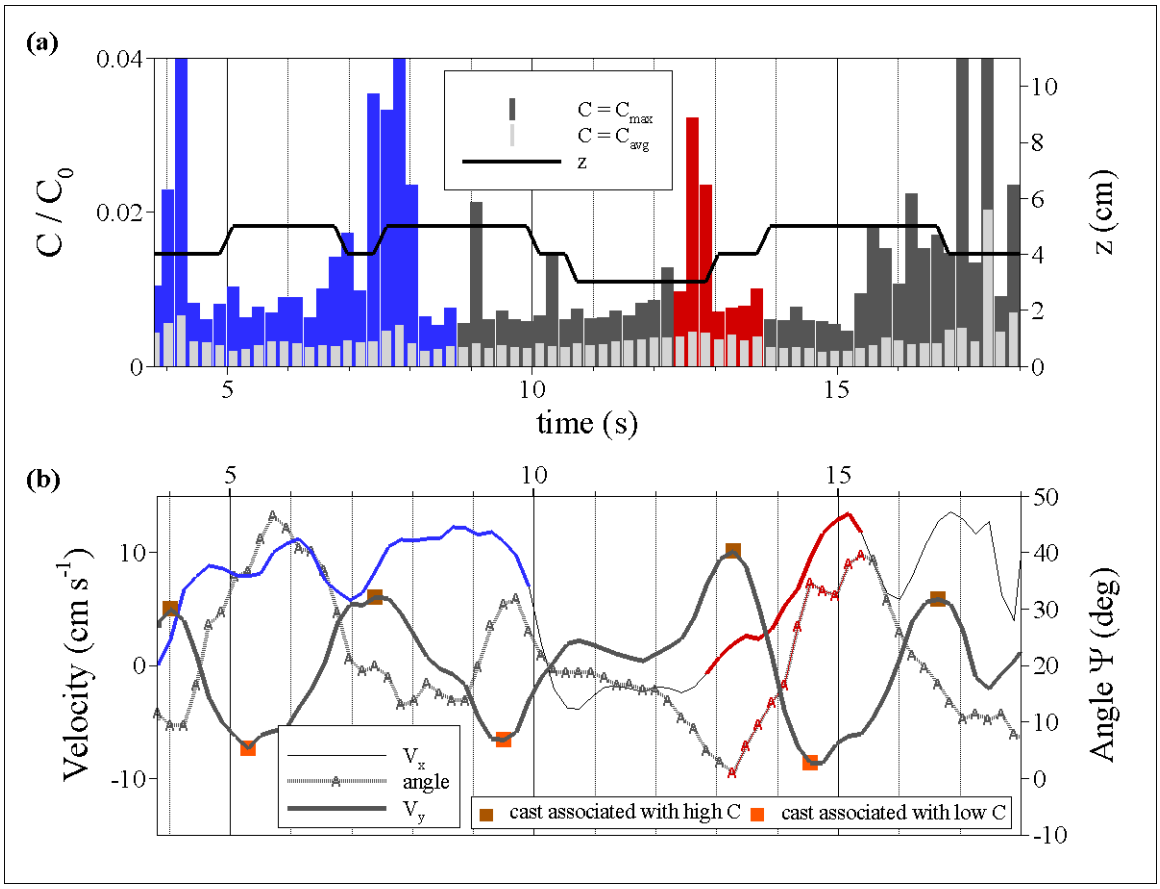

Figure 5.22 Extracted time traces for crab **1352Q** in the continuous plume. (a) Concentration and elevation data. (b) Streamwise and transverse walking velocities and crab orientation angle data. Initially, a high concentration signal arrived at the antennules and the upstream walking velocity was large, shown in blue. Subsequent lower concentration signals resulted in reduced streamwise walking velocity until transverse movement intercepted an odorant burst, shown as red. Subsequent streamwise walking velocity increased along with an increase in the crab orientation angle (shown in red). Peaks in transverse velocity seem correlated with concentration bursts or periods of low concentrations, shown as orange and brown squares.

Figure 5.22 is a track for the crab labeled 1352Q. Relative to crab 116O in Figure 5.21, 1352Q intercepted higher concentration bursts and stayed slightly lower in the boundary layer. Crab 1352Q also casted from side to side with a larger amplitude. Initially, a train of concentration bursts shown in blue occurred coincident with rapid upstream movement. Peak transverse velocities corresponded to either a low or high

concentrations shown as orange and brown squares, respectively. The crab received the concentration burst, shown in red, during one cast after a period of approximately 2 s with zero or negative upstream velocity. After the concentration burst, the crab accelerated in the upstream direction while increasing the orientation angle Ψ. Unlike the crab in Figure 5.21, no apparent trend can be seen in the evolution of the angle Ψ.

Time traces for the other 13 crab tracks with extracted antennules information for the continuous plume are included in Appendix A.

5.3.1.2 Meandering Plume Tracks

The meandering crab tracks differed from those of the continuous case primarily in the magnitude of transverse motions and the amount of time spent stationary. A comparison of the tracks overlaid on the intermittency factor field, Figures 5.9 and 5.13, highlights the navigational differences between the two plume types. A crab intercepting a packet of high odorant concentration in the meandering plume could be located at the point of maximum meander amplitude. Initiating upstream movement would supposedly bring the crab closer to the source, yet in that case would result in entering a zone of low concentration. The distribution shown in Figure 5.15 shows the meandering plume structure often led crabs to stop or even move downstream, presumably chasing odorant packets. The crab body angles Ψ were higher and varied more, perhaps in attempts at increasing the spatial integration factor (SIF) defined in Chapter 2. A higher SIF would lead to an increased probability of at least one sensor receiving an odorant burst. The orientation of the crab movements also appeared to rely less on the flow vector than the continuous case. The wider distribution of the angles between the displacement vector and the mean velocity vector in Figure 5.11 for the meandering plume versus Figure 5.7

for the continuous plume indicates that movements in the meandering plume were less aligned with the flow vector.

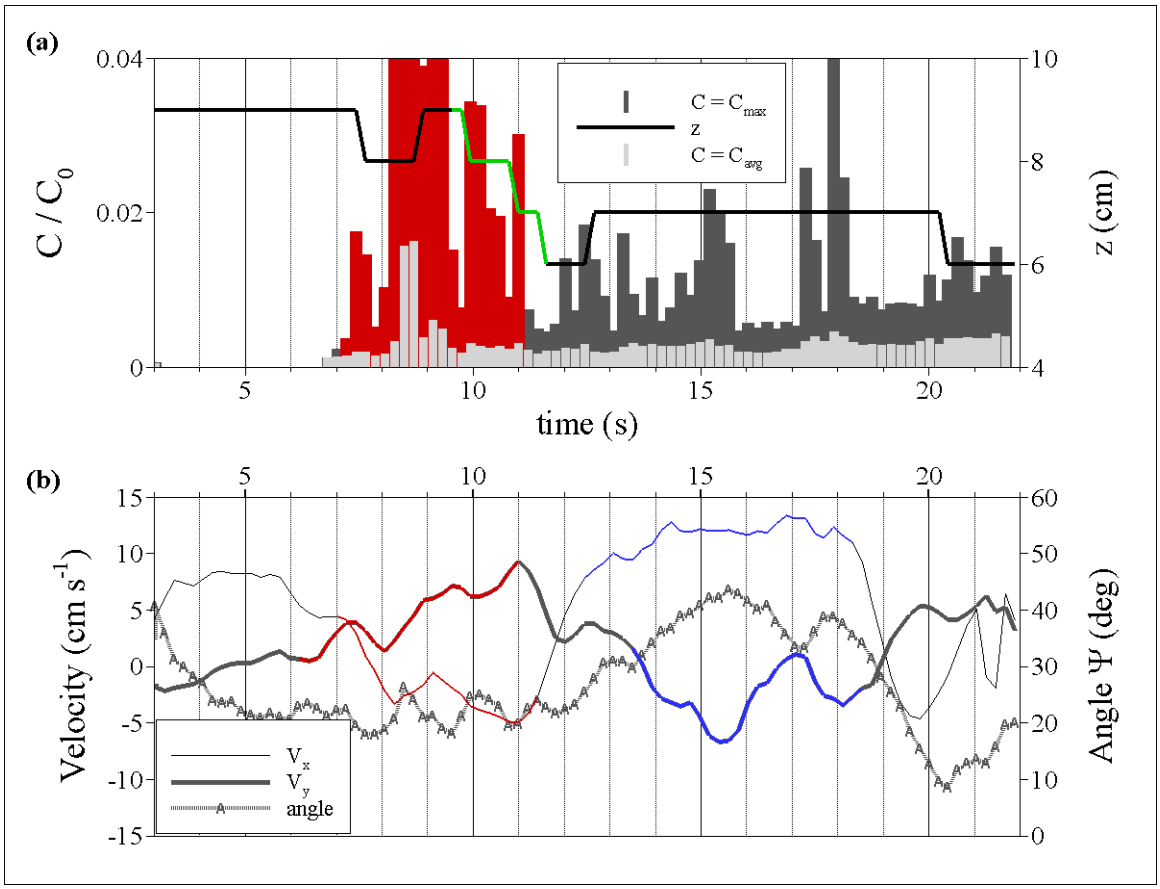

Figure 5.23 Extracted time traces for crab **1286Q** in the meandering plume. (a) Concentration and elevation data. (b) Streamwise and transverse walking velocities and crab orientation angle data. High concentration bursts, shown in red, occurred after the crab moved transversely (also shown in red in (b)). The interception of the high concentration bursts resulted in a lowering of the crab body by about 2.5 cm (shown in green). The crab moved rapidly upstream after the transverse and vertical adjustments (shown in blue) while making transverse adjustments in the opposite direction of those shown in red. The crab's body orientation angle remained between 20 and 30 degrees throughout most of the track.

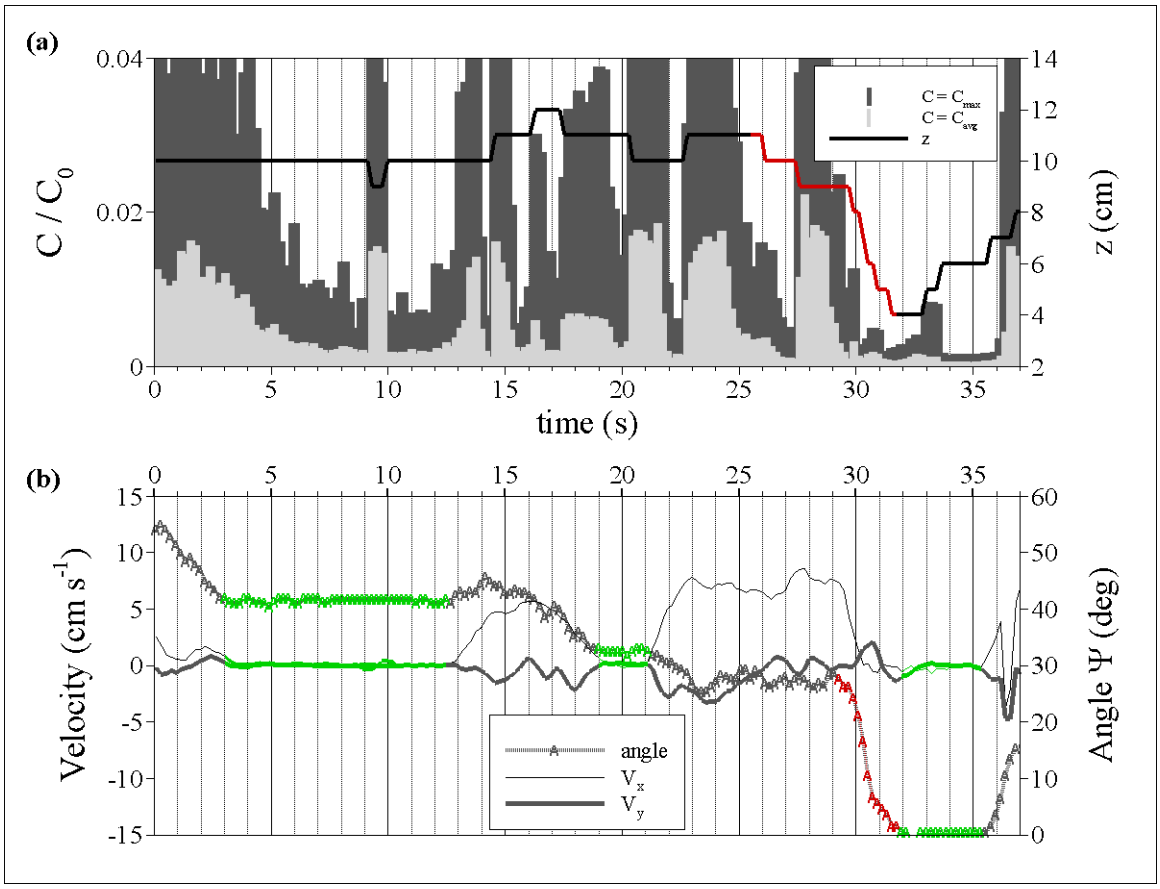

Figure 5.24 Extracted time traces for crab **1317S** in the meandering plume. (a) Concentration and elevation data. (b) Streamwise and transverse walking velocities and crab orientation angle data. The crab remained stationary for prolonged periods during the track, shown in green. At approximately 25 s, the crab made a major adjustment in the boundary layer by lowering nearly 8 cm (shown in red). The crab orientation angle also decreased during the vertical adjustment.

Figure 5.23 shows a time trace for crab 1286Q. Up to $t = 7$ s, the crab received no odorant signal at the antennules yet maintained a modest upstream velocity. High concentration bursts were intercepted for $t > 7$ s as the crab moved transversely. The crab eventually chased an odorant packet in the downstream direction for several seconds, as shown in red. During this period of time, the crab also lowered itself in the boundary layer, shown in green. At $t = 12$ s the crab accelerated upstream and

maintained a relatively high x-velocity while casting in the negative y-direction. No general trend in the evolution of the orientation angle Ψ is apparent.

Figure 5.24 shows a time trace of crab 1317S, which received numerous high intensity odorant bursts at the antennules. Crab 1317S displayed counterintuitive behavior by remaining stationary for periods of 2 to 10 s independent of strong odorant signals passing the antennules region. The track also extended for a long period, with the crab remaining in the measurement arena for 37 s. The crab behavior was consistent with other observations of reducing its body angle Ψ, and consequent SIF, as the source was approached. Shown in red is a period during which the crab made adjustments to its alignment to the flow and height within the boundary layer. The lowest and highest points in the boundary layer differed significantly, by approximately 8 cm. The crab decelerated to zero streamwise velocity during the adjustments and began lifting itself during a stationary period from t = 30 to 35 s.

Time traces for the other 12 crab tracks with extracted antennules information for the meandering plume are included in Appendix C.

5.3.1.3 Pulsed Plume Tracks

Successful crab tracks for the pulsed plume generally displayed periods of latency where the crab remained stationary after passing through a cloud of odorant. Velocities in the downstream direction away from the source occurred at many instances where the crab chased a particular odorant cloud downstream for a short period. Crab time traces are characterized by latency intervals lasting several seconds followed by upstream acceleration. The crab angle Ψ and casting behavior are similar to those found in the

continuous plume case. Vertical movement is less than in both the continuous and meandering cases.

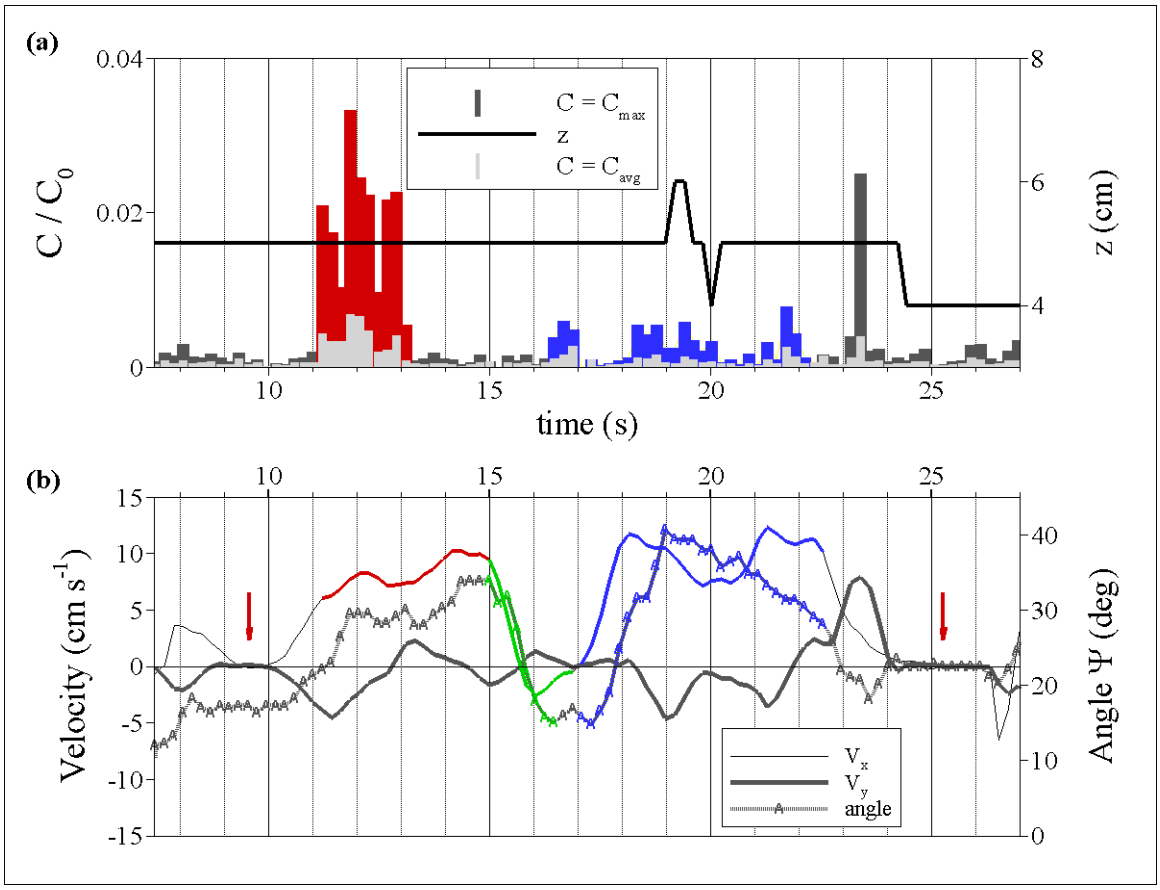

Figure 5.25 Extracted time traces for crab **1201M** in the pulsed plume. (a) Concentration and elevation data. (b) Streamwise and transverse walking velocities and crab orientation angle data. Periods of latency are noted with red arrows. The crab accelerated upstream after receiving a burst of odorant (shown in red) following a latency period. After passing through the odorant cloud, the crab decelerated and rotated and even headed downstream for about 1 s (shown in green). The concentration bursts shown in blue correspond to a second period of acceleration and body rotation.

Figure 5.25 shows time traces for crab 1201M tracking the pulsed plume. After the first latency period (red arrow), the crab received a burst of odorant at approximately 11 s, which was followed by upstream movement (shown in red). After passing through the odorant cloud, the crab decelerated and actually moved downstream for approximately 1

s (shown in green). During deceleration, the crab altered its body orientation. A train of low-intensity odorant bursts, shown in blue, corresponded to upstream acceleration and movement of the crab body perhaps to aid in bilateral comparison. After the low-intensity odorant cloud passed, the crab decelerated and remained latent for several seconds, as noted by the second red arrow. The high concentration burst at approximately 23 s did not elicit a response and could be a false signal.

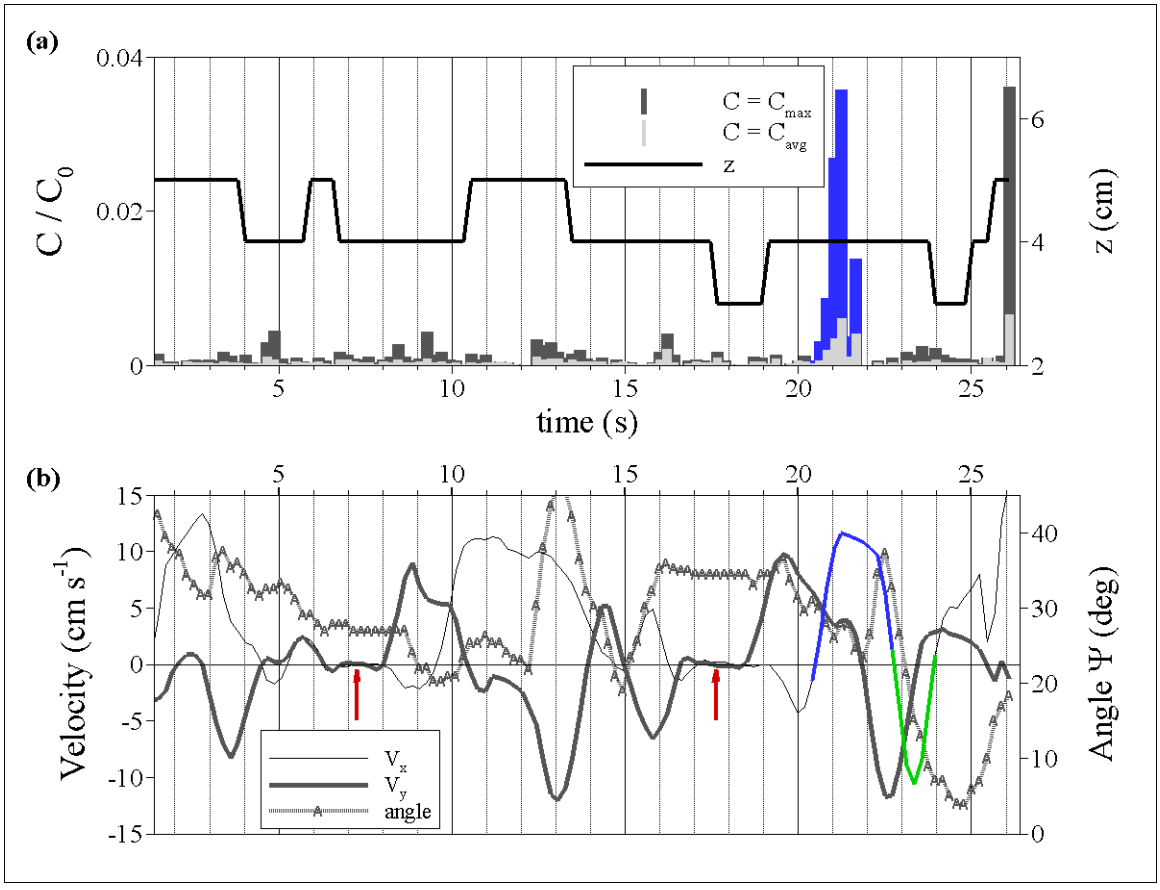

Figure 5.26 Extracted time traces for crab **1358M** in the pulsed plume. (a) Concentration and elevation data. (b) Streamwise and transverse walking velocities and crab orientation angle data. Periods of latency are noted with red arrows. The crab accelerated upstream after receiving a burst of odorant (shown in blue) following a brief period of downstream movement. After passing through the odorant cloud, the crab decelerated and rotated, heading rapidly downstream for about 1 s (shown in green).

Figure 5.26 is a time trace for crab 1358M tracking the pulsed plume. The red arrows indicate two latency periods. Between the red arrows, the crab casted transversely and moved upstream while measurable concentrations in the antennules zone remained rather low. The largest odorant burst occurred at approximately 20 s and corresponded to an upstream acceleration, both shown in blue. Concentrations abruptly fell to zero and the crab reversed direction, chasing the odorant packet downstream (shown in green). Elevation of the antennules region remained approximately constant throughout the track. The crab made frequent adjustments to its angular orientation, although no trends are discernible.

Time traces for the other 10 crab tracks with extracted antennules information for the pulsed plume are included in Appendix E.

The traces shown in figures 5.21 through 5.26 illustrate several important features of crab tracking behavior. Crabs tend to stop or reverse direction when losing contact with an odorant plume or cloud. After short latency periods with no movement, they either cast in one direction or resume upstream. Moths behave similarly, initiating casting behavior after a short latency period (Vickers 2000), although stopping is not available to a tracking moth. In contrast to moths, figures 5.21 to 5.26 show transverse casting to be a characteristic of crab tracking whether located in plume gaps or not. The behavior may be an attempt at increasing the intermittency of the odorant signal or to reduce adaptation of chemosensors to what would normally be a perceptible burst of odorant (Vickers 2000). Correlating upstream movement with odorant bursts at the antennules is not straightforward, perhaps complicated by input from outer chemosensors. Odorant bursts

tend to induce upstream movement, but this is by no means a rule as Figure 5.24 demonstrates. Crabs also constantly shifted their orientation with respect to the flow vector. The adjustments could originate in two sometimes contrary mechanisms, drag reduction and an increasing ability to span the instantaneous plume. Thus, no discernible trend becomes apparent in crab orientation.

5.3.2 Outer chemosensors

The deafferentation experiments of Keller et al. (2003) indicated that chemosensory organs on the legs affect transverse adjustments and enable the tracking crab to sense the outer boundary of the odorant plume. A left-right contrast, where one chemosensor lies outside the instantaneous plume, could permit detection of the plume edge and guide a turn (Webster et al. 2001, Weissburg et al. 2002). The classical picture of contrast across the distal (left-right) chemosensors of a tracking crustacean was not realized in many trials as the general blue crab orientation with respect to the flow vector, and consequently the odorant plume, was at an acute angle ($|\Psi| < 30$ degrees). In many cases the left legs were located directly upstream of the right legs, thereby corrupting any useful bilateral (left-to-right) comparison. Signal structure passing over the left legs and body also became more homogeneous before arriving at the chemosensors on the right legs. When the orientation angle is small, the exact function of the outer chemosensors becomes ambiguous and a strict bilateral comparison across the body would yield a spurious indicator for potential turning.

A further complication is determining the precise location of the outer chemosensors. Shadows cast by the legs and claws obscured the plume structure close to the legs in many instances. As with the antennules region, light reflected from the crab body and

appendages could not be clearly distinguished from the intense fluorescence of high concentration filaments. The legs could not be located with any accuracy either where illuminated by the laser light or within a shadow. Therefore, light reflection and shadows prevented the direct analysis of instantaneous odorant concentration at the legs. In place of direct measurement, an estimate of the chemical signal reaching the crab could be determined by looking at the structure of the approaching plume. A sampling region projected in front of the crab and moved upstream the equivalent distance of advection by the mean flow velocity was used to infer odorant stimulus received by the tracking crab during the 3DLIF sampling time. The box was shifted sufficiently in time and space to prevent false signals within the box from crab appendages, especially the claws. The box size in the streamwise direction was determined by dividing the relative velocity of the crab by the 3DLIF frequency (approximately 4.8 Hz). For example, a crab traveling 5 cm/s, a relative velocity of 10 cm/s with respect to the mean flow, would have a streamwise box dimension of approximately 2.1 cm (i.e., 10 cm/s / 4.8 Hz). The box dimension in the transverse direction varied with crab orientation angle Ψ. Figure 5.27 shows an example of box placement and relative position in time.

A simple means of quantifying the contrast is to compare transverse locations of the crab and a concentration centroid calculated for the sampling box shifted upstream. Using discrete data, the concentration centroid is defined at a given spatial location (see Figure 5.28) as:

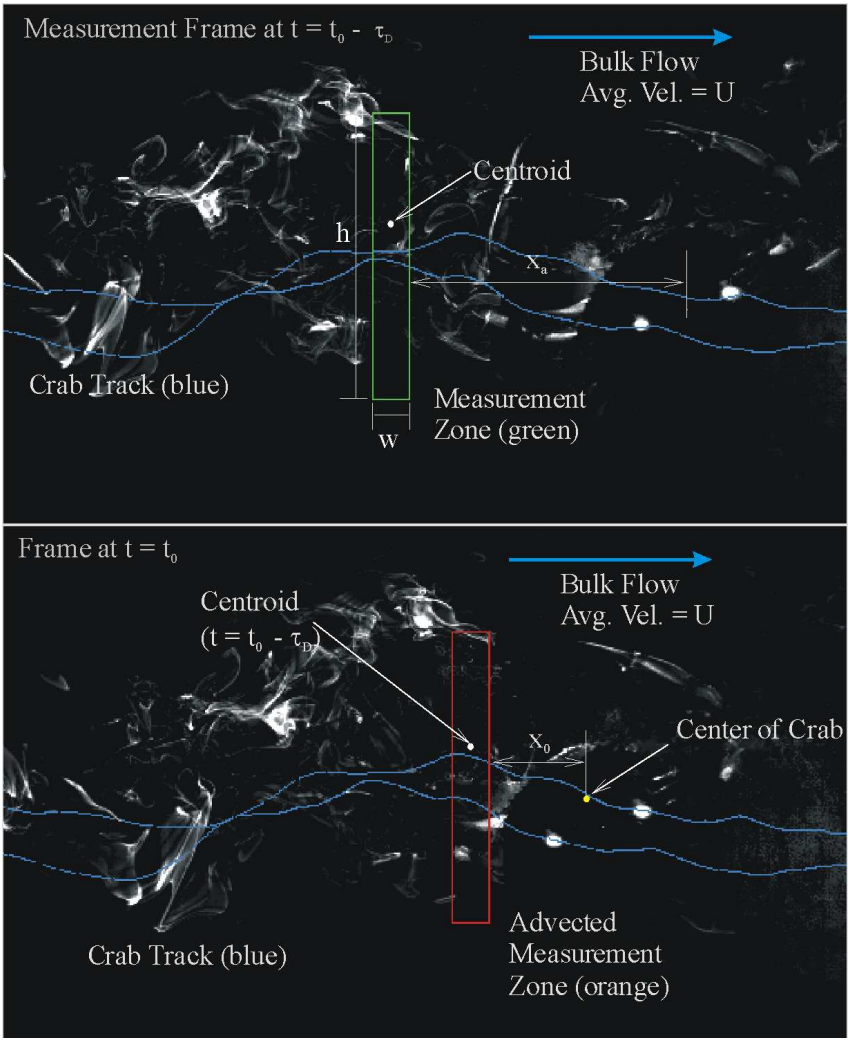

Figure 5.27 The location of the sampling zone for evaluating the signal at the walking appendage chemosensors. Due to shadowing concerns, concentration data are extracted at an earlier upstream location (green box in upper panel) and assumed to be advected to the chemosensory location (orange box in lower panel). Note that the bright spots in the lower portion of the orange measurement zone are crab legs and claws, which demonstrates the challenge of extracting accurate concentration data near the crab body. The sampling region position is initially located a distance X_0 upstream of the crab center position, which corresponds to the upstream position of the crab body (shown in lower image). To evaluate the sampling region location at an earlier time ($t_o - \tau_D$), the sampling region is shifted upstream by the advection distance $U\tau_D$. Hence, the distance from the crab center to the sampling zone, X_a, equals $U\tau_D + X_0 + \Delta X_{crab}$ (shown in upper image). The streamwise width of the sampling region, w, is determined by the advection distance $U\Delta t$ and the distance that the crab travels Δx between measurement samples, such that all chemosensory structure encountered by the crab between samples ($\Delta t \approx 0.21$ s) is included. The time delay (τ_D) shown corresponds to approximately 1 s.

$$h(x_0, y_0, t) = \frac{\sum_{x_0 - w/2}^{x_0 + w/2} \sum_{y_0 - H_B/2}^{y_0 + H_B/2} y\tilde{\theta}(x, y, t)}{w \sum_{x_0 - w/2}^{x_0 + w/2} \sum_{y_0 - H_B/2}^{y_0 + H_B/2} \tilde{\theta}(x, y, t)} \tag{5.11}$$

A concentration centroid location that deviates by more than a set distance from the crab center would suggest a transverse bias in the signal and presumably that movement in the bias direction would be advantageous. Similarly, if the center of the crab coincided with the concentration centroid, then upstream movement without change in direction would be suggested. Hence, a broad indicator of navigational turning could be extracted by comparing the relative locations of the centroid of the concentration signal versus the crab position.

Based on experimental limitations of the sampling procedure and the assumed sampling ability of blue crabs, a difference of more than 0.5 cm in the transverse direction between the centroid location of the concentration distribution in the sampling box and the crab center position was taken as an indicator for transverse contrast. Thus, if the centroid calculated for the earlier upstream sampling box deviated by more than 0.5 cm in either direction from the center of the crab at the later time, the signal provided bias to one side (either left or right) and presumably a turning cue.

Time lags τ_D for the crab trials varied from 0.6 to 1.4 s. Time lags were determined for each individual crab track by trial-and-error, where the box had to be advected upstream and backward in time sufficiently to avoid false positives or shadowing effects of crab appendages. The time lags were dependent primarily upon the sweeping behavior of each crab's claws and secondarily upon crab size. Relative to the continuous plume, time

lags were slightly higher for the pulsed and meandering plumes as crabs tended to sweep their claws more for those plume types.

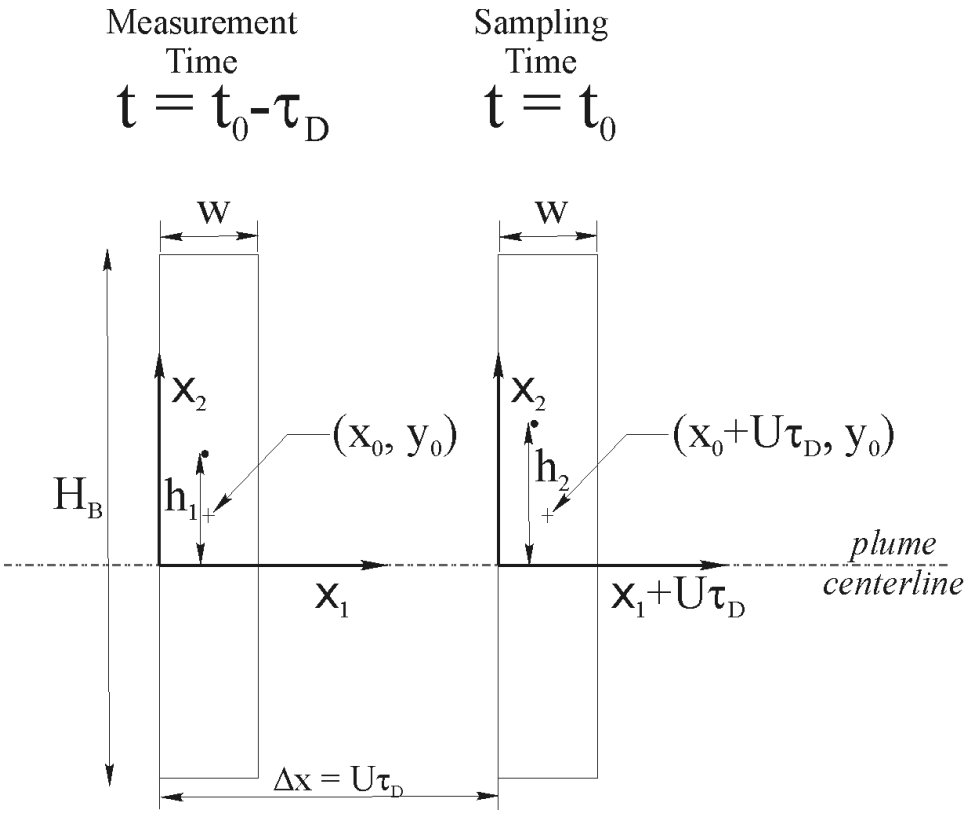

Figure 5.28 Definition sketch for the analysis of concentration centroid evolution. h_1 and h_2 are the concentration centroids within the sampling volumes at the measurement $(t_0 - \tau_D)$ and sampling (t_0) times, respectively. The depth of the sampling volume is along the x_3 axis, which projects into and out of the paper and is not shown.

5.3.2.1 Validity of the Measurement Technique

To be meaningful, the bias calculated at the earlier time for the upstream shifted sampling box must remain unchanged over the delay time τ_D. The probability of the bias calculated at the earlier time changing over the time period τ_D varies with spatial location. Figure 5.29 shows several representative sampling box locations overlaid upon

the mean concentration field at nozzle centerline for the three plume types using data taken without crabs present. The box sizes and locations are typical of the crab trials.

Table 5.2 Conditions Necessary for a Change in Bias ($\Delta\mathbf{BIAS} = 1$)

Upstream Time-Delayed Centroid	Downstream Centroid
$h_1 > 0.5\,\text{cm}$	$0.5\,\text{cm} > h_2$
$0.5\,\text{cm} > h_1 > -0.5\,\text{cm}$	$h_2 > 0.5\,\text{cm}$ or $-0.5\,\text{cm} > h_2$
$-0.5\,\text{cm} > h_1$	$h_2 > -0.5\,\text{cm}$

The probability of the bias changing over a given time delay τ_D for the four representative boxes is shown in figures 5.30 and 5.31 using plume data taken without tracking crabs present. The probability was calculated by dividing the number of occurrences with no bias change ($\Delta\mathbf{BIAS} = 0$) by the number of ensembles. Table 5.2 summarizes the conditions necessary for a bias change.

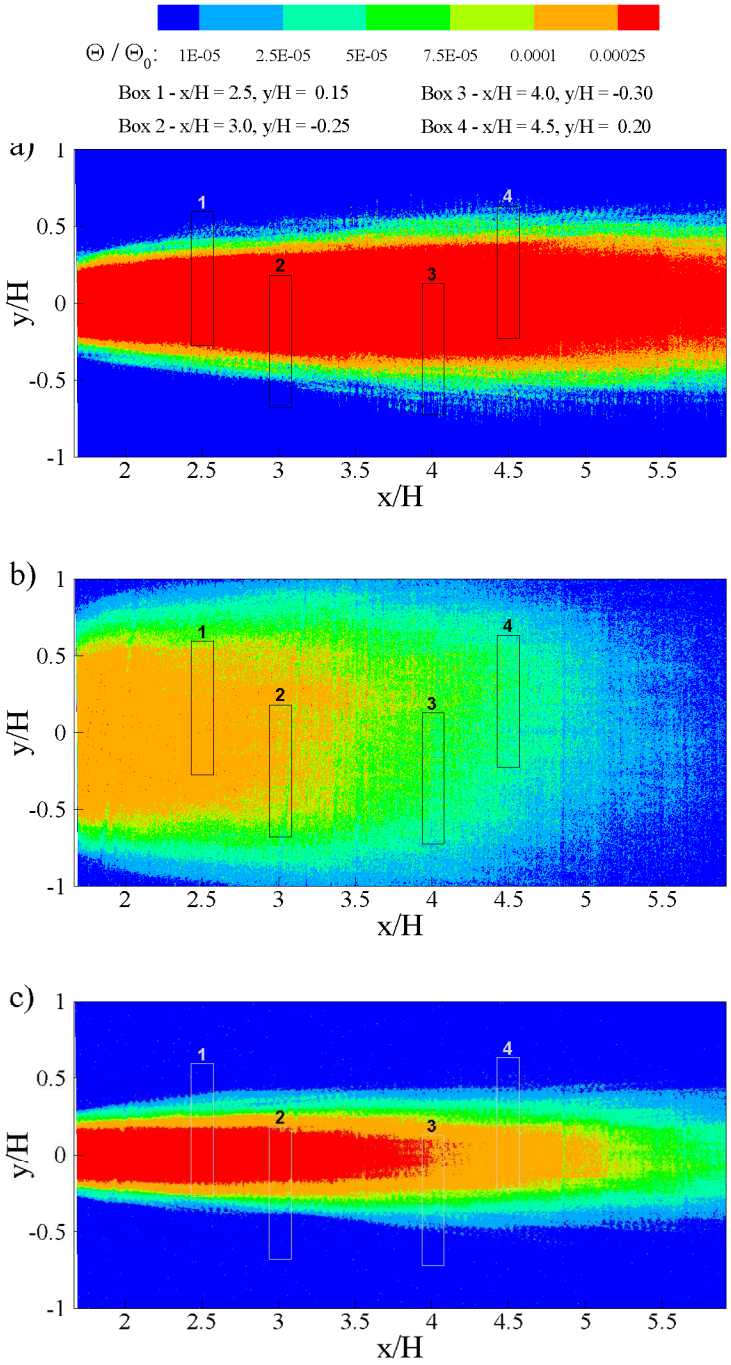

Figure 5.29 Location of test sampling boxes shown on the average concentration field for a) the continuous plume, b) the meandering plume, and c) the pulsed plume. The sampling boxes are 3.1 cm by 18.1 cm (in the streamwise and transverse directions, respectively), which is a typical size used in the analysis of the tracking trial data.

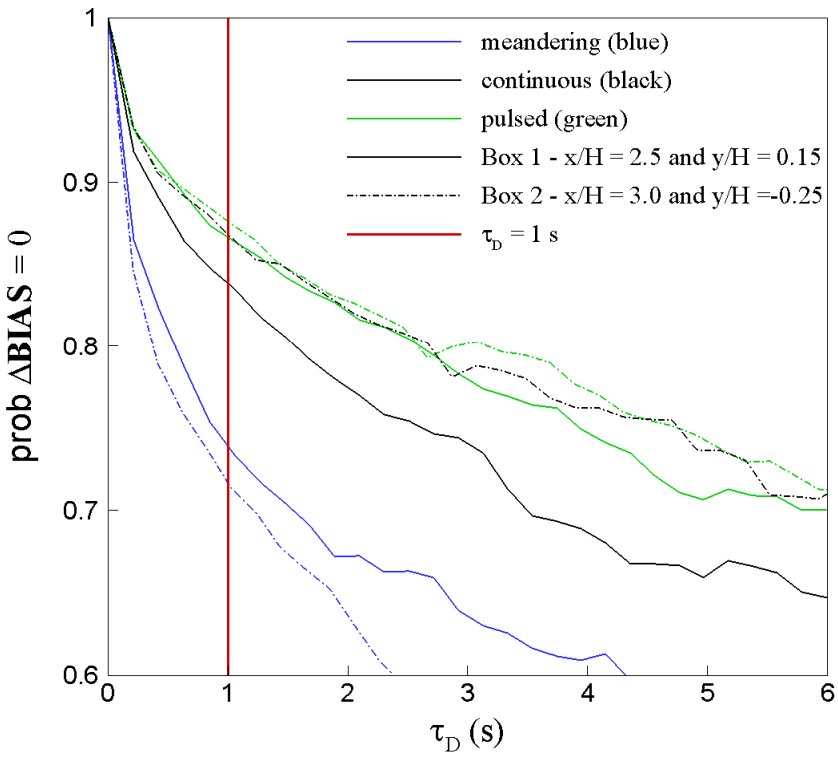

Figure 5.30 The probability of the change in bias being greater than zero for sampling boxes 1 and 2 (labeled in Figure 5.29). For the typical delay period, τ_D, of 1 second, the probability of the bias remaining unchanged is approximately 85 percent or greater for the pulsed and continuous plumes and approximately 70 to 75 percent for the meandering plume.

Figure 5.30 shows the probability of bias remaining unchanged for the two close boxes (numbers 1 and 2 in Figure 5.29). The pulsed and continuous plumes have similar trends, with about an 85 percent probability of a bias remaining unchanged over a typical time lag of 1 s. The probability for the meandering plume, between 70 and 75 percent, decreases more rapidly due to the large-scale meandering induced by the upstream cylinder. Figure 5.31 is the probability of the bias remaining unchanged for the two far boxes (numbers 3 and 4 in Figure 5.29). Moving farther from the source decreases the probability of the bias remaining unchanged for the box sizes and locations analyzed.

Again, the pulsed and continuous have comparable probabilities of the bias remaining unchanged, about 75 to 80 percent. For the meandering plume, the probabilities decrease to between 65 and 75 percent.

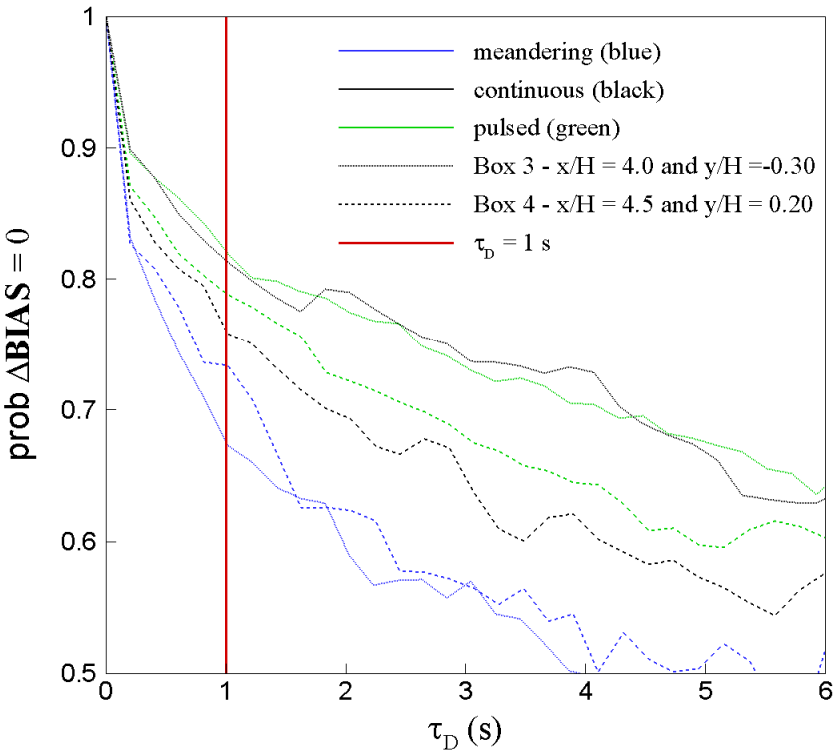

Figure 5.31 The probability of the change in bias being greater than zero for sampling boxes 3 and 4 (labeled in Figure 5.29). For the typical delay period, τ_D, of 1 second, the probability of the bias remaining unchanged is approximately 80 percent for the pulsed and continuous plumes and approximately 68 to 74 percent for the meandering plume.

The evolution of the concentration centroid for the four sampling boxes shown in Figure 5.29 can also be shown in spatial terms. The growth of the time-averaged plume width is reflected in the calculations in this section because the results correspond to time-averages of the plume data taken in the absence of blue crabs. While these results provide insight, it is important to note that they do not provide clear information about

the downstream evolution of the instantaneous filament structure. Figure 5.32 shows the centroid evolution for the boxes numbered 1 and 2. The colored symbols show the average change in the centroid location with time delay from the initial sample.

$$\Delta y_c = \frac{1}{T}\sum_{i=1}^{T}\left(h_i\left(x+U\tau_D, t+\tau_D\right)-h_i\left(x,t\right)\right) \tag{5.12}$$

The curves to either side of the average symbols are the average plus and minus one standard deviation.

$$\sigma_c = \left[\frac{1}{T-1}\sum_{i=1}^{T}\left[h_i\left(x+U\tau_D, t+\tau_D\right)-h_i\left(x.t\right)\right]^2\right]^{1/2} \tag{5.13}$$

The black dash-dot lines are the limits corresponding to ±0.5 cm. The pulsed and continuous plume data show similar trends, reflecting the movement of the average centroid away from mean plume centerline. The average centroid deviation for the meandering plume is close to zero for distances relatively far from the initial point, although the standard deviation is about twice the other plume types.

Figure 5.33 is a plot of the centroid evolution for the sampling boxes labeled 3 and 4. In all three cases, the average centroid deviation from the initial location follows trends similar to Figure 5.32. The standard deviation of the centroid difference is both larger and grows at a faster rate relative to the boxes located closer to the source. The increase in the standard deviation of the centroid difference can be attributed to sampling boxes located farther from the source including additional portions of the expanding plume. In contrast, the top of box 1 and the bottom of box 2 are located at the edge of the average

plume width, particularly for the continuous and pulsed cases, and the instantaneous plume structure is more likely to be centered on the plume centerline.

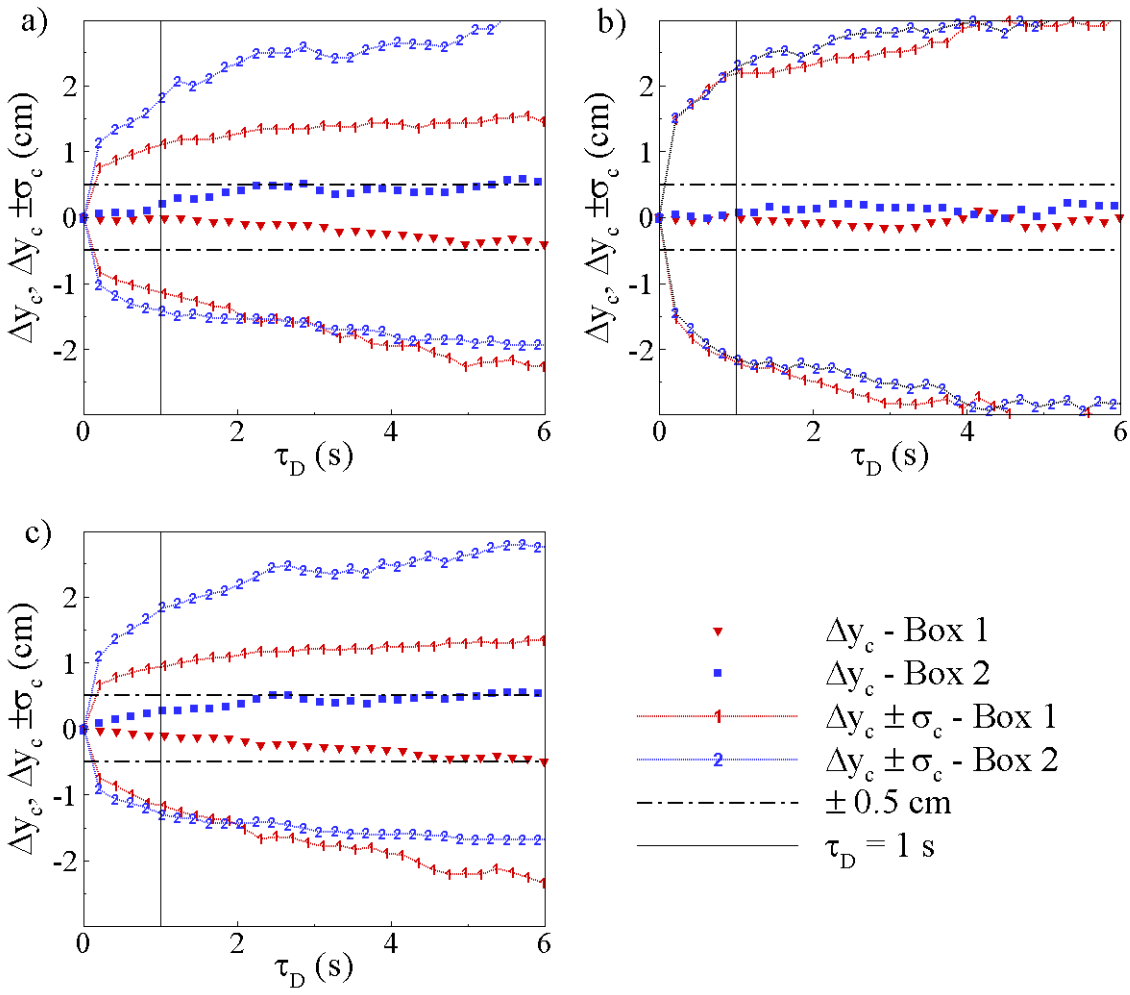

Figure 5.32 The evolution of the average (equation 5.12) and standard deviation of the concentration centroid (equation 5.13) for the sampling boxes labeled 1 and 2 in Figure 5.29 for a) the continuous plume, b) the meandering plume, and c) the pulsed plume. The symbols show the average, and the dotted lines show the average plus and minus one standard deviation. The dashed-dot black lines indicate the threshold of ±0.5 cm. The vertical line at 1 s corresponds to a typical time delay used in the outer chemosensor analysis.

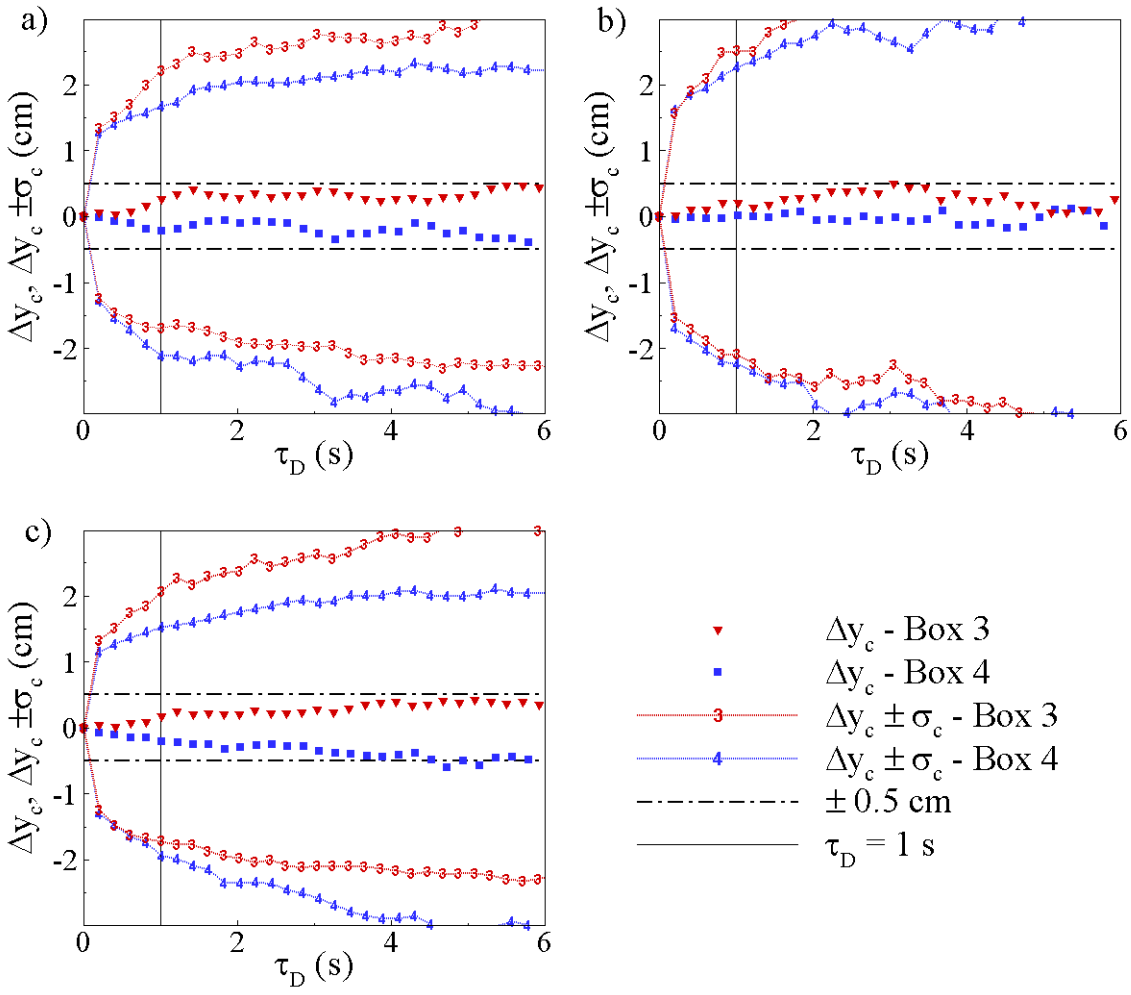

Figure 5.33 The evolution of the average (equation 5.12) and standard deviation of the concentration centroid (equation 5.13) for the sampling boxes labeled 3 and 4 in Figure 5.29 for a) the continuous plume, b) the meandering plume, and c) the pulsed plume. The symbols show the average, and the dotted lines show the average plus and minus one standard deviation. The dashed-dot black lines indicate the threshold of ±0.5 cm. The vertical line at 1 s corresponds to a typical time delay used in the outer chemosensor analysis.

The data presented in figures 5.32 and 5.33 indicate the average centroid location to change less than the 0.5 cm tolerance for the four sampling boxes used. Figures 5.30 through 5.33 indicate the outer chemosensor sampling procedure is suitable to indicate a

transverse bias signal except in approximately 20 percent of the cases where the instantaneous plume structure expands into the box over the period of the time delay.

5.3.3 Sampling Procedure Results

5.3.3.1 Continuous plume

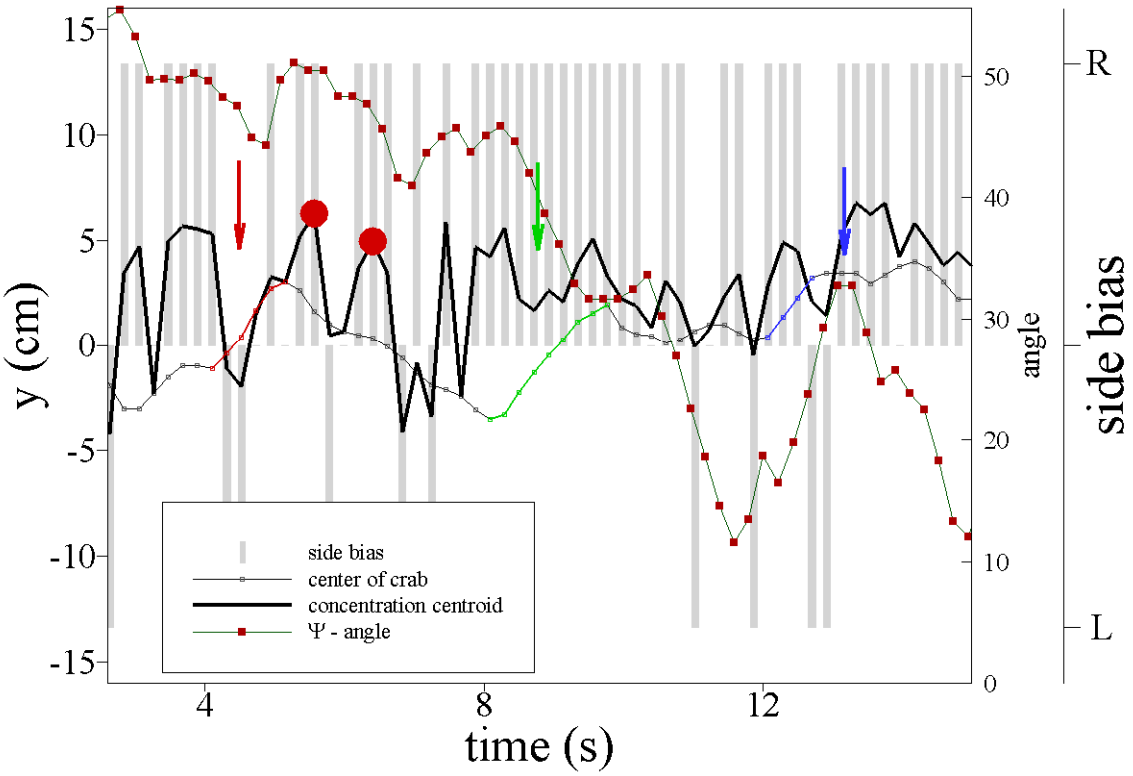

Figure 5.34 Time traces of concentration centroid location, crab center, and side bias for crab **116O** in the continuous plume. The crab generally moves transversely based upon information contained in the approaching plume. The two red circles indicate a bias which appears to be ignored by the crab.

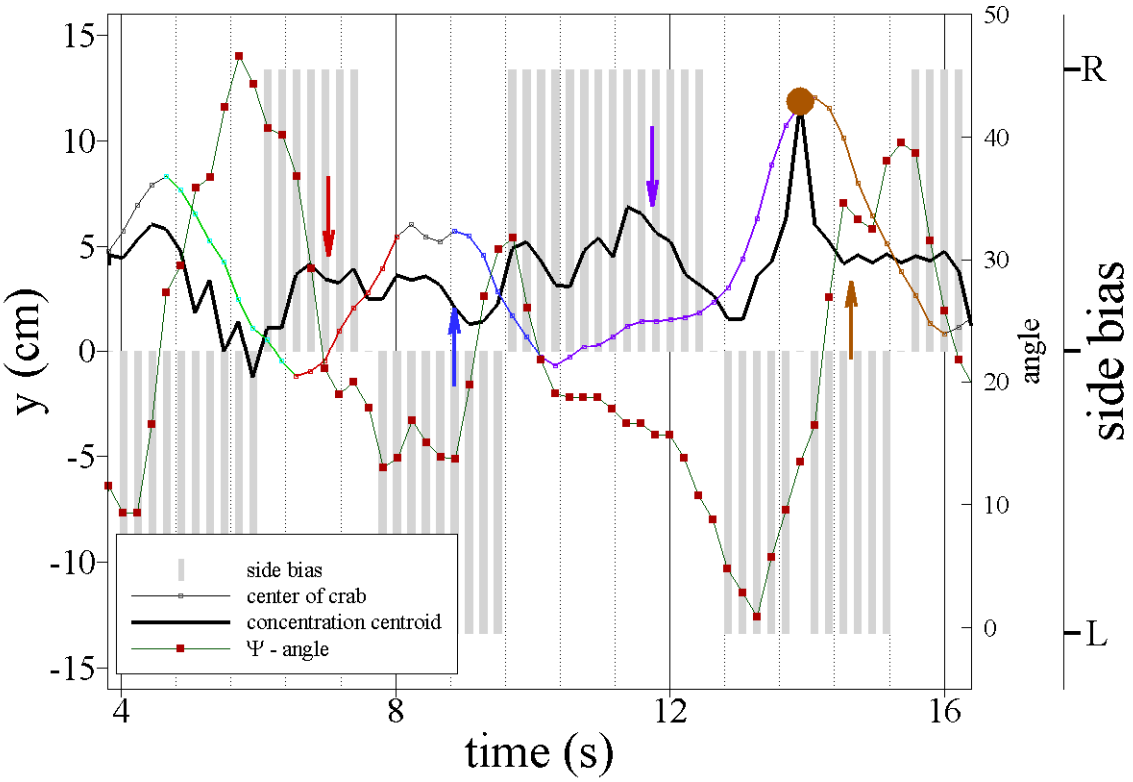

Figure 5.35 Time traces of concentration centroid location, crab center, and side bias for crab **1352Q** in the continuous plume. The crab appeared to react to the signal in the advancing plume as noted by the colored arrows. The brown dot indicates an indeterminate bias, as the upstream box did not contain measurable concentrations, and is not a bias to the right.

Figures 5.34 and 5.35 are two sample time traces for crabs 116O and 1352Q in the continuous plume using data extracted by the procedure outlined above. The bars indicate a general bias towards the right or left, depending upon the transverse distance between the concentration centroid calculated at $t_0 - \tau_D$ and the crab location at time t_0. Positions along the time trace where bars do not appear correspond to two circumstances. When the distance between the concentration centroid and crab position differed by less than 0.5 cm, the bias was set to zero, indicating neither left nor right. When the crab wandered beyond the instantaneous plume structure, the sampling box lacked detectable

concentration signal and the centroid was placed coincident with the crab center. The bias was considered indeterminate and set to neutral when all concentrations were undetectable. Note that the time traces are shorter than those for the antennules as the sampling box placed upstream at $t_0 - \tau_D$ cannot be advanced farther than the upstream limit of the measurement arena.

Crab 116O (Figure 5.34) followed the general transverse bias in the advancing concentration signal. The distribution of the side bias bars mostly to the right shows the crab positioned itself generally to the left of the advancing plume structure. The three colored arrows highlight time periods of significant bias with subsequent crab movement in that direction. The two red dots were placed at times where the crab casted to the left, apparently ignoring the right side bias provided by the plume structure.

Figure 5.35 is a time trace for crab 1352Q. The crab generally followed the signal provided in the advancing plume. The four colored arrows indicate times of significant bias followed by crab movement in that direction. Towards the end of the time trace, the crab wandered quite far from centerline for the continuous plume trials. Concentrations within the sampling box were undetectable at the time highlighted by the brown dot. When concentrations fell to undetectable levels within the sampling box, the centroid was placed coincident with the crab center with a zero bias. Thus, what appears to suggest a bias on the time trace of the concentration centroid is actually indeterminate and set to zero. The overall side bias was nearly balanced between the right and left, a good indicator of the crab's ability to locate the center of the instantaneous plume.

The remaining 20 time traces of signal bias for the continuous plume can be found in Appendix B.

5.3.3.2 Meandering plume

Crabs tracking the meandering plume had more difficulties following the instantaneous plume structure relative to those tracking the continuous release. Crabs frequently followed a concentration burst at the fringe of the intermittency factor field shown in Figure 5.13 only to find themselves moments later in fluid with ostensibly undetectable odor. As a result, the time traces for the meandering plume tracks split into two general patterns, either the crab followed the instantaneous meandering plume in a manner that was similar to those tracking the continuous plume or the crab remained to one side of the instantaneous plume structure throughout the measurement arena. The two time traces shown in Figures 5.36 and 5.37 are examples of each track type. The remaining 14 time traces of signal bias for crabs in the meandering plume can be found in Appendix D.

Figure 5.36 is a time trace for crab 1286Q. The crab started tracking at a rather extreme distance from the plume centerline. The red arrow indicates a period of persistent bias to the right for several seconds during the track. From Figure 5.23, the crab received undetectable odorant concentrations at the antennules during this period and was oriented nearly parallel with the flow direction. The crab turned to the right after presumably receiving an odorant signal at an outer chemosensor. The crab followed the instantaneous plume meander structure for the remainder of the track while receiving relatively high concentrations at the antennules.

Figure 5.37 is a time trace for the signal bias for crab 1317S. Counterintuitive behavior was displayed in Figure 5.24 as high odorant concentrations occurred at the antennules

while the crab remained stationary (first red arrow in Figure 5.37). The stationary behavior coincided with a bias to the right. Some movement to the left occurred starting at 12 s followed by another shorter stationary period starting at roughly 17 s. From t = 20 s to approximately 28 s, the crab followed a meander of the instantaneous plume structure. The crab lost the structure at approximately t = 30 s, eventually stopping for a third time (third red arrow). Towards the end of the track, the crab intercepted a bias signal to turn back to the right. The crab eventually moved back towards centerline and the source was successfully found (not shown in the time record).

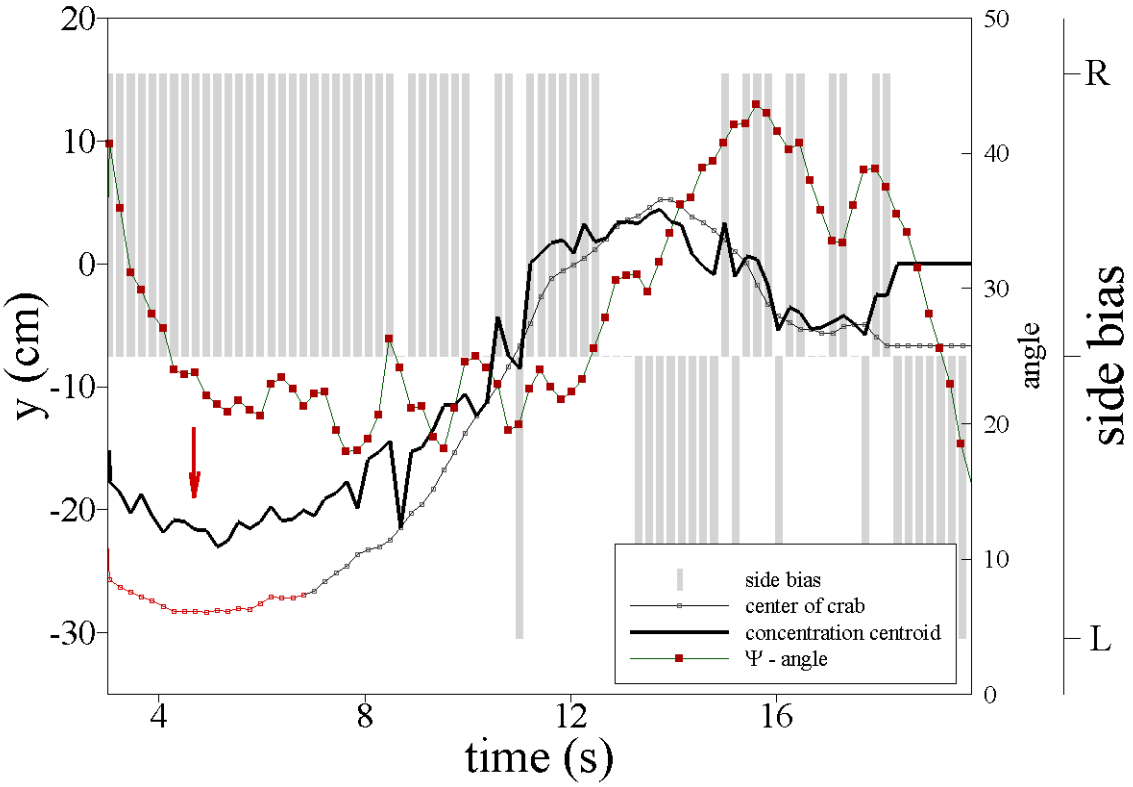

Figure 5.36 Time traces of concentration centroid location, crab center, and side bias for crab **1286Q** in the meandering plume. The crab started at a large distance from the plume centerline before turning into the plume and following the meander structure.

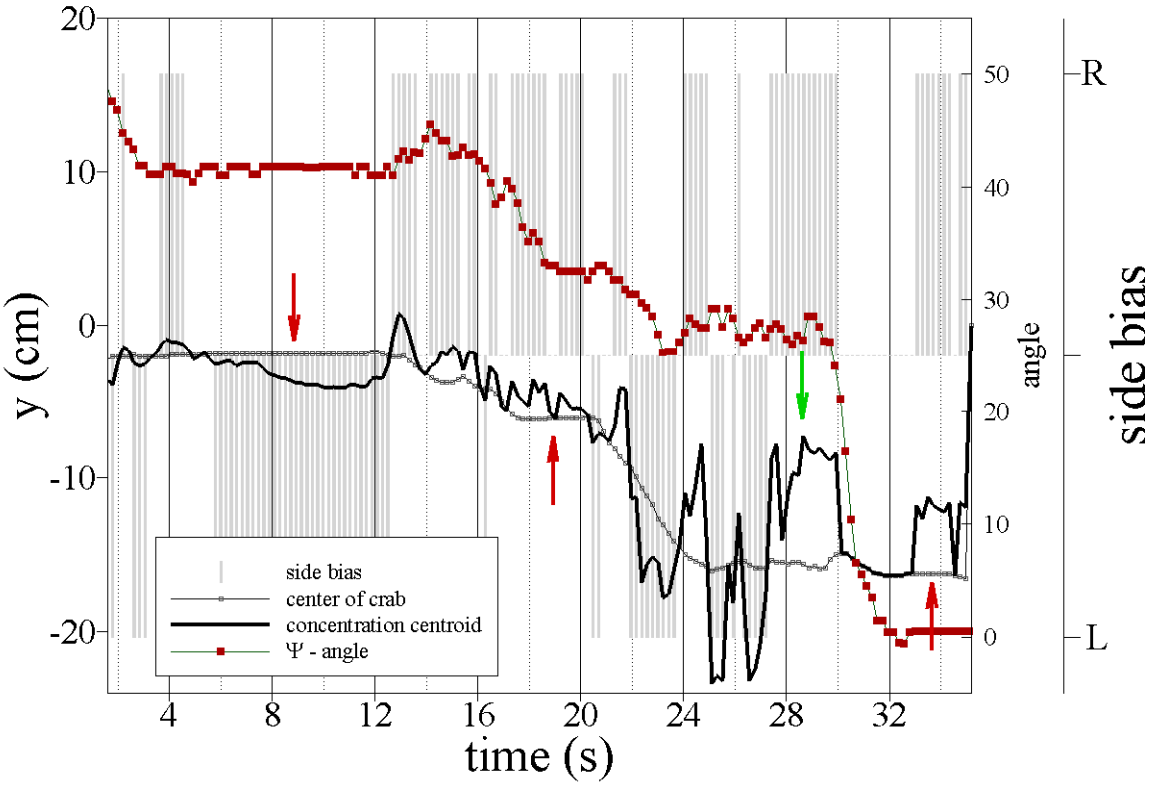

Figure 5.37 Time traces of concentration centroid location, crab center, and side bias for crab **1317S** in the meandering plume. The crab had several stationary periods, noted by red arrows. The crab generally followed the plume bias although contact with the plume was lost after disregarding the right-side signal noted by the green arrow.

5.3.3.3 Pulsed Plume

Crabs tracking the pulsed plume spent more time stationary relative to those tracking the continuous release. After intercepting a passing odorant cloud, crabs generally ceased upstream motion, entering a period of latency prior to initiation of upstream movement upon contact with the next odorant cloud. Alternatively, crabs chased the odorant cloud downstream for brief periods. Time traces of crab walking velocities are periodic, usually characterized by upstream acceleration and deceleration, and often included stopping (see figures 5.25 and 5.26 for example). Periods of latency were shorter than periods of upstream movement as blue crabs continued upstream motion beyond the

upstream edge of a passing odorant cloud. Two time traces for the transverse signal bias experienced by crabs tracking the pulsed plume are shown in figures 5.38 and 5.39. The remaining 13 time traces of signal bias for the pulsed plume can be found in Appendix F.

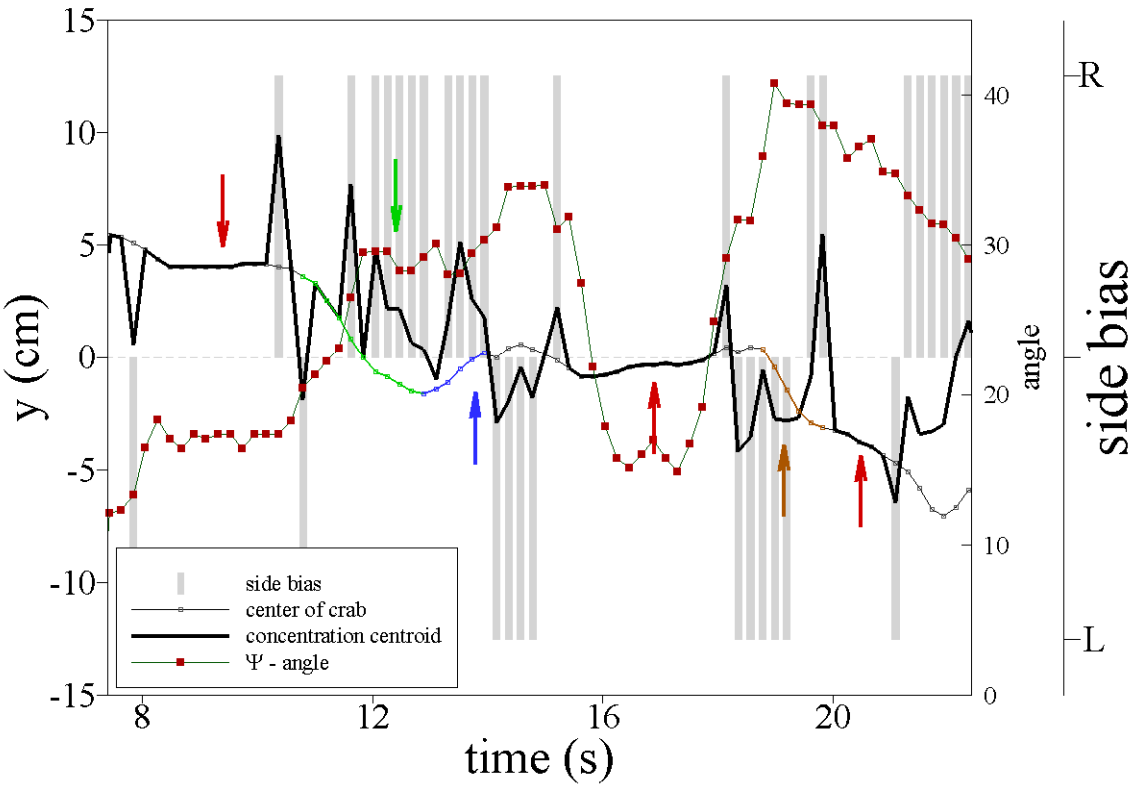

Figure 5.38 Time traces of concentration centroid location, crab center, and side bias for crab **1201M** in the pulsed plume. The crab passed through fluid with undetectable concentration in the three instances highlighted by the red arrows. The crab responded to the bias shown by the brown and blue arrows, yet seemingly ignored the one noted in green.

Figure 5.38 is a time trace for crab 1201M tracking in the pulsed plume. Two periods of latency occurred during the track, where the crab was apparently between passing odorant clouds and moved very little (indicated by the red arrows). Once the next odorant cloud became perceptible, the crab proceeded upstream and followed the

instantaneous plume location. This crab performed minimal casting and moved upstream in response to passing odorant clouds. Towards the end of the time trace, the crab was relatively far from the plume centerline for this release type. Signal bias was towards the right after approximately 20 s, and the crab presumably responded as the track was successful.

Figure 5.39 is the time trace of transverse signal bias for crab 1358M in the pulsed plume. Two latency periods occurred (again indicated with the green arrows). The first period occurred after the crab entered a gap in the plume structure at approximately 4 s. A signal bias to the right occurred while the crab was stationary. The crab moved back towards the centerline and was able to generally follow the plume as another odorant cloud passed. After wandering to the left, the crab again stopped, either because it was too far from centerline to sense the plume structure or was in another gap. Transverse movement back toward centerline occurred despite a lack of a side bias. The crab regained contact with the plume and subsequently followed the transverse bias signal to the right. The crab eventually moved back towards centerline and the source was successfully found.

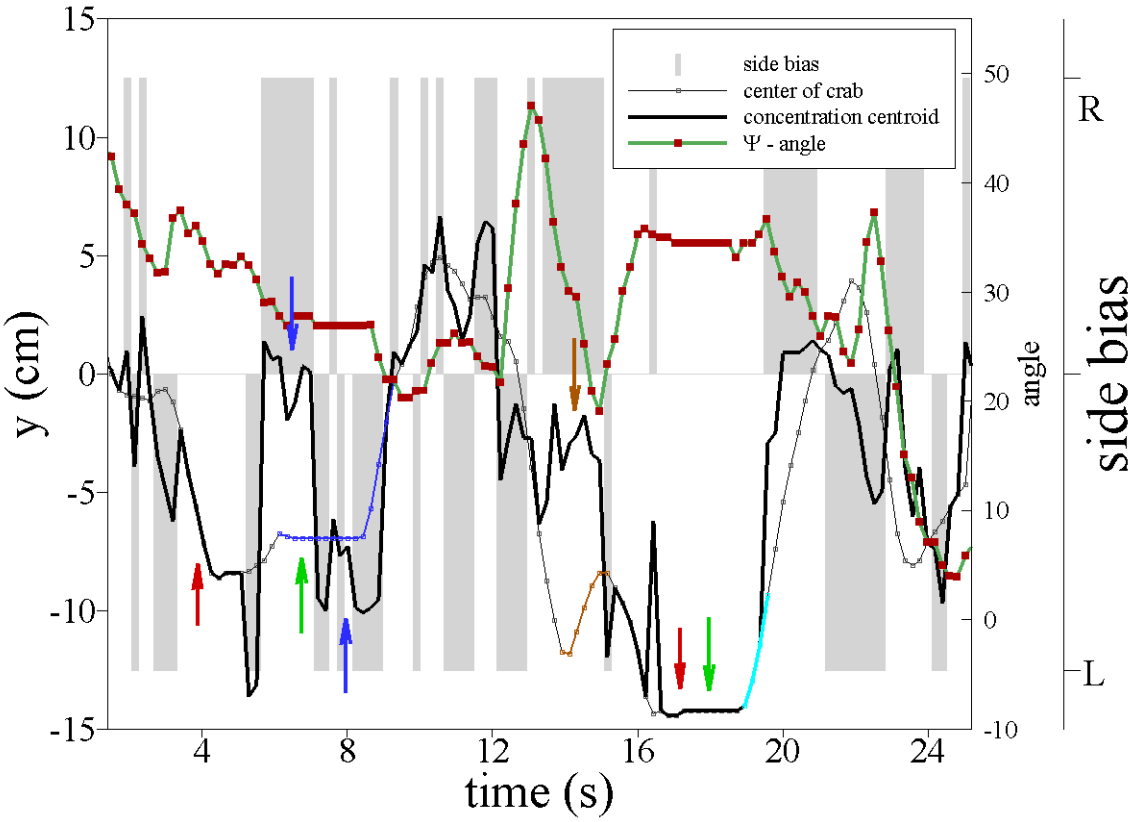

Figure 5.39 Time traces of concentration centroid location, crab center, and side bias for crab **1358M** in the pulsed plume. The crab passed through fluid with undetectable concentration at times noted by the red arrow. Periods of latency are noted by green arrows. The blue arrows indicate a latency period where bias to both the left and right lacked a behavioral response. The crab appeared to respond to the bias pointed out by the brown arrow yet subsequently turned in the opposite direction when no apparent bias was present.

Chapter 6

Summary and Discussion

This study details the physical measurement of olfactory stimulus, through laser-induced fluorescence (LIF), experienced by a blue crab during navigation to a source. A three-dimensional measurement system was necessary as olfactory organs are located at different spatial locations on the body of a blue crab, such as the antennules and legs. The 3DLIF experimental setup was a non-intrusive means of determining the odorant stimulus leading to blue crab navigational behavior such as acceleration upstream and side-to-side movement. The effects of large-scale spatial and temporal intermittency were introduced through meandering and pulsed releases, respectively. Algorithms and methods for extracting useful odorant concentration data impinging upon the inner (antennules and mouth parts) and outer (primarily the legs) chemosensory organs are described in Chapter 5. Chapter 4 presents statistical analyses of the three plume types in the absence of blue crabs and the potential utility of such measures to a tracking organism. Important conclusions and contributions from this study are summarized in this chapter. Suggestions for future research are also presented. In addition, a companion thesis to be published in spring of 2009 by Jennifer Page will extend the statistical and behavioral conclusions of this study.

6.1 Summary

6.1.1 Odorant concentrations at the antennules and mouth parts

Chapter 5 details the methods associated with extracting concentration data from the mouth region and antennules. Due to shadowing effects, concentration data at the antennules and mouth region were limited to crabs facing the laser. The location of the

mouth parts and antennules was found by examining each 3DLIF sequence for laser reflections from the front of the crab. A sampling zone was placed directly in front of the mouth parts and oriented at the instantaneous angle of the animal. Odorant concentrations within the sampling box were then extracted. Time traces were developed of crab upstream velocity and concentrations within the antennules sampling zone. The time traces demonstrated a correlation between concentration bursts at the antennules and upstream movements.

Crabs responded to spatial and temporal intermittency. Time traces of the continuous plume had few instances of zero or negative upstream velocity. Crabs stopped when losing contact with the instantaneous continuous plume structure and resumed upstream progress after receiving odorant bursts at an inner or outer chemosensor. While tracking the pulsed or meandering plumes, crabs would frequently stop or even move downstream apparently chasing packets of odorant. The frequency of downstream movement was greatest for the pulsed plume as crabs entering clear fluid would reverse direction to follow the previously passed cloud of odorant. For the three plume types, upstream movement from a stopped position was usually initiated after receiving stimulus at an inner or outer chemosensor. The downstream movement was particularly apparent when viewing the raw image data.

6.1.2 Transverse movements and outer chemosensory organs

The challenges introduced by shadowing effects and laser reflections prevented the direct measurement of odorant concentration at the outer chemosensory organs. A general bias contained in the approaching plume was used in place of a direct measurement, as described in Chapter 5. The transverse concentration centroid of the approaching plume

calculated at a time reversed on the order of one second was compared with the location of the crab. A deviation of more than 0.5 cm between the centroid location of the concentration field in the advancing plume and crab location indicated a bias towards left or right. Time traces were developed comparing the concentration signal bias with crab orientation and transverse location.

Crabs appeared to follow the bias provided by the approaching plume, although behavioral response varied with plume type. Crabs remained close to the average plume centerline for the continuous plume, with their tracks converging onto centerline with decreasing distance towards the source. Blue crabs were able to follow the meander pattern, or bias, contained within the instantaneous meandering plume. The meandering plume induced the highest amplitude of casting with crabs wandering the farthest from the average plume centerline for the three plume cases. The bias provided by the pulsed plume was discontinuous, with numerous gaps in the time record due to passing clear fluid. Although crabs tended to follow the bias provided by the pulsed plume, temporal intermittency prevented the convergence of tracks to the plume centerline with decreasing distance from the source that was observed for the continuous plume.

6.1.3 Hypotheses concerning blue crab tracking behavior

The tracking mechanism for blue crabs differed from those of flying moths, where filament contact induces upwind movement and casting initiates upon entering clear fluid for greater than a set amount of time (Kennedy 1983). In place of casting, crabs tended to stop or reverse direction when losing contact with an odorant plume or cloud, an option unavailable to a flying insect. After short latency periods with no movement, blue crabs either casted towards the instantaneous plume or accelerated upstream. Casting

towards the instantaneous plume was generally associated with an odorant burst at an outer chemosensor, in contrast to casting in flying insects which is initiated after entering clear fluid for longer than a certain amount of time.

The time traces of odorant concentration with upstream velocity and plume bias with transverse coordinate supported the hypothesis proposed by Keller, et al. (2003) that odorant stimulus at the antennules maintains upstream movement while transverse movements are modulated by the outer chemosensors. While receiving frequent odorant bursts at the antennules, crabs generally maintained upstream progress towards the source for the three plume types. Deceleration, stopping, or major tracking adjustments occurred when odorant concentrations at the antennules were low. Acceleration upstream or casting back into the instantaneous plume generally occurred after receiving a turning bias provided by the approaching plume.

6.1.4 Statistics of crab tracking kinematics

Streamwise and transverse crab displacements were correlated in time, displaying general exponential decay. The correlation decayed most rapidly for the pulsed plume with the displacement correlation decaying the slowest for the meandering plume. The exponential decay suggested that crabs follow a stochastic process during source location. A simplified Ornstein-Uhlenbeck model resulted in decreased success relative to actual behavioral tracks.

The majority of crab displacements during successful navigation remained well-aligned with the shortest direction towards the source. For the continuous plume, the angle between the mean flow and crab displacement vectors closely followed a Gaussian distribution with the exception of a skew towards positive angles. The Gaussian

distribution did not fit data from the meandering and pulsed plume cases as movements away from the source skewed the distributions.

The distribution of the angles between the crab displacement vectors and a vector pointing towards the source peaked close to zero. The angular distributions displayed bimodal peaks for the three plume types, as crab displacements were more likely aligned with the mean flow vector. Displacements for the meandering plume remained the least aligned with the source and mean flow vectors, as crabs generally followed the meander of the instantaneous plume.

6.1.5 Plume characteristics

Three-dimensional plume data was collected for the three plume types, continuous, meandering and pulsed. The relative roughness of the boundary layer was transitional and data was collected mostly within the zone of established flow. For the three cases, the time-averaged concentration and the standard deviation of the concentration fluctuations decayed rapidly with distance from the source. The instantaneous photographs and plots shown for each plume type in Chapter 4 reveal a filamentous structure with packets of high concentration fluid. Fluid turbulence mixes the instantaneous plumes to nearly uniform concentration levels at the downstream limits of the photographs. The photographs show the instantaneous odor landscape, as named by Atema (1996), that crabs must navigate to find a source.

6.1.5.1 Continuous plume

The time-averaged concentration and the standard deviation of the concentration fluctuations decayed rapidly with distance from the source. The standard deviation of the concentration fluctuations was larger than the mean concentration as large fluctuations

predominantly contributed to the average value. Transverse profiles of the time-averaged concentration and standard deviation of the concentration fluctuations displayed self-similar behavior with a Gaussian shape. The mean plume width increased with distance from the source in agreement with the Gaussian dispersion model. The diffusivity coefficient was $0.074\,Hu_*$, higher than the $0.060\,Hu_*$ determined by Rahman (2002) under similar flow conditions, but lower than the $0.109\,Hu_*$ reported by Webel and Schatzmann (1984) for open channel flow with a smooth bed.

6.1.5.2 Meandering plume

The upstream cylinder introduced additional turbulence and a pseudo-cyclical nature to the meandering plume. The Reynolds number of the cylinder was about 5100 with a resulting Strouhal number of 0.20. The resulting wake flow, although fully turbulent, had a pseudo-cyclical frequency of approximately 0.1 cycles per second.

The time-averaged concentrations and standard deviation of the concentration fluctuations decayed more rapidly relative to the continuous plume as turbulence introduced by the upstream cylinder spread the passive scalar over a larger volume. The time-averaged concentration decreased downstream according to a modified meandering plume model proposed by Gifford (1959). Transverse average concentration profiles generally followed the modified Gifford model and were not self-similar. Transverse profiles of the standard deviation of the concentration fluctuations were modeled by a simplified two-source model, although self-similarity was not apparent. At the nozzle centerline, the average concentration is nearly uniform across the depth at a relative distance of $x/H = 6.0$.

6.1.5.3 Pulsed plume

Flow visualization of the pulsed plume showed the development of a train of distinct clouds moving downstream. Average concentrations decayed more rapidly than that of the continuous plume as longitudinal dispersion was not negligible. The cloud dispersal model of Townsend (1951) predicted a slightly greater rate of decay for the time-averaged concentration relative to that of the data. Transverse profiles of the time-averaged concentration and standard deviation of the concentration fluctuations displayed self-similar behavior and good agreement with a Gaussian shape. The average plume width grew at a faster rate than for the continuous plume case.

6.2 Conclusions

Despite various experimental constraints from shadows and reflections, meaningful concentration data can be acquired from the 3DLIF setup described in Chapter 3. Concentrations around the antennules and outer chemosensors, primarily the legs, cannot be measured directly due to ambiguity in the chemosensor location in the raw 3DLIF images. As a substitute for direct measurement, stimulus patterns at the antennules and legs can be approximated through the analysis of plume zones around the mouth region and in an upstream zone at an earlier time. Data taken from the mouth zone confirmed the function of the antennules in maintaining upstream progress. The upstream (and earlier) sampling region provided a general bias towards one side of the blue crab by comparing the sampling-zone concentration centroid with the crab location. Blue crabs tended to follow the transverse signal bias as they proceeded upstream towards the source.

The effects of large-scale spatial and temporal intermittency were examined through three plume types: continuous, meandering, and pulsed. The continuous plume resulted in the shortest search times and a general convergence of paths as the source was approached. Blue crabs that were tracking the meandering plume wandered the farthest from mean plume centerline and casted from side-to-side with the greatest amplitude. The temporal intermittency of the pulsed plume induced latency periods during navigation, where crabs remained stationary until sensing the next odorant cloud. Crabs that were tracking the pulsed plume moved upstream at the highest rates, although the velocities were maintained over short lengths of time. Crab tracks for the meandering and pulsed plumes did not converge towards mean plume centerline at the upstream limit of the measurement area.

6.3 Unique contributions and applications

Unique contributions to the field of odor-source navigation include the following:

- The construction of the first three-dimensional laser-induced fluorescence (3DLIF) system for measuring odorant concentrations around a tracking animal with a complex set of chemosensory organs.
- The quantification of odorant stimulus experienced by a tracking blue crab, essentially combining physical measurements of plume structure with behavioral studies.
- The extraction of odorant concentrations at a zone around the crab antennules that both rotated and moved with the crab during successful navigation.

- The determination of a turning bias provided by the approaching plume signal structure through analysis of an upstream region of the plume sampled earlier in time.
- Validation of the hypothesis that odorant signal at the antennules mediates upstream movement, while odorant signal at the outer chemosensors provides the impetus for turns.
- The large-scale temporal intermittency of the pulsed plume created periods of latency during tracks followed by pronounced upstream movement.
- Blue crabs were able to follow the spatial pattern of the meandering plume, casting back and forth with the instantaneous plume structure while moving towards the source.
- Kinematics of blue crabs tracks appeared to follow a stochastic Ornstein-Uhlenbeck (OU) process when examining the displacement autocorrelation function. However, modeling crab tracking as an OU process resulted in decreased navigational success relative to behavioral tracks.

Additional contributions provided by the analysis of the three plume types in the absence of tracking crabs are:

- Successful application of the modified meandering plume model of Gifford (1959) to a plume with an induced meander in order to describe the average structure of the meandering plume.
- The plume width for the pulsed plume grew at a rate slower than the x^{-1} rate predicted by the Gaussian plume model.

- For the pulsed plume, the transverse profiles of average concentration and standard deviation of the concentration fluctuations followed a Gaussian form and were self-similar.

Applications of the current research include the development of algorithms for autonomous robots tracking plumes in turbulent environments. The advantageous aspects that robotic algorithms should incorporate include:

- Move upstream when sensing a burst of concentration at a centrally located sensor.
- Mimic the response of blue crabs to temporal intermittency whereby stopping is preferred to immediate casting from side-to-side for a searcher in contact with the substrate.
- Employ multiple sensors; at least two sensors separated transversely would permit a robot to sense a transverse signal contrast to locate the edge of the instantaneous plume.
- Employ casting behavior exhibited by blue crabs while in contact with the instantaneous plume, particularly for plumes smaller than the tracking robot.

6.4 Future directions

The current research provides several directions for future study of the tracking of turbulent plumes. Brief descriptions of these ideas are summarized in the following paragraphs.

Improvements to 3DLIF system

The use of laser-induced fluorescence as a non-intrusive concentration measurement technique with a tracking organism introduces the challenge of locating the edge of the

animal. The measurement of odorant concentration at individual chemosensory locations, such as the antennules, is by nature imprecise due to movement into and out of a particular laser plane. To obtain more detailed information at the antennules, the placement of a backpack capable of transmitting the instantaneous elevation of the crab could be used to control the elevation of the laser scans. In this way, a continuous record of the elevation of the antennules along with odorant concentrations could be extracted. More detailed information of odorant concentrations at the level of the antennules would provide an improved means of correlating stimulus with upstream movement.

Improving the sampling box technique for determining the transverse bias contained in the approaching plume would be a greater challenge. The elevation of a crab's legs varies more than the antennules as it navigates an odorant plume. Shadows produced by other appendages, particularly the claws, and the carapace frequently obscure the precise location of the legs. One means of improving data collection at the legs would be to limit the highest 3DLIF scan elevation to the approximate highest leg elevation. Collecting fluorescence with a camera mounted below the flume with a transparent floor would enable improved detail for odorant concentrations at the legs.

Collection of concentration data at the antennules and legs by means described in the previous paragraphs could be combined. Two cameras, one mounted below the flume and the other above the flume, could be used to collect fluorescence data at the legs and antennules using 3DLIF. The lowest ten to fifteen LIF planes could collect data on the legs while the upper five or ten are collected around the antennules. Such an arrangement

would require a variable signal to the vertical scanning mirror for data collection at the antennules.

Role of the claws in tracking

During navigation, blue crabs generally moved their claws and in some cases, seemed to respond solely to olfactory signals received by chemosensors on the claws. In many instances, blue crabs moved their claws outward and inward, sweeping fluid towards their antennules. Claw movements were more pronounced for the meandering and pulsed plumes relative to the continuous plume. Crabs maintained their claws retracted and stationary towards their body during several of the continuous plume trials where the crab remained within the instantaneous plume throughout the track. Although the outer olfactory organs on the legs and the antennules have been proposed as the primary chemosensory input (Keller et al. 2003), movements of the claws raises several questions. Do crabs use their claws as an additional chemosensory input or for the increasing odorant flux at the antennules? Despite dilution introduced by the wake of the claw, such a mechanism may increase the overall transport of odorant to the antennules region. Are claw motions correlated to periods where the crab is receiving conflicting information about the instantaneous plume location, such as odorant bursts at both sets of legs with an imperceptible odorant concentration at the antennules, or a reaction to limited plume contact? Or are claw movements simply attempts to introduce clear fluid to the antennules to reduce adaptation to perceptible odorant concentrations?

The precise role of the claws in navigation would be difficult to isolate from responses due to chemosensory signal at the legs and/or antennules. Deafferentation of chemosensory organs on the claws could provide information on whether sweeping of

claws is simply to increase transport of odorant past the antennules or an attempt at sampling the instantaneous plume with an additional chemosensor. Whether crabs use the claws to move back into the instantaneous plume could be determined by examining the 3DLIF sequences of the current studies for cases where claw information appeared to induce movement. Knowledge of the function of the claws could be incorporated into autonomous tracking vehicles where outer arms sweep towards a central chemical sensor with movement triggered by certain instantaneous plume conditions.

Improvements to tracking algorithms using blue crab kinematic data

The kinematic data collected for the three plume types provide insights into possible algorithms for autonomous turbulent plume tracking. Figure 6.1 shows two representative tracks for the continuous plume for crab number 1363N (purple) and 1238Q (blue). The tracks consist of movements correlated in time between major adjustments in alignment, presumably a response to a signal at an outer chemosensor. Crab 1363N casted back and forth throughout the measurement area, while 1238Q appears to have maintained contact with the instantaneous plume after reaching within $x/H = 4$ of the source. Although the simplified OU process described in Chapter 5 did not adequately describe a typical crab track, the movements could be modeled by stochastic equations similar to equation 5.7 coupled through the diffusion tensor $\mathbf{B}_{ij}(\mathbf{x}(t), t)$. Major tracking adjustments would occur at time intervals set by the modeled arrival time of concentration bursts, or a random input, which would modify the diffusion tensor over a short period of time. Between arrival times, the diffusion tensor would take a different form, where crab displacements were more correlated (see Figure 6.2).

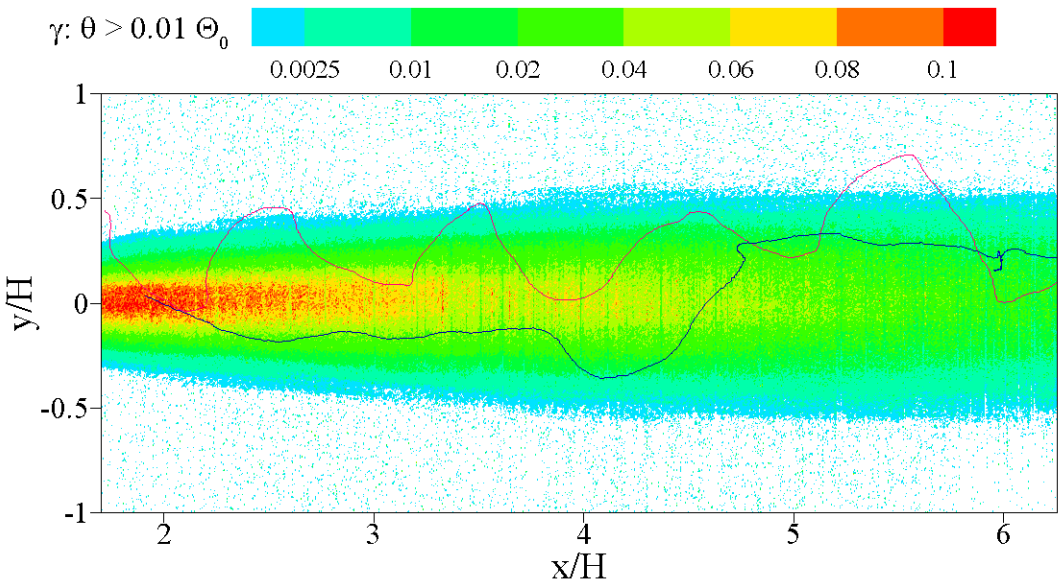

Figure 6.1 Two crab tracks shown on the field of intermittency factor based on a threshold of 1% of the source concentration. The tracks shown are for crabs 1363N (purple) and 1238Q (blue) in the continuous plume. The tracks consist of movements correlated in time between periodic major track adjustments.

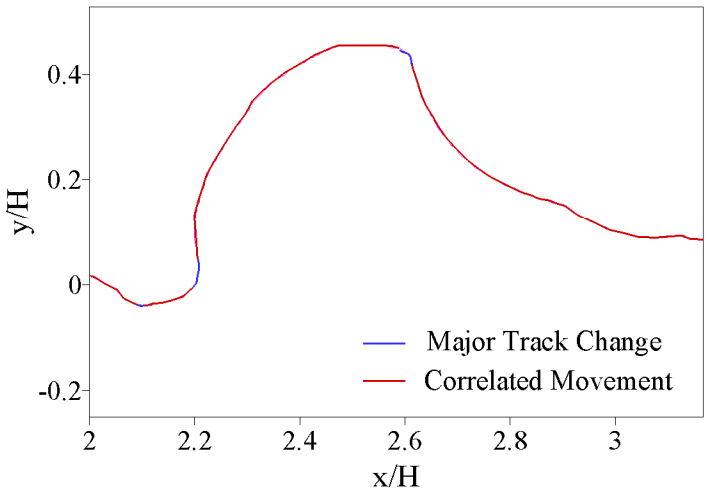

Figure 6.2 Detail of crab track for crab 1363N from Figure 6.1. The track can be broken into short periods where turns occur between longer periods of correlated movement.

Knowledge of the form of the diffusion tensor could be used in tracking algorithms for a robot with multiple sensors, where the chemical input modifies the diffusion tensor. After a major tracking adjustment, movements remain well-correlated until interception of another chemical signal. Stopping would occur upon losing contact with the instantaneous plume. Modeling crab displacements by a coupled stochastic system requires more detail on the displacement time record. The backpack LED's used in this study usually resulted in pixel saturation over a field of several pixels. Smaller LED's would permit the location of crabs to sub-pixel accuracy and consequently more detail on crab displacement correlations. Additionally, the collection of kinematic data for crabs tracking in natural environments where tracking occurs at distances greater than 1.5 m would permit the development of tracking algorithms for devices starting at larger distances from a source.

Appendix A

Time traces of antennules sampling zone – Continuous plume

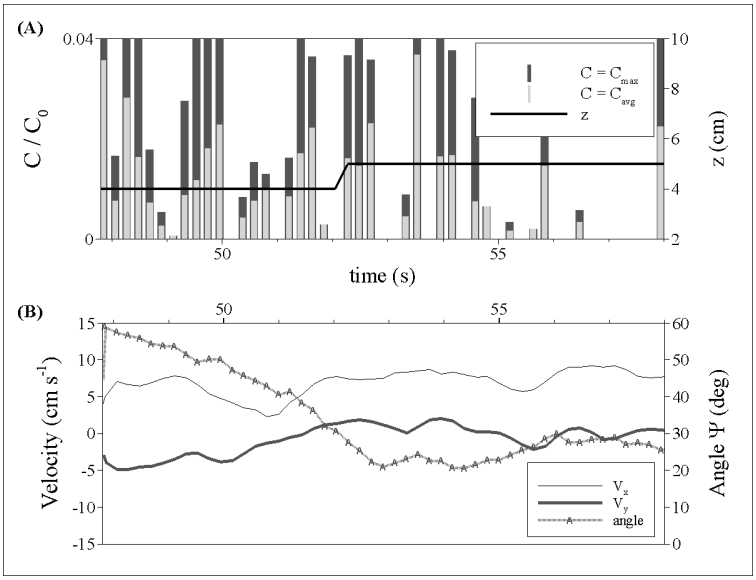

Figure A1. (A) **Crab 1305H** time trace of maximum and average relative concentrations at antennules and body elevation above substrate (cm). (B) Time traces of streamwise V_x velocity, transverse V_y velocity and crab angle with respect to the flow Ψ.

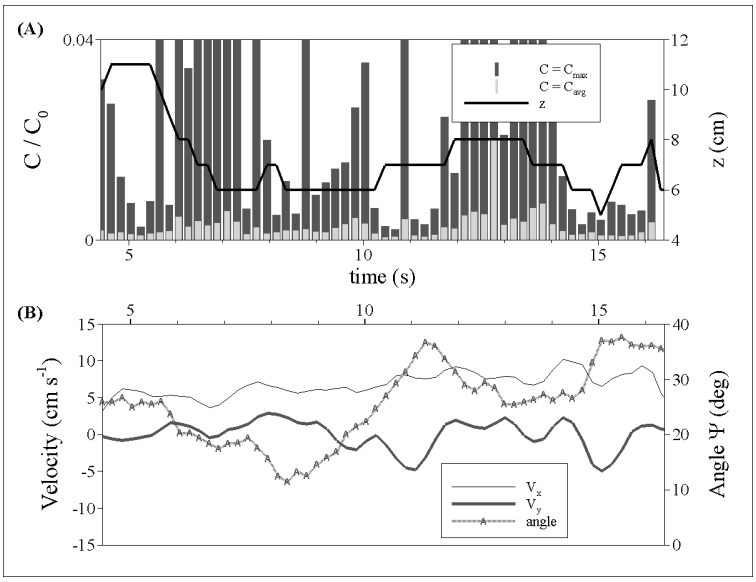

Figure A2. (A) **Crab 1364L** time trace of maximum and average relative concentrations at antennules and body elevation above substrate (cm). (B) Time traces of streamwise V_x velocity, transverse V_y velocity and crab angle with respect to the flow Ψ.

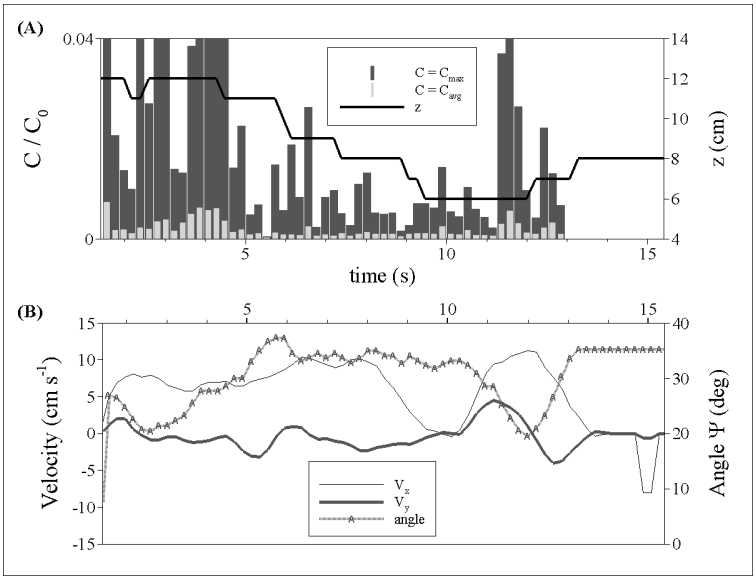

Figure A3. (A) **Crab 465L** time trace of maximum and average relative concentrations at antennules and body elevation above substrate (cm). (B) Time traces of streamwise V_x velocity, transverse V_y velocity and crab angle with respect to the flow Ψ.

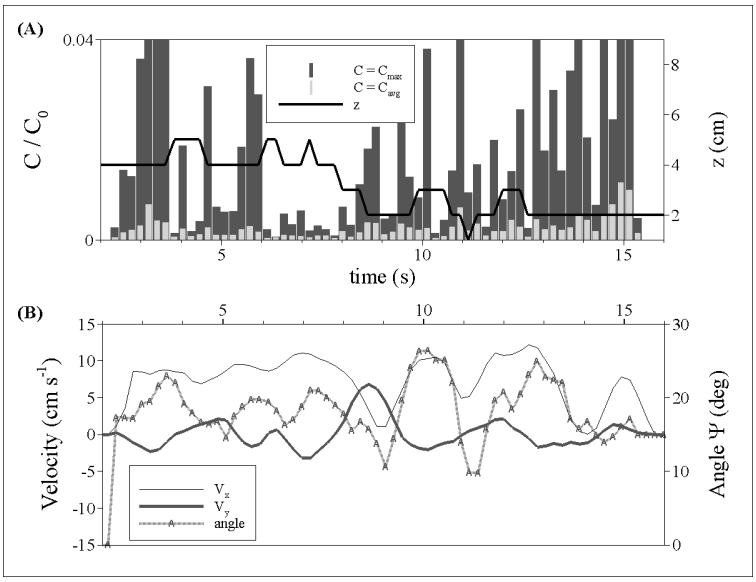

Figure A4. (A) **Crab 105N** time trace of maximum and average relative concentrations at antennules and body elevation above substrate (cm). (B) Time traces of streamwise V_x velocity, transverse V_y velocity and crab angle with respect to the flow Ψ.

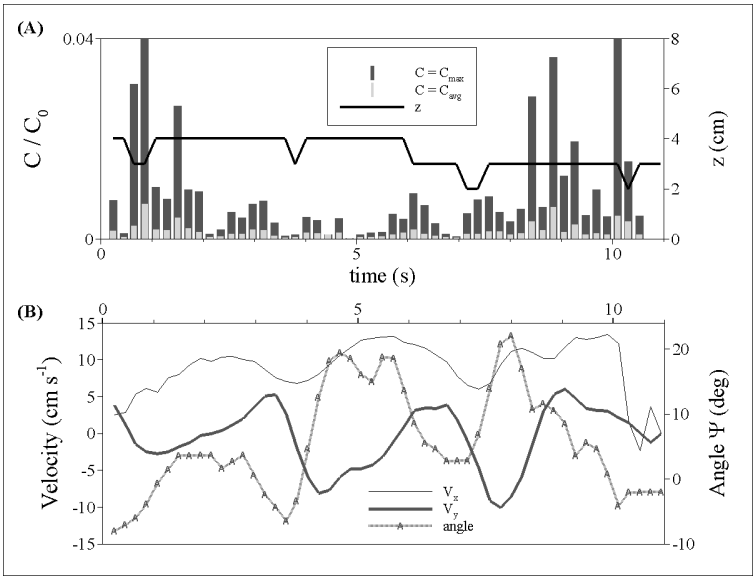

Figure A5. (A) **Crab 1305N** time trace of maximum and average relative concentrations at antennules and body elevation above substrate (cm). (B) Time traces of streamwise V_x velocity, transverse V_y velocity and crab angle with respect to the flow Ψ.

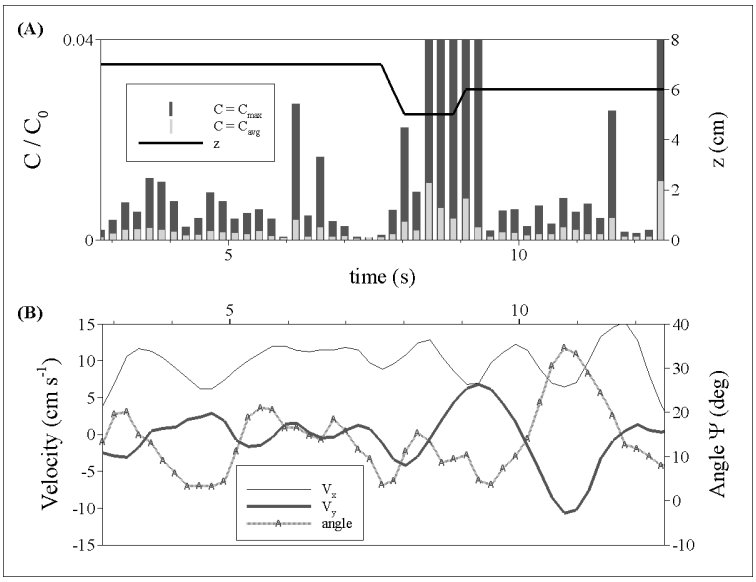

Figure A6. (A) **Crab 1221N** time trace of maximum and average relative concentrations at antennules and body elevation above substrate (cm). (B) Time traces of streamwise V_x velocity, transverse V_y velocity and crab angle with respect to the flow Ψ.

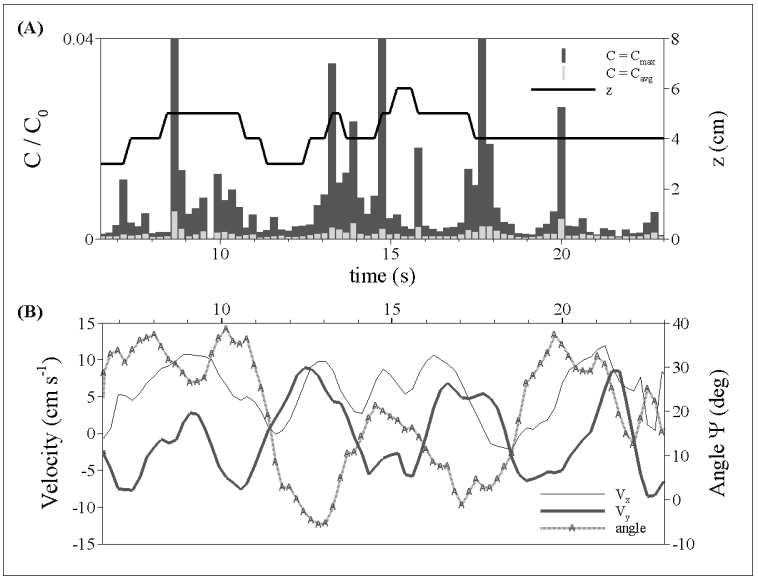

Figure A7. (A) **Crab 1271O** time trace of maximum and average relative concentrations at antennules and body elevation above substrate (cm). (B) Time traces of streamwise V_x velocity, transverse V_y velocity and crab angle with respect to the flow Ψ.

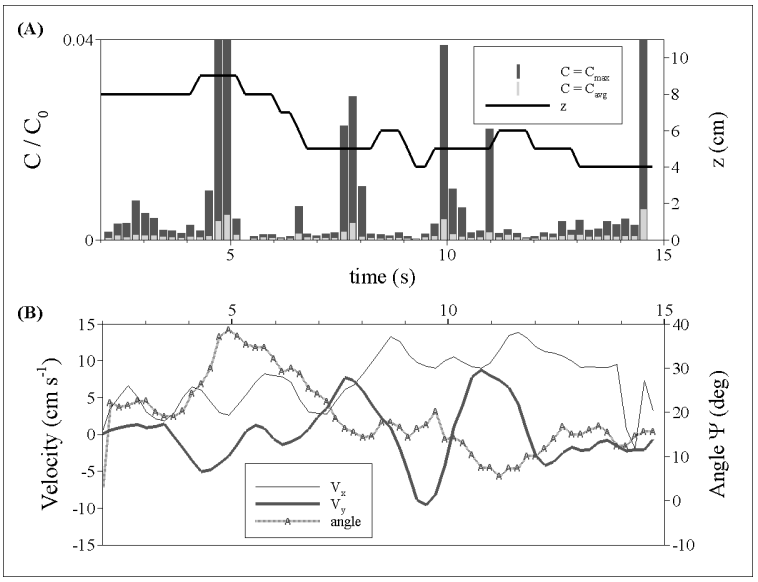

Figure A8. (A) **Crab 435O** time trace of maximum and average relative concentrations at antennules and body elevation above substrate (cm). (B) Time traces of streamwise V_x velocity, transverse V_y velocity and crab angle with respect to the flow Ψ.

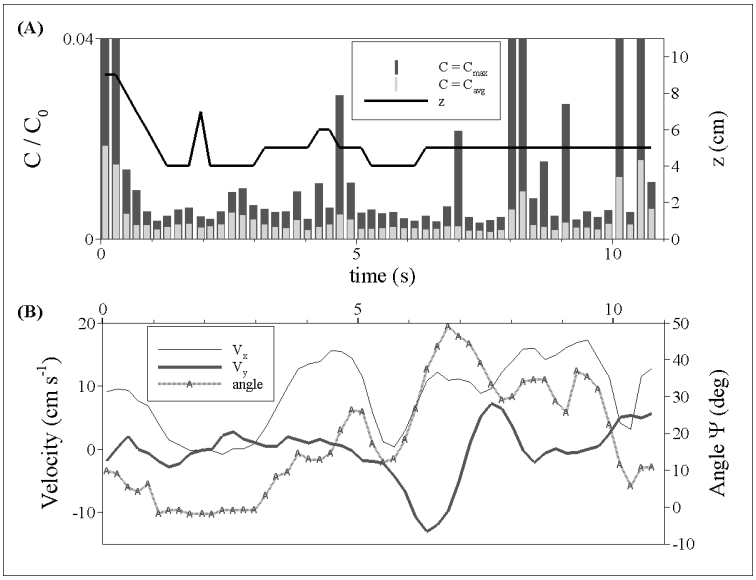

Figure A9. (A) **Crab 1238Q** time trace of maximum and average relative concentrations at antennules and body elevation above substrate (cm). (B) Time traces of streamwise V_x velocity, transverse V_y velocity and crab angle with respect to the flow Ψ.

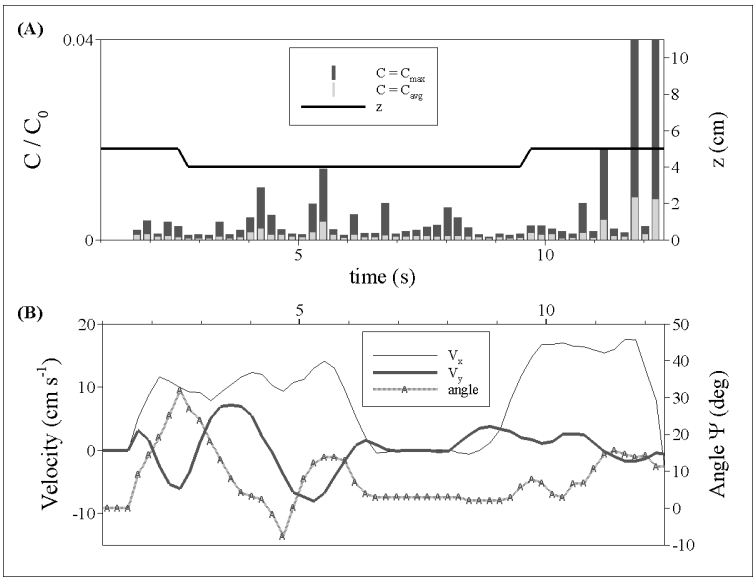

Figure A10. (A) **Crab 1399R** time trace of maximum and average relative concentration at antennules and body elevation above substrate (cm). (B) Time traces of streamwise V_x velocity, transverse V_y velocity and crab angle with respect to the flow Ψ.

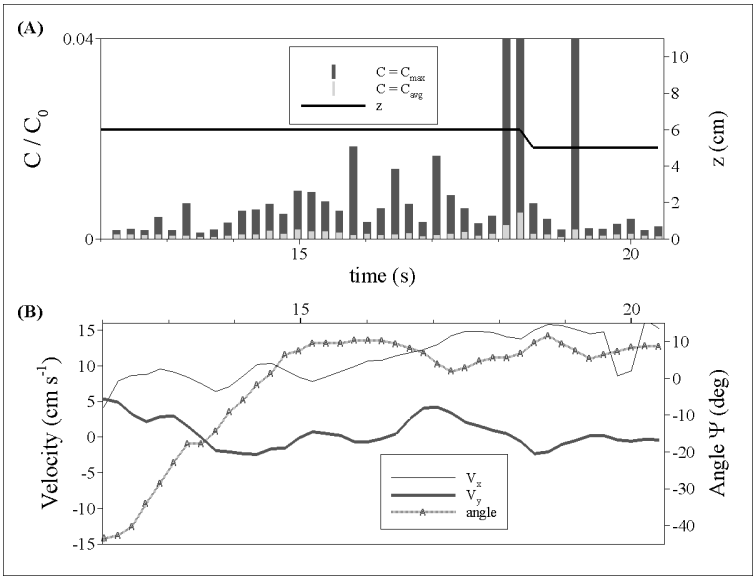

Figure A11. (A) **Crab 105R** time trace of maximum and average relative concentrations at antennules and body elevation above substrate (cm). (B) Time traces of streamwise V_x velocity, transverse V_y velocity and crab angle with respect to the flow Ψ.

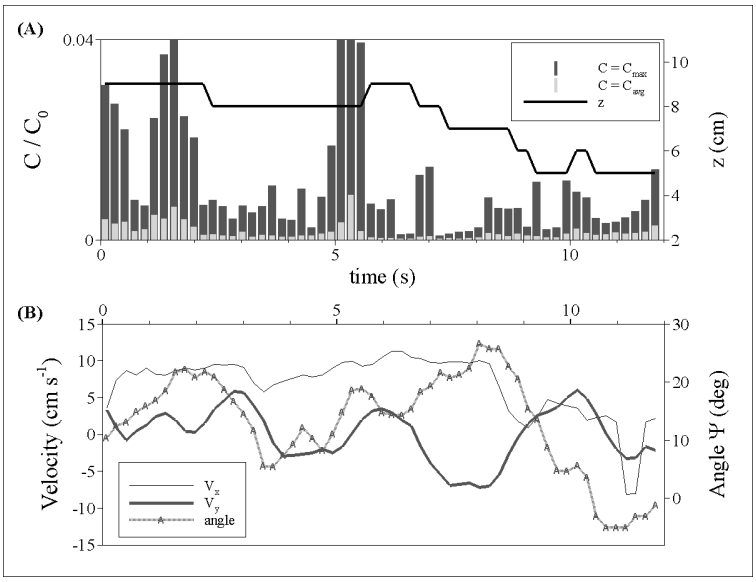

Figure A12. (A) **Crab 1394R** time trace of maximum and average relative concentrations at antennules and body elevation above substrate (cm). (B) Time traces of streamwise V_x velocity, transverse V_y velocity and crab angle with respect to the flow

Ψ.

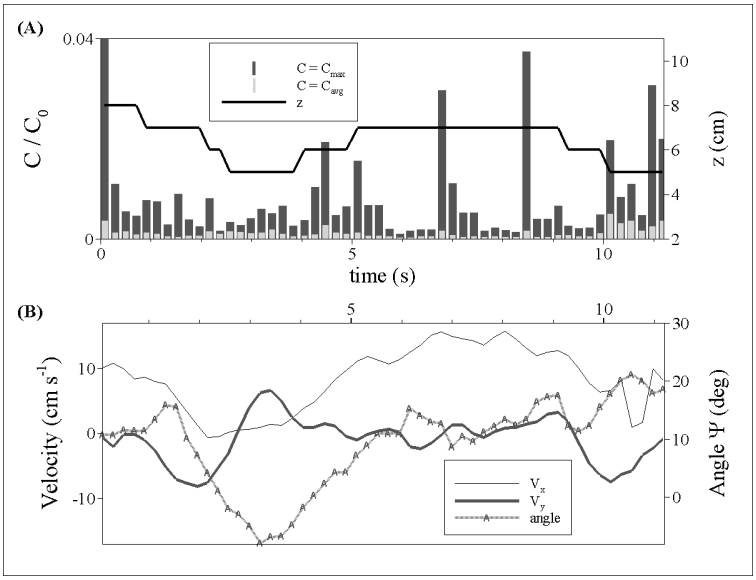

Figure A13. (A) **Crab 1238R** time trace of maximum and average relative concentrations at antennules and body elevation above substrate (cm). (B) Time traces of streamwise V_x velocity, transverse V_y velocity and crab angle with respect to the flow Ψ.

APPENDIX B

Time traces for outer chemosensors – Continuous plume

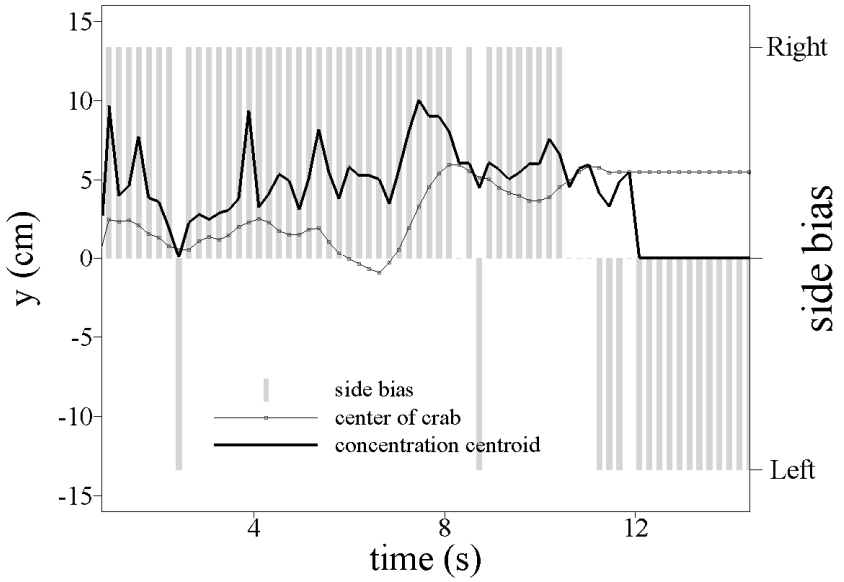

Figure B1. **Crab 105N** time trace of transverse coordinates (cm) of the center of crab and concentration centroid. Side bias shown to indicate where two transverse coordinates differ by more than 0.5 cm.

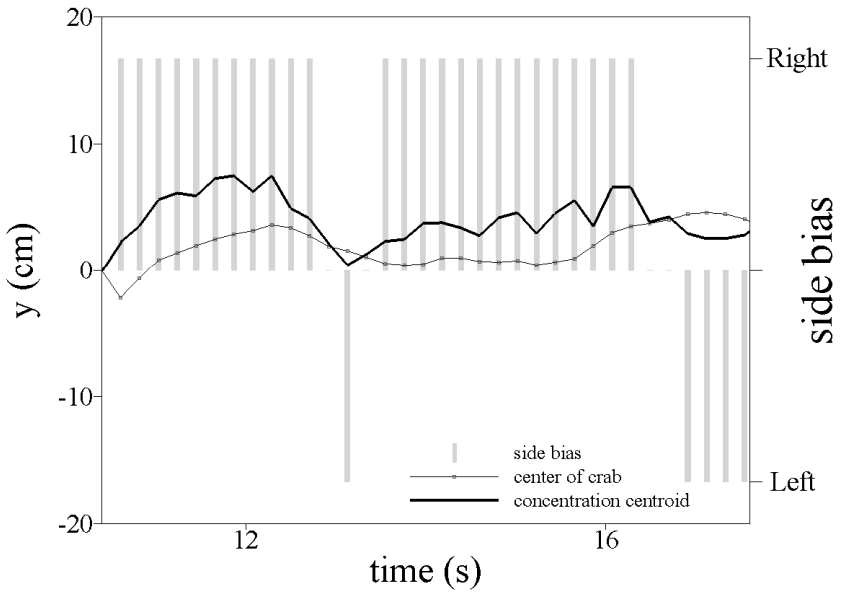

Figure B2. **Crab 105R** time trace of transverse coordinates (cm) of the center of crab and concentration centroid. Side bias shown to indicate where two transverse coordinates differ by more than 0.5 cm.

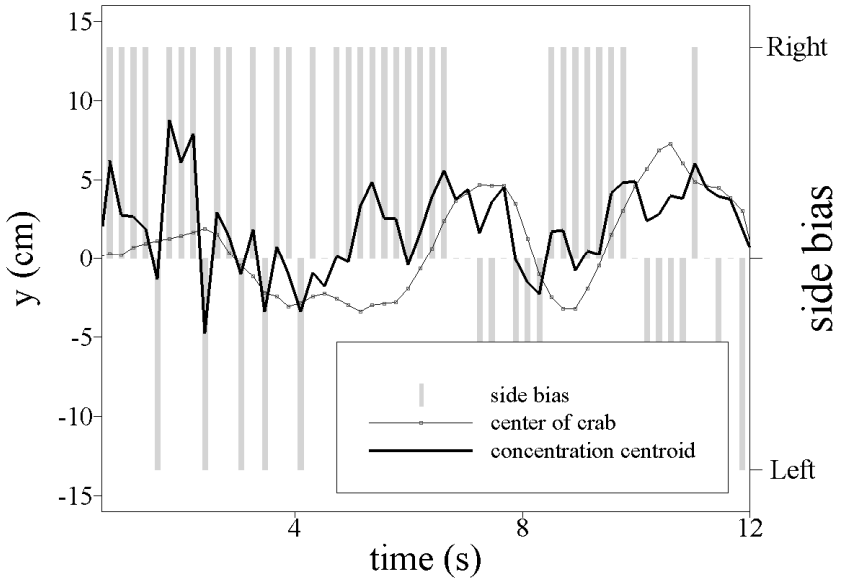

Figure B3. **Crab 435O** time trace of transverse coordinates (cm) of the center of crab and concentration centroid. Side bias shown to indicate where two transverse coordinates differ by more than 0.5 cm.

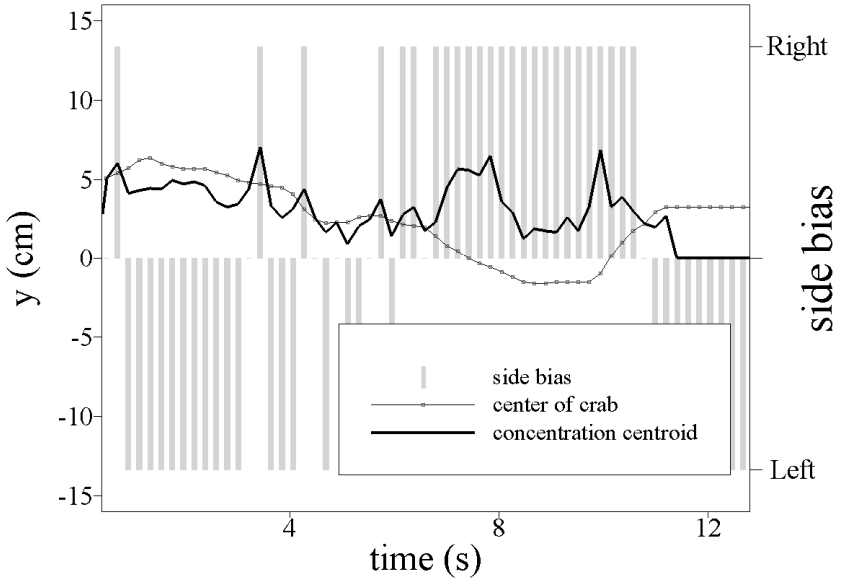

Figure B4. **Crab 465L** time trace of transverse coordinates (cm) of the center of crab and concentration centroid. Side bias shown to indicate where two transverse coordinates differ by more than 0.5 cm.

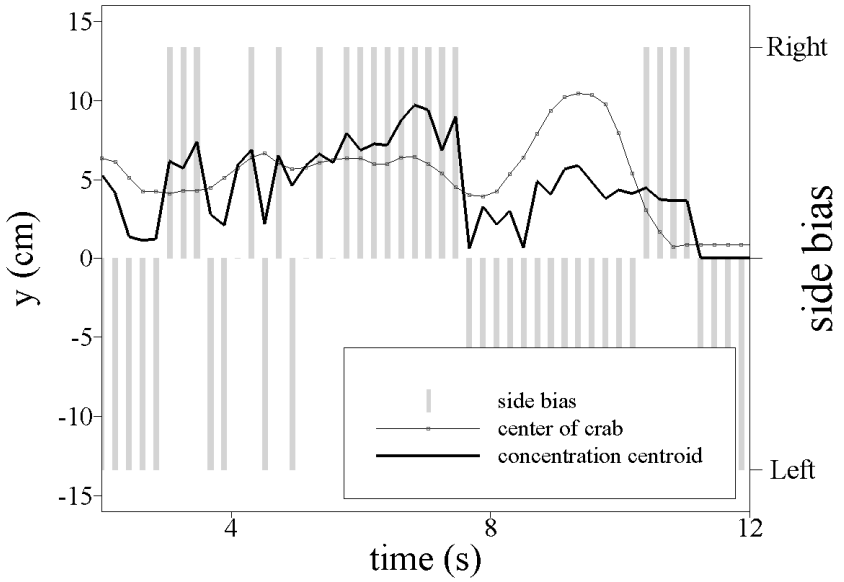

Figure B5. **Crab 1221N** time trace of transverse coordinates (cm) of the center of crab and concentration centroid. Side bias shown to indicate where two transverse coordinates differ by more than 0.5 cm.

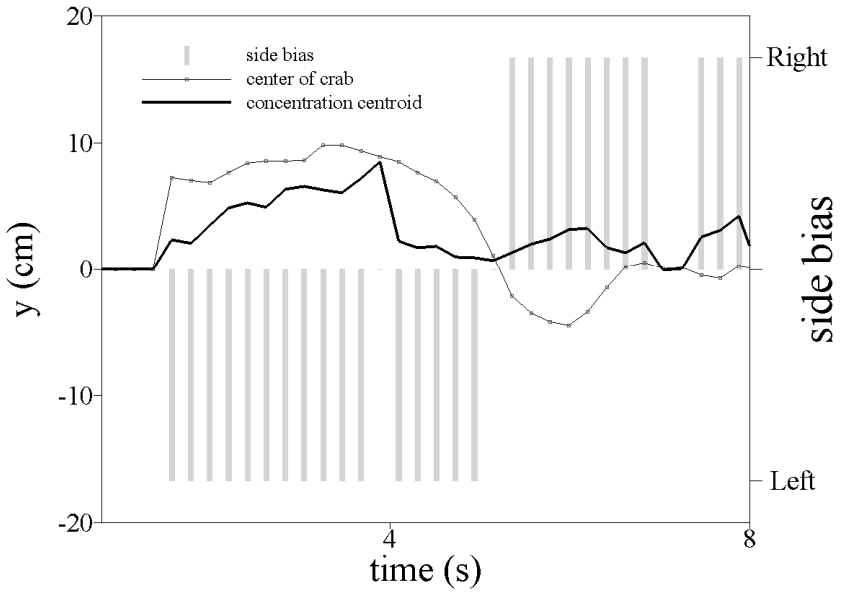

Figure B6. **Crab 1238Q** time trace of transverse coordinates (cm) of the center of crab and concentration centroid. Side bias shown to indicate where two transverse coordinates differ by more than 0.5 cm.

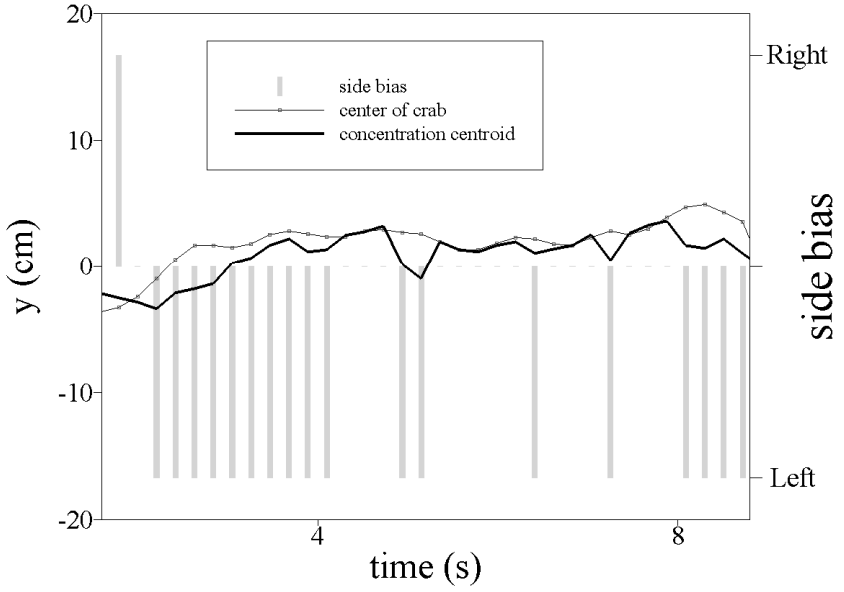

Figure B7. **Crab 1238R** time trace of transverse coordinates (cm) of the center of crab and concentration centroid. Side bias shown to indicate where two transverse coordinates differ by more than 0.5 cm.

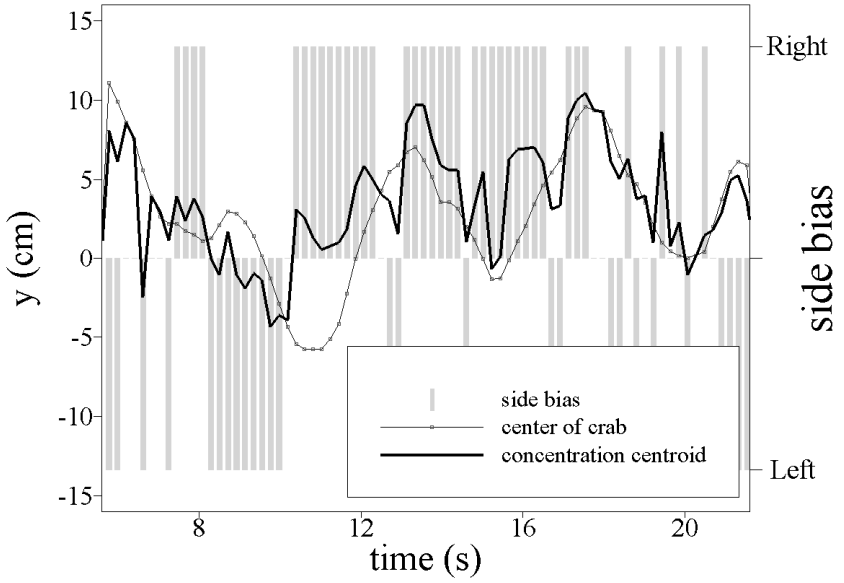

Figure B8. **Crab 1271O** time trace of transverse coordinates (cm) of the center of crab and concentration centroid. Side bias shown to indicate where two transverse coordinates differ by more than 0.5 cm.

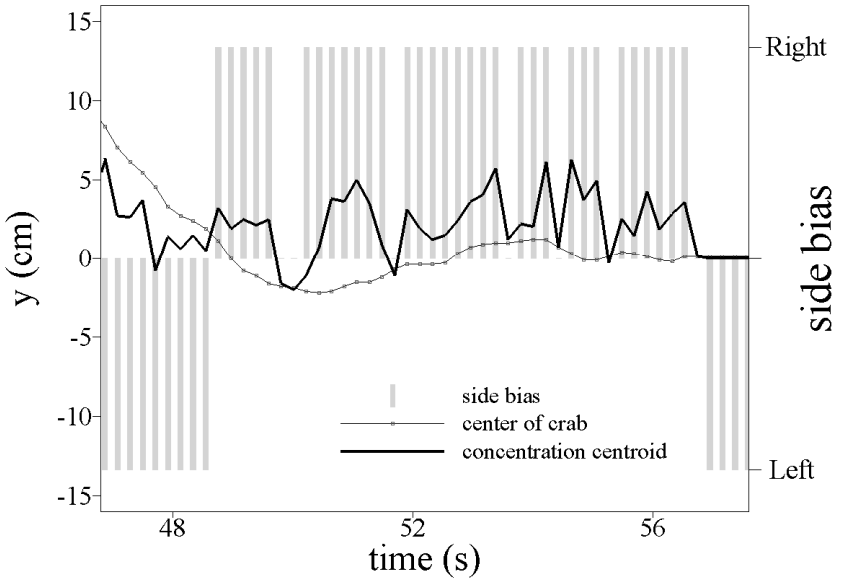

Figure B9. **Crab 1305H** time trace of transverse coordinates (cm) of the center of crab and concentration centroid. Side bias shown to indicate where two transverse coordinates differ by more than 0.5 cm.

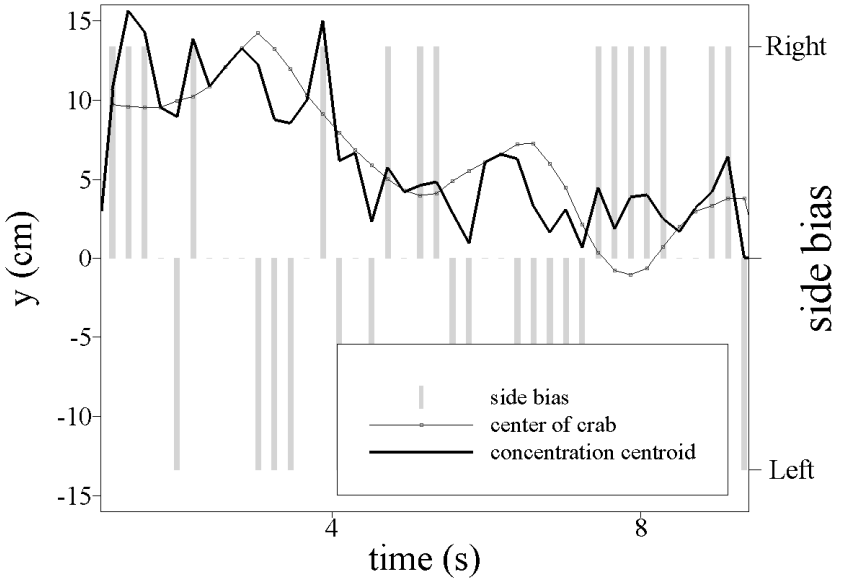

Figure B10. **Crab 13O5N** time trace of transverse coordinates (cm) of the center of crab and concentration centroid. Side bias shown to indicate where two transverse coordinates differ by more than 0.5 cm.

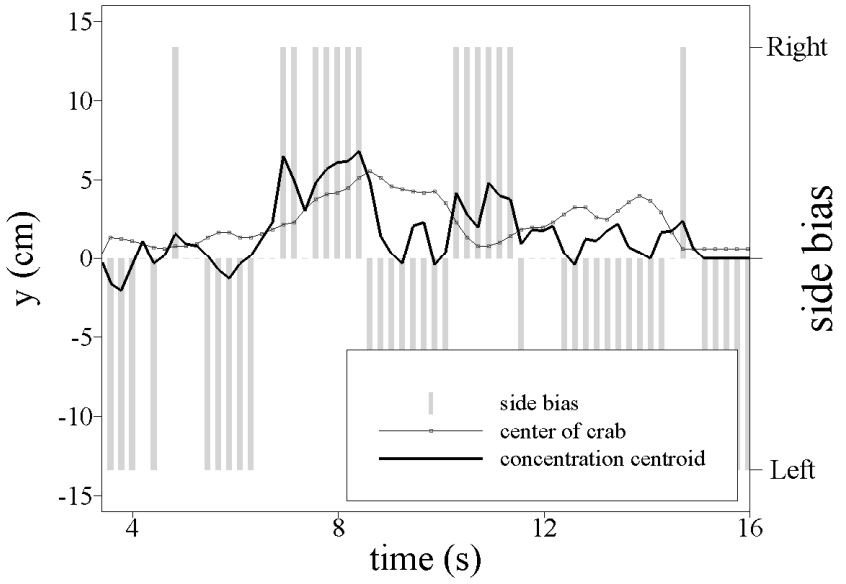

Figure B11. **Crab 1364L** time trace of transverse coordinates (cm) of the center of crab and concentration centroid. Side bias shown to indicate where two transverse coordinates differ by more than 0.5 cm.

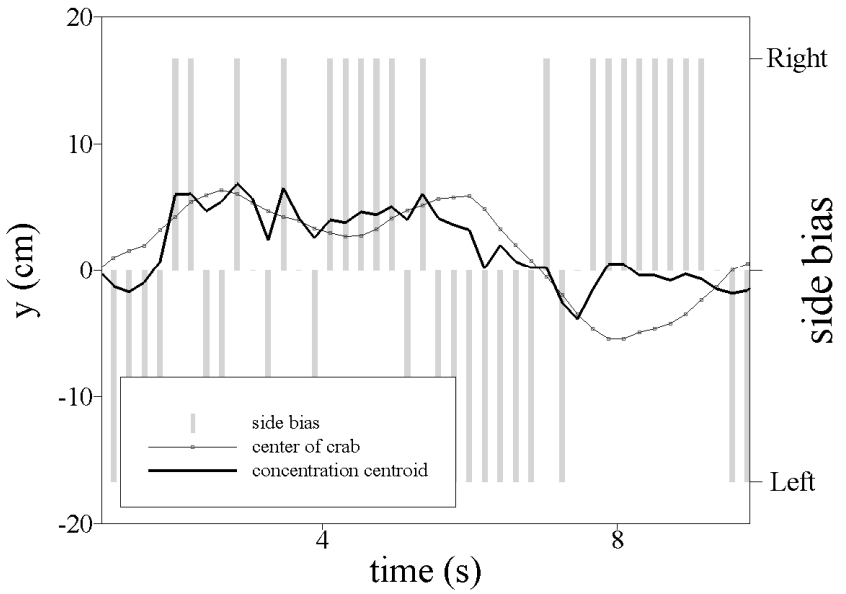

Figure B12. (A) **Crab 1394R** time trace of transverse coordinates (cm) of the center of crab and concentration centroid. Side bias shown to indicate where two transverse coordinates differ by more than 0.5 cm.

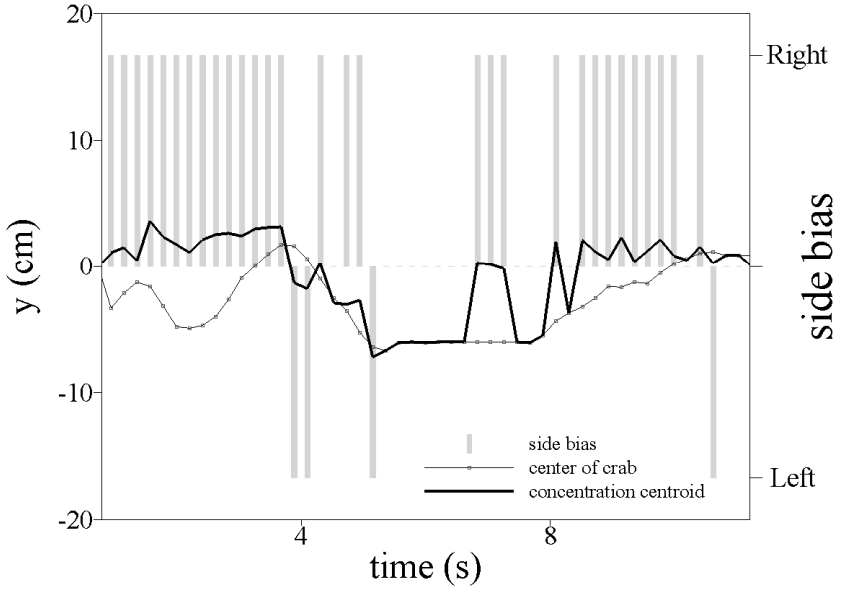

Figure B13. **Crab 1399R** time trace of transverse coordinates (cm) of the center of crab and concentration centroid. Side bias shown to indicate where two transverse coordinates differ by more than 0.5 cm.

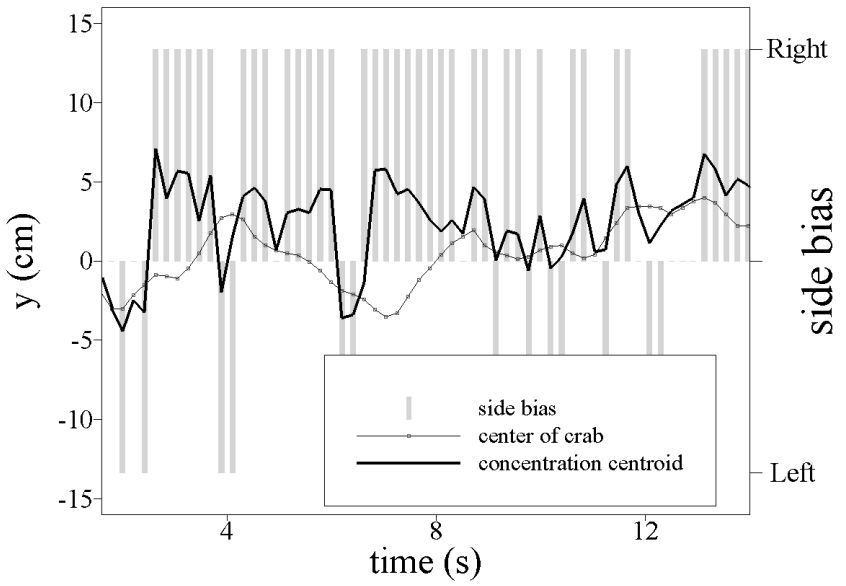

Figure B14. **Crab 119O** time trace of transverse coordinates (cm) of the center of crab and concentration centroid. Side bias shown to indicate where two transverse coordinates differ by more than 0.5 cm.

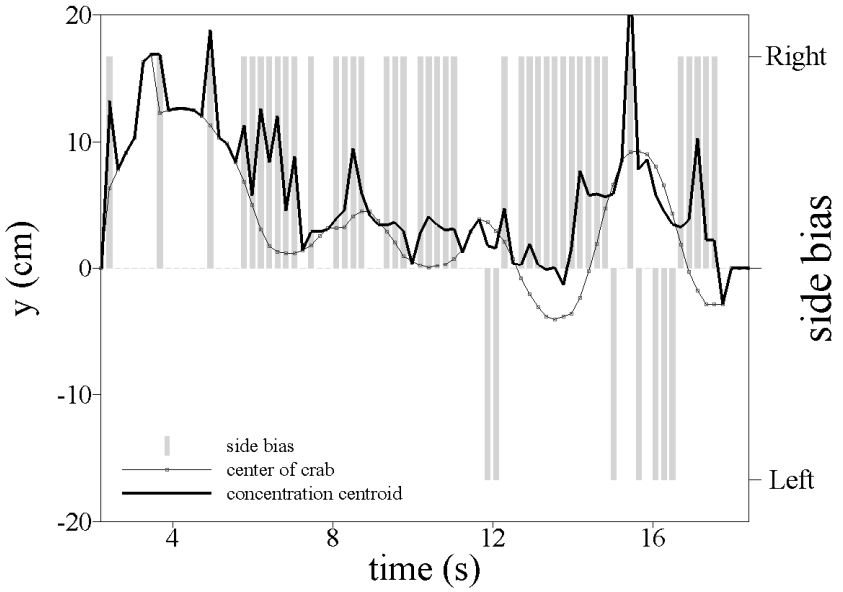

Figure B15. **Crab 1357N** time trace of transverse coordinates (cm) of the center of crab and concentration centroid. Side bias shown to indicate where two transverse coordinates differ by more than 0.5 cm.

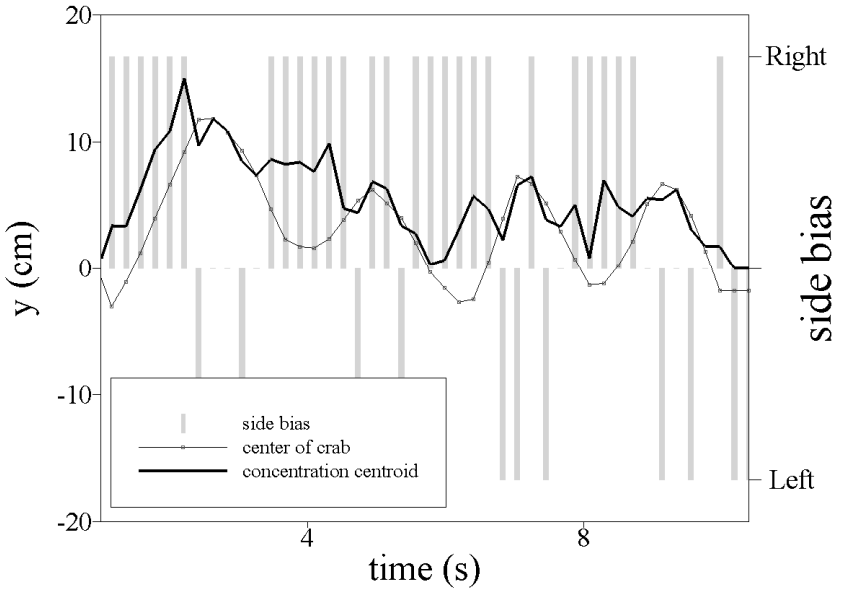

Figure B16. **Crab 1363N** time trace of transverse coordinates (cm) of the center of crab and concentration centroid. Side bias shown to indicate where two transverse coordinates differ by more than 0.5 cm.

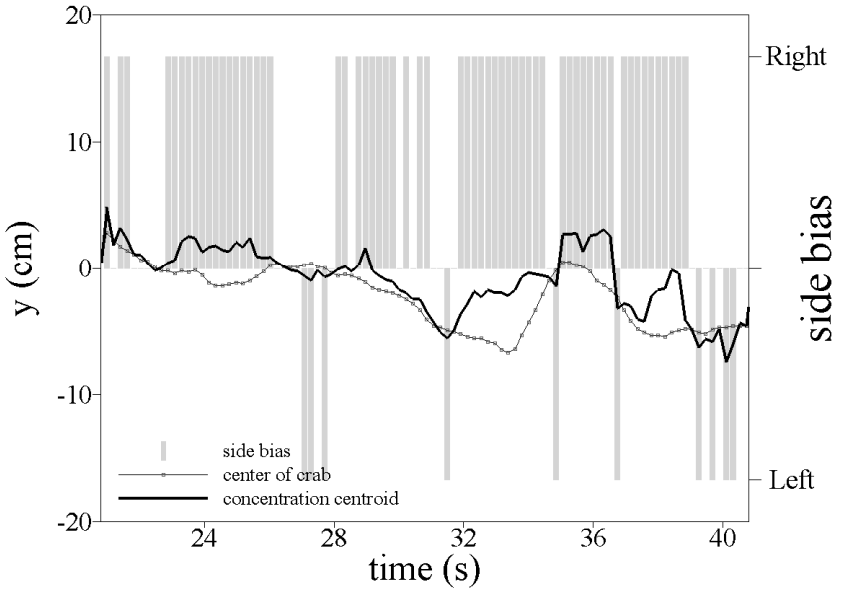

Figure B17. **Crab 1314L** time trace of transverse coordinates (cm) of the center of crab and concentration centroid. Side bias shown to indicate where two transverse coordinates differ by more than 0.5 cm.

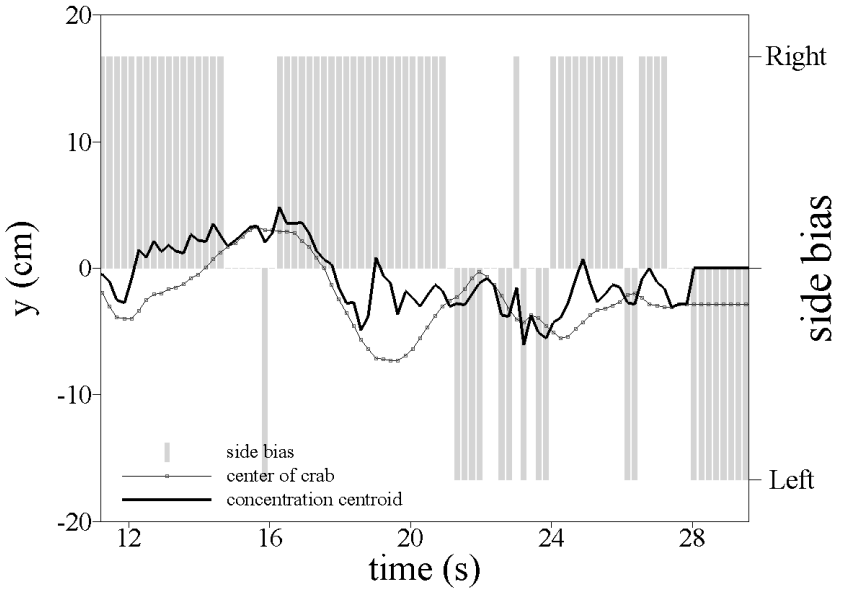

Figure B18. **Crab 1347L** time trace of transverse coordinates (cm) of the center of crab and concentration centroid. Side bias shown to indicate where two transverse coordinates differ by more than 0.5 cm.

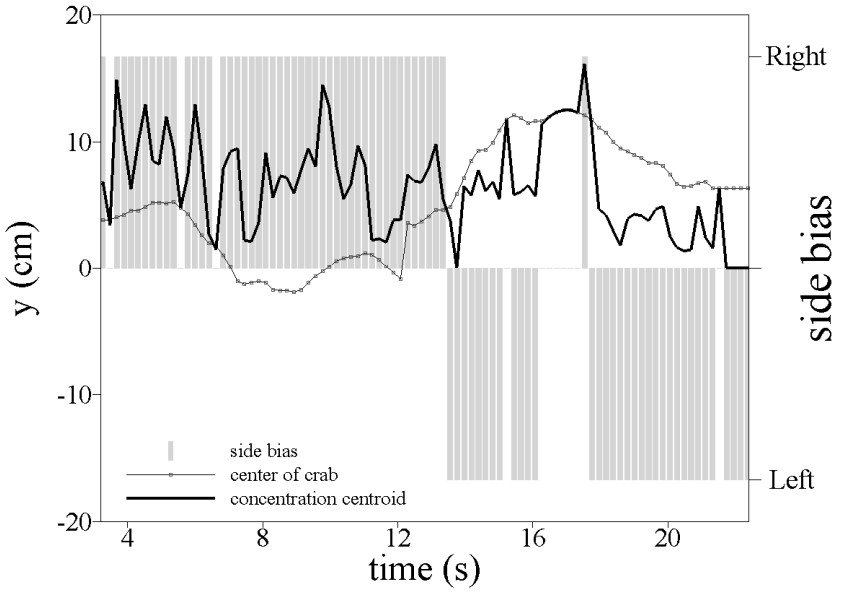

Figure B19. **Crab 1331N** time trace of transverse coordinates (cm) of the center of crab and concentration centroid. Side bias shown to indicate where two transverse coordinates differ by more than 0.5 cm.

Appendix C

Time traces of antennules sampling zone – Meandering plume

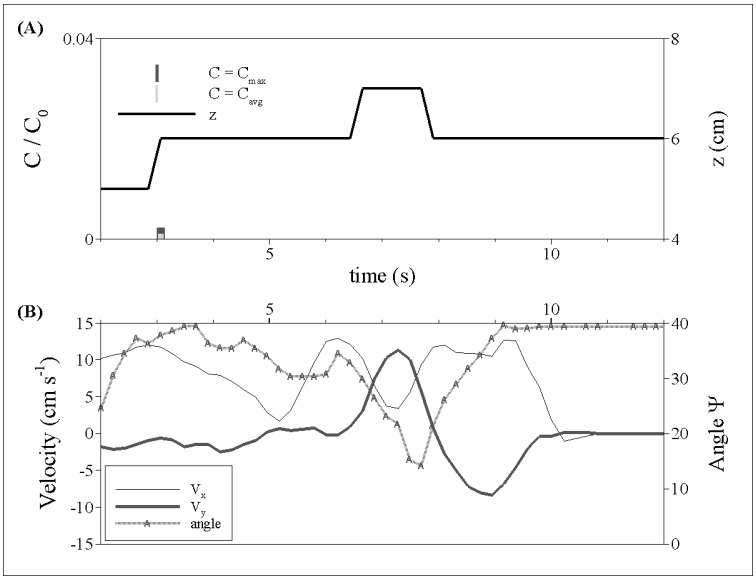

Figure C1. (A) **Crab 417K** time trace of maximum and average relative concentrations at antennules and body elevation above substrate (cm). (B) Time traces of streamwise V_x velocity, transverse V_y velocity and crab angle with respect to the flow, Ψ.

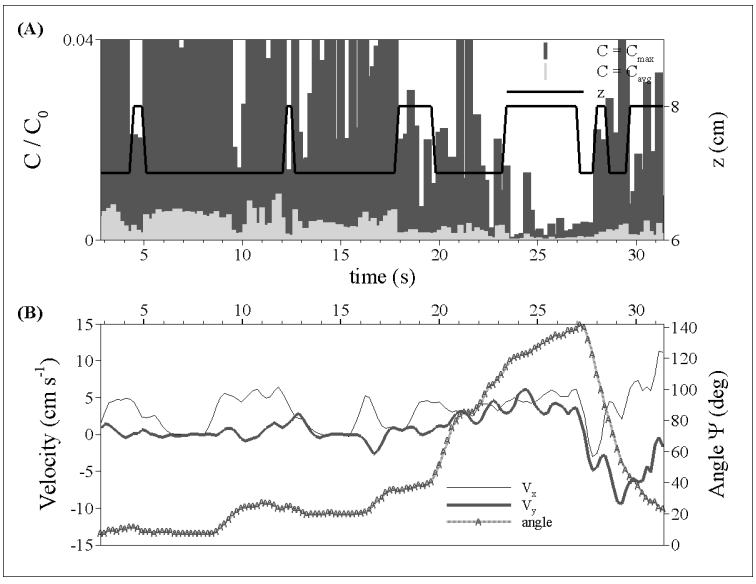

Figure C2. (A) **Crab 1034P** time trace of maximum and average relative concentrations at antennules and body elevation above substrate (cm). (B) Time traces of streamwise V_x velocity, transverse V_y velocity and crab angle with respect to the flow, Ψ.

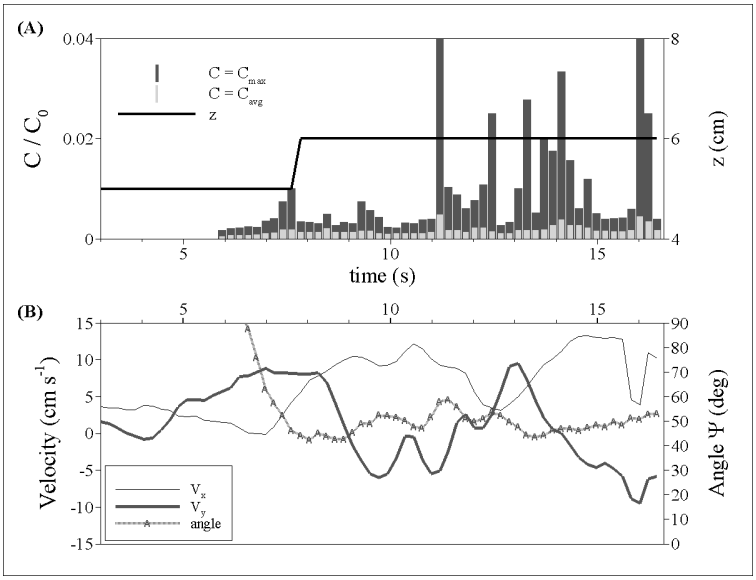

Figure C3. (A) **Crab 1213Q** time trace of maximum and average relative concentrations at antennules and body elevation above substrate (cm). (B) Time traces of streamwise V_x velocity, transverse V_y velocity and crab angle with respect to the flow, Ψ.

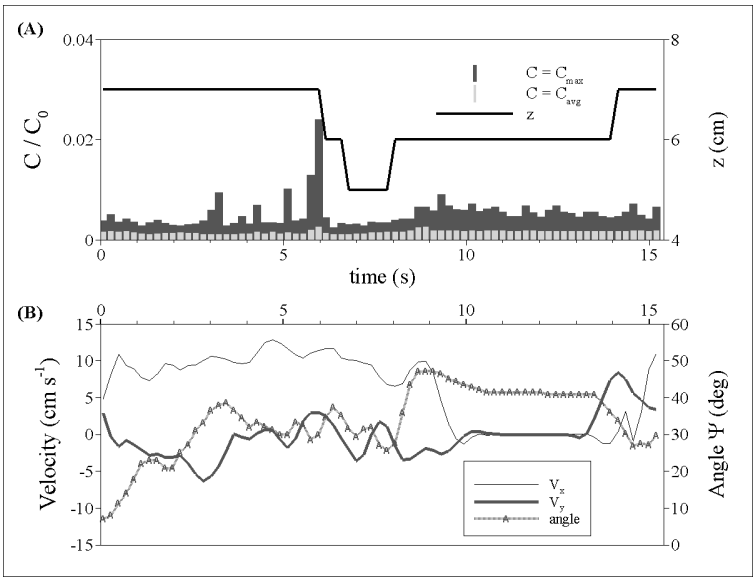

Figure C4. (A) **Crab 1237Q** time trace of maximum and average relative concentrations at antennules and body elevation above substrate (cm). (B) Time traces of streamwise V_x velocity, transverse V_y velocity and crab angle with respect to the flow, Ψ.

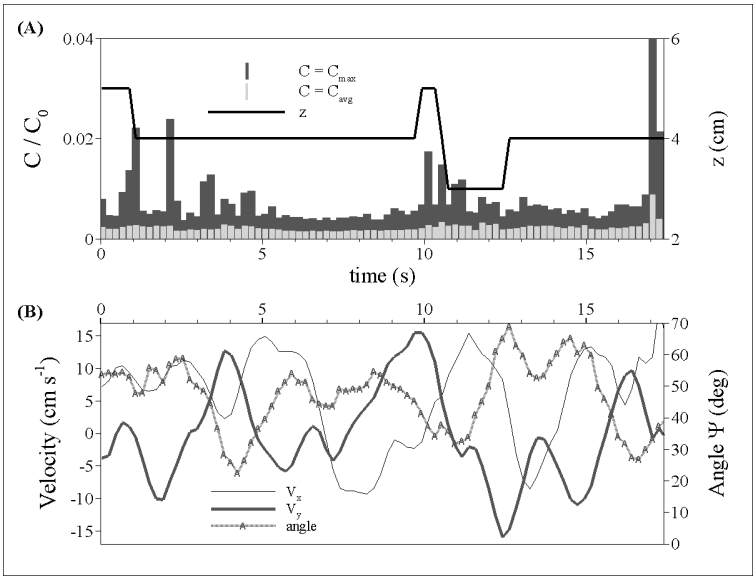

Figure C5. (A) **Crab 1262Q** time trace of maximum and average relative concentrations at antennules and body elevation above substrate (cm). (B) Time traces of streamwise V_x velocity, transverse V_y velocity and crab angle with respect to the flow, Ψ.

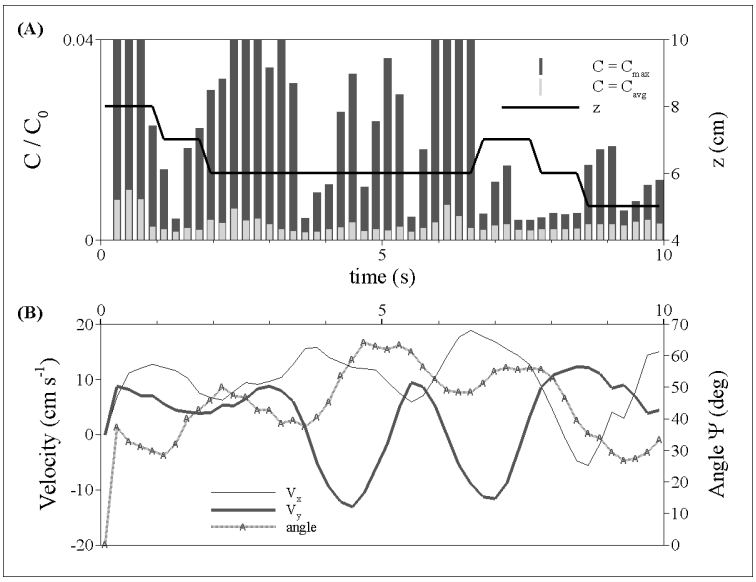

Figure C6. (A) **Crab 1115Q** time trace of maximum and average relative concentrations at antennules and body elevation above substrate (cm). (B) Time traces of streamwise V_x velocity, transverse V_y velocity and crab angle with respect to the flow, Ψ.

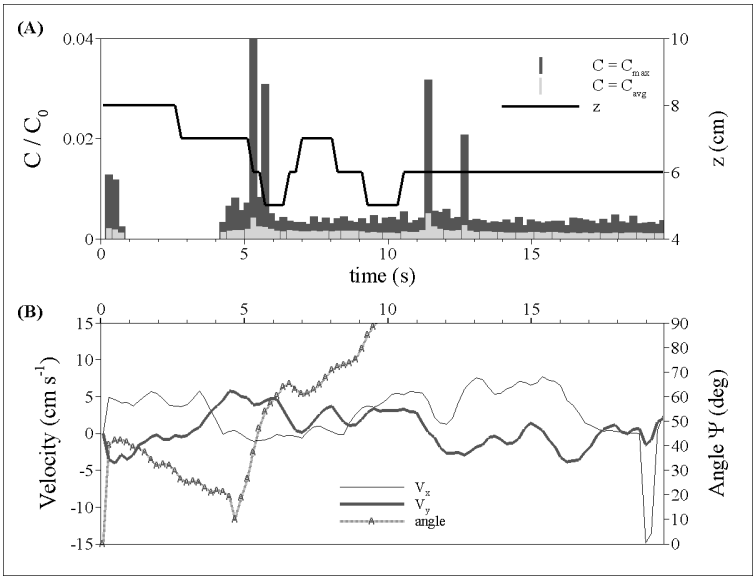

Figure C7. (A) **Crab 1241Q** time trace of maximum and average relative concentrations at antennules and body elevation above substrate (cm). (B) Time traces of streamwise V_x velocity, transverse V_y velocity and crab angle with respect to the flow, Ψ.

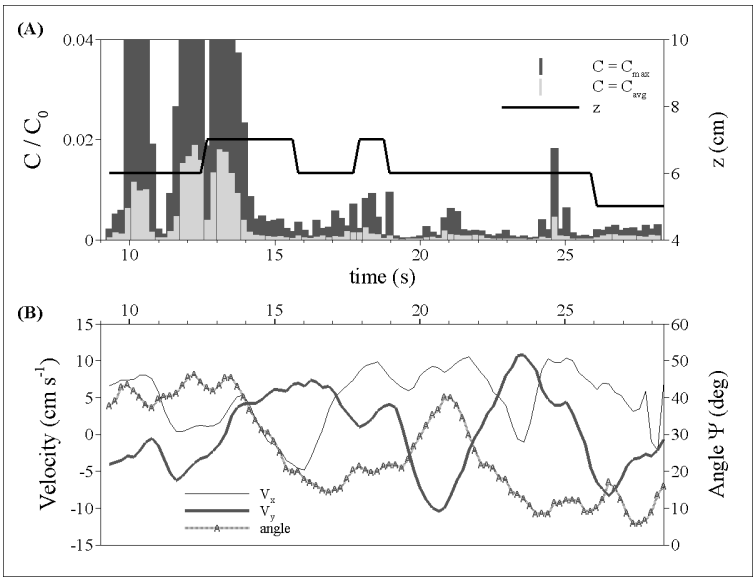

Figure C8. (A) **Crab 1265S** time trace of maximum and average relative concentrations at antennules and body elevation above substrate (cm). (B) Time traces of streamwise V_x velocity, transverse V_y velocity and crab angle with respect to the flow, Ψ.

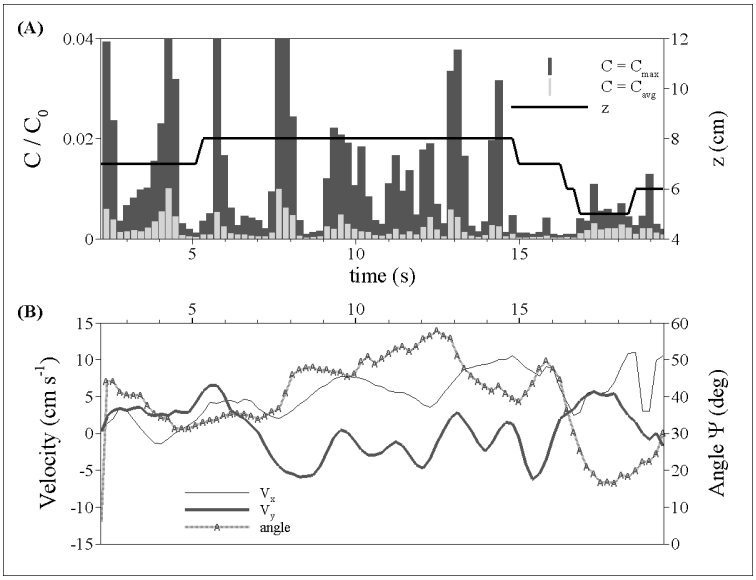

Figure C9. (A) **Crab 1351S** time trace of maximum and average relative concentrations at antennules and body elevation above substrate (cm). (B) Time traces of streamwise V_x velocity, transverse V_y velocity and crab angle with respect to the flow, Ψ.

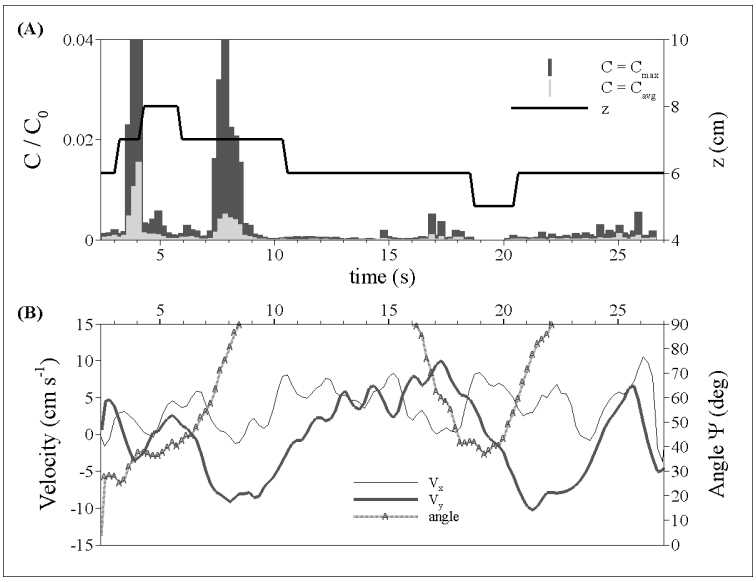

Figure C10. (A) **Crab 1393S** time trace of maximum and average relative concentrations at antennules and body elevation above substrate (cm). (B) Time traces of streamwise V_x velocity, transverse V_y velocity and crab angle with respect to the flow, Ψ.

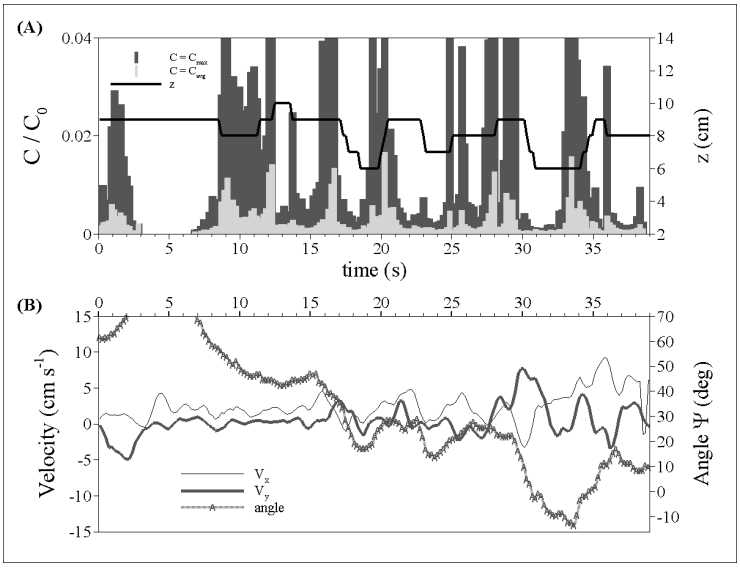

Figure C11. (A) **Crab 1336S** time trace of maximum and average relative concentrations at antennules and body elevation above substrate (cm). (B) Time traces of streamwise V_x velocity, transverse V_y velocity and crab angle with respect to the flow, Ψ.

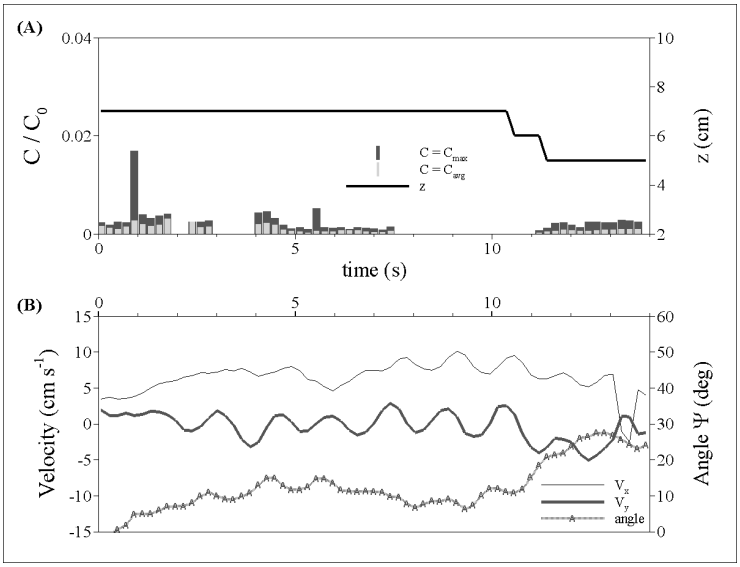

Figure C12. (A) **Crab 1306S** time trace of maximum and average relative concentrations at antennules and body elevation above substrate (cm). (B) Time traces of streamwise V_x velocity, transverse V_y velocity and crab angle with respect to the flow, Ψ.

APPENDIX D

Time traces for outer chemosensors – Meandering plume

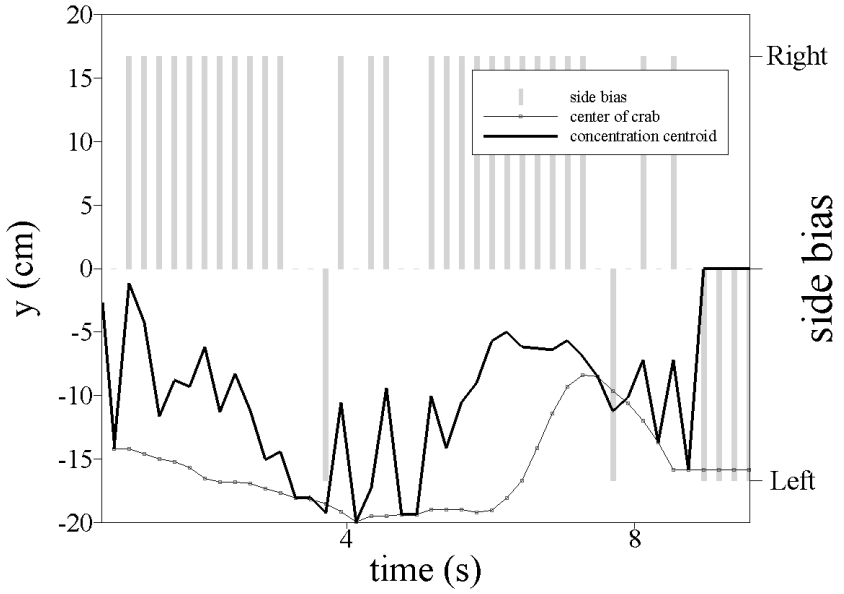

Figure D1. **Crab 417K** time trace of transverse coordinates (cm) of the center of crab and concentration centroid. Side bias shown to indicate where two transverse coordinates differ by more than 0.5 cm.

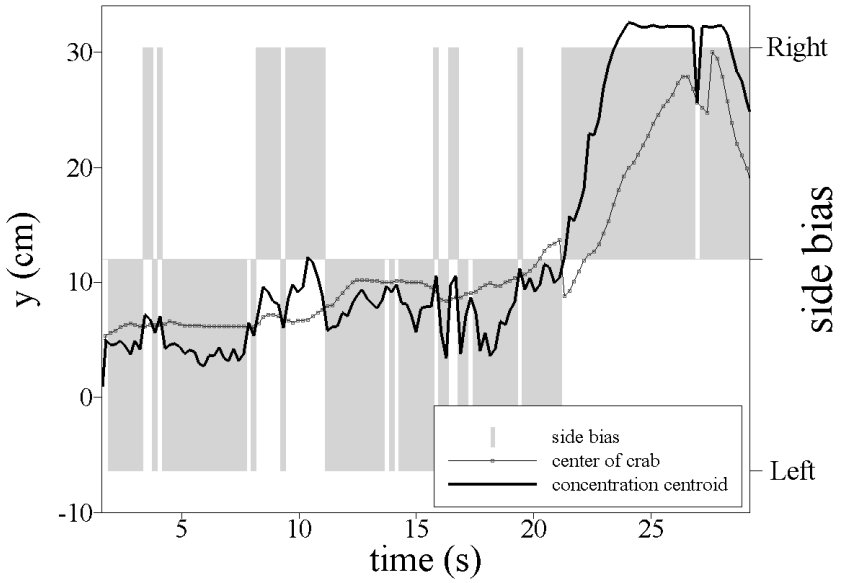

Figure D2. **Crab 1034P** time trace of transverse coordinates (cm) of the center of crab and concentration centroid. Side bias shown to indicate where two transverse coordinates differ by more than 0.5 cm.

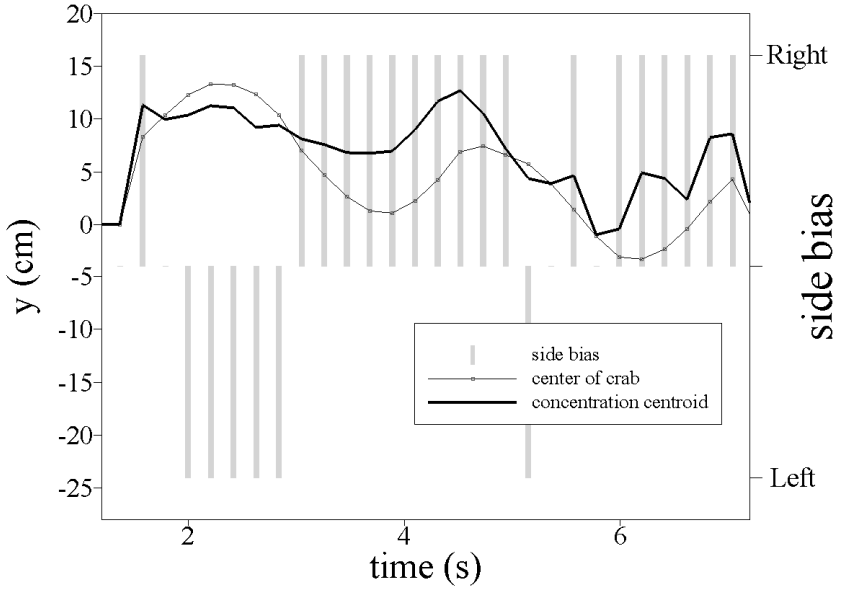

Figure D3. **Crab 1115Q** time trace of transverse coordinates (cm) of the center of crab and concentration centroid. Side bias shown to indicate where two transverse coordinates differ by more than 0.5 cm.

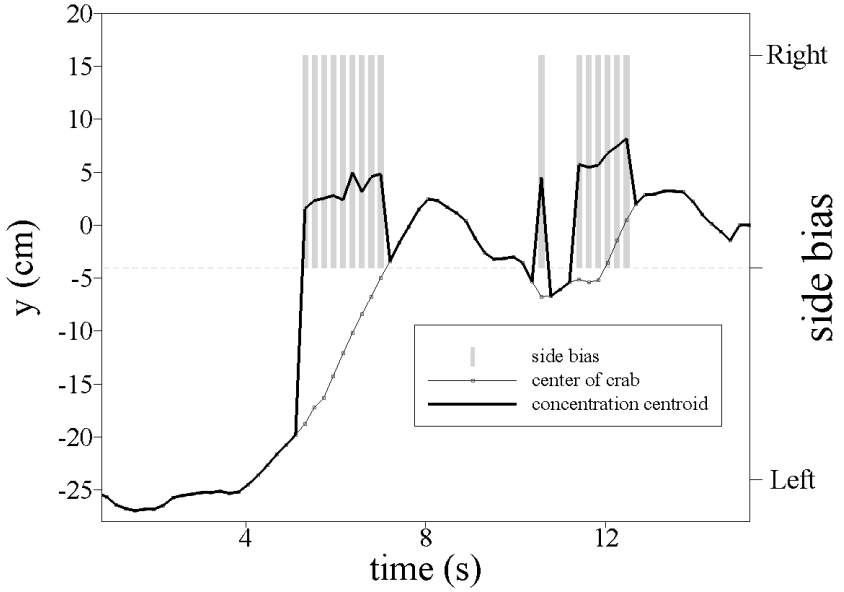

Figure D4. **Crab 1213Q** time trace of transverse coordinates (cm) of the center of crab and concentration centroid. Side bias shown to indicate where two transverse coordinates differ by more than 0.5 cm.

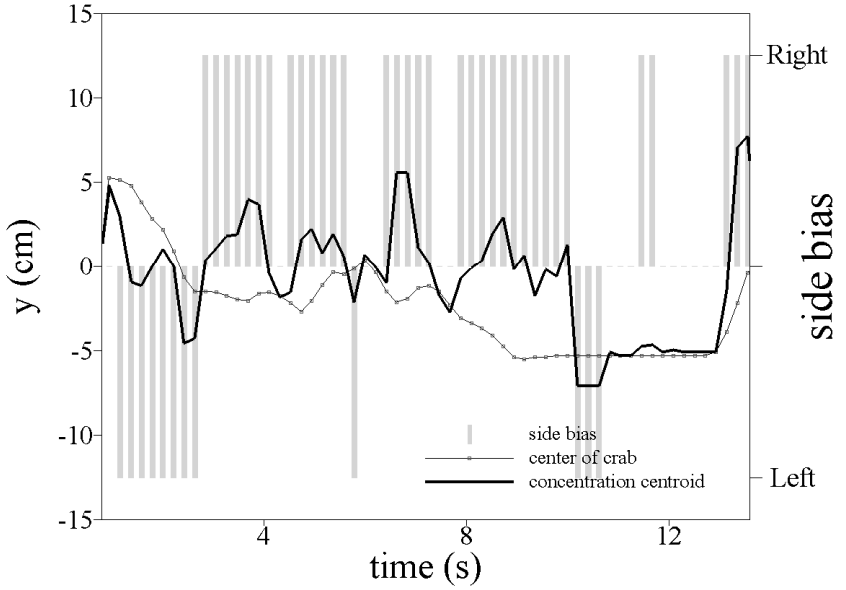

Figure D5. **Crab 1237Q** time trace of transverse coordinates (cm) of the center of crab and concentration centroid. Side bias shown to indicate where two transverse coordinates differ by more than 0.5 cm.

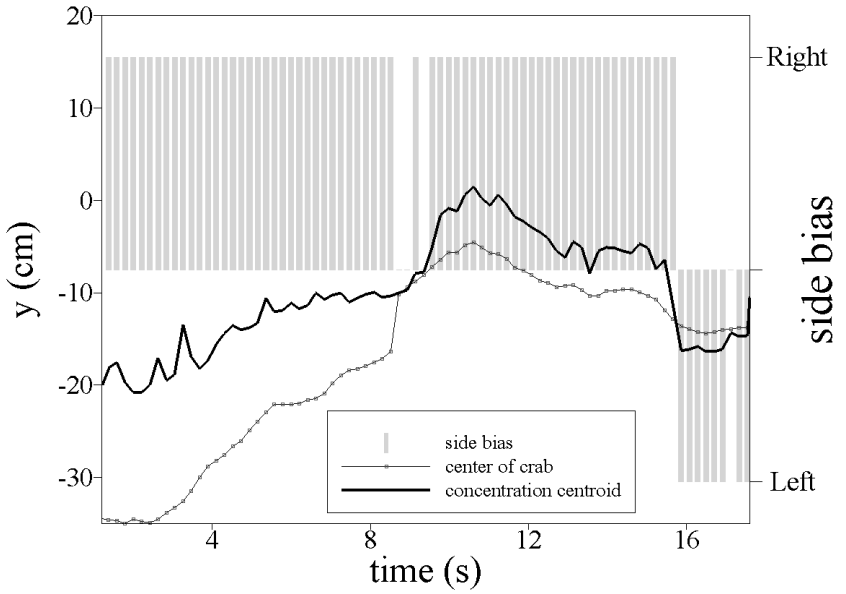

Figure D6. **Crab 1241Q** time trace of transverse coordinates (cm) of the center of crab and concentration centroid. Side bias shown to indicate where two transverse coordinates differ by more than 0.5 cm.

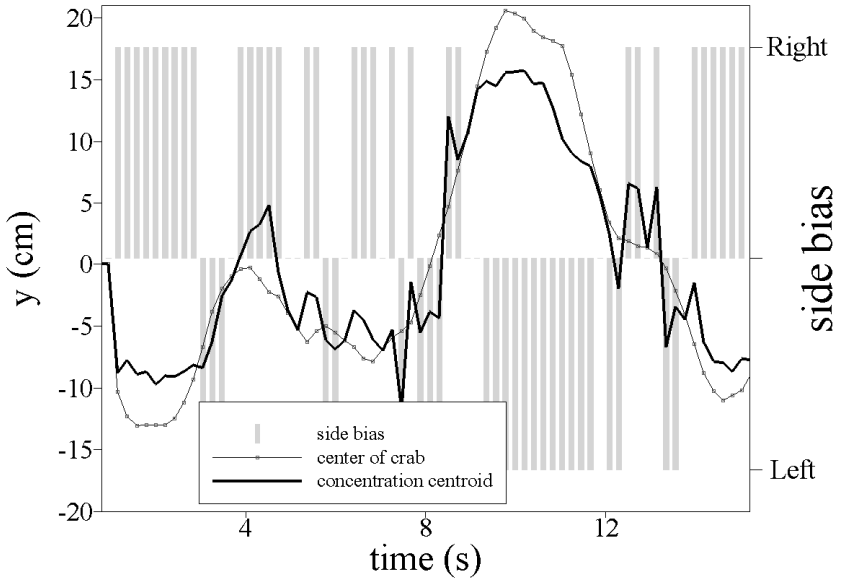

Figure D7. **Crab 1262Q** time trace of transverse coordinates (cm) of the center of crab and concentration centroid. Side bias shown to indicate where two transverse coordinates differ by more than 0.5 cm.

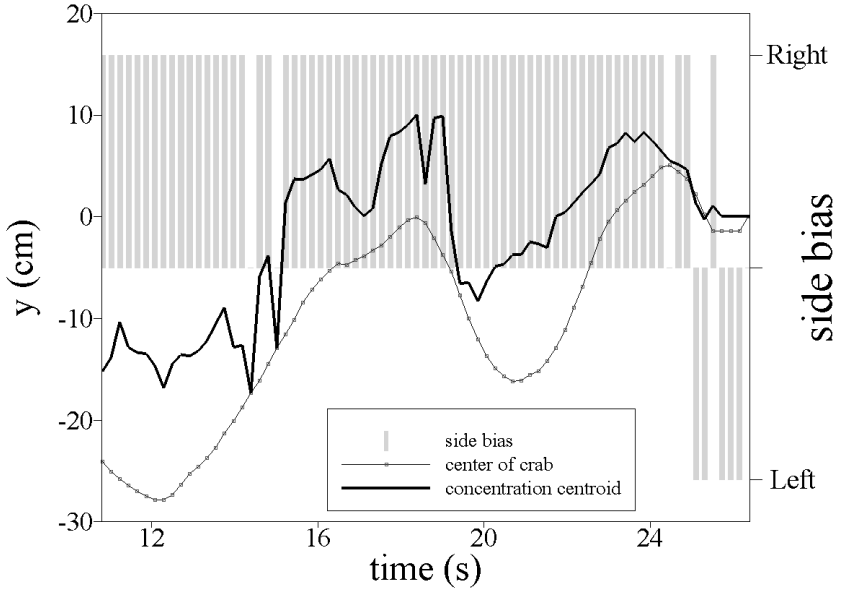

Figure D8. **Crab 1265S** time trace of transverse coordinates (cm) of the center of crab and concentration centroid. Side bias shown to indicate where two transverse coordinates differ by more than 0.5 cm.

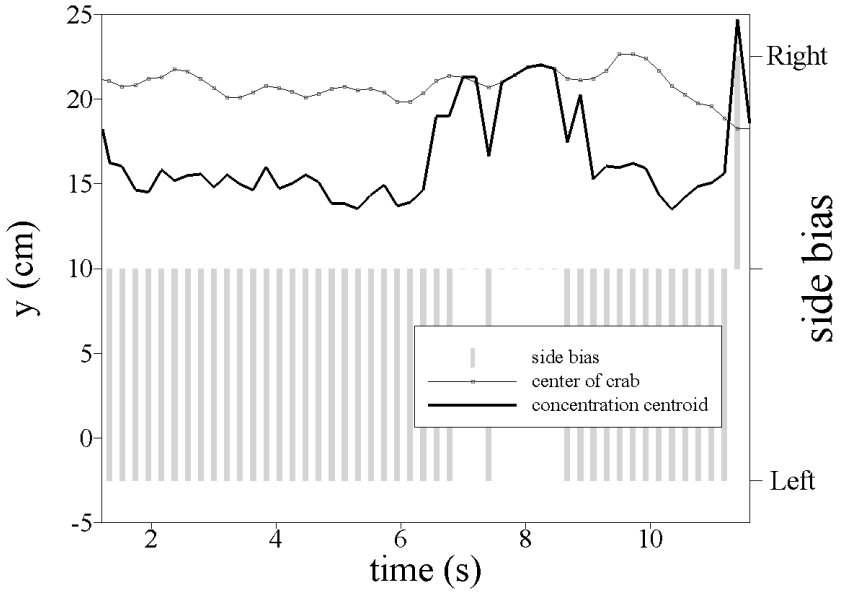

Figure D9. **Crab 1306S** time trace of transverse coordinates (cm) of the center of crab and concentration centroid. Side bias shown to indicate where two transverse coordinates differ by more than 0.5 cm.

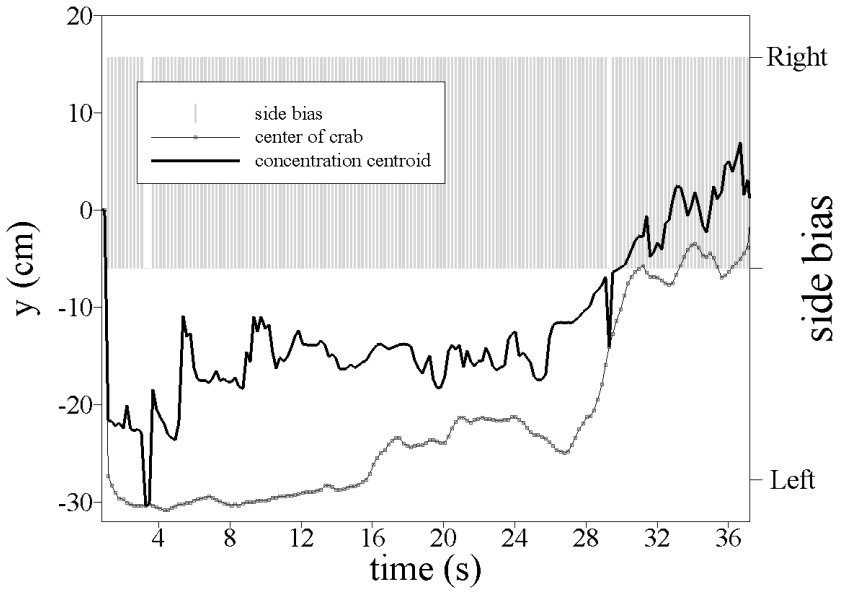

Figure D10. **Crab 1336S** time trace of transverse coordinates (cm) of the center of crab and concentration centroid. Side bias shown to indicate where two transverse coordinates differ by more than 0.5 cm.

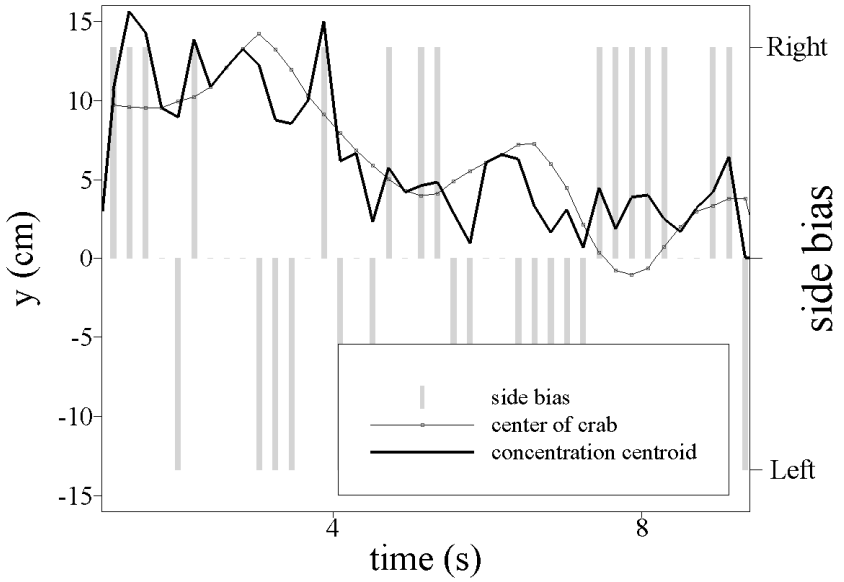

Figure D11. **Crab 1351S** time trace of transverse coordinates (cm) of the center of crab and concentration centroid. Side bias shown to indicate where two transverse coordinates differ by more than 0.5 cm.

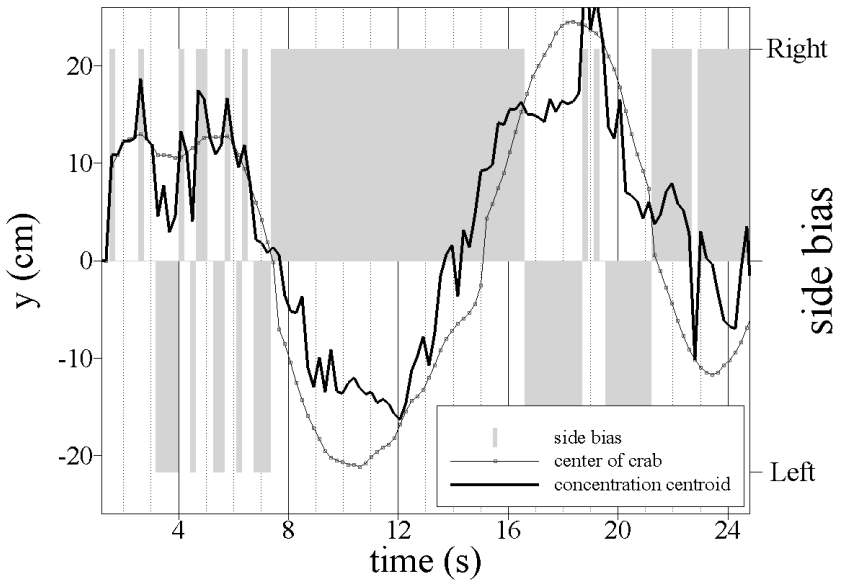

Figure D12. **Crab 1393S** time trace of transverse coordinates (cm) of the center of crab and concentration centroid. Side bias shown to indicate where two transverse coordinates differ by more than 0.5 cm.

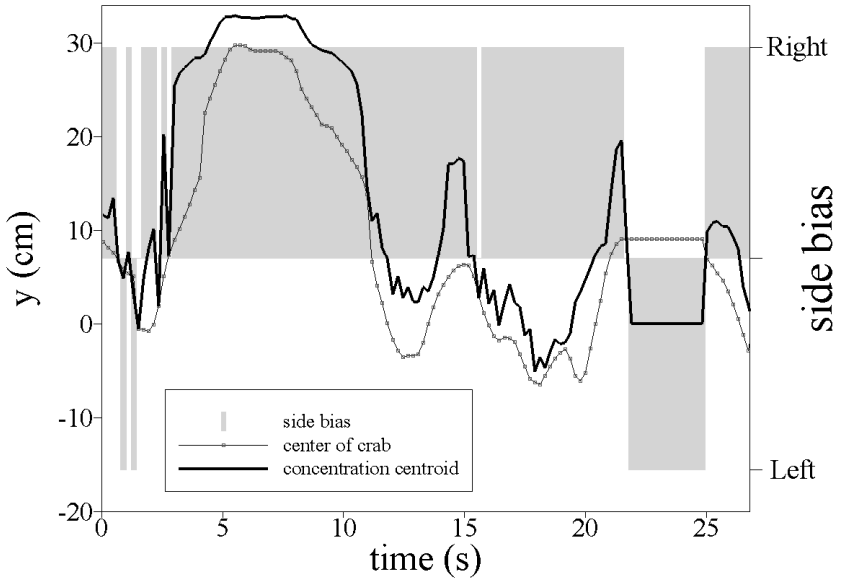

Figure D13. **Crab 105O** time trace of transverse coordinates (cm) of the center of crab and concentration centroid. Side bias shown to indicate where two transverse coordinates differ by more than 0.5 cm.

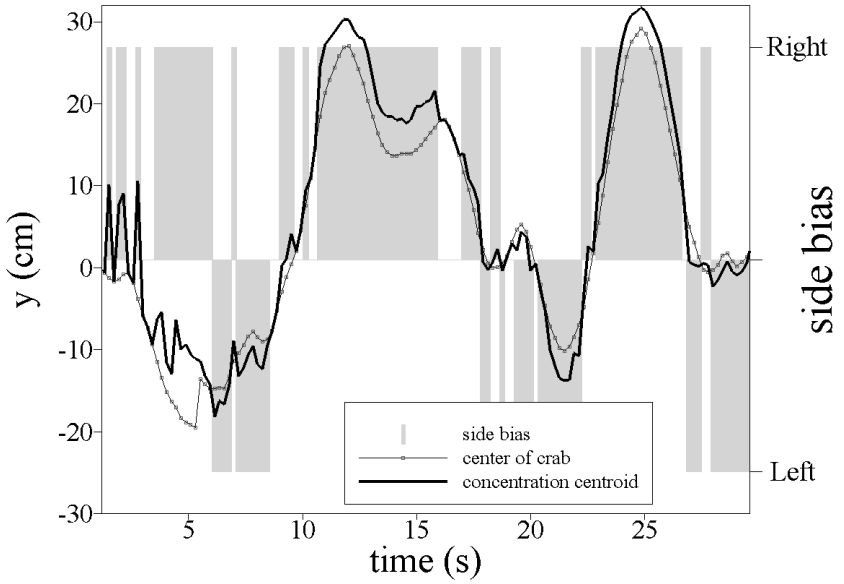

Figure D14. **Crab 122O** time trace of transverse coordinates (cm) of the center of crab and concentration centroid. Side bias shown to indicate where two transverse coordinates differ by more than 0.5 cm.

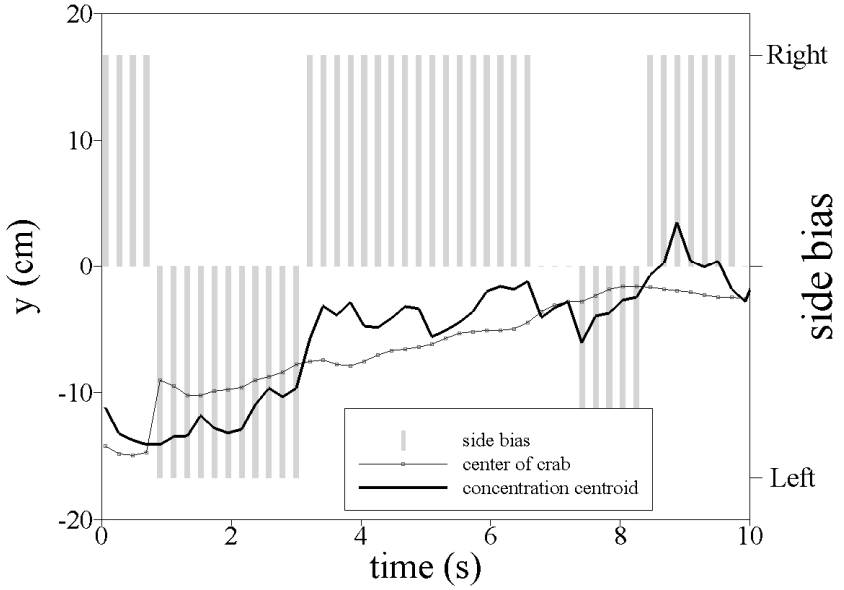

Figure D15. **Crab 1249O** time trace of transverse coordinates (cm) of the center of crab and concentration centroid. Side bias shown to indicate where two transverse coordinates differ by more than 0.5 cm.

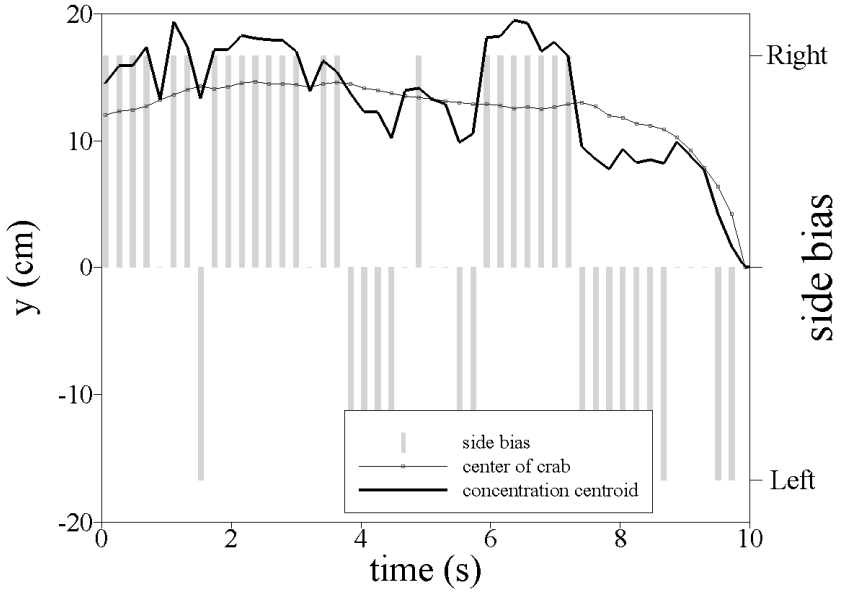

Figure D16. **Crab 1305O** time trace of transverse coordinates (cm) of the center of crab and concentration centroid. Side bias shown to indicate where two transverse coordinates differ by more than 0.5 cm.

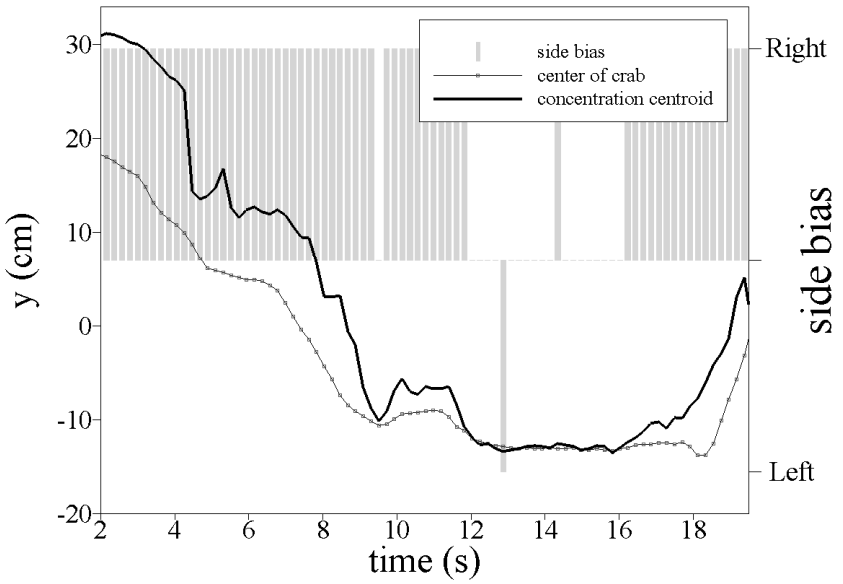

Figure D17. **Crab 1336O** time trace of transverse coordinates (cm) of the center of crab and concentration centroid. Side bias shown to indicate where two transverse coordinates differ by more than 0.5 cm.

Appendix E

Time traces of antennules sampling zone – Pulsed plume

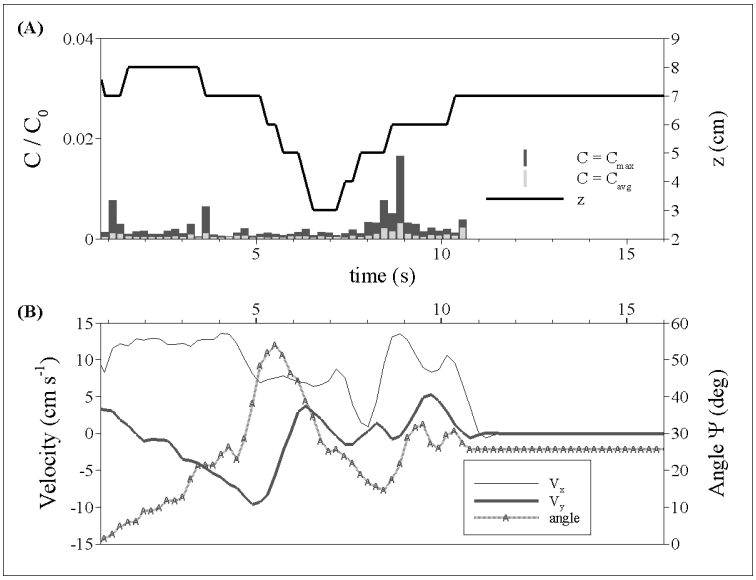

Figure E1. (A) **Crab 112M** time trace of maximum and average relative concentrations at antennules and body elevation above substrate (cm). (B) Time traces of streamwise V_x velocity, transverse V_y velocity and crab angle with respect to the flow, Ψ.

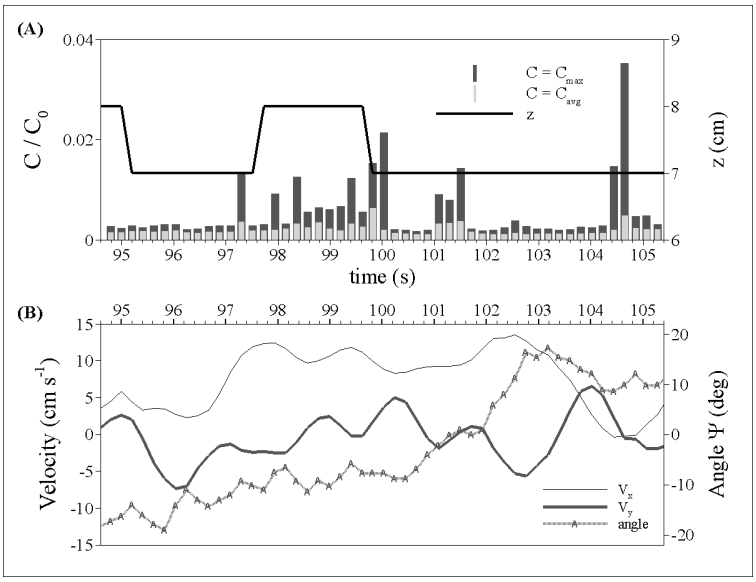

Figure E2. (A) **Crab 122T** time trace of maximum and average relative concentrations at antennules and body elevation above substrate (cm). (B) Time traces of streamwise V_x velocity, transverse V_y velocity and crab angle with respect to the flow, Ψ.

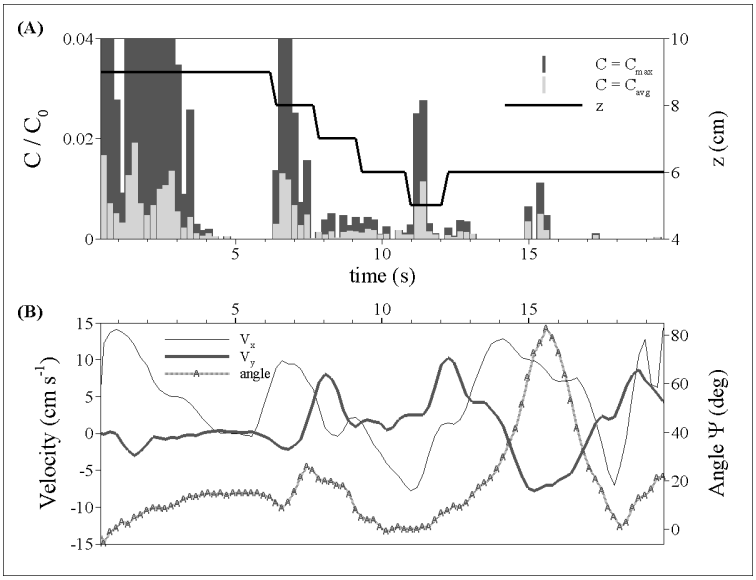

Figure E3. (A) **Crab 1209T** time trace of maximum and average relative concentrations at antennules and body elevation above substrate (cm). (B) Time traces of streamwise V_x velocity, transverse V_y velocity and crab angle with respect to the flow, Ψ.

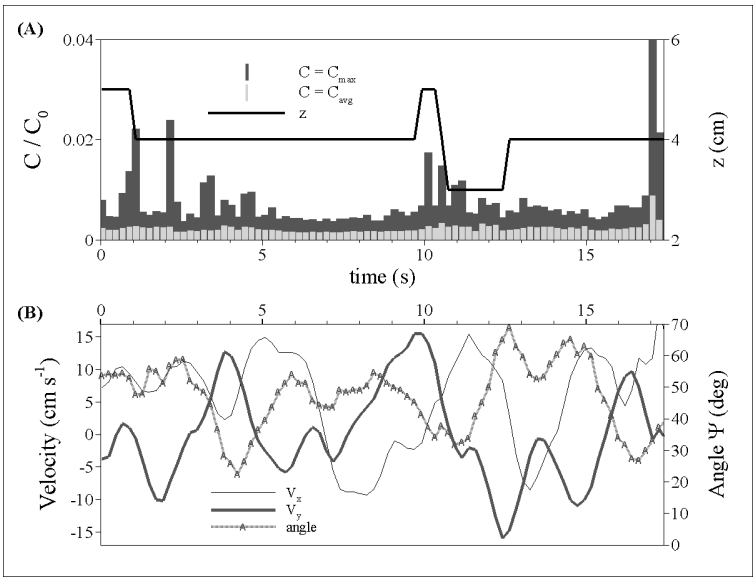

Figure E4. (A) **Crab 1237T** time trace of maximum and average relative concentrations at antennules and body elevation above substrate (cm). (B) Time traces of streamwise V_x velocity, transverse V_y velocity and crab angle with respect to the flow, Ψ.

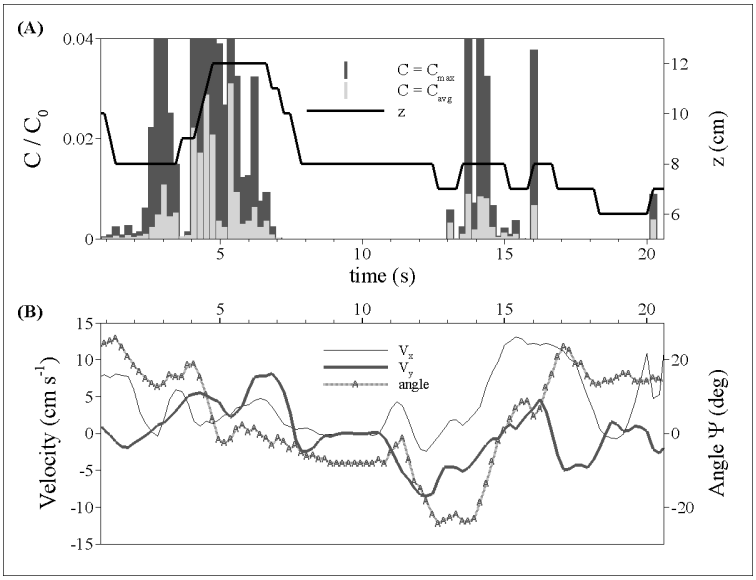

Figure E5. (A) **Crab 1241T** time trace of maximum and average relative concentrations at antennules and body elevation above substrate (cm). (B) Time traces of streamwise V_x velocity, transverse V_y velocity and crab angle with respect to the flow, Ψ.

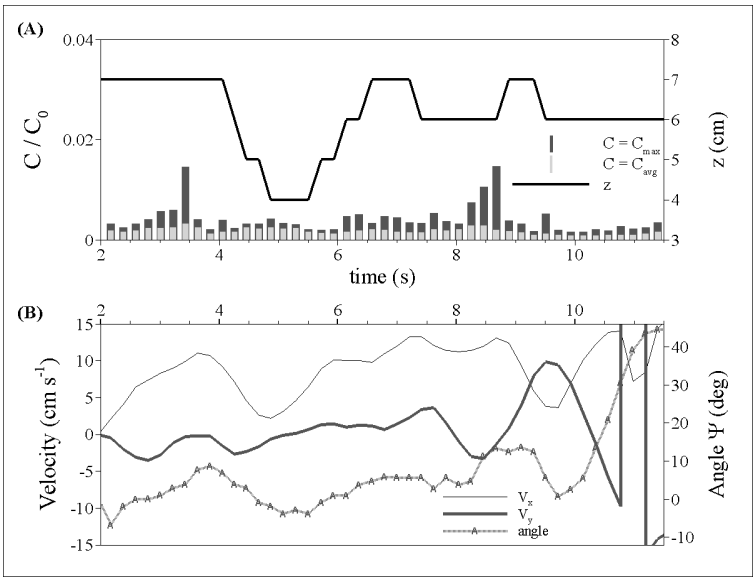

Figure E6. (A) **Crab 1269T** time trace of maximum and average relative concentrations at antennules and body elevation above substrate (cm). (B) Time traces of streamwise V_x velocity, transverse V_y velocity and crab angle with respect to the flow, Ψ.

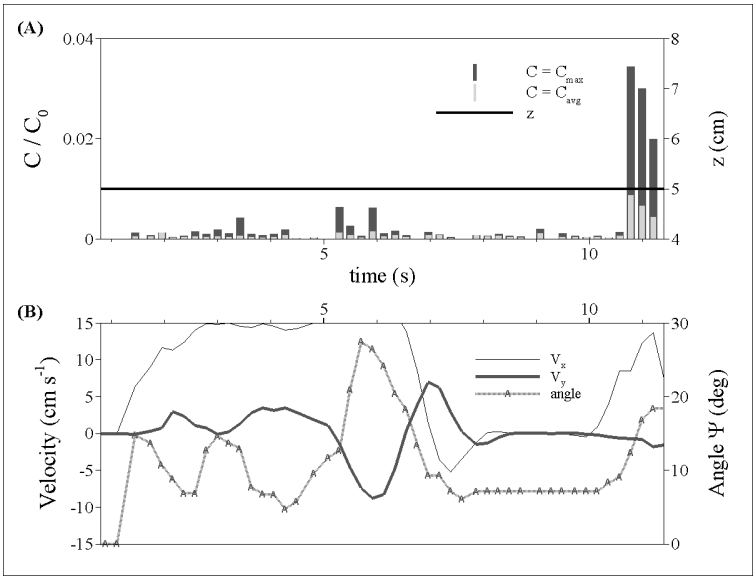

Figure E7. (A) **Crab 1271M** time trace of maximum and average relative concentrations at antennules and body elevation above substrate (cm). (B) Time traces of streamwise V_x velocity, transverse V_y velocity and crab angle with respect to the flow, Ψ.

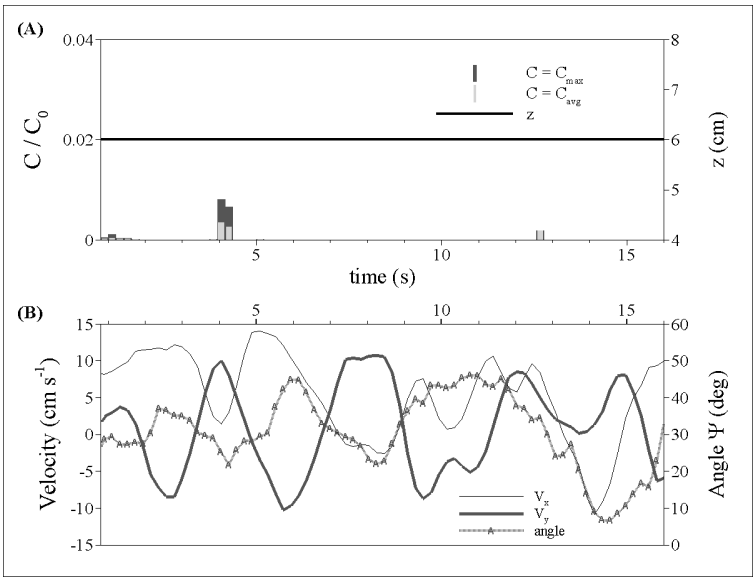

Figure E8. (A) **Crab 1341T** time trace of maximum and average relative concentrations at antennules and body elevation above substrate (cm). (B) Time traces of streamwise V_x velocity, transverse V_y velocity and crab angle with respect to the flow, Ψ.

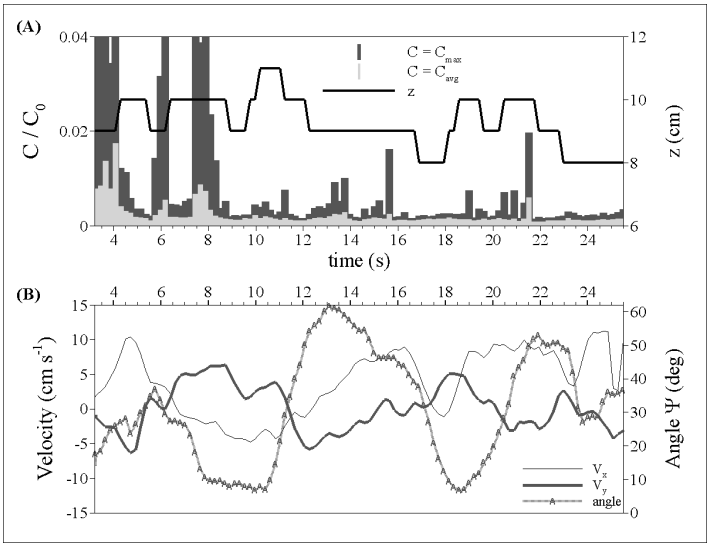

Figure E9. (A) **Crab 1354T** time trace of maximum and average relative concentrations at antennules and body elevation above substrate (cm). (B) Time traces of streamwise V_x velocity, transverse V_y velocity and crab angle with respect to the flow, Ψ.

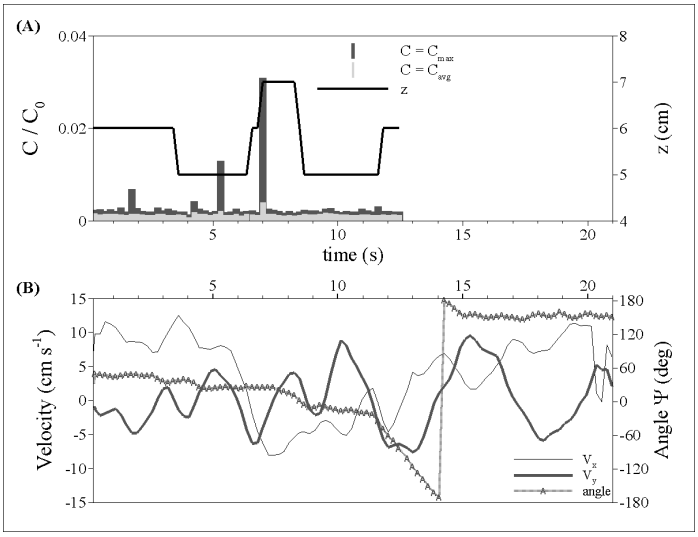

Figure E10. (A) **Crab 1395T** time trace of maximum and average relative concentrations at antennules and body elevation above substrate (cm). (B) Time traces of streamwise V_x velocity, transverse V_y velocity and crab angle with respect to the flow, Ψ. Traces is discontinuous around t = 13 s as the crab rotated and the antennules region no longer faced the laser.

APPENDIX F

Time traces for outer chemosensors – Pulsed plume

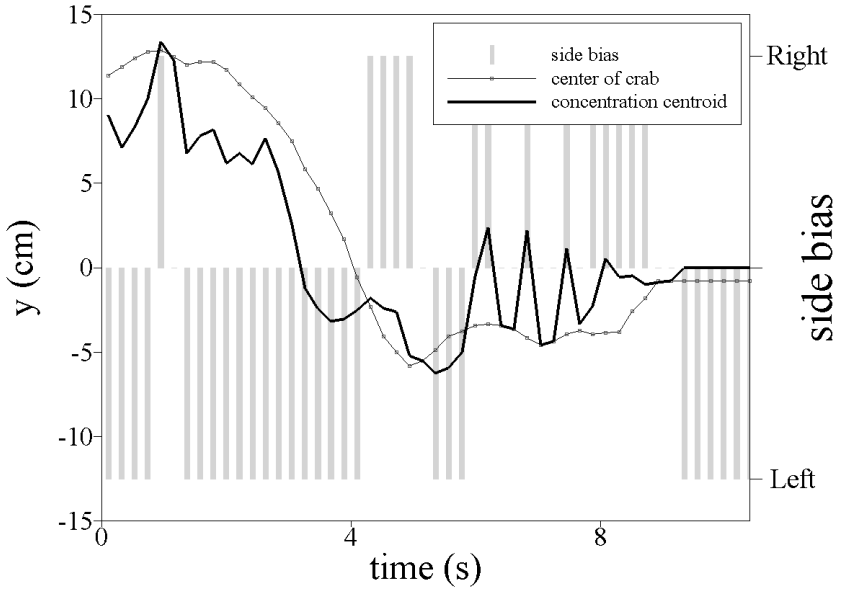

Figure F1. **Crab 112M** time trace of transverse coordinates (cm) of the center of crab and concentration centroid. Side bias shown to indicate where two transverse coordinates differ by more than 0.5 cm.

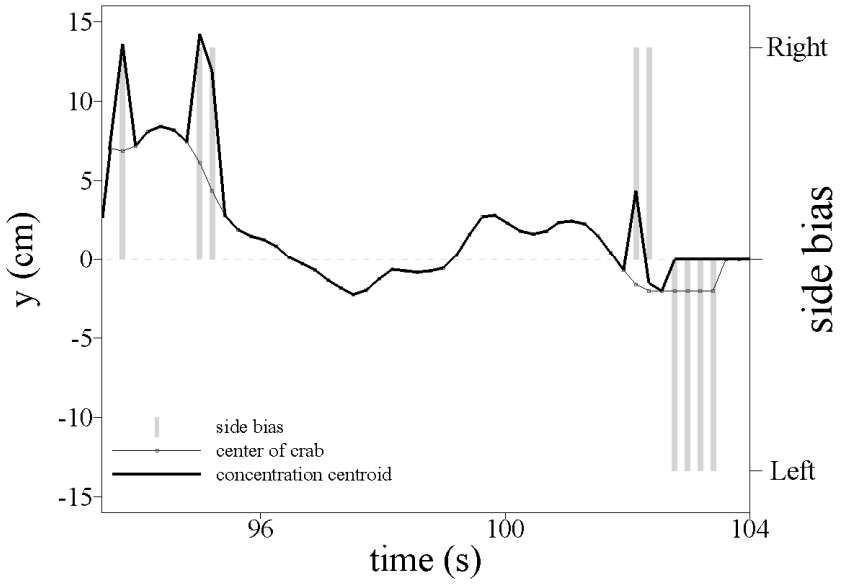

Figure F2. **Crab 122T** time trace of transverse coordinates (cm) of the center of crab and concentration centroid. Side bias shown to indicate where two transverse coordinates differ by more than 0.5 cm.

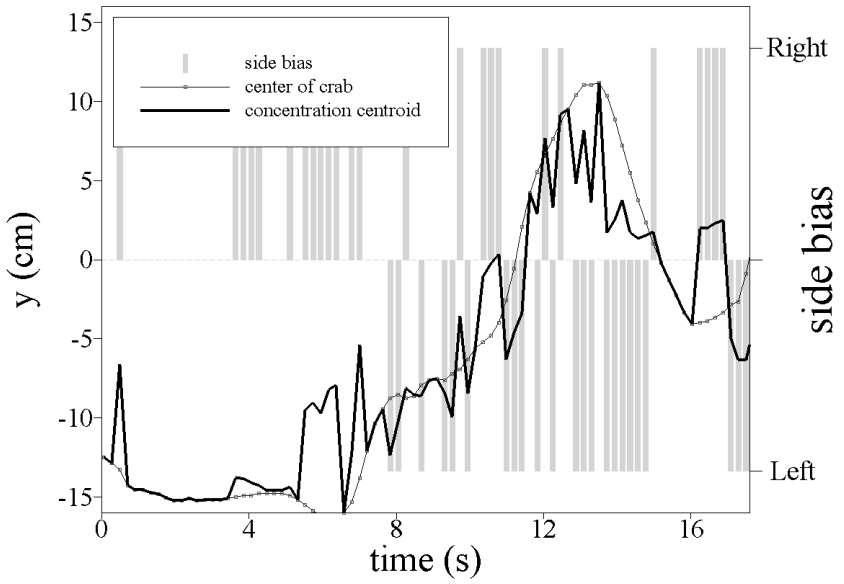

Figure F3. **Crab 1209T** time trace of transverse coordinates (cm) of the center of crab and concentration centroid. Side bias shown to indicate where two transverse coordinates differ by more than 0.5 cm.

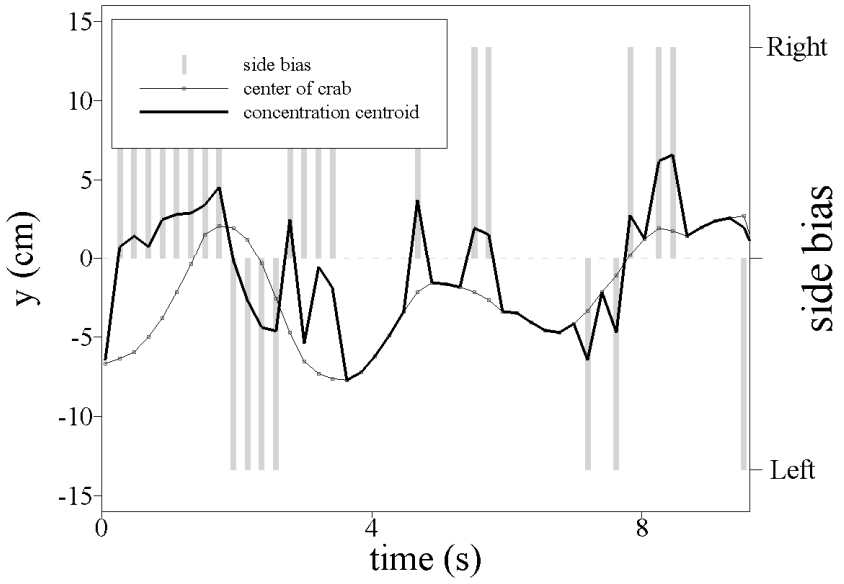

Figure F4. **Crab 1237T** time trace of transverse coordinates (cm) of the center of crab and concentration centroid. Side bias shown to indicate where two transverse coordinates differ by more than 0.5 cm.

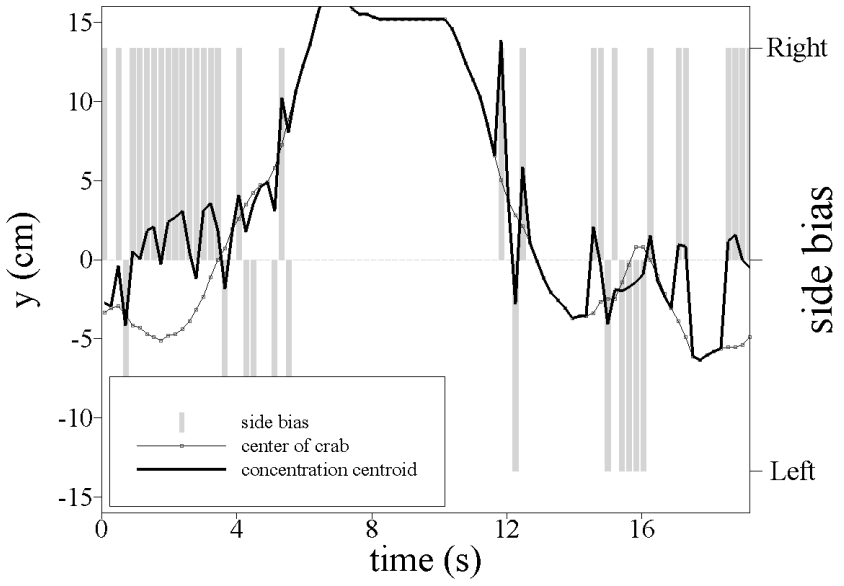

Figure F5. **Crab 1241T** time trace of transverse coordinates (cm) of the center of crab and concentration centroid. Side bias shown to indicate where two transverse coordinates differ by more than 0.5 cm.

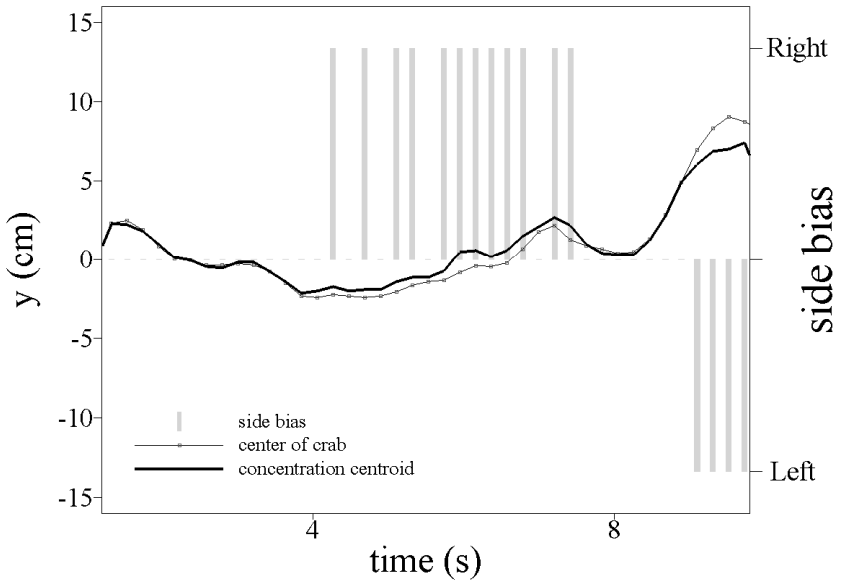

Figure F6. **Crab 1269T** time trace of transverse coordinates (cm) of the center of crab and concentration centroid. Side bias shown to indicate where two transverse coordinates differ by more than 0.5 cm.

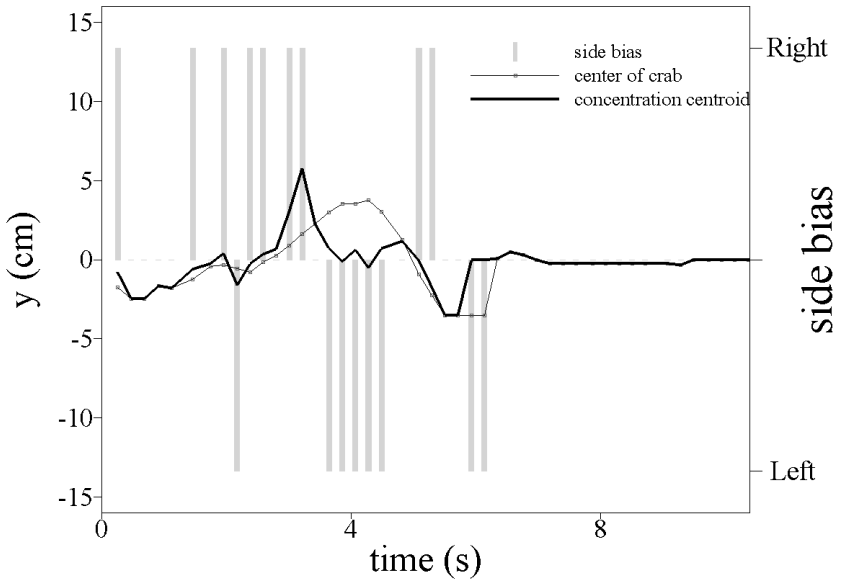

Figure F7. **Crab 1271M** time trace of transverse coordinates (cm) of the center of crab and concentration centroid. Side bias shown to indicate where two transverse coordinates differ by more than 0.5 cm.

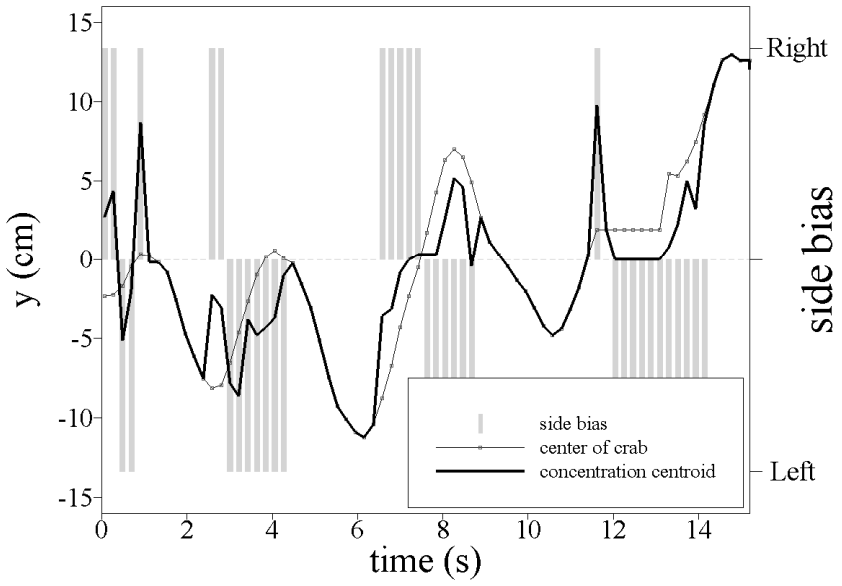

Figure F8. Crab **1341T** time trace of transverse coordinates (cm) of the center of crab and concentration centroid. Side bias shown to indicate where two transverse coordinates differ by more than 0.5 cm

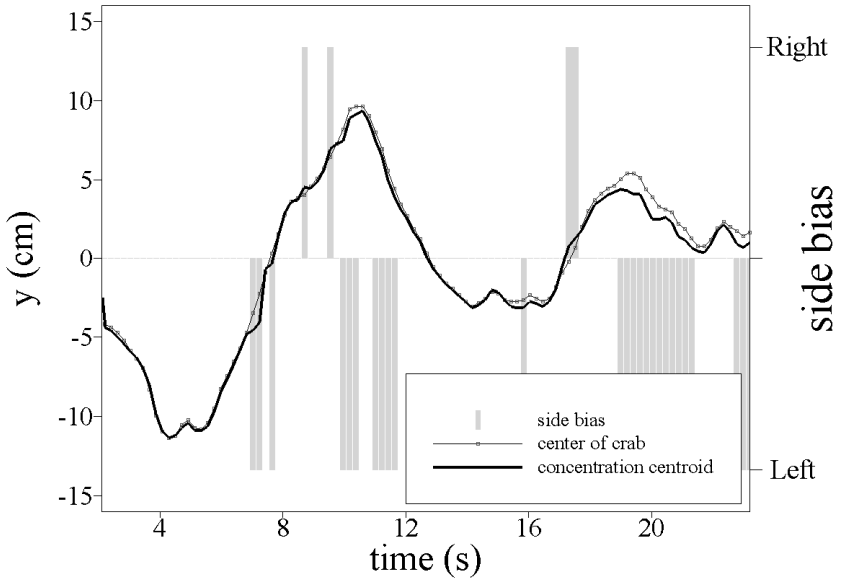

Figure F9. **Crab 1354T** time trace of transverse coordinates (cm) of the center of crab and concentration centroid. Side bias shown to indicate where two transverse coordinates differ by more than 0.5 cm.

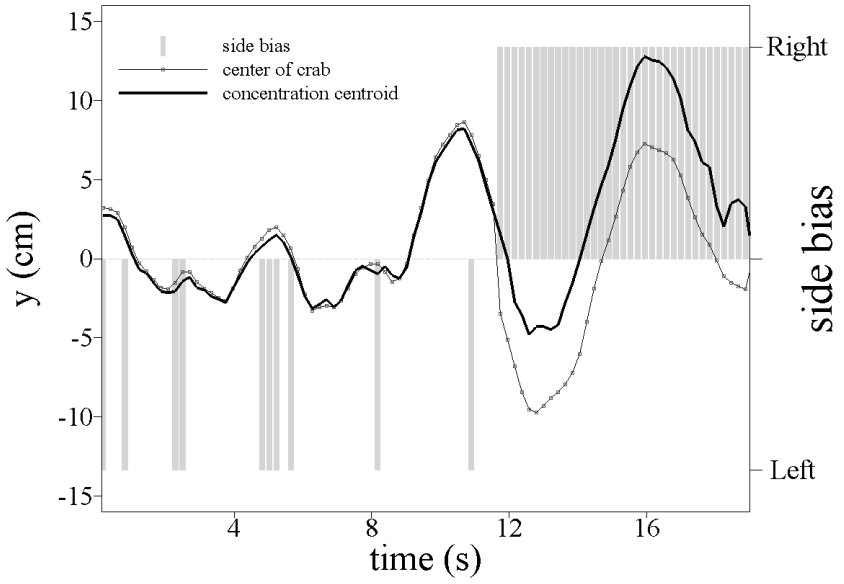

Figure F10. **Crab 1395T** time trace of transverse coordinates (cm) of the center of crab and concentration centroid. Side bias shown to indicate where two transverse coordinates differ by more than 0.5 cm.

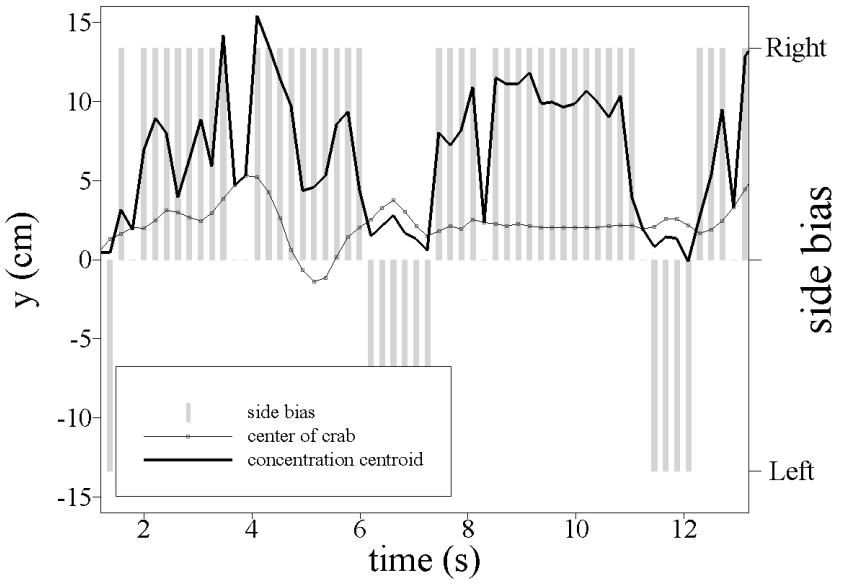

Figure F11. **Crab 105M** time trace of transverse coordinates (cm) of the center of crab and concentration centroid. Side bias shown to indicate where two transverse coordinates differ by more than 0.5 cm.

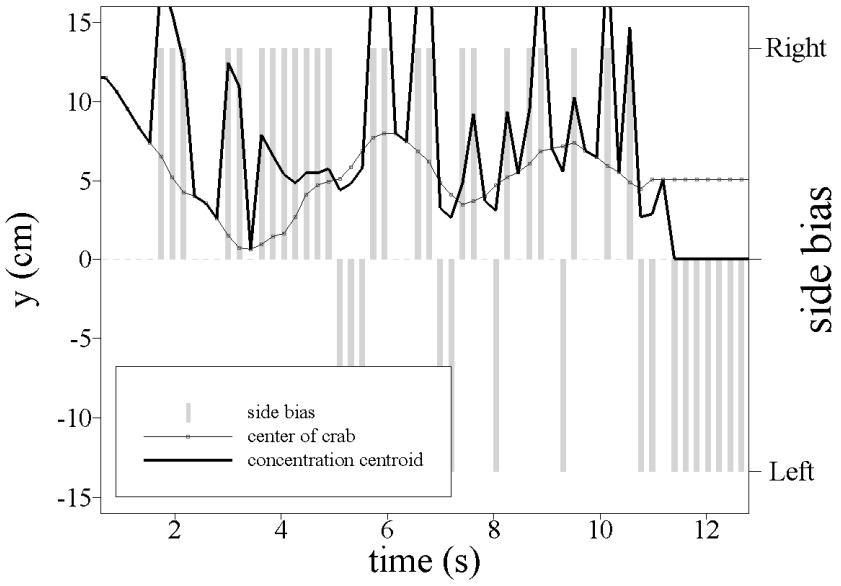

Figure F12. **Crab 461M** time trace of transverse coordinates (cm) of the center of crab and concentration centroid. Side bias shown to indicate where two transverse coordinates differ by more than 0.5 cm.

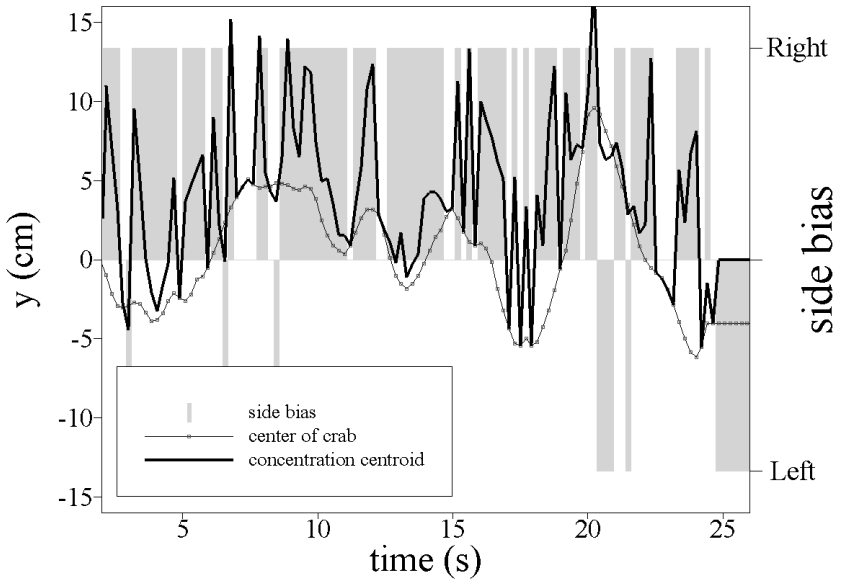

Figure F13. **Crab 471M** time trace of transverse coordinates (cm) of the center of crab and concentration centroid. Side bias shown to indicate where two transverse coordinates differ by more than 0.5 cm.

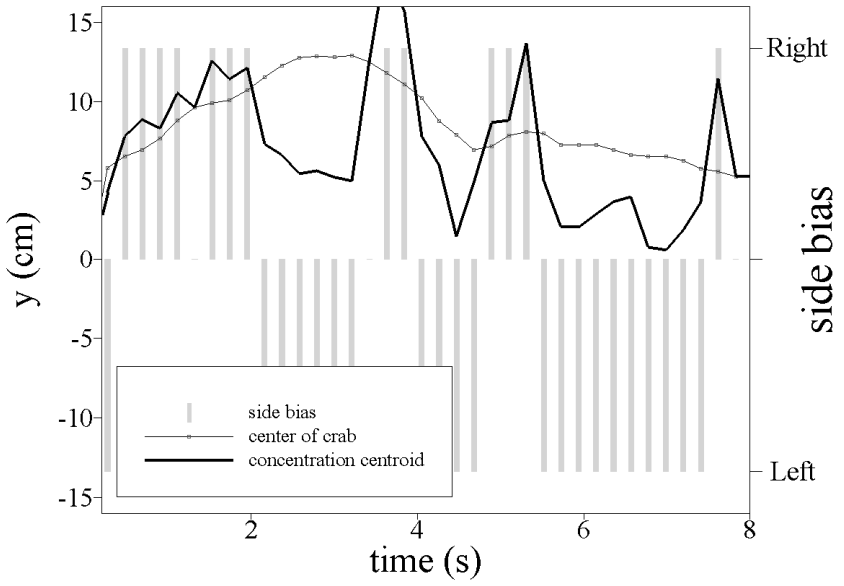

Figure F14. **Crab 1249M** time trace of transverse coordinates (cm) of the center of crab and concentration centroid. Side bias shown to indicate where two transverse coordinates differ by more than 0.5 cm.

REFERENCES

Akinlade, O. G., D. J. Bergstrom, M. F. Tachie, and L. Castillo. 2004. Outer flow scaling of smooth and rough wall turbulent boundary layers. Exp. Fluids **37**: 604-612.

Albertson, M. L., Y. B. Dai, R. A. Jensen, and H. Rouse. 1950. Diffusion of submerged jets. Trans. ASCE **115**: 639-664.

Arcoumanis, C., J. J. McGuirk, and J. M. L. M. Palma. 1990. On the use of fluorescent dyes for concentration measurements in water flows. Exp. Fluids **10**: 177-180.

Atema, J. 1996. Eddy chemotaxis and odor landscapes: Exploration of nature with animal sensors. Biol. Bull. **191**: 129-138.

Bara, B. M., D. J. Wilson, and B. W. Zelt. 1992. Concentration fluctuation profiles from a water channel simulation of a ground-level release. Atmos. Environ. **26A**: 1053-1062.

Barenblatt, G. I. 1993. Scaling laws for fully developed turbulent shear flows. Part 1. Basic hypotheses and analysis. J. Fluid Mech. **248**: 513-520.

Barenblatt, G. I., and V. M. Prostokishin. 1993. Scaling laws for fully developed turbulent shear flows. Part 2. Processing of experimental data. J. Fluid Mech. **248**: 521-529.

Barrett, T. K. 1989. Nonintrusive optical measurements of turbulence and mixing in a stably stratified fluid. Ph.D. thesis, University of California, San Diego.

Batchelor, G. K., and A. A. Townsend. 1956. Turbulent diffusion, p. 352-397. *In* G. K. Batchelor and R. M. Davies [eds.], Surveys in Mechanics. Cambridge at the University Press.

Batchelor, G. K. 1959. Small-scale variation of convected quantities like temperature in turbulent fluid. Part 1. General discussion and the case of small conductivity. J. Fluid Mech. **5**: 113-133.

Brackmann, U. 2000. Lambdachrome laser dyes. Lambda Physik, Göttingen.

Brater, E. F., and H. W. King. 1976. Handbook of Hydraulics. 6th ed. McGraw-Hill.

Brethouwer, G., J. C. R. Hunt, and F. T. M. Nieuwstadt. 2003. Micro-structure and Lagrangian statistics of the scalar field with a mean gradient in isotropic turbulence. J. Fluid Mech. **474**:193-225

Buschmann, M. H., and M. Gad-el-Hak. 2003. Debate concerning the mean-velocity profile of a turbulent boundary layer. AIAA J. **41**: 565-572.

Cantwell, B., and D. Coles. 1983. An experimental study of entrainment and transport in the turbulent near wake of a circular cylinder. J. Fluid Mech. **136**: 321-374.

Carslaw, H. S., and J. C. Jaeger. 1959. Conduction of heat in solids. Oxford, Clarendon Press.

Castleman, K. R. 1996. Digital Image Processing. Prentice Hall.

Cate, H. S., and C. D. Derby. 2001. Morphology and distribution of setae on the antennules of the Caribbean spiny lobster *Panulirus argus* reveal new types of bimodal chemo-mechanosensilla. Cell Tissue Res. **304**: 439-454.

Chandrasekhar, S. 1943. Stochastic problems in physics and astronomy. Rev. Mod. Phys. **15**: 1-89.

Coles, D. 1956. The law of the wake in the turbulent boundary layer. Adv. Appl. Mech. **4**: 1-51.

Corrsin, S. 1951. On the spectrum of isotropic temperature fluctuations in an isotropic turbulence. J. Appl. Phys. **22**: 469-473.

Chatwin, P. C., and P. J. Sullivan. 1979. The relative diffusion of a cloud of passive contaminant in incompressible turbulent flow. J. Fluid Mech. **91**: 337-355.

Chatwin, P. C., and P. J. Sullivan. 1989. The intermittency factor of scalars in turbulence. Phys. Fluids A **1**: 761-763.

Crimaldi, J. P. 1997. The effect of photobleaching and velocity fluctuations on single-point LIF measurements. Exp. Fluids **23**: 325-330.

Crimaldi, J. P., and J. R. Koseff. 2001. High-resolution measurements of the spatial and temporal scalar structure of a turbulent plume. Exp. Fluids **31**: 90-102.

Crimaldi, J. P., M. B. Wiley, and J. R. Koseff. 2002. The relationship between mean and instantaneous structure in turbulent passive scalar plumes. J. Turbul. **3**: 1-24.

Crimaldi, J. P., M. A. R. Koehl, and J. R. Koseff. 2002a. Effects of the resolution and kinematics of olfactory appendages on the interception of chemical signals in a turbulent odor plume. Environ. Fluid Mech. **2**: 35-63.

Crimaldi, J. P., and J. R. Koseff. 2006. Structure of turbulent plumes from a momentumless source in a smooth bed. Environ. Fluid Mech. **6**: 573-592.

Csanady, G. T. 1967. Concentration fluctuations in turbulent diffusion. J. Atmos. Sci. **24**: 21-28.

Dasi, L. P. 2004. The small-scale structure of passive scalar mixing in turbulent boundary layers. Ph.D. thesis, Georgia Institute of Technology.

Dinar, N., H. Kaplan and M. Kleinman. 1988. Characterization of concentration fluctuations of a surface plume in a neutral boundary layer. Bound.-Lay. Meterol. **45**: 157-175.

Dusenbery, D. B. 2001. Performance of basic strategies for following gradients in two dimensions. J. Theor. Biol. **208**: 345-360.

Elder, J. W. 1959. The dispersion of marked fluid in turbulent shear flow. J. Fluid Mech. **5**:544-560.

Elkinton, J. S., R. T. Cardé, and C. J. Mason. 1984. Evaluation of time-average dispersion models for estimating pheromone concentration in a deciduous forest. J. Chem. Ecol. **10**:1081-1108.

Fackrell, J. E., and A. G. Robins. 1982. Concentration fluctuations and fluxes in plumes from point sources in a turbulent boundary layer. J. Fluid Mech. **117**: 1-26.

Ferrier, A. J., D. R. Funk, and P. J. W. Roberts. 1993. Application of optical techniques to the study of plumes in stratified fluids. Dynam. Atmos. Oceans **20**: 155-183.

Finelli, C. M., N. D. Pentcheff, R. K. Zimmer-Faust, and D. S. Wethey. 1999. Odor transport in turbulent flows: Constraints on animal navigation. Limnol. Oceanogr. **44**: 1056-1071.

Fischer, H. B., E. J. List, R. C. Y. Koh, J. Imberger and N. H. Brooks. 1979. Mixing in inland and coastal waters. Academic Press.

Gifford, F. 1959. Statistical properties of a fluctuating plume dispersion model. Adv. Geophysics **6**: 117-136.

Gleeson, R. A. 1980. Pheromone communication in the reproductive behavior of the blue crab, *Callinectes sapidus.* Mar. Behav. Physiol. 7:119-134.

Gomez, G., and J. Atema. 1996. Temporal resolution in olfaction: Stimulus integration time of lobster chemoreceptor cells. J. Exp. Biol. **199**: 1771-1779.

Gulitski, G., M. Kholmyansky, W. Kinzelbach, B. Lüthi, A. Tsinober, and S. Yorish. 2007. Velocity and temperature derivatives in high-Reynolds-number turbulent flows in the atmospheric surface layer. Part 3. Temperature and joint statistics of temperature and velocity derivatives. J. Fluid Mech. **589**: 103-123.

Hanna, S. R. 1984. Concentration fluctuations in a smoke plume. Atmos. Environ. **18**:1091-1106.

Jackson, J. L., D. R. Webster, S. Rahman, and M. J. Weissburg. 2007. Bed-roughness effects on boundary-layer turbulence and consequences of odor-tracking behavior of blue crabs (*Callinectes sapidus*). Limnol. Oceanogr. **52**: 1883-1897.

Jones, C. D. 1983. On the structure of instantaneous plumes in the atmosphere. J. Hazard. Mater. **7**: 87-112.

Keller, T. A., A. M. Tomba, and P. A. Moore. 2001. Orientation in complex chemical landscapes: Spatial arrangement of chemical sources influences crayfish food-finding efficiency in artificial streams. Limnol. Oceanogr. **46**: 238-247.

Keller, T. A., I. Powell, and M. J. Weissburg. 2003. Role of olfactory appendages in chemically mediated orientation of blue crabs. Mar. Ecol. Prog. Ser. **261**: 217-231.

Keller, T. A., and M. J. Weissburg. 2004. Effects of odor flux and pulse rate on chemosensory tracking in turbulent odor plumes by the blue crab, *Callinectes sapidus*. Biol. Bull. **207**: 44-55.

Kennedy, J. S. 1983. Zigzagging and casting as a programmed response to wind-borne odour: a review. Physiol. Entomol. **8**: 109-120.

Koehl, M. A. R., J. R. Koseff, J. P. Crimaldi, M. G. McCay, T. Cooper, M. B. Wiley, and P. A. Moore. 2001. Lobster sniffing: Antennule design and hydrodynamic filtering of information in an odor plume. Science **294**: 1948-1950.

Koehl, M. A. R. 2006. The fluid mechanics of arthropod sniffing in turbulent odor plumes. Chem. Senses **31**: 93-105.

Kolmogorov, A. N. 1941. The local structure of turbulence in incompressible viscous fluid for very large Reynolds numbers. Dolk. Akad. Nauk. SSSR **30**: 301.

Koochesfahani, M. M., and P. E. Dimotakis. 1985. Laser-induced fluorescence measurements of mixed fluid concentration in a liquid plane shear layer. AIAA J. **23**: 1700-1707.

Koochesfahani, M. M., and P. E. Dimotakis. 1986. Mixing and chemical reactions in a turbulent liquid mixing layer. J. Fluid Mech. **170**: 83-112.

Kozlowski, C., R. Voigt, and P. A. Moore. Changes in odour intermittency influence the success and search behaviour during orientation in the crayfish (*Orconectes rusticus*). Mar. Fresh. Behav. Physiol. **36**: 97-110.

Larsen, L. G., and J. P. Crimaldi. 2006. The effect of photobleaching on PLIF. Exp. Fluids **41**: 803-812.

Leonard, A. E., R. Voigt, and J. Atema. 1994. Lobster orientation in turbulent odor plumes: Electrical recording of bilateral olfactory sampling (antennular flicking). Biol. Bull. 187:273.

Lozano, A., B. Yip, and R. K. Hanson. 1992. Acetone – A tracer for concentration measurements in gaseous flows by planar laser-induced fluorescence. Exp. Fluids **13**: 369-376.

Mafra-Neto, A., and R. T. Cardé. 1994. Fine-scale structure of pheromone plumes modulates upwind orientation of flying moths. Nature **369**:142-144.

Mafra-Neto, A., and R. T. Cardé. 1998. Rate of realized interception of pheromone pulses in different wind speeds modulates almond moth orientation. J. Comp. Physiol. A **182**: 563-572.

McKeon, B. J., J. Li, W. Jiang, J. F. Morrison, and A. J. Smits. 2004. Further observations on the mean velocity distribution in fully developed pipe flow. J. Fluid Mech. **501**: 135-147.

Mead, K. S. 2002. From odor molecules to plume tracking: An interdisciplinary, multilevel approach to olfaction in stomatopods. Integ. Comp. Biol. **42**: 258-264.

Mead, K. S., M. B. Wiley, M. A. R. Koehl, and J. R. Koseff. 2003. Fine-scale patterns of odor encounter by the antennules of mantis shrimp tracking turbulent plumes in wave-affected and unidirectional flow. J. Exp. Biol. **206**: 181-193.

Monin, A. S., and A. M. Yaglom. 1975. Statistical fluid mechanics: Mechanics of turbulence. Vol. 2. MIT Press.

Moore, P. A., and J. Atema. 1991. Spatial information in the three-dimensional fine structure of an aquatic odor plume. Biol. Bull. **181**: 408-418.

Moore, P. A., N. Scholz, and J. Atema. 1991. Chemical orientation of lobsters, *Homarus americanus*, in turbulent odor plumes. J. Chem. Ecol. **17**: 1293-1307.

Moore, P. A., and J. L. Grills. 1999. Chemical orientation to food by the crayfish *Orconectes rusticus*: influence of hydrodynamics. Anim. Behav. **58**: 953-963.

Moore, P., and J. Crimaldi, 2004. Odor landscapes and animal behavior: tracking odor plumes in different physical worlds. J. Marine Syst. **49**: 55-64.

Murlis, J., J. S. Elkinton, and R. T. Cardé. 1992. Odor plumes and how insects use them. Annu. Rev. Entomol. **37**: 505-532.

Mydlarski, L., and Z. Warhaft. 1998. Passive scalar statistics in high-Peclet-number grid turbulence. J. Fluid Mech. **358**: 135-175.

Mylne, K. R. 1993. The vertical profile of concentration fluctuations in near-surface plumes. Bound.-Lay. Meterol. **65**: 111-136.

Obukhov, A. M. 1949. Structure of the Temperature Field in Turbulence. Izv. Acad. Nauk. USSR, Ser. Geogr. Geophys. **13**: 55.

Pasternak, Z., B. Blasius, and A. Abelson. 2004. Host location by larvae of a parasitic barnacle: larval chemotaxis and plume tracking in flow. 2004. J. Plankton Res. **26**: 487-493.

Pope, S. B. 2000. Turbulent Flows. Cambridge University Press.

Rahman, S. 2002. Effect of bed roughness on scalar mixing in turbulent boundary layers. Ph.D. thesis, Georgia Institute of Technology.

Rahman, S., and D. R. Webster. 2005. The effect of bed roughness on scalar fluctuations in turbulent boundary layers. Exp. Fluids **38**: 372-384.

Rehab, H., R. A. Antonia, and L. Djenidi. 2001. Streamwise evolution of a high-Schmidt-number passive scalar in a turbulent plane wake. Exp. Fluids **31**: 186-192.

Reynolds, W. C., and A. K. M. F. Hussain. 1972. The mechanics of an organized wave in turbulent shear flow. Part 3. Theoretical models and comparisons with experiments. J. Fluid Mech. **54**: 263-288.

Richardson, L. F. 1926. Atmospheric diffusion shown on a distance-neighbour graph. P. Roy. Soc. Lond. A Mat. **110**: 709-737.

Roshko, A. 1954. On the development of turbulent wakes from vortex streets. NACA TN 1191.

Shaughnessy, E. J., and J. B. Morton. 1977. Laser light-scattering measurements of particle concentration in a turbulent jet. J. Fluid Mech. **80**: 129-148.

Smee, D. L., and M. J. Weissburg. 2006. Clamming up: Environmental forces diminish the perceptive ability of bivalve prey. Ecology **87**: 1587-1598.

Speiser, S., and N. Shakkour. 1985. Photoquenching parameters for commonly used laser dyes. Appl. Phys. B **38**: 191-197.

Sutton, O. 1953. Micrometeorology. McGraw-Hill.

Tennekes, H., and J. L. Lumley. 1972. A first course in turbulence. MIT Press.

Tian, X., and P. J. W. Roberts. 2003. A 3D LIF system for turbulent buoyant jet flows. Exp. Fluids **35**: 636-647.

Townsend, A. A. 1951. The diffusion of heat spots in isotropic turbulence. Proc. Roy. Soc. A **209**: 418-430.

Van Vliet, E., S. M. Van Bergen, J. J. Derksen, L. M. Portela, H. E. A. Van der Akker. 2004. Time-resolved, 3D, laser-induced fluorescence measurements of fine-structure passive scalar mixing in a tubular reactor. Exp. Fluids **37**: 1-21.

Vickers, N. J., and T. C. Baker. 1994. Reiterative responses to single strands of odor promote sustained upwind flight and odor source location by moths. Proc. Natl. Acad. Sci. USA **91**: 5756-5760.

Vickers, N. J. 2000. Mechanisms of animal navigation in odor plumes. Biol. Bull. **198*:*** 203-212.

Vickers, N. J., T. A. Christensen, T. C. Baker, and J. G. Hildebrand. Odour-plume dynamics influence the brain's olfactory code. Nature **410**:466-470.

Visser, A. W. 2008. Lagrangian modelling of plankton motion: From deceptively simple random walks to Fokker-Planck and back again. J. Marine Syst. **70**: 287-299.

Wang, G. R., and H. E. Fiedler. 2000. On high spatial resolution scalar measurement with LIF. Exp. Fluids **29**: 257-264.

Warhaft, Z. 2000. Passive scalars in turbulent flows. Annu. Rev. Fluid Mech. **32**: 203-240.

Webel, G., and M. Schatzmann. 1984. Transverse mixing in open channel flow. J. Hydraul. Eng.-ASCE **110**:423-435.

Webster, D. R., and M. J. Weissburg. 2001. Chemosensory guidance cues in a turbulent chemical odor plume. Limnol. Oceanogr. **46**: 1034-1047.

Webster, D. R., P. J. W. Roberts and L. Ra'ad. 2001a. Simultaneous DPTV/PLIF measurements of a turbulent jet. Exp. Fluids **30**: 65-72.

Webster, D. R., S. Rahman, and L. P. Dasi. 2001. On the usefulness of bilateral comparison to tracking turbulent chemical odor plumes. Limnol. Oceanogr. **46**: 1048-1053.

Webster, D. R., S. Rahman, and L. P. Dasi. 2003. Laser-induced fluorescence measurements of a turbulent plume. J. Eng. Mech.-ASCE **129**: 1130-1137.

Weissburg, M. J., and R. K. Zimmer-Faust. 1993. Life and death in moving fluids: Hydrodynamic effects on chemosensory-mediated predation. Ecology **74**: 1428-1443.

Weissburg, M. J. and R. K. Zimmer-Faust. 1994. Odor plumes and how blue crabs use them in finding prey. J. Exp. Biol. **197**: 349-375.

Weissburg, M. J. 1997. Chemo- and mechanosensory orientation by crustaceans in laminar and turbulent flows: From odor trails to vortex streets. *In* M. Lehrer [ed.], Orientation and communication in arthropods. Birkhäuser Verlag.

Weissburg, M. J. 2000. The fluid dynamical context of chemosensory behavior. Biol. Bull **198**: 188-202.

Weissburg, M. J., D. B. Dusenbery, H. Ishida, J. Janata, T. Keller, P. J. W. Roberts, and D. R. Webster. 2002. A multidisciplinary study of spatial and temporal scales containing information in turbulent chemical plume tracking. Environ. Fluid Mech. **2**: 65-94.

Weissburg, M. J., and D. B. Dusenbery. 2002. Behavioral observations and computer simulations of blue crab movement to a chemical source in a controlled turbulent flow. J. Exp. Biol. **205**: 3387-3398.

Weissburg, M. J., C. P. James, D. L. Smee, and D. R. Webster. 2003. Fluid mechanics produces conflicting constraints during olfactory navigation of blue crabs, *Callinectes sapidus*. J. Exp. Biol. **206**: 171-180.

White, F. M. 2005. Viscous Fluid Flow, 3rd ed., McGraw-Hill.

Willis, M. A., and R. T. Cardé. 1990. Pheromone-modulated optomotor response in male gypsy moths, *Lymantria dispar* L., upwind flight in a pheromone plume in different wind velocities. J. Comp. Physiol. A, **167**: 169-176.

Wolf, M. C., R. Voigt, and P. A. Moore. 2004. Spatial arrangement of odor sources modifies the temporal aspects of crayfish search strategies. J. Chem. Ecol., **30**: 501-517.

Yee, E., D. J. Wilson, and B. W. Zelt. 1993. Probability distributions of concentration fluctuations of a weakly diffusive passive plume in a turbulent boundary layer. Bound.-Lay. Meterol., **64**: 321-354.

Yeung, P. K., S. Xu, D. A. Donzis, and K. R. Sreenivasan. 2004. Simulations of three-dimensional turbulent mixing for Schmidt numbers of the order 1000. Flow Turbul. Combust., **72**: 333-347.

Yoda, M., L. Hesselink, and M. G. Mungal. 1994. Instantaneous three-dimensional concentration measurements in the self-similar region of a round high-Schmidt-number jet. J. Fluid Mech., **279**: 313-350.

Zagarola, M. V., A. E. Perry, and A. J. Smits. 1997. Log laws or power laws: The scaling in the overlap region. Phys. Fluids, **9**: 2094-2100.

Zagarola, M. V., and A. J. Smits. 1998. Mean-flow scaling of turbulent pipe flow. J. Fluid Mech., **373**: 33-79.